Numerical and Experimental Study of Shared Mooring Systems for Prototype Floating Wind Farms

Guodong Liang

UiA University of Agder

Doctoral Dissertations at the University of Agder 431

Numerical and Experimental Study of Shared Mooring Systems for Prototype Floating Wind Farms

Guodong Liang

Numerical and Experimental Study of Shared Mooring Systems for Prototype Floating Wind Farms

Doctoral Dissertation for the Degree *Philosophiae Doctor (Ph.D.)*
at the Faculty of Engineering and Science, Specialisation in Engineering Sciences,
Civil and Structural Engineering

University of Agder
Faculty of Engineering and Science
2023

Doctoral Dissertations at the University of Agder 431
ISSN: 1504-9272
ISBN: 978-82-8427-148-4

Printed by 07 Media
Kristiansand

Abstract

Conventional mooring systems represent a substantial portion of the cost of a floating offshore wind farm (FOWF). The concept of shared mooring was initially proposed to reduce the overall usage of mooring lines and the number of anchors required by connecting adjacent floating offshore wind turbines (FOWTs) in an FOWF. Although such a concept offers cost-saving potential, extra complexity has been introduced to the floating system as the platform motions of FOWTs are coupled. To demonstrate the feasibility of shared mooring systems, it is of great interest and importance to understand the fundamental influence of shared mooring systems on the dynamic characteristics of FOWFs.

Limited research has been conducted concerning detailed dynamic analyses of shared mooring systems and experimental investigations of FOWFs. This thesis addresses this knowledge gap by conducting numerical and experimental studies on prototype dual-spar FOWFs with shared mooring systems. Extensive investigations are carried out considering various shared mooring configurations, different turbine spacings and water depths, and varying mooring properties, configurations, and load scenarios.

In the numerical study, a modeling method is developed for shared mooring systems utilizing Irvine's elastic catenary theory for hanging cables, which serves as the basis for the mooring stiffness linearization and eigenvalue analysis of FOWFs with shared mooring systems. For a dual-spar FOWF, a shared line connecting two FOWTs is the basic shared mooring configuration. The influence of the shared line on the system's natural periods and eigenmodes are investigated through a comparison to a single spar FOWT. The investigation reveals the significant influence of the shared line on the natural periods of surge and sway degrees of freedom (DOFs) of the spar platforms due to the dominance of mooring stiffness in the relevant terms of restoring stiffness. Moreover, the natural periods of these DOFs are found to be sensitive to variations in the mooring properties of both the single lines connecting the FOWTs to the seabed and the shared line connecting adjacent FOWTs. The basic shared mooring configuration is then modeled with a numerical simulation tool to perform fully coupled time-domain simulations under varying environmental conditions (ECs). A comparison with a single spar FOWT demonstrates larger motion ranges and dynamic motions of FOWTs in the FOWF, along with higher tension levels in the single lines. The shared line experiences high dynamic tension and snap load events. The studied mooring layout displays sensitivity to loading directions due to its inherent asymmetry. An alternative shared mooring system is considered

by connecting neighboring FOWTs to a shared tethered buoy and by replacing the single lines of the FOWTs with hanging lines connected to individual tethered buoys. Through dynamic analyses under various load scenarios and comparison against the basic shared mooring configuration, it is concluded that the proposed tethered-buoy shared mooring system can achieve a significant reduction in tension levels across all mooring lines and alleviate potential threats associated with snap loads, with a trade-off for increased mean offset and dynamic motions of the FOWTs. Therefore, the proposed tethered-buoy shared mooring system is a preferred solution for future applications involving inter-array cables, where the excursion restrictions of FOWTs become less critical.

A hydrodynamic model test campaign is conducted for dual-spar FOWFs with different shared mooring systems. Decay tests are carried out, and regular and irregular wave tests are performed under various ECs. Detailed physical modeling of the FOWTs and shared mooring systems are documented. Through a comparison to the results of a previously tested single spar FOWT, the findings from the numerical study are verified. A clump weight is introduced at the midpoint of the shared line in the basic shared mooring configuration, and its effects are investigated through a comparative analysis where the natural periods, motion response, and mooring tension before and after the inclusion of the clump weight are analyzed. The added clump weight leads to a decrease in the natural periods of horizontal DOFs and reduced dynamic motions of the FOWTs. Despite an increase in the pretension of all mooring lines, dynamic tension in these lines is reduced, and a reduced number of snap load events in the shared line is observed.

In summary, this thesis investigates shared mooring systems for prototype dual-spar FOWFs by numerical and experimental approaches. A quasi-static modeling method of shared mooring systems is developed and applied. The dynamic characteristics of FOWFs with five shared mooring configurations are revealed, and the station-keeping performance of the FOWF systems are highlighted in the comparison. These research outcomes augment the current understanding of and expand the existing knowledge base related to shared mooring systems. The analysis methods developed and employed in this study can be further utilized in the design and optimization of FOWFs.

Abstract in Norwegian

Konvensjonelle fortøyningssystemer utgjør en betydelig del av kostnadene ved en flytende havvindpark (FOWF). Konseptet med delt fortøyning ble opprinnelig foreslått for å redusere den samlede bruken av fortøyningsliner og antall ankere, ved å koble sammen nærliggende flytende havvindturbiner (FOWT-er) i en FOWF. Selv om et slikt konsept potensielt kan gi kostnadsbesparelser, har det ført til større kompleksitet i det flytende systemet, ettersom det blir et samvirke mellom bevegelsene til de sammenkoblede FOWT-ene. For å demonstrere gjennomførbarheten av delte fortøyningssystemer er det av stor interesse å forstå de grunnleggende påvirkningene delte fortøyningssystemer har på de dynamiske egenskapene til FOWF-er.

Det er begrenset forskning på detaljerte dynamiske analyser av delte fortøyningssystemer og eksperimentelle undersøkelser av FOWF-er. Denne avhandlingen tar sikte på å fylle dette kunnskapsgapet, ved å utføre numeriske og eksperimentelle studier på prototyper til dual-spar FOWF-er med delte fortøyningssystemer. Omfattende undersøkelser ble gjennomført med ulike delte fortøyningskonfigurasjoner, ulike avstander mellom turbinene, ulike vanndybder, samt varierende fortøyningsparametere, konfigurasjoner og lastscenarioer.

I den numeriske studien utvikles en modelleringsmetode for delte fortøyningsystemer ved hjelp av Irvine's elastiske catenary-teori for hengende kabler. Denne danner grunnlaget for fortøyningsstivhetens linearisering og egenverdianalyse for FOWF-er med delte fortøyningsystemer. For en dual-spar FOWF er den grunnleggende delte fortøyningskonfigurasjonen en delt fortøyningsline som kobler to FOWT-er sammen. Innflytelsen av den delte fortøyningslinen på systemets naturlige perioder og egenmoder undersøkes gjennom sammenligning med en enkelt spar FOWT. Undersøkelsen viser den store innflytelsen fra den delte linen på de naturlige periodene til frihetsgadene (DOF) representert ved jaging (surge) and svaiing (sway) til spar-plattformene, på grunn av den dominerende fortøyningsstivheten i de relevante termer for gjenopprettingsstivheten. Videre viser det seg at de naturlige periodene til disse frihetsgradene er følsomme for variasjoner i fortøyningsegenskapene til både de enkelte linene som forbinder FOWT-ene til havbunnen og den delte linen som forbinder tilstøtende FOWT-er. Den grunnleggende delte fortøyningskonfigurasjonen modelleres deretter med et numerisk simuleringverktøy for å utføre fullt koplet tidsdomene-simuleringer under varierte lastkondisjoner. En sammenligning med en enkelt spar FOWT viser større bevegelsesomfang og dynamiske bevegelser av FOWT-er i FOWF, sammen med høyere strekk-kraft i de enkelte linene. Den delte linen opplever høy dynamisk strekk-kraft og «snap loads». Den undersøkte fortøyn-

ingskonfigurasjonen viser sensitivitet for lastretninger på grunn av sin iboende asymmetri. Et alternativt fortøyninssystem er også undersøkt der tilstøtende FOWT-er er koblet sammen med en delt fortøyd bøye i tillegg til at de enkelte linene til ankerne er byttet ut med hengende liner til egne individuelle flytende bøyer som videre har en strekk forbindelse ned til et eget anker. Gjennom dynamiske analyser under ulike lastscenarioer og sammenligning med den grunnleggende delte fortøyningskonfigurasjonen, konkluderes det med at det alternative delte fortøyningsystemet med fortøyd bøye kan oppnå en betydelig reduksjon i strekk-last nivåer på alle fortøyningsliner. I tillegg til å redusere potensielle risikoer knyttet til «snap-load» belastninger, med et kompromiss for økt gjennomsnittlig bevegelsesradius og dynamiske bevegelser av FOWT-ene. Derfor er det foreslåtte delt fortøyningsystemet med delt fortøyd bøye en foretrukket løsning for fremtidige anvendelser som involverer delte kabelsystemer, der begrensningene i bevegelsesradiusen til FOWT-ene blir mindre kritiske.

En hydrodynamisk modelltestkampanje er gjennomført for dual-spar FOWF-er med ulike delte fortøyningssystemer. Eksperimenter for å undersøke dynamiske egenskaper er utført,samt eksperimenter med regelmessige og uregelmessige bølger under ulike last betingelser. Detaljerte fysiske modelleringer av FOWT-er og delte fortøyningsystemer er dokumentert. Gjennom sammenligning med resultatene fra en tidligere testet enkelt spar FOWT, er funnene fra den numeriske studien verifisert. En klumpvekt blir introdusert ved midtpunktet av den delte linen i den grunnleggende delte fortøyingskonfigurasjonen, og effektene blir undersøkt gjennom en sammenlignings analyse. I denne analysen undersøkes naturlige perioder, bevegelsesrespons og linenes strekk-kraft før og etter inkluderingen av klumpvekten. Den tilføyde klumpvekten fører til en reduksjon i naturlige perioder for horisontale frihetsgrader og redusert dynamisk bevegelse for FOWT-ene. Til tross for en økning i forspenning i alle fortøyningsliner, reduseres dynamisk strekk-kraft i disse linene, og et redusert antall «snap-load» hendelser i den delte linen observeres.

Oppsummert undersøker denne avhandlingen delte fortøyningsystemer for prototyper av dual-spar FOWF-er ved hjelp av numeriske og eksperimentelle tilnærminger. En kvasi-statisisk modelleringsmetode for delte fortøyningsystemer er utviklet og anvendt. De dynamiske egenskapene til fem forskjellige delte fortøyningskonfigurasjoner for FOWF-er presenteres og evnen til å opprettholde forventet posisjon blir fremhevet i sammenligningen. Disse forskningsresultatene bidrar til å styrke den nåværende forståelsen og utvide den eksisterende kunnskapsbasen knyttet til delte fortøyningsystemer. Analysemetodene som er utviklet og benyttet i denne studien kan videre benyttes i design og optimalisering av FOWF-er.

Preface

This thesis is submitted to the University of Agder (UiA) for partial fulfillment of the requirements for the degree of philosophiae doctor.

This doctoral work was performed at the Department of Engineering Sciences, UiA, Grimstad, with Associate Professor Zhiyu Jiang as main supervisor and with Karl Otto Merz at Framti Production AS as co-supervisor.

The thesis was financially supported by the Norwegian Ministry of Education and Research through the Department of Engineering Sciences, UiA. This support is greatly appreciated.

Acknowledgments

I would like to express my sincere thanks to my supervisor, Associate Professor Zhiyu Jiang. I have gained invaluable knowledge and experience from his expertise as well as his great enthusiasm for and discipline in scientific research. His guidance has greatly contributed to shaping my academic thinking and fostering my development as an independent researcher. It has been a great pleasure and privilege to work with him.

I am also grateful to my co-supervisor, Dr. Karl Otto Merz, for his invaluable support, professional guidance, insightful discussions, and unwavering patience during my PhD work.

I extend my appreciation to my wonderful colleagues at the University of Agder, who have created a joyful and motivating atmosphere. I would like to give special thanks to my office mates, Mohammad Ali Mahdavipour, Vidar Hellum, and Zbigniew Mikulski, for their engaging discussions and the enjoyable working environment they have fostered. I would also like to express my gratitude to Ingrid Lande and Vidar Hellum for their assistance with my Norwegian abstract. I am also grateful to Emma Elisabeth Horneman and Paul Ragnar Svennevig for their consistent assistance and support with administrative and financial matters.

I would like to thank all of my friends, both new and old, for their companionship and support.

Finally, my warmest gratitude goes to my parents and my elder brother for their love and support throughout my PhD journey.

List of Appended Papers

This thesis consists of an introductory part and eight papers, which are appended.

Journal papers

JP1:
Mooring Analysis of a Dual-Spar Floating Wind Farm with a Shared Line
Authors: Guodong Liang, Zhiyu Jiang, Karl Otto Merz
Published in *Journal of Offshore Mechanics and Arctic Engineering, 143(6), 2021.*

JP2:
Dynamic Analysis of a Dual-Spar Floating Offshore Wind Farm with Shared Moorings in Extreme Environmental Conditions
Authors: Guodong Liang, Zhiyu Jiang, Karl Otto Merz
Published in *Marine Structures, 90, 103441, 2023.*

JP3:
Experimental Investigation of Two Shared Mooring Configurations for a Dual-Spar Floating Offshore Wind Farm in Irregular Waves
Authors: Guodong Liang, Tomas Lopez-Olocco, Antonio Medina-Manuel, Leandro Antonio Saavedra-Ynocente, Antonio Souto-Iglesias, Zhiyu Jiang
Submitted to *Renewable Energy* for review.

JP4:
Experimental Comparison of a Dual-Spar Floating Wind Farm with Shared Mooring against a Single Floating Wind Turbine under Wave Conditions
Authors: Tomas Lopez-Olocco, Guodong Liang, Antonio Medina-Manuel, Leandro Antonio Saavedra-Ynocente, Zhiyu Jiang, Antonio Souto-Iglesias
Published in *Engineering Structures, 292, 116475, 2023.*

JP5:
Numerical Analysis of a Tethered-Buoy Mooring System for a Prototype Floating Wind Farm
Authors: Guodong Liang, Finn-Christian Wickmann Hanssen, Karl Otto Merz, Zhiyu Jiang
Submitted to *Wind Energy* for review.

Conference papers

CP1:
Modeling of a Shared Mooring System for a Dual-Spar Configuration
Authors: Guodong Liang, Karl Otto Merz, Zhiyu Jiang
Published in *Proceedings of the 39th International Conference on Offshore Mechanics and Arctic Engineering (Vol. 84416, p. V009T09A057). American Society of Mechanical Engineers, 2020.*

CP2:
Influence of Aerodynamic Loads on a Dual-Spar Floating Offshore Wind Farm with a Shared Line in Parked Conditions
Authors: Guodong Liang, Zhiyu Jiang, Karl Otto Merz
Published in *Proceedings of the 41st International Conference on Offshore Mechanics and Arctic Engineering (Vol. 85932, p. V008T09A023). American Society of Mechanical Engineers, 2022.*

CP3:
Model Test of a Dual-Spar Floating Wind Farm in Regular Waves
Authors: Zhiyu Jiang, Guodong Liang, Tomas Lopez-Olocco, Antonio Medina-Manuel, Leandro Antonio Saavedra-Ynocente, Antonio Souto-Iglesias
Published in *Proceedings of the 9th International Conference on Marine Structures, 2023.*

Symbols and Abbreviations

ABS	American Bureau of Shipping
ALS	Accidental limit state
BEM	Blade element momentum
CEHIPAR	*Canal de Ensayos Hidrodinámicos de el Pardo*
CFD	Computational fluid dynamics
COG	Center of gravity
CPMC	Computerized Planar Motion Carriage
DNV	Det Norske Veritas
DOF	Degree of freedom
EC	Environmental condition
FE	Finite element
FLS	Fatigue limit state
FOWF	Floating offshore wind farm
FOWT	Floating offshore wind turbine
GW	Gigawatt
H_s	Significant wave height
IEC	International Electrotechnical Commission
ITTC	International Towing Tank Conference
LC	Load case
LCOE	Levelized cost of energy
MBS	Minimum breaking strength
MPME	Most probable maximum extreme
MW	Megawatt
NREL	National Renewable Energy Laboratory
PSD	Power spectral density

RMS	Root mean square
RS	Response surface
RSM	Response surface method
SD	Standard deviation
SLS	Serviceability limit state
SWL	Still water level
TBBM	Tower-base bending moment
TLP	Tension leg platform
T_p	Spectral peak period
ULS	Ultimate limit state
U_w	Mean wind speed

Contents

List of Figures

List of Tables

Chapter 1

Introduction

1.1 Background and motivation

As one of the clean and abundant energy sources available, wind energy has been utilized by people for thousands of years. Starting in 1887 [1], wind turbines have been built to transform wind energy into electricity. A wind farm is a group of wind turbines built together in the same place for electricity production, which needs a lot of space. Depending on the location of the site, wind farms are categorized into onshore and offshore wind farms. Nowadays, wind farms are widely deployed onshore and offshore. In 2022, 17% of the electricity demand in Europe was covered by wind energy, with 14% from onshore wind and 3% from offshore wind [2].

In order to meet national and United Nations' goals for decarbonizing the energy supply, an increase in production from wind energy is urgently needed. The Global Wind Energy Council expects 680 gigawatt (GW) of newly installed wind capacity globally between 2023 and 2027, which is 75% of the total global wind power capacity (2022) [3]. Benefiting from more abundant space and wind resources in the ocean

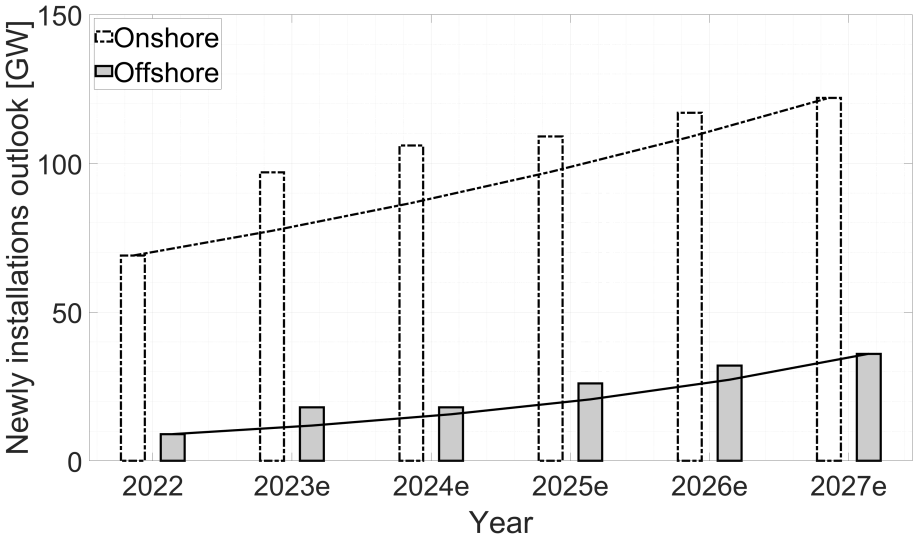

Figure 1.1: New installation outlook of onshore and offshore wind (data from [3], 2023e: expectation in 2023).

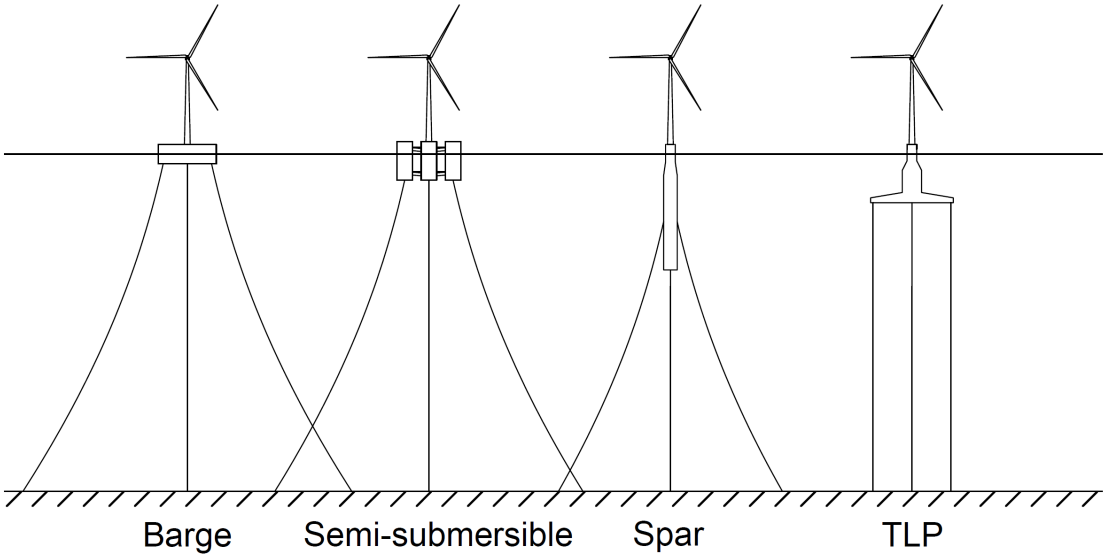

Figure 1.2: Main types of floating substructures for offshore wind turbines.

and the advantage of less visual impact compared to onshore wind, offshore wind grows rapidly as a commercially available energy technology. As shown in Fig. 1.1, the predicted new installations of offshore wind will continually increase from 2023 to 2027. The compound annual growth rate of offshore wind is 32%, much higher than that of onshore wind, which is 12% [3]. The offshore wind industry inherits experience from the conventional offshore oil and gas industry. Different types of substructures are adopted to support wind turbines in the ocean. In the shallow water region, with water depth up to 60 m, bottom-fixed substructures are preferred in practice, such as monopile, jacket, tripod, and gravity-based substructures. For the region with water depth deeper than 60 m, floating substructures, such as spar, semi-submersible, barge, and tension-leg-platform (TLP) substructures, are feasible solutions.

Currently, the vast majority of commercial offshore wind farms are constructed with bottom-fixed wind turbines, whose technology is relatively mature. Monopiles are the dominant substructure type, accounting for 64% of total offshore wind foundations [4]. However, 80% of the global offshore wind resource potential lies in areas deeper than 60 m [3]. As the seabed areas suitable for bottom-fixed offshore projects are used up, the market of floating wind is garnering more interest. Floating wind has just entered the commercialization phase and is expected to have a rapid acceleration from 2030 [3]. Fig. 1.2 shows an illustration of the four mainstream types of floating substructures for offshore wind turbines, developed with different stabilization methods adapted from offshore oil and gas platforms. A spar floating offshore wind turbine (FOWT) is mainly ballast stabilized, with its center of gravity (COG) much lower than the center of buoyancy. Semi-submersible and barge FOWTs are buoyancy stabilized, as they have large water-plane areas. For a TLP FOWT, the restoring force mainly comes from its mooring system. Currently, the dominant floating substructure types are semi-submersible and spar. Approximately 65% of the reported operating floating wind projects (2021) use semi-submersible substruc-

tures, and 31% of them use spar substructures, and for the announced floating wind projects (2021), semi-submersible substructures comprise 80%, and spar substructures comprise 9% [4]. There are two floating offshore wind farms (FOWFs) at present, both of which consist of spar FOWTs. The first pilot-scale FOWF, Hywind Scotland, contains five 6-megawatt (MW) spar FOWTs and has been in operation since 2017 [5]. The second FOWF, Hywind Tampen, consists of 11 spar FOWTs with a total capacity of 88 MW, and it is expected to be in full operation during 2023 [6]. In 2022, 66.4 MW floating wind capacity was commissioned globally, with 60.2 MW from Norway's Hywind Tampen project and a 6.2 MW from a semi-submersible FOWT installed in China, called "Fuyao" [3].

The levelized cost of energy (LCOE) is a useful index to compare different methods of electricity generation. According to the National Renewable Energy Laboratory (NREL), in 2021, the LCOE estimate of bottom-fixed offshore wind was \$78/MWh, which was comparable to the LCOE of fossil fuels, such as coal and natural gas, while the LCOE estimate of floating wind from reference projects was \$133/MWh [7]. Despite the promising prospects of floating wind, cost reductions are needed to make floating wind cost-competitive in the energy market. Det Norske Veritas (DNV) estimates that from 2020 to 2050, with the experience of installation and operation built up, the LCOE of floating wind will be reduced to 16% of its present cost, mainly benefiting from the increased capacity factor and the decreased non-turbine investment costs [8]. The design of mooring systems for FOWTs draws on experience from the offshore oil and gas industry, and presently, the mooring system is a significant contributor to the cost of an FOWF. It is estimated that the mooring system can take 10% to 15% of the capital expenditure of an FOWF project [9]. As floating wind goes further offshore and into deeper water with larger farm sizes and bigger wind turbines, to pave the way for the maturity of floating wind technology and its wide deployment, it is of interest to explore innovative mooring solutions with cost-saving potential.

1.2 Mooring systems for floating offshore wind turbines

1.2.1 Mooring configurations for floating offshore wind turbines

To secure the production and transmission of electricity in FOWFs, the mooring system is vital to keep the FOWTs in position. A typical mooring system for an FOWT has three components, as follows:

- **Mooring lines**, which connect an FOWT through fairleads to anchors on the seabed. In practice, mooring lines can have segments with different materials or cross-sectional properties for different purposes.

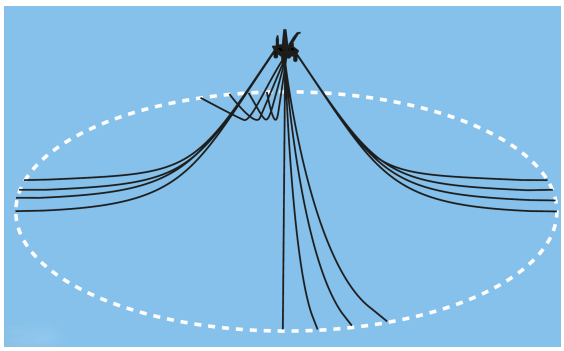

(a) Catenary mooring system

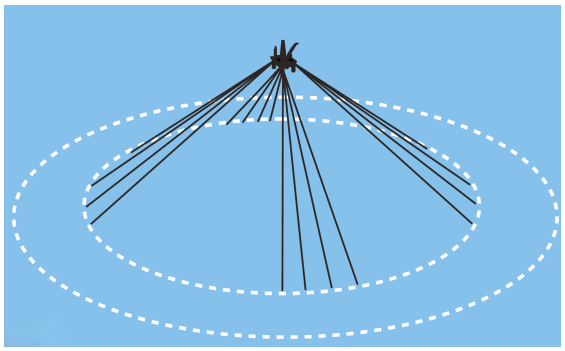

(b) Taut mooring system

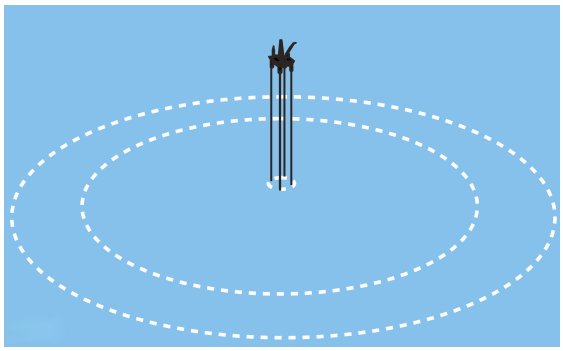

(c) Tendon system

Figure 1.3: The three main types of mooring configurations [10].

- **Mooring connectors**, which are used for the connections between the mooring line and the fairlead or the anchor. If a mooring line has a multi-segment design, connectors are also used to connect different mooring line segments. Swivels, a type of connector, can be placed close to the anchor or between different segments to relieve the twist and torque building up in the mooring line [10].
- **Anchors**, which fix mooring lines on the seabed. Various types of anchors, e.g., drag embedment anchors and pile anchors, can be chosen based on the consideration of loading-bearing requirements, the geographical conditions of the site, and the relevant cost.

In addition, mooring components, such as clump weights and buoyancy components, can be used to improve the performance of the mooring system. In this thesis, analyses of mooring systems focus on mooring lines and mooring components.

For the mainstream types of floating substructures shown in Fig. 1.2, the catenary and taut mooring systems or the tendon systems are usually applied; see Fig. 1.3. In addition, thruster-assisted dynamic positioning may also be considered for the station keeping of FOWTs [11]. The choices of the floater and the mooring system depend on the geographical conditions of the offshore site. Barge and semi-submersible floaters are depth independent. Spar floaters and TLPs are suitable for deep water. Three main types of mooring systems for FOWTs are briefly introduced below.

Catenary mooring system

The catenary mooring system is widely applied for FOWTs. The restoring forces of catenary mooring systems come from the weight of the hanging parts of the mooring lines, which present a catenary shape, and, in extreme cases, from the elastic elongation of the mooring lines. Pretension is applied to the fairlead end of the mooring lines. A sufficient part of the mooring line should lie on the seabed, as the anchor is normally designed to only take horizontal loads. Therefore, the catenary mooring system requires a large footprint; see Fig. 1.3(a). Vertical loads acting on the anchor should be avoided in any case, or anchors that can take vertical loads should be used. As interactions between the mooring lines and the seabed are expected, special care should be given to the corrosion resistance of the mooring lines. The catenary mooring system is applied in Hywind Scotland [12].

Taut mooring system

Pretension is applied to both ends of the mooring lines in a taut mooring system. The elasticity of the mooring lines provides the restoring forces. As the mooring lines are stretched and suspended in the water, the anchors should be designed to take both horizontal and vertical loads from the mooring lines. As shown in Fig. 1.3(b), compared to a catenary mooring system, a taut mooring system has a smaller footprint. Though the total mooring length is reduced, the installation and strength requirements of the mooring lines and anchors should be considered when estimating the cost of a taut mooring system.

Tendon system

The tendon system is applicable for TLP FOWTs. The restoring forces are provided by the large tension in the tendons due to the difference between the buoyancy and weight of the floating body. Anchors for a tendon system are capable of taking vertical loads. If three or more tendons are used with sufficient separation, the heave, pitch, and roll motions of the FOWT are restrained; see the TLP FOWT in Fig. 1.2. If only one central tendon is used, then the FOWT is restrained in the heave direction but compliant with roll and pitch motions [13]. Compared to a catenary mooring system, a tendon system has an even smaller footprint, as shown in Fig. 1.3(c) and requires less mooring material, but the price is extra complexity in the mooring system which leads to high installation cost and risk of failure. In addition, the tendon system provides little resistance to the planar motions of the FOWT and, therefore, is unsuitable for offshore sites with strong tidal currents or storm surges [14].

1.2.2 Materials and components of mooring lines for floating offshore wind turbines

Chain, steel wire rope, and synthetic fiber rope are widely used as mooring materials for floating offshore structures [15]. The main types of mooring materials and mooring components are briefly introduced in this section.

Chain

Chain is most commonly used in mooring lines and is available in various diameters,

grades, and designs (e.g., studlink or studless chain). Provisions are provided by design standards for mooring chain; for example, see [16]. Since studlink chain prevents the mooring line from tangling, it is commonly used for mooring systems that need to be reset during their service life, e.g., semi-submersible structures, though it requires more material than studless chain. Studless chain is usually used for offshore structures with a permanent mooring system, e.g., spar structures. Compared to other mooring materials with the same diameter, chain is quite heavy, which means a large restoring force from its self weight. Chain also has good abrasion characteristics. Therefore, it is commonly used in the catenary mooring system, especially in relatively shallow water. In Hywind Scotland, each of the five spar FOWTs is moored to suction anchors by three mooring chains with a total length of 2,400 m and a total weight of 1,200 tonnes [12].

Steel wire rope

Steel wire rope contains multiple strands, and each strand consists of many wires. The steel wire ropes commonly used in mooring lines are six-strand and spiral-strand ropes [10]. A six-strand steel wire rope has six strands spun closely around a center strand, which makes it flexible, and it has a good resistance against bending fatigue. A spiral-strand steel wire rope consists of multiple layers that are concentric about the strand axis, and each layer is made of helically laid wires. The spiral-strand steel wire rope has a high modulus, good tension fatigue resistance, and torsional balance [17]. For the same breaking strength, a steel wire rope is lighter and more elastic than chain, but it is also more vulnerable to damage and corrosion [10]. Therefore, steel wire rope is recommended to be protected against corrosion by, for example, sacrificial coating or plastic sheathing [18].

Synthetic fiber rope

Synthetic fiber rope can be made of various fiber materials. Low modulus materials, such as polyester and nylon, are likely to be used for compliant mooring systems,

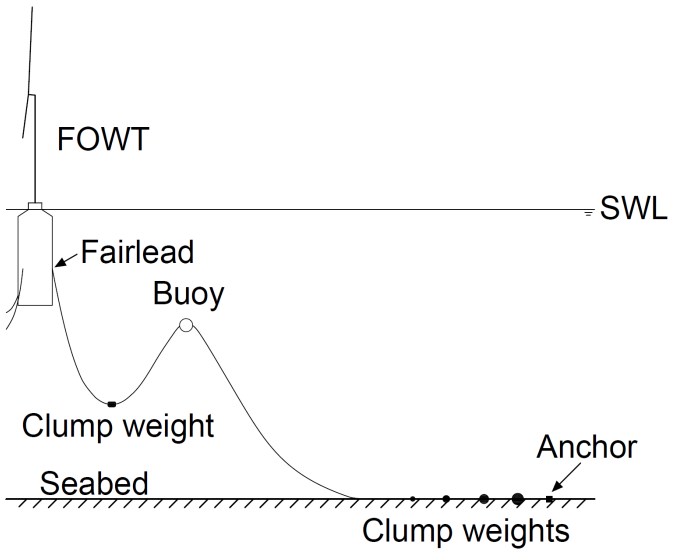

Figure 1.4: Illustration of an FOWT with clump weights and a buoy (SWL: still water level).

and high modulus materials, such as high modulus polyethylene, liquid crystal polymer, and aramid fiber, are suitable for taut mooring systems [24]. Synthetic fiber rope has been widely used in mooring lines for deep water mooring, as it has the advantages of a light weight, high elasticity, and high long-term durability in the face of environmental exposure and fatigue loading [10]. Synthetic fiber rope has a relatively low melting point and is susceptible to sharp objects. Compared to chain and steel wire rope, synthetic fiber rope has more complex material behaviors [25]. Therefore, comprehensive knowledge from tests is required for synthetic fiber rope, or conservative designs should be applied in practice.

Mooring components

As shown in Fig. 1.4, mooring components can be applied to adjust the stiffness characteristics of mooring lines. A clump weight is a concentrated weight mounted on a mooring line to change its geometrical stiffness. It can be used to adjust the

Table 1.1: Selected guidelines and standards for the mooring system design of FOWTs.

Organization	Standards/guidelines
DNV	*DNV-ST-0119 Floating wind turbine structures* [13] supersedes DNV-OS-J103 (2013); it covers the design of floating wind turbine structures, including the tower, substructure, station-keeping systems, and power cables. *DNV-RP-0286 Coupled analysis of floating wind turbines* [19] provides guidance for the modeling, load analysis, and model testing of FOWTs. *DNV-OS-E301 Position mooring* [15] is applicable to the design of mooring systems for floating offshore units. Detailed requirements for chain, steel wire rope, and fiber rope are provided in standards DNV-OS-E302 [16], DNV-OS-E303 [20], and DNV-OS-E304 [18].
ABS	*ABS Guide for Building and Classing Floating Offshore Wind Turbine Installations* [21] covers the design of the floating substructure, the station-keeping system and onboard machinery, etc. *Guidance Notes on Global Performance Analysis for Floating Offshore Wind Turbine Installations* [22] provides suggestions for the global performance analysis, modeling, and numerical simulations of FOWTs.
IEC	*IEC TS 61400-3-2 Wind energy generation systems - Part 3-2: Design requirements for floating offshore wind turbines* [23] specifies the design requirements for the engineering integrity of FOWTs and additional requirements for the assessment of the external conditions at an FOWT site.

pretension level of the mooring line or be fitted on a mooring line lying on the seabed to increase the restoring force when the substructure experiences a large offset.

A buoyancy component, e.g., a buoy, applies an upward force on the mooring line, which changes its geometrical stiffness. Buoyancy components are widely used in deep water mooring to reduce the line weight, and they can also be used on mooring lines to avoid contact with the seabed.

Some innovative concepts of mooring components, such as active dampers [26], have also been proposed to improve the performance of mooring systems.

1.3 Guidelines and analysis methods for mooring systems of floating offshore wind turbines

1.3.1 Guidelines and standards for the mooring system design of floating offshore wind turbines

Technical standards have been produced for the offshore wind industry by international standardization organizations, such as the International Electrotechnical Commission (IEC) and the International Organization for Standardization, regional standardization organizations, such as the European Committee for Standardization, and national standardization organizations, such as the British Standards Institute and the Standard Norge in Norway. In addition, classification bodies have also set specific guidelines and standards for the offshore wind industry, such as DNV, the American Bureau of Shipping (ABS), Bureau Veritas, and Class NK. Some selected guidelines and standards for the mooring system design of FOWTs are summarized in Table 1.1. A more detailed summary of standardization bodies and their offshore wind standards can be found in [27]. This thesis mainly refers to design standards from DNV. Standards and guidelines for the mooring system design of FOWTs released by DNV are briefly discussed in this section.

In DNV-ST-0119 [13], a methodology of consequence class is used to ensure the structural safety of FOWTs. Two consequence classes are defined, i.e., consequence class 1 for the case where failures are unlikely to cause unacceptable consequences, such as loss of life, and consequence class 2 for the case where failures may result in unacceptable consequences. Target safety levels are set for the two consequence classes in the form of an annual probability of failure, which is 10^{-4} for consequence class 1 and 10^{-5} for consequence class 2. According to DNV-ST-0119, as the floating structure of an FOWT is unmanned during severe environmental conditions (ECs), the floating structure and the station-keeping system of an FOWT shall be designed to consequence class 1 unless otherwise indicated. For a station-keeping system without redundancy, such as the tendon system of an FOWT if failure of a tendon causes capsizing, all structural components in the station-keeping system shall be designed to consequence class 2. For an FOWT, limit states define conditions beyond which the FOWT or a structural component of the FOWT no longer satisfies the design requirements. Four categories of limit states are considered in the design of

an FOWT [13], as follows:

- Ultimate limit states (ULSs) correspond to the maximum load-carrying resistance.
- Fatigue limit states (FLSs) correspond to failure due to the effect of cyclic loading.
- Accidental limit states (ALSs) correspond to survival conditions in a damaged condition or in the presence of abnormal ECs.
- Serviceability limit states correspond to project-defined criteria applicable to intended use.

DNV-ST-0119 [13] is based on the partial safety factor method by which the target safety level is achieved by applying load and resistance factors to characteristic values of the governing variables, namely loads acting on the structure or load effects in the structure, and resistance of the structure or strength of the materials in the structure. The partial safety factor format is written as follows:

$$S_d \leq R_d \tag{1.1}$$

where S_d is the design load effect and R_d is the design resistance. DNV-ST-0119 specifies design requirements for the mooring lines of FOWTs in terms of the ULS, ALS, and FLS.

ULS and ALS

The design criteria for mooring lines in the ULS and ALS are as folows:

$$S_C > T_d \tag{1.2}$$

where S_C is the characteristic capacity and T_d is the design tension. Here, T_d consists of the following two factored components:

$$T_d = \gamma_{mean} \cdot T_{c,mean} + \gamma_{dyn} \cdot T_{c,dyn} \tag{1.3}$$

where $T_{c,mean}$ and $T_{c,dyn}$ are the characteristic mean tension and the characteristic dynamic tension, respectively. The calculation procedures for $T_{c,mean}$ and $T_{c,dyn}$ are provided in DNV-OS-E301 [15]. Meanwhile, γ_{mean} and γ_{dyn} are the corresponding

Table 1.2: Load factors for design of mooring lines in DNV-ST-0119 [13].

Consequence class	ULS		ALS	
	γ_{mean}	γ_{dyn}	γ_{mean}	γ_{dyn}
1	1.30	1.75	1.00	1.10
2	1.50	2.20	1.00	1.25

load factors for the two tension components. The load factors are specified in DNV-ST-0119 [13] in terms of consequence class, as presented in Table 1.2.

Here, S_C is defined as a function of the statistics of the breaking strength of the mooring components that make up the main body of the mooring line. When the statistics are not available, S_C may be calculated as follows:

$$S_C = 0.95 \cdot S_{mbs} \tag{1.4}$$

where S_{mbs} is the minimum breaking strength (MBS) of new components.

FLS

The design criterion for mooring lines in the FLS is as follows:

$$D_D \leq 1.0 \tag{1.5}$$

where D_D is the design cumulative fatigue damage. Here, D_D is defined as follows:

$$D_D = DFF \cdot D_C \tag{1.6}$$

where D_C is the characteristic cumulative fatigue damage caused by the stress history in the mooring line over its design life. Here, D_C can be calculated by Miner's sum, and more details are given in [13]. Finally, DFF is the design fatigue factor. For chain and steel wire rope, the value of DFF is 5 for consequence class 1 and 10 for consequence class 2.

1.3.2 Numerical and experimental methods for mooring systems of floating offshore wind turbines

For the design and analysis of FOWTs, the integrated system with moorings under environmental loading is the focus. FOWTs face complex and severe ECs. Wind, waves, and currents are the most common ECs to be included in the design and analysis of FOWTs. Depending on the site location, site-specific ECs, such as tide, tsunami, typhoon, and sea ice, may be taken into account. In addition, for FOWTs in an FOWF, interactions with other FOWTs or structures, such as wake effects and hydrodynamic coupling, may need to be considered. As presented in Sec. 1.3.1, the load effects in the design criteria for the mooring system of FOWTs are expressed by mooring tension. The extreme values and time series of mooring tension are required to demonstrate compliance with the design criteria. Numerical and experimental methods have been developed for the design and analysis of FOWTs. Guidelines and recommendations from the standardization organizations are also available, e.g., [19, 22]. Numerical and experimental methods for the mooring system of an FOWT are briefly discussed in this section.

Numerical method

In general, two alternative numerical methods are usually applied to model mooring lines, namely quasi-static modeling and dynamic modeling. Quasi-static modeling is computationally efficient and often used in the preliminary design phase or for global

performance analysis, while dynamic modeling can predict the loads on mooring lines accurately and is recommended for detailed design and analysis of mooring lines.

In quasi-static modeling, a mooring line is assumed in static equilibrium. The mooring line is modeled as a single line element with a continuous line profile. The effects of inertia, hydrodynamics, and damping of the mooring line are ignored. Tension in the mooring line is modeled by a (linear or nonlinear) force-displacement relationship derived from analytical equations. As formulated in [28], the basic quasi-static modeling only accounts for tension in the vertical plane determined by the line shape. Modifications have been made to consider the tension in arbitrary directions [29]. Quasi-static modeling is available in commercial analysis tools such as Mimosa [30]. Using quasi-static modeling, quick estimations of mooring response can be made in frequency-domain approaches [31]. However, for a catenary mooring system, quasi-static modeling may lead to as much as 30% inaccuracy in the calculation of extreme loads [32].

In dynamic modeling, the inertia and drag forces on mooring lines are important, while hydrodynamic excitation forces acting on mooring lines are normally negligible. In order to account for all relevant loads and dynamic features, the whole FOWT system needs to be modeled and analyzed. This is, however, quite challenging due to the complex coupling of hydrodynamics, aerodynamics, and structural dynamics. An integrated, fully coupled global dynamic response analysis is recommended, in which the evaluation of aerodynamic loads can be completed via blade element momentum (BEM) theory [33], the vortex lattice method [34], or computational fluid dynamics (CFD) [35], and the calculation methods of hydrodynamic loads can be selected from among the Morison equation, potential flow theory, a combination of the Morison equation and potential flow theory, or CFD based on the requirement for fidelity and computational cost. The tension in the mooring lines is then obtained from the global analysis and can be further analyzed in post-processing. In dynamic modeling, a mooring line has multiple elements with the consideration of the inertia and drag forces acting along the line. A lumped-mass method can be applied to discretize the mooring line dynamics over the length [36], in which the mooring line is modeled as node points with lumped weight connected by segments with stiffness and internal damping. Differential equations are established based on the dynamic equilibrium and continuity at each node. The finite element (FE) method can also be adopted to model mooring lines [37], which could capture more accurate dynamic behaviors of the mooring lines. The torsional and bending stiffness of mooring lines can be incorporated in the FE model.

Experimental method

Model tests can be performed to demonstrate the feasibility of a design or provide data for calibration and validation of numerical models. Full-scale tests of FOWT components, such as blades, are usually conducted to test or validate the properties of the components, such as strength and durability, in controlled ECs. There are also tests for mooring components or specimens for MBS tests and fatigue tests, which are needed for certification of mooring systems following classification rules [15] but are not focused on here. Small-scale model tests with a scale of 1:30 to 1:100 are

commonly carried out to test the integrated system of an FOWT with mooring systems under environmental loading [38]. For the model tests of FOWTs subjected to wind, wave, and current loads, physical scaling is a challenge. Froude scaling does well with the hydrodynamic effects of gravity waves, and Reynolds scaling ensures proper modeling of viscous forces and aerodynamic phenomena. It is convenient to apply Froude scaling in a model test, but then the Reynolds number at model scale is usually too small compared to the value in full scale. Conventional model tests of FOWTs in combined wind-wave conditions are commonly carried out based on Froude scaling, with additional setups to deal with the mismatch between the Froude and Reynolds scaling (e.g., using a disk to replace the rotor or using a rotor with modified blades to achieve equivalent thrust force [39, 40]; or using a hybrid model testing solution that simulates the dynamics of the rotor and the generator in a numerical model and applies the simulated force to the turbine tower in real time [41]).

In the model tests of FOWTs with realistic mooring systems, the elastic properties of mooring lines, mainly the axial stiffness, can be important for the total restoring stiffness of the floating system and, therefore, need to be scaled correctly. Axial springs can be installed along a mooring line at one or several places to model the axial stiffness of the mooring line properly. In the case where the water depth of the test facility may limit proper scaling for the model tests, a truncated mooring system may be applied [42, 43]. The pretension in mooring lines needs to be adjusted properly to reproduce the same initial configuration. Prior to the model test, pretension in mooring lines should be checked to assure the accuracy of the physical modeling and model setup. During the test, tension in mooring lines needs to be measured and recorded properly for further analysis.

1.4 State-of-the-art research on floating offshore wind farms with shared mooring systems

As described above, the conventional mooring systems of an FOWF normally consists of several mooring lines or tendons with corresponding anchors for each FOWT.

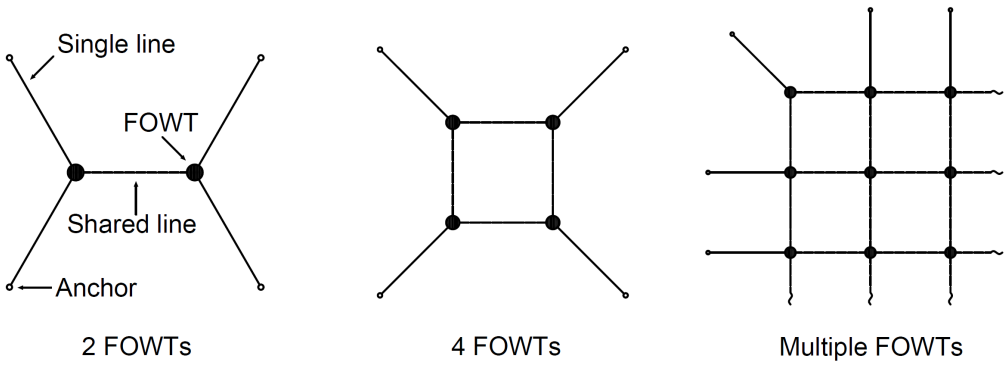

Figure 1.5: Illustration of layout patterns for FOWFs with shared mooring systems.

Thus, longer mooring lines are needed in deeper water, which will increase the mooring cost. Innovative mooring design concepts with cost-saving potentials have been proposed, such as shared moorings [44] and shared anchors [45]. The shared anchor concept reduces the total number of anchors required for an FOWF by sharing anchors among FOWTs. It has already been applied in Hywind Tampen [6].

For an FOWF with a shared mooring system, mooring lines or mooring components are shared among adjacent FOWTs. As shown in Fig. 1.5, a shared mooring system consists of single lines that moor FOWTs to anchors on the seabed and shared lines or shared mooring components that connect neighboring FOWTs, which leads to reductions in the total length of the mooring lines and in the number of anchors and, therefore, brings about reductions in the material and installation costs of the mooring system. However, different from the conventional practice, shared mooring systems introduce coupling between neighboring FOWTs, which makes the FOWF as a whole and includes extra complexity in its dynamic characteristics. Therefore, to demonstrate the feasibility of shared mooring systems, it is essential to investigate the influence of the shared moorings and to study the dynamic behaviors of FOWFs with shared mooring systems. Heretofore, a few numerical studies have been published on shared mooring systems for FOWFs. This section presents a brief review of interesting studies.

For pilot-scale FOWFs (e.g., number of FOWTs ≤ 5), Goldschmidt and Muskulus [46] investigated the dynamics of row-, triangular-, and square-shaped FOWFs with shared moorings. Both frequency-domain and time-domain methods were applied to simplified models. The results showed the great cost-saving potential of the shared mooring system but also the increased displacements and strength requirements of the mooring lines when the farm size increases. Hall and Connolly [47] developed a master program coupling FAST [48] and MoorDyn [36] and studied the dynamic behaviors of a square-shaped four-turbine FOWF with shared mooring lines. Complex restoring properties introduced by the shared moorings were reflected in the motions of the FOWTs, and a great tendency of resonance was reported for the shared moorings due to the absence of seabed contact. Later on, Connolly and Hall [49] proposed an algorithm for the preliminary design of shared mooring systems based on a quasi-static modeling method. Different shared mooring configurations were studied for the square-shaped four-turbine FOWF in different water depths. The dynamic behaviors of a dual-turbine FOWF with a shared line were studied by Munir et al. [50]. Two different turbine spacings were considered, and the motions of the FOWTs were checked. Zhang and Liu [51] integrated FAST into the hydrodynamic software ANSYS AQWA [52] to model FOWFs with shared moorings. Two different shared mooring configurations were investigated for a square-shaped four-turbine FOWF, and the mooring line failure was also studied. Anisotropy was observed in the stiffness of the studied shared mooring configurations, and a high risk of progressive failure was reported when a windward mooring line failed.

For relatively large-scale FOWFs (e.g., number of FOWTs > 5), Wilson et al. [53] proposed an approach for the preliminary design of shared mooring systems based on a linearized model of the force-displacement response of shared mooring systems.

FOWFs with different sizes and layouts were designed using the proposed approach. FOWTs with more shared lines were found to experience larger motions. Hall et al. [54] presented a systematic design process for a ten-turbine FOWF with shared moorings and shared anchors, in which the linearized approach developed in [53] was applied, and coupled analysis was performed in FAST.Farm [55]. The design using shared lines and shared anchors reduced the installation cost of the mooring system by 26% compared to an FOWF with conventional, individually moored FOWTs. In a following research, a comparative study was conducted by Lozon and Hall [56] between the mooring system designed in [54], with shared moorings and shared anchors, and a conventional, individually moored mooring system. Dynamic analysis was performed in FAST.Farm, and motions of FOWTs and structural responses were investigated. It was concluded that for that specific design case, the shared mooring system did not introduce additional dynamic response concerns and showed a high failure tolerance compared to the conventional, individually moored mooring system.

In the aforementioned numerical studies, FOWFs with semi-submersible FOWTs were studied in [46,47,49–51], and FOWFs with spar FOWTs were studied in [54,56]. To the best of the author's knowledge, no experimental studies on FOWFs with shared mooring systems have been published.

1.5 Aim and scope

As discussed in Sec. 1.1, it is beneficial and inexorable that offshore wind turbines will be deployed in intermediate or deep water depths where floating solutions are economically viable. Innovative designs and cost reductions are therefore desired for floating wind to accelerate this progress. Based on the discussion of mooring systems of FOWTs in Sec. 1.3 and the review of related studies on shared mooring systems in Sec. 1.4, the key research challenges for FOWFs with shared mooring systems can be summarized as follows:

1. Lack of fundamental understanding of the dynamic characteristics of integrated systems of FOWFs with different shared mooring configurations and under complex environmental loading.

2. Lack of design and optimization methods for shared mooring systems.

3. Lack of experimental methods for testing of multibody FOWFs with shared mooring systems.

4. Lack of systematic economic assessments of FOWFs with shared mooring systems considering whole life-cycle costs, the value chain, etc.

This thesis focuses on contributing to addressing challenges 1 and 3. To achieve this, the following sub-objectives are defined:

- To develop a numerical modeling method for shared mooring systems and investigate the influence of shared mooring systems on natural periods and eigenmodes of FOWFs.

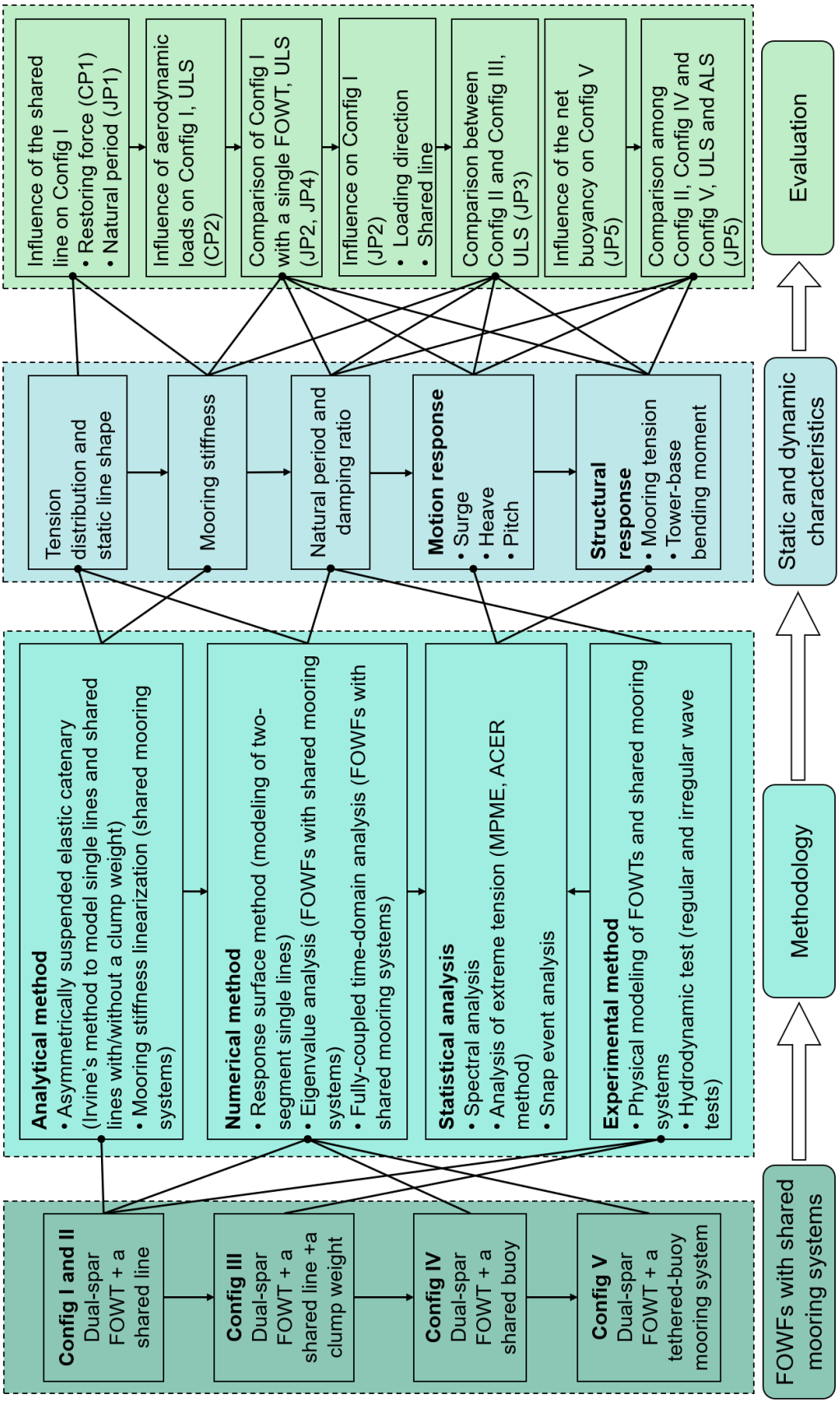

Figure 1.6: Scope of the thesis and interconnections between appended papers.

- To assess the influence of shared mooring systems on dynamic characteristics of FOWFs through comparison to a single, individually moored FOWT and detailed study of the mooring properties of the shared mooring systems.
- To conduct an experimental study on FOWFs with shared mooring systems in different ECs and validate and support the numerical studies.
- To design novel shared mooring systems for FOWFs and compare the pros and cons of different shared mooring configurations through detailed analyses.
- To provide recommendations for the design and analysis of shared mooring systems for FOWFs.

This thesis is written as a summary of published and submitted papers, including five journal articles and three conference papers, as attached in the appendix. The scope of this thesis is shown in Fig. 1.6, in which the main topics and the interconnections between the appended papers are illustrated.

CP1:

This paper applies the theory in elastic catenary of hanging cables [57] to model a shared line. The method is verified by FE modeling in SIMA [58, 59] and further applied in a case study of a prototype FOWF with two OC3 Hywind spar FOWTs [60, 61] and a shared line. First, the relationship between the offset of the FOWTs and tension in the mooring lines is studied. Then, the shared line is modeled with different materials and diameters to investigate its influence on the total restoring curves of the FOWTs. A single, individually moored spar FOWT is analyzed for comparison. The results show that in the direction aligned with the shared line, the mooring restoring effects of the FOWF are significantly influenced by the presence of the shared line.

JP1:

In this paper, an analysis method is proposed to linearize mooring stiffness and perform eigenvalue analysis for FOWFs with shared moorings, in which Irvine's modeling method [57] is extended to model a two-segment single line and the response surface method is introduced to replace iterations. To get a more realistic mooring system, a mooring design is made for a single, individually moored Hywind spar FOWT according to the design standard [13]. The present analysis method is applied in a case study of a dual-spar FOWF with a shared line, i.e., configuration I, whose mooring properties are adopted from the mooring design. First, eigenvalue analysis is performed for configuration I. Then, the influence of mooring properties of single lines and the shared line on the natural periods of the floating system is investigated. The results indicate that the shared line has a significant influence on the natural periods of the FOWF in the surge and sway degrees of freedom (DOFs). Natural periods in these DOFs are also sensitive to the mooring properties of both the single lines and the shared line.

CP2:

This paper presents a study on the influence of aerodynamic loads in extreme conditions on the dynamic behaviors of configuration I. The aerodynamic loads acting

on the rotor and the drag force acting on the tower are modeled. Two load cases (LCs) with a return period of 50 years are selected for a case study. The platform motions, mooring response, and tower-based bending moments (TBBMs) are investigated and compared between the "wave-only" condition and "combined wind and wave" condition. The results reveal that for configuration I, the extreme response is not entirely wave-dominant, and the aerodynamic loads have a significant influence even though the blades are feathered.

JP2:

In this paper, a detailed investigation is conducted on the dynamic characteristics of configuration I. Critical LCs are selected from the 50-year environmental contour surface of an offshore site. First, selected variables, such as linearized mooring stiffness, platform motions, mooring responses, and TBBMs, of configuration I are compared to those of a single, individually moored spar FOWT. Then, for configuration I, the influence of loading directions and shared line properties is investigated. The selected variables are analyzed and compared for different loading directions and different shared line diameters. It is concluded that compared to a single, individually moored FOWT, configuration I experiences larger horizontal platform motions and higher mooring tension. Snap events are experienced by the shared line. From the sensitivity study, platform motions are sensitive to the loading direction, as the mooring layout has anisotropic station-keeping performance, and the mooring responses of all lines are sensitive to the shared line properties.

CP3:

In this paper, two shared mooring configurations for a dual-spar FOWF are investigated in regular wave tests, in which two spar FOWTs are connected by a shared line with or without a clump weight, i.e., configurations II and III. Two regular-wave conditions are tested, where one represents mild sea states and the other represents survival conditions. Platform motions and mooring tension are compared between the two configurations. The results show that the platform surge motion is reduced by the addition of the clump weight. For configuration III, the tension level in the single lines increases, but the dynamic tension in the shared line is effectively reduced.

JP3:

This paper presents an experimental investigation of two shared mooring configurations, with and without a clump weight, for a dual-spar FOWF (configurations II and III) in irregular waves. Irvine's modeling method [57] is extended to model a shared line with a clump weight, and the linearized mooring stiffness is compared between two configurations. Single lines of the spar FOWTs are redesigned for a water depth of 235 m. One operational sea state and one extreme sea state with a return period of 50 years are tested. First, natural periods and damping ratios from decay tests are compared. Then, the platform motion responses are checked in terms of time series, statistics, and motion spectra. Mooring tension is measured, and the data is used to characterize the extreme values and identify snap events. The results indicate that by adding a clump weight to the shared line, the natural periods of horizontal DOFs decrease, and reduced dynamic surge motions, higher pretension,

and lower dynamic tension are observed. The extreme tension in the shared line decreases significantly for configuration III; so does the likelihood of snap events.

JP4:

This paper presents an experimental study of a single, individually moored spar FOWT and configuration II. Two ECs, one operational and one extreme, are selected for the hydrodynamic model tests with irregular waves. Wave elevation, platform motion, and mooring tension are measured during the model test. First, natural frequencies and damping ratios obtained from decay tests are compared between the two configurations. Then, the first-order response amplitude operators of the platform motion and mooring tension are compared based on the results from regular wave tests and the white noise test. Finally, the statistics and spectra of the platform motion and mooring tension from irregular wave tests are compared between the two configurations. Larger platform surge motion is observed for configuration II than for the single FOWT. For the tension in the shared line, spectral energy is concentrated in the first-order wave-frequency range, and large peaks and dynamic oscillations are observed.

JP5:

In this paper, a tethered-buoy mooring system, a new type of shared mooring system, is investigated for a dual-spar FOWF, in which both FOWTs are moored by tethered buoys (configuration V). In the analysis, configuration V is compared to a shared-line configuration and a shared-buoy configuration, i.e., configurations II and IV, respectively. First, numerical decay tests are performed, and natural periods of different configurations are compared. Then, the influence of the net buoyancy of the buoys is studied for configuration V. Finally, numerical simulations are performed for the three configurations in one accidental scenario with an operational EC, in which one FOWT is parked, and in one extreme scenario with an extreme EC. Platform motions and fairlead tension in two load scenarios are compared among the three configurations. Compared to the other two configurations, the FOWTs in configuration V experience larger mean motions, but the tension levels at all fairleads decrease substantially.

1.6 Thesis outline

This thesis consists of five chapters. A brief description of each chapter is provided as follows:

Chapter 1:

This chapter includes the background and motivation, a brief introduction to the mooring systems for FOWTs and the relevant guidelines and analysis methods, a review of the studies on shared mooring systems, and the aim, scope, and outline of the thesis.

Chapter 2:
This chapter introduces details of the dual-spar FOWF and the different shared mooring configurations studied in all papers. The design procedures of single lines applied in *JP1*, *JP3*, and *JP4* are also described.

Chapter 3:
This chapter addresses the numerical analysis of the dual-spar FOWF with shared moorings. First, the static analyses performed for the shared mooring systems are discussed, and the main results from *CP1* and *JP1* are covered. Then, the numerical modeling, LCs, and numerical simulations of dual-spar FOWFs with shared mooring configurations are presented, and the main results in *CP2*, *JP2*, and *JP5* are covered.

Chapter 4:
This chapter presents the hydrodynamic model tests conducted for the dual-spar FOWF with shared mooring systems. The physical modeling, experimental setups, and test matrix are described. The main results in *CP3*, *JP3*, and *JP4* are discussed.

Chapter 5:
The thesis' conclusions and original contributions, and recommendations for future work are presented.

Chapter 2

Floating offshore wind farms with shared mooring systems

2.1 General

As mentioned in Sec. 1.1, floating wind is expected to facilitate the transformation to a decarbonized society, and cost reductions are vital to achieving this. As one of the novel design concepts for FOWFs, a shared mooring system has the potential to reduce costs related to moorings and anchors, which are estimated to be 10% to 15% of the capital cost of an FOWF project [9]. However, fundamental knowledge is required for a shared mooring system to be applied in commercial floating wind projects. This thesis focuses on a dual-spar prototype FOWF to fully understand the changes that shared moorings could bring to the floating system. Spar FOWTs are used, which have the simplest structure and dynamic properties. In the dual-spar FOWF, two spar FOWTs are deployed along a line with a certain turbine spacing. The shared part of the mooring system could be simply a shared line, a shared line with mooring components, or a more complex configuration, such as a shared tethered buoy.

This chapter describes the dual-spar FOWF and shared mooring systems, by which the design procedures of single lines are briefly discussed, and mooring properties are presented for all shared mooring configurations investigated in this thesis.

2.2 Dual-spar floating offshore wind farms

The dual-spar FOWF consists of two OC3 Hywind spar FOWTs with NREL 5 MW reference wind turbines [60] and OC3 spar floaters [61].

The wind turbine is upwind, which means the rotor plane faces the wind. The shaft of the wind turbine is tilted by 5 degrees. As the floater top is 10 m above the still water level (SWL), the tower height is adjusted to 77.6 m to maintain the same hub height as the land-based version of the wind turbine. The geometry of the spar floater can be simplified as two cylinders with different diameters connected by a truncated cone (taper). The upper cylinder has a diameter of 6.5 m, and the lower

Table 2.1: Main design parameters of the OC3 Hywind spar FOWTs [60, 61].

Parameter	Value
Turbine type [−]	Upwind, 3 blades
Rated power capacity [MW]	5
Rotor diameter [m]	126
Hub height, diameter [m]	90, 3
Tower height [m]	77.6
Shaft tilt [deg]	5
Cut-in, rated, cut-out wind speed [m/s]	3, 11.4, 25
Cut-in, rated rotor speed [rpm]	6.9, 12.1
Rated tip speed [m/s]	80
Elevation of platform top above SWL [m]	10
Depths to top and bottom of taper below SWL [m]	4, 12
Floater diameters above and below the taper [m]	6.5, 9.4
Total draft [m]	120

Table 2.2: Main design parameters of the mooring system of the OC3 Hywind Spar FOWT [61].

Design parameter	Value
Water depth [m]	320
Number of mooring lines [−]	3
Projected angle between neighboring lines [deg]	120
Depth to fairleads below SWL [m]	70
Radius to fairleads from floater centerline [m]	5.2
Diameter of mooring lines [m]	0.09
Unstretched length of mooring lines [m]	902.2
Equivalent mass density of mooring lines [kg/m]	77.71
Equivalent weight in water per unit length [N/m]	698.10
Equivalent axial stiffness [N]	3.84E+08
Radius to anchors from floater centerline [m]	853.87

cylinder has a diameter of 9.4 m. The main design parameters of the OC3 Hywind spar FOWT are summarized in Table 2.1.

The OC3 Hywind spar FOWT has a catenary mooring system with three mooring lines distributed evenly around the floater. The water depth for the FOWT is 320 m. All three fairleads are located 70 m below SWL. In the OC3 definition report [61], only artificial mooring properties are provided. The main design parameters of the mooring system of the OC3 Hywind spar FOWT are presented in Table 2.2.

Behind an operating wind turbine, there is a wake, i.e., a region in which the wind is more turbulent and slowed down. This follows the law of conservation of energy, as a wind turbine takes part of the wind energy to generate electricity. In a wind farm, every wind turbine slows down the wind behind it; therefore, a large space is needed when deploying the wind turbines to alleviate the wake effects, which can affect the performance of the downwind wind turbines [62]. The parameter turbine spacing describes how closely wind turbines are placed in a wind farm, and the rotor diameter is used to normalize the measure of the turbine spacing. In practice, the rule of thumb is that in a wind farm, wind turbines are usually spaced apart from each other between five and nine times the rotor diameter in the prevailing wind direction and between three to five times the rotor diameter in the direction perpendicular to the prevailing winds [63]. Different from onshore or bottom-fixed offshore wind farms, in an FOWF, FOWTs experience horizontal offset due to environmental loads. The mean and dynamic horizontal offset of FOWTs should be considered in the layout design of FOWFs. In this thesis, the investigated dual-spar FOWFs have an initial turbine spacing of 750 or 1,000 m, which is approximately six and eight times the rotor diameter, respectively.

2.3 Design of single mooring lines

The mooring system of the OC3 Hywind spar FOWT with unified and equivalent mooring properties shows suboptimal station-keeping performance in operational and extreme ECs. In numerical simulations performed under extreme wind and wave conditions, the FOWT model experiences large horizontal offset, and vertical tension is found at the anchor points. To investigate the dynamics of an FOWF with a realistic mooring system, preliminary mooring design is performed for a single, individually moored OC3 Hywind spar FOWT in [64]. In the hydrodynamic model tests of the dual-spar FOWF, the full-scale water depth is according to the scaling ratio and the water depth of the ocean basin. Similar procedures as those in [64] are applied in the mooring design for a single, individually moored OC3 Hywind spar FOWT with the updated water depth [65, 66]. Based on [64], the simple mooring design approach is briefly described as follows:

1. **Environmental conditions**. Select the ECs for the mooring design, based on which the LCs for the design check are decided.
   For the mooring design in [64], the water depth is 320 m, as specified in the OC3 report [61]. The ECs of a European offshore site, "Norway 5" (water depth 202 m) [67], are selected. One operational LC and one extreme LC are considered based on the joint distribution of the mean wind speed (U_w) at 10-m height, significant wave height (H_s) and spectral peak period (T_p). The rated wind speed is selected for the operational LC together with the H_s and T_p as the mean value of the conditional distributions. According to the offshore standard [13], a return period of 50 years is considered for the extreme LC. The sea state with the highest H_s is selected on the 50-year environmental

Table 2.3: ECs of the two LCs for the mooring design of the OC3 Hywind spar FOWT.

Environmental parameter	Operational	Parked (50-yr extreme)
U_w (at hub-height) $[m/s]$	11.40	42.71
I (Turbulence intensity) $[-]$	0.17	0.12
H_s $[m]$	2.57	15.50
T_p $[s]$	11.12	14.45

Table 2.4: Design space for the mooring design of the OC3 Hywind spar FOWT.

Design variable	Sampling range	Sampling interval
Wire segment length L_{wire} $[m]$	[400, 560]	10
Wire segment diameter D_{wire} $[mm]$	[90, 130]	5
Chain segment diameter D_{chain} $[mm]$	[110, 150]	5

contour surface generated based on the joint distribution of "Norway 5". The wind and waves are assumed to be unidirectional in the global surge direction. The environmental parameters of the two LCs are listed in Table 2.3.

2. **Design procedure**. Determine the design procedure, including the design space, the design objective, and the design constraints.
   In [64], a two-segment mooring design with no mooring component is considered, and the delta connection [68] is omitted for simplicity. The upper segment is made of steel wire rope and the lower segment is made of R3 studless mooring chain. To avoid lift forces acting on the anchors when the FOWT experiences large horizontal offset, the unstretched length of the mooring line is increased to 1002.2 m. As the total length of mooring lines is kept unchanged in the design, three design variables are considered, i.e., the length and diameter of the wire segment and the diameter of the chain segment. The design space in [64] is presented in Table 2.4. Mooring properties are calculated based on offshore standards [15, 16, 18] and commercial data.
   The design objective is to minimize the material costs of mooring lines related to the production and manufacture. Scaled cost coefficients for chain and steel wire rope from manufacturers are provided in [64].
   Both static and dynamic analyses are performed in the mooring design. In the static analyses performed in Mimosa [30], a program for moored vessel analysis, the stiffness curves and pretension are checked first. Then, an offset limit of 20 m is assumed considering the structural integrity of the power cable. An offset of 20 m is applied to the fairlead, and the line shape is checked

so that the wire segment does not touch the seabed and there is no vertical force acting on the anchor point. For the dynamic analyses, fully coupled time-domain simulations are performed in SIMA [58, 59], a state-of-the-art numerical tool for coupled analysis of FOWTs. Turbulent wind and irregular waves are simulated for both LCs. The utilization factor, u, is calculated according to DNV-ST-0119 [13], as follows:

$$u = \frac{(\gamma_{mean} \cdot T_{c,mean} + \gamma_{dyn} \cdot T_{c,dyn}) \cdot f_s}{f_m \cdot S_{mbs}} \tag{2.1}$$

where f_s is the non-redundant factor and f_m is the material factor. The other terms in Eq. (2.1) are the same as those in Eqs. (1.3) and (1.4). The factors are determined according to the offshore standards [13, 15], and values for consequence class 1 are selected as FOWTs are unmanned structures. For the operational LC, the mean values of $T_{c,mean}$ and $T_{c,dyn}$ from six one-hour time-domain simulations are used in the calculation of utilization factors. The 90% quantile of a Gumbel distribution [69] fitted by $T_{c,dyn}$ from 30 one-hour time-domain simulations is taken as the $T_{c,dyn}$ in the calculation for the extreme LC, as suggested in [67].

3. **Selection of the design**. Based on the design objectives and constraints, the final design is selected.
   From the design space in Table 2.4, the sample that fulfills the design constraints with the lowest mooring cost is selected. Readers are referred to [64] for more details on the selected design.

2.4 Shared mooring systems

In this thesis, several shared mooring systems at different water depths are analyzed and tested for the dual-spar FOWF. The mooring properties of these shared mooring

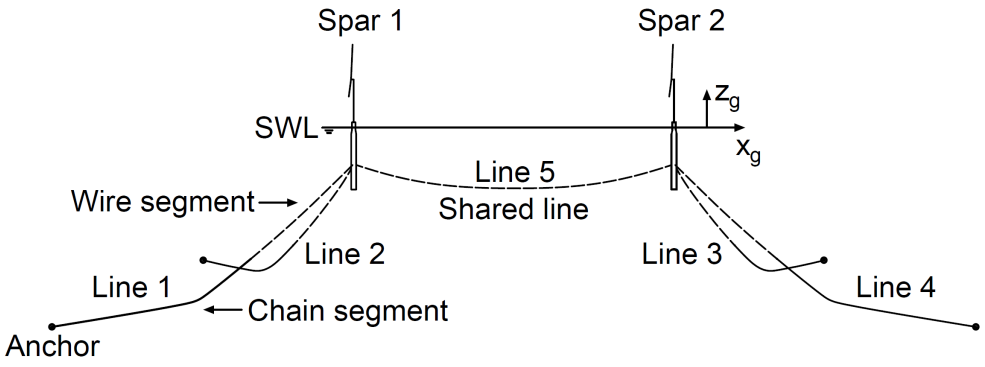

Figure 2.1: Illustration of the dual-spar FOWF with a shared line.

systems are described in the following subsections. As there is no design rule or guideline for a shared mooring system as a novel concept, the properties of shared mooring systems used in this thesis are for the purpose of analysis. For a specific FOWF project, a detailed design is required to find the shared mooring configuration that provides the best station-keeping performance.

2.4.1 Shared mooring configuration with a shared line

The simplest configuration for the shared mooring system is that in which neighboring FOWTs are connected by a shared mooring line; see Fig. 2.1 for the case of a dual-spar FOWF. In this thesis, a dual-spar FOWF with a shared line is investigated for two different water depths. In *JP1*, *CP2* and *JP2*, configuration I is modeled for a water depth of 320 m, and the initial turbine spacing of the two FOWTs is 1,000 m. In *CP3*, *JP3*, *JP4*, and *JP5*, configuration II is analyzed for a water depth of 235 m, and the initial turbine spacing is 750 m.

In both configurations, each FOWT is connected to two single lines with a two-segment design, in which the upper segment is made of R3 studless mooring chain and the lower segment is made of sheathed steel wire rope. The design of the single lines is carried out following the procedure described in Sec. 2.3. A one-segment shared line is used to connected the two FOWTs. Wire is lighter than chain, so the shared line is made of sheathed steel wire rope. For simplicity, the wire properties of the single lines are used for the shared line. The mooring properties of the two configurations are summarized in Table 2.5. For each FOWT, three fairleads are located 70 m below the SWL and 5.2 m away from the center axis of the corresponding FOWT. The projected angle between any two adjacent mooring lines is 120 degrees. The radius from the center axis of the FOWT to the corresponding anchors is 953.87 m for configuration I and 623.53 m for configuration II.

Table 2.5: Mooring properties of configuration I and configuration II.

Configuration	I			II		
Water depth $[m]$	320			235		
Initial turbine spacing $[m]$	1000			750		
Mooring line	Single line		Shared line	Single line		Shared line
Segment	Chain	Wire	-	Chain	Wire	-
Length $[m]$	550	452.2	989.6	415	250	739.6
Diameter $[mm]$	115	90	90	140	95	95
Sheath thickness $[mm]$	-	10	10	-	10	10
Mass density $[kg/m]$	264.50	42.77	42.77	392.00	47.39	47.39
Weight in water per unit length $[N/m]$	2385.86	324.00	324.00	3535.94	360.42	360.42
Axial stiffness EA $[N]$	1.06E+09	7.64E+08	7.64E+08	1.53E+09	8.47E+08	8.47E+08
MBS $[N]$	1.03E+07	8.38E+06	8.38E+06	1.43E+07	9.34E+06	9.34E+06

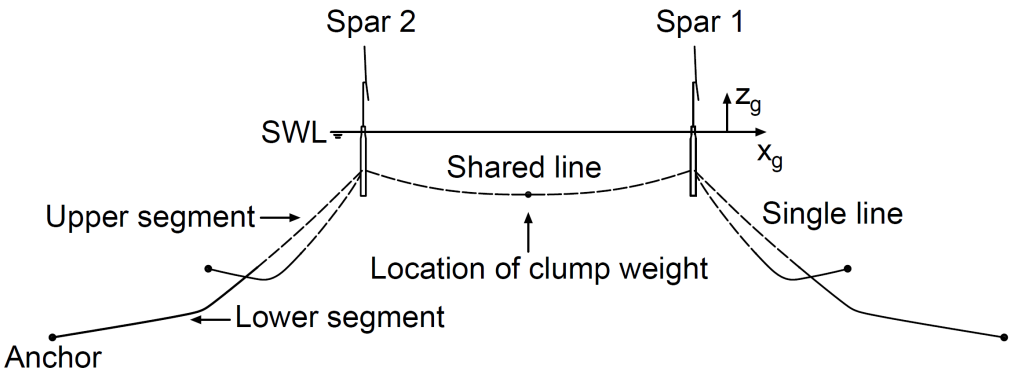

Figure 2.2: Illustration of configuration III.

2.4.2 Shared mooring configuration with a shared line and a clump weight.

As described in Sec. 1.2.2, in practice, clump weights can be attached to mooring lines to improve the station-keeping performance of mooring systems for floating structures. It is of interest to investigate how a clump weight will influence the station-keeping performance of a shared mooring system.

In *CP3* and *JP3*, experimental investigations are conducted for configuration II and configuration III in which a clump weight is mounted to the shared line; see Fig. 2.2. The water depth is 235 m, and the initial turbine spacing is 750 m for both configurations. The mooring properties of configuration III are the same as those of configuration II presented in Table 2.5, including the locations of the fairleads and the radius from the center axis of each FOWT to the corresponding anchors. The projected angle between any two neighboring mooring lines is 120 degrees. The added clump weight is attached to the midpoint of the shared line and has a submerged weight of 15 tonnes at full scale.

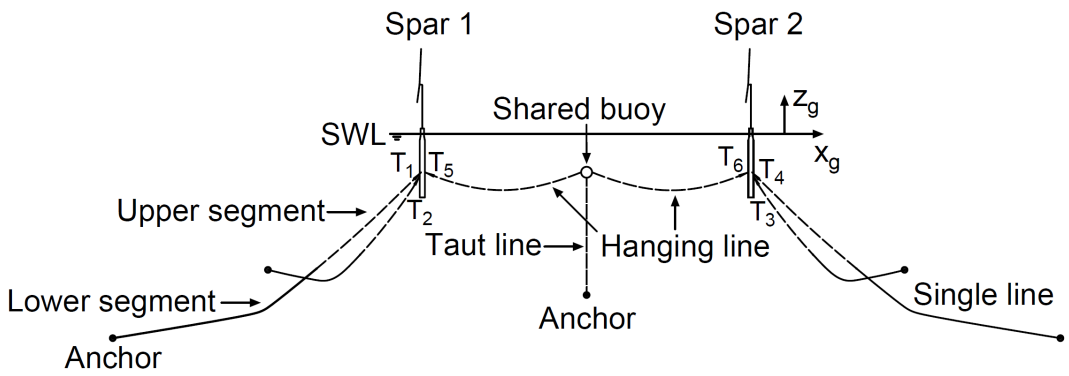

Figure 2.3: Illustration of configuration IV.

2.4.3 Shared mooring configuration with a shared buoy

In the study, the shared line of configuration I experiences a high tension level, and snap events are observed in extreme ECs. To explore alternative shared mooring systems for the dual-spar FOWF, configuration IV introduces a tethered buoy to the connection part, as illustrated in Fig. 2.3, aiming to alter the geometric stiffness of the shared line and partially decouple the motions of the two FOWTs.

For configuration IV, the water depth is 235 m, and the initial turbine spacing is 750 m. Each FOWT is connected to two single lines, which have an upper wire segment and a lower chain segment. Instead of being connected by a shared line, the two FOWTs are connected through hanging lines to a shared tethered buoy, which is moored to the seabed through a taut line. The mooring properties of the single lines of configuration IV are the same as those for configuration II, including the locations of the fairleads and the radius from the center axis of each FOWT to the corresponding anchors. The hanging lines and the taut line are made of sheathed steel wire rope with the same diameter as the wire segment of the single lines. The taut line is always tightened because of the net buoyancy of the shared buoy. For each FOWT, the projected angle between any two adjacent mooring lines is 120 degrees. The properties of the mooring lines of configuration IV are summarized in

Table 2.6: Mooring properties of configuration IV.

Mooring line	Single line		Hanging line	Taut line
Segment	Chain	Wire	-	-
Length $[m]$	415	250	366.51	161.71
Diameter $[mm]$	140	95	95	95
Sheath thickness $[mm]$	-	10	10	10
Mass density $[kg/m]$	392.00	47.39	47.39	47.39
Weight in water per unit length $[N/m]$	3535.94	360.42	360.42	360.42
Axial stiffness EA $[N]$	1.53E+09	8.47E+08	8.47E+08	8.47E+08
MBS $[N]$	1.43E+07	9.34E+06	9.34E+06	9.34E+06

Table 2.7: Properties of the shared buoy in configuration IV.

Parameter	Value
Mass $[kg]$	4.53E+04
Diameter [1] $[m]$	6.58
Volume $[m^3]$	149.17
Net buoyancy $[N]$	10.38E+05

[1] Approximate diameter of the spherical buoy.

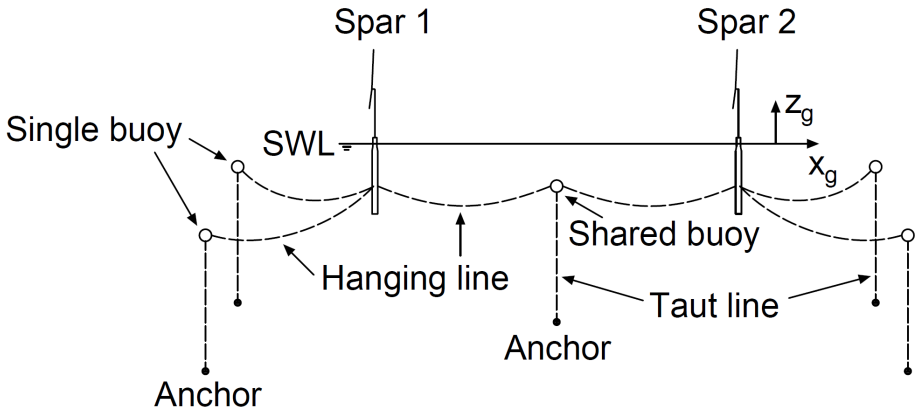

Figure 2.4: Illustration of configuration V.

Table 2.6. The shared buoy is fully submerged in the water, with a distance of 70 m from the center of the buoy to the SWL. The anchor of the shared buoy is on the seabed and located at the midpoint of the center axes of two FOWTs. In this study, a spherical buoy is used, and the properties are presented in Table 2.7.

2.4.4 Shared mooring configuration with tethered buoys

Inspired by the "Honeymooring^{TM}" concept by Semar AS [70], an innovative shared mooring system with tethered buoys is proposed and studied for the dual-spar FOWF, i.e., configuration V; see Fig. 2.4. Different from configuration IV, single lines are replaced by hanging lines connected to submerged tethered buoys in configuration V.

As shown in Fig. 2.4, each FOWT is connected to two single buoys by hanging lines. A shared buoy is used to connect the hanging lines from the two FOWTs, just as with the shared mooring part of configuration IV. The initial turbine spacing is 750 m, and the water depth is 235 m. For each FOWT, the projected angle of any two adjacent hanging lines are 120 degrees. Three fairleads on each FOWT are located

Table 2.8: Mooring properties of configuration V.

Mooring property	Hanging line	Taut line
Material	Sheathed steel wire rope	
Unstretched length $[m]$	366.51	161.71
Diameter $[mm]$	95	95
Sheath thickness $[mm]$	10	10
Mass density $[kg/m]$	47.39	47.39
Weight in water per unit length $[N/m]$	360.42	360.42
Axial stiffness EA $[N]$	8.47E+08	8.47E+08
MBS $[N]$	9.34E+06	9.34E+06

70 m below the SWL and 5.2 m away from the center axis of the corresponding FOWT. Five tethered buoys are used in total for the dual-spar FOWF. Each buoy is moored to an anchor on the seabed by a taut line. Due to the net buoyancy of the buoys, taut lines are always tightened. The radius from the center axis of each FOWT to the corresponding anchors is 375 m. Each buoy is fully submerged and initially placed right above the corresponding anchor, with a distance of 70 m from the center of the buoy to the SWL. All five buoys have the same properties as the shared buoy in configuration IV, shown in Table 2.7. All hanging lines and all taut lines have the same unstretched length and are made of sheathed steel wire rope with the same diameter. As there are no specific design requirements for the shared mooring system of an FOWF in the design standards, i.e., [13], the properties of the steel wire rope from configuration II are used for configuration V for study purposes. The properties of the mooring lines of configuration V are summarized in Table 2.8.

2.4.5 Summary of shared mooring configurations

The five shared mooring configurations studied in this thesis are summarized in Table 2.9.

Table 2.9: Summary of the shared mooring configurations.

Configuration	Water depth $[m]$	Initial turbine [1] spacing $[m]$	Shared mooring system		Appended papers
			Individual part [2]	Shared part [3]	
I	320	1000	Two-segment single lines	A shared line	CP1, JP1, CP2, JP2
II	235	750	Two-segment single lines	A shared line	CP3, JP3, JP4, JP5
III	235	750	Two-segment single lines	A shared line with a clump weight	CP3, JP3
IV	235	750	Two-segment single lines	Hanging lines connected to a submerged tethered shared buoy	JP5
V	235	750	Hanging line connected to a submerged tethered single buoy	Hanging lines connected to a submerged tethered shared buoy	JP5

[1] Initial turbine spacing refers to the distance between the centerlines of two FOWTs in the initial configuration.
[2] The individual part refers to the part of the mooring system that is connected to individual FOWTs.
[3] The shared part refers to the part of the mooring system that is shared between adjacent FOWTs.

Chapter 3

Numerical analysis of floating offshore wind farms with shared mooring systems

3.1 General

Numerical methods have been developed and widely applied in the design and analysis of FOWTs. As briefly described in Sec. 1.3.2, various modeling methods are available for the quasi-static modeling or dynamic modeling of FOWTs. In this thesis, both a quasi-static modeling method based on elastic catenary equations and a dynamic modeling method are applied to study the dual-spar FOWFs with shared mooring systems.

Based on Irvine's modeling method for hanging cable structures [57], an analytical modeling method is developed in *CP1* and *JP1* to model the shared mooring system, for both single lines and shared lines, from which the tension distribution along the line and the static line shape can be computed. By applying the present quasi-static modeling method, the linearized mooring stiffness matrix of shared mooring systems can be calculated and further used in eigenvalue analysis of FOWFs with shared moorings. Natural periods and eigenmodes obtained from this approach are verified by results from numerical decay tests.

Dynamic modeling of the dual-spar FOWFs with shared mooring systems is conducted in SIMA [58, 59], a numerical simulation tool. Using the established numerical models, fully coupled time-domain simulations are performed for various shared mooring configurations under different LCs. The results are post-processed and analyzed to study the influence of shared moorings and dynamic behaviors of different shared mooring systems.

This chapter first describes the analysis approach based on quasi-static modeling in Sec. 3.2, in which the results from *JP1* are mainly presented and discussed. Then, the numerical modeling in SIMA is introduced in Sec. 3.3, followed by the setups of the numerical simulations. The main results of the dynamic analysis of configuration I in *JP2* are presented in Sec. 3.3.4. The interesting findings of the dynamic analysis

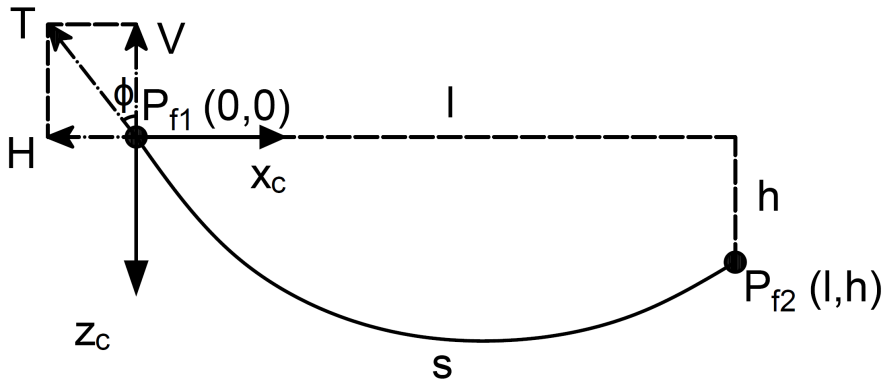

Figure 3.1: Illustration of a shared line in the catenary plane.

of configurations II, IV, and V in *JP5* are presented in Sec. 3.3.5. Finally, a summary of the observations from the numerical analysis is given in Sec. 3.4.

3.2 Static analysis of shared mooring systems

3.2.1 Analytical modeling method of shared mooring systems

The theory of elastic catenary for hanging cable structures [57] is applied to model single lines and a shared line in [71]. The modeling method is further developed to model a two-segment single line in [64] and to model a shared line with a clump weight in [65]. In this section, the modeling methods for different mooring lines are introduced.

Modeling of a shared line

To model a shared mooring system, it is assumed that the bending stiffness of the mooring lines and the dynamic effects and effects of current forces acting on the mooring lines can be neglected. With such assumptions, based on Hooke's law, Newton's first law, and the principle of mass conservation, the asymmetrically suspended elastic catenary can be solved with a Lagrangian approach and used to model a shared line. Detailed derivations can be found in [57]. The shared line is modeled in its catenary plane, i.e., the plane determined by its catenary line shape, as shown in Fig. 3.1, where P_{f1} and P_{f2} are two fairleads of the shared line and P_{f1} is the origin of the catenary plane x_c-z_c. The nonlinear elastic catenary equations for the shared line are as follows:

$$l = \frac{Hs}{EA} + \frac{Hs}{\omega}\left[\sinh^{-1}(\frac{V}{H}) - \sinh^{-1}(\frac{V-\omega}{H})\right] \tag{3.1}$$

$$h = \frac{\omega s}{EA}\left[\frac{V}{\omega} - \frac{1}{2}\right] + \frac{Hs}{\omega}\left[\sqrt{1+\left(\frac{V}{H}\right)^2} - \sqrt{1+\left(\frac{V-\omega}{H}\right)^2}\right] \tag{3.2}$$

where l and h are the horizontal and vertical distances between the two fairleads, respectively. Moreover, H and V are the horizontal and vertical components, re-

spectively, of mooring tension T at fairlead P_{f1}. Mooring angle ϕ is defined as the angle between fairlead tension T and its vertical component V. Here, s and ω are the total unstrained length and the total submerged weight of the mooring line, respectively; EA is the axial stiffness of the line, where E is the elastic modulus and A is the cross-sectional area. The fairlead positions, P_{f1} and P_{f2}, are usually known in practice. Mooring tension at the fairlead, H and V, can be obtained by solving Eqs. (3.1) and (3.2) numerically. The application of Irvine's modeling method in shared line modeling is verified by FE modeling in the RIFLEX module of SIMA in [71].

The static line shape can be calculated using the Lagrangian coordinate. Given fairlead tension H and V, the coordinates of a point on the shared line, P_p, can be calculated by solving the following:

$$x(P_p) = \frac{Hs_p}{EA} + \frac{Hs}{\omega}\left[\sinh^{-1}(\frac{V}{H}) - \sinh^{-1}(\frac{V-\omega s_p/s}{H})\right] \tag{3.3}$$

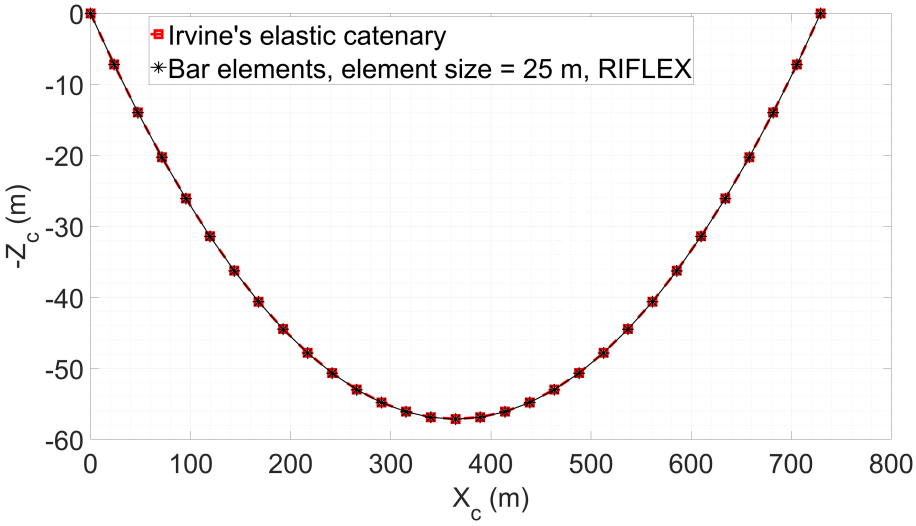

Figure 3.2: Static line shape of a shared line in the catenary plane.

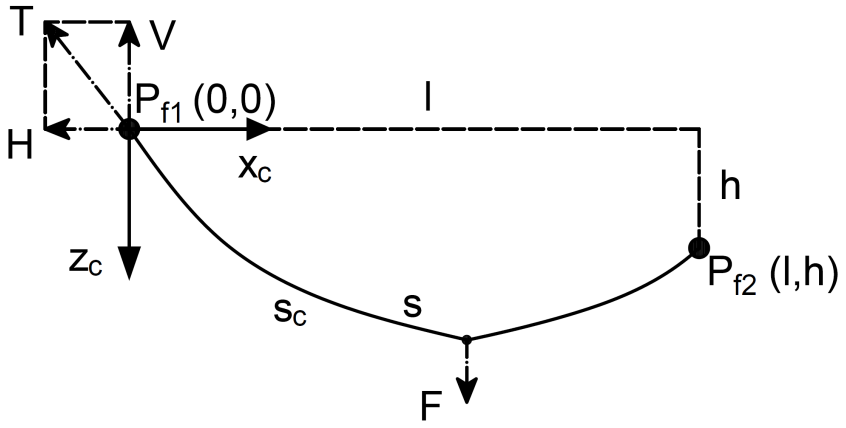

Figure 3.3: Illustration of a shared line with a clump weight in the catenary plane.

$$z(P_p) = \frac{\omega s_p}{EA}\left[\frac{V}{\omega} - \frac{s_p}{2s}\right] + \frac{Hs}{\omega}\left[\sqrt{1+\left(\frac{V}{H}\right)^2} - \sqrt{1+\left(\frac{V-\omega s_p/s}{H}\right)^2}\right] \tag{3.4}$$

where $x(P_p)$ and $z(P_p)$ are the coordinates of point P_p in the catenary plane. Here, s_p is the unstretched length along the line from origin P_{f1} to P_p. The static line shape of a shared line with the original mooring properties in the OC3 report [61] is calculated by Irvine's modeling method and FE modeling in RIFLEX [71]. The results are plotted in Fig. 3.2.

If a clump weight is mounted on the shared line, it can be treated as a vertical force acting on the shared line. The catenary plane of a shared line with a clump weight is illustrated in Fig. 3.3, where F is the submerged weight of the clump weight and s_c is the unstretched length along the line from origin P_{f1} to the point where the clump weight is attached. Then, the mooring tension at fairlead P_{f1}, H and V, can be computed by solving Eqs. (3.5) and (3.6) numerically.

$$\begin{aligned} l = {} & \frac{Hs}{EA} + \frac{Hs}{\omega}\left[\sinh^{-1}\left(\frac{V}{H}\right) - \sinh^{-1}\left(\frac{V-F-\omega}{H}\right)\right] \\ & + \frac{Hs}{\omega}\left[\sinh^{-1}\left(\frac{V-F-\omega s_c/s}{H}\right) - \sinh^{-1}\left(\frac{V-\omega s_c/s}{H}\right)\right] \end{aligned} \tag{3.5}$$

$$\begin{aligned} h = {} & \frac{\omega s}{EA}\left(\frac{V}{\omega} - \frac{1}{2}\right) + \frac{Hs}{\omega}\left[\sqrt{1+\left(\frac{V}{H}\right)^2} - \sqrt{1+\left(\frac{V-F-\omega}{H}\right)^2}\right] \\ & + \frac{Hs}{\omega}\left[\frac{F}{H}\frac{\omega}{EA}\left(\frac{s_c}{s}-1\right) + \sqrt{1+\left(\frac{V-F-\omega s_c/s}{H}\right)^2}\right] \\ & - \frac{Hs}{\omega}\left[\sqrt{1+\left(\frac{V-\omega s_c/s}{H}\right)^2}\right] \end{aligned} \tag{3.6}$$

Modeling of a single line

Usually, part of a single line is lying on the seabed. In practice, the positions of the fairlead and the anchor are known, and the mooring tension at the fairlead needs to be calculated. If we separate the single line into two parts by the touchdown point, the hanging part of the single line can be modeled by Eqs. (3.1) and (3.2) by treating the touchdown point as the second fairlead. The position of the touchdown point is usually unknown; therefore, an initial guess can be made for the length of the line lying on the seabed. Then, the touchdown point is located, and the fairlead tension is calculated. As the vertical component of the fairlead tension, H, is only caused by the submerged weight of the hanging part of the single line, the length of the line lying on the seabed is updated based on H. After some iterations, the calculation converges. The position of the touchdown point is found, and the fairlead tension

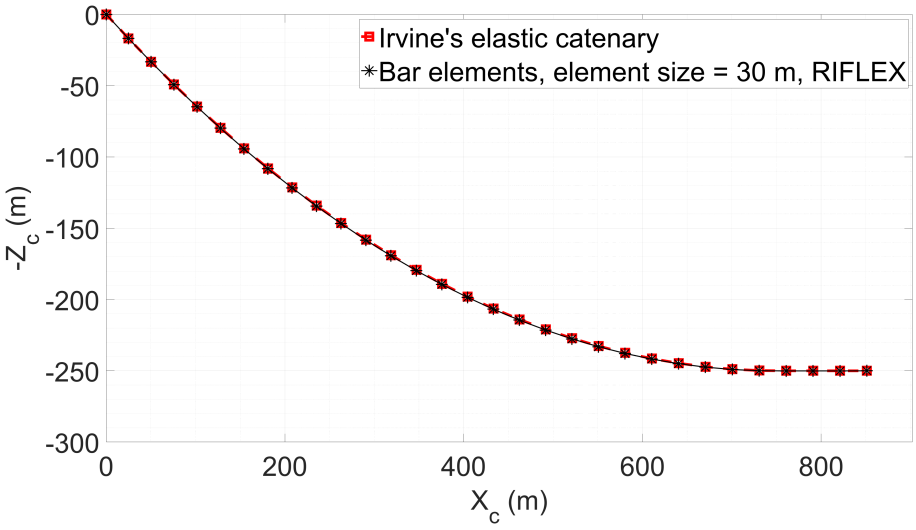

Figure 3.4: Static line shape of a single line in the catenary plane.

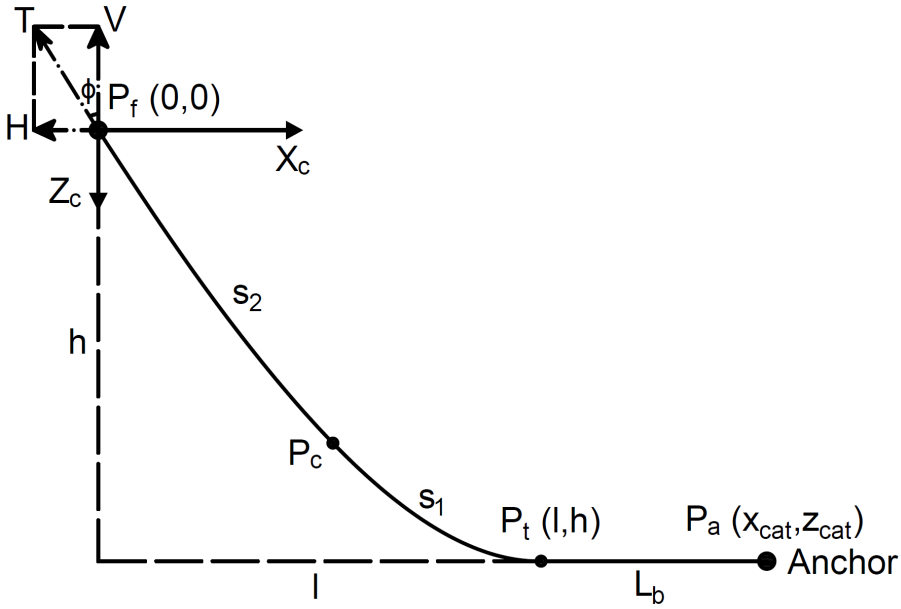

Figure 3.5: Illustration of a two-segment single line in the catenary plane.

is calculated. The application of Irvine's method in the modeling of a single line is verified by FE modeling [71]. The static line shape of a single line with the original mooring properties in the OC3 report [61] is calculated by Irvine's modeling method and FE modeling in the RIFLEX module of SIMA [71]. The results are plotted in Fig. 3.4.

The modeling method is extended to model a two-segment single line, in which the two segments have different mooring properties. The catenary plane of a two-segment single line is shown in Fig. 3.5, where P_f, the fairlead, is the origin; P_c is the connecting point of the two segments; P_t is the touchdown point; and P_a is the anchor point. Here, l and h are the horizontal and vertical distances, respectively, between P_f and P_t, and x_{cat} and z_{cat} are the horizontal and vertical distances, respectively, between P_f and P_a. Moreover, L_b is the distance between P_t and P_a, i.e., the length

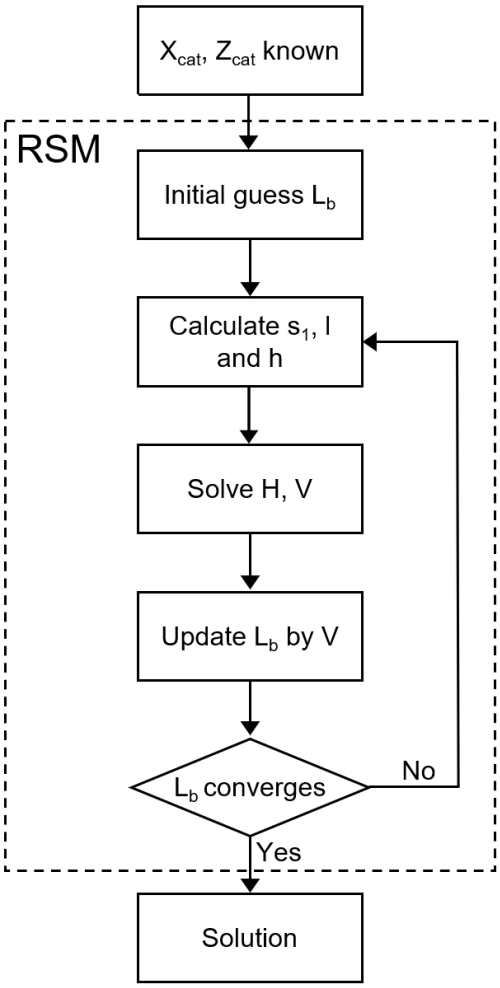

Figure 3.6: Illustration of the modeling approaches for a two-segment single line, with and without the RSM.

of the line lying on the seabed. Finally, s_1 is the unstrained length of the hanging part of the lower segment, and s_2 is the unstrained length of the upper segment. By establishing the nonlinear elastic catenary equations for the upper segment and the hanging part of the lower segment and the force equilibrium equations at P_c, the elastic catenary equations for the two-segment single line are expressed as follows:

$$\begin{aligned} l = &\frac{Hs_1}{E_1A_1} + \frac{Hs_1}{\omega_1}\sinh^{-1}\left(\frac{V-\omega_2}{H}\right) + \frac{Hs_2}{E_2A_2} \\ &+ \frac{Hs_2}{\omega_2}\left[\sinh^{-1}\left(\frac{V}{H}\right) - \sinh^{-1}\left(\frac{V-\omega_2}{H}\right)\right] \end{aligned} \tag{3.7}$$

$$\begin{aligned} h = &\frac{\omega_1 s_1}{E_1A_1}\left[\frac{V-\omega_2}{\omega_1} - \frac{1}{2}\right] + \frac{Hs_1}{\omega_1}\left[\sqrt{1+\left(\frac{V-\omega_2}{H}\right)^2} - 1\right] \\ &+ \frac{\omega_2 s_2}{E_2A_2}\left[\frac{V}{\omega_2} - \frac{1}{2}\right] + \frac{Hs_2}{\omega_2}\left[\sqrt{1+\left(\frac{V}{H}\right)^2} - \sqrt{1+\left(\frac{V-\omega_2}{H}\right)^2}\right] \end{aligned} \tag{3.8}$$

where l and h are the horizontal and vertical distances, respectively, between P_f and P_t; H and V are the horizontal and vertical components, respectively, of mooring tension T at P_f; s_1 is the unstrained length of the hanging part of the lower segment; and s_2 is the unstrained length of the upper segment. Moreover, ω_1 is the total submerged weight of the hanging part of the lower segment, and ω_2 is the total submerged weight of the upper segment. Here, E_1A_1 and E_2A_2 are the axial stiffness of the lower segment and the upper segment, respectively. As shown in Fig. 3.6, an iteration procedure similar to that for a one-segment single line is needed to model a two-segment single line. With given positions of the fairlead and the anchor point, an initial guess of L_b can be made. Based on the computed tension component, H, the value of L_b is updated. The position of the touchdown point and the fairlead tension can be obtained when the calculation converges after some iterations.

In the modeling of single lines, the nonlinear elastic catenary equations need to be solved in each iteration to locate the touchdown point. To reduce the computational costs, the response surface method (RSM) [72] is applied in [64] to model a two-segment single line. As shown in Fig. 3.6, in this specific application, the RSM approximates the original response surface (RS), i.e., the complex and nonlinear relationship between the positions of the fairlead and the anchor, x_{cat}, z_{cat}, and fairlead tension H and V, using an approximated RS (in this case, an explicit polynomial function). The coefficients of the polynomial function are determined by sampling in the original RS and minimizing the error by the least squares method. The selection of the approximated RS and the sampling of inputs should be determined to reach a balance between the accuracy and the time required to establish the approximated RS. Details can be found in [64], where the approach of using RSM to model a two-segment single line is verified and applied in analyses.

3.2.2 Mooring stiffness linearization

If considering the dynamic response of a shared mooring system, the mooring stiffness is nonlinear because of the nonlinear contribution from each mooring line and the varying positions of the FOWTs due to environmental loads. By applying Irvine's modeling method, the mooring stiffness of a shared mooring system can be linearized about a specific position of the floating system. For instance, in [64], the mooring stiffness of configuration I mentioned in Sec. 2.4.1 is linearized about the static equilibrium position of the FOWF and further applied in the eigenvalue analysis. The procedure of mooring stiffness linearization is briefly summarized as follows:

- Model four single lines and the shared line in MATLAB [73], as described in Sec. 3.2.1.
- Calculate the total mooring loads acting on each FOWT based on the fairlead tension.
- Develop an iteration algorithm to find the static equilibrium position of the system based on the mooring tension equilibrium given the initial positions of the FOWTs and the fairleads.

- Linearize the mooring stiffness by imposing a unit deflection (translation or rotation) in each DOF and calculating the resultant change in the mooring tension once the static configuration of the system is found.

In addition to the static equilibrium position, the mooring stiffness of a shared mooring system can also be linearized about mean dynamic positions in different ECs [74]. In this case, the mean dynamic positions are directly calculated from the time-domain responses, and no iteration is needed.

3.2.3 Eigenvalue analysis of floating offshore wind farms with shared mooring systems

Eigenvalue analysis

The system natural periods are important in the design of FOWTs. To avoid possible resonance, the floating system should be designed so that its natural periods are away from major excitation frequencies present in environmental loads. Eigenvalue analysis can be performed to obtain natural periods and eigenmodes of an FOWF with a shared mooring system in an efficient way. The general eigenvalue problem of an FOWF with a shared mooring system is formulated as follows:

$$[\boldsymbol{M} + \boldsymbol{A}(\omega)]\,\ddot{\boldsymbol{X}}(\omega) + [\boldsymbol{C_H} + \boldsymbol{C_M}]\,\boldsymbol{X}(\omega) = \mathbf{0} \tag{3.9}$$

where $\mathbf{M}$ and $\mathbf{A}(\omega)$ are the system mass matrix and the system frequency-dependent added mass matrix, respectively; $\mathbf{C_H}$ is the hydrostatic stiffness matrix of the FOWF; and $\mathbf{C_M}$ is the linearized mooring stiffness matrix of the FOWF, which can be calculated by the method described in Sec. 3.2.2. Moreover, $\mathbf{X}(\omega)$ is the system state vector of the FOWF. In this thesis, only the six-DOF rigid-body motions of an FOWT, i.e., surge, sway, heave, roll, pitch, and yaw, are considered in the eigenvalue analysis. Therefore, for a dual-spar FOWF, $\mathbf{X}(\omega)$ is a 12×1 vector.

To solve the eigenvalue problem, a frequency range and a sampling interval are set to search for eigenfrequencies of the system. Then, the sampling frequency increases stepwise by the sampling interval from the lower bound. For each sampling frequency, $\mathbf{A}(\omega)$ is determined, and the eigenvalue problem is solved. If the eigenfrequencies in the solution equal the sampling frequency, then the eigenfrequencies are the natural frequencies of the FOWF, and the corresponding eigenvectors describe the corresponding eigenmodes of the FOWF. The number of eigenmodes of an FOWF is equal to the number of DOFs of the system. For example, considering the rigid-body motions of FOWTs, configuration I has 12 natural periods and corresponding eigenmodes.

As the system states might be scaled differently in the obtained eigenvectors, modal participation factors are introduced to correct the scaling so that, in each eigenmode, the degree to which each state participates is indicated in a metric [75]. The modal participation factors are calculated as follows:

$$\boldsymbol{\Pi} = \left(\boldsymbol{\Phi}^{-1}\right)^{\top} \circ \boldsymbol{\Phi} \tag{3.10}$$

where $\mathbf{\Phi}$ is a matrix of eigenvectors. The number of rows of $\mathbf{\Phi}$ equals the total number of system states. Each column of $\mathbf{\Phi}$ is an eigenvector and represents an eigenmode. Here, "$\circ$" indicates the elementwise multiplication. Moreover, $\mathbf{\Pi}$ is the matrix of modal participation factors, and the sum of elements in each row and each column equals one. Each column of $\mathbf{\Pi}$ corresponds to one eigenmode. The element π_{ij} in matrix $\mathbf{\Pi}$ indicates the relative participation of system state x_i in the j-th eigenmode.

Eigenvalue analysis for configuration I

A detailed investigation is conducted focusing on the eigenvalue analysis of configuration I in [64]. It should be noted that in the eigenvalue analysis of configuration I, the two FOWTs are deployed in the global sway direction, i.e., along y_g axis. First, the aforementioned method for eigenvalue analysis is used for the original configuration I. The modal participation factors are calculated and presented in Table 3.1, in which the positive and minus signs indicating opposite motion directions are added from eigenvectors. Rigid-body motions of Spar 1 are defined as DOFs 1-6, and rigid-body motions of Spar 2 are defined as DOFs 7-12. There are, in total, 12 eigenmodes, and two modes are associated with each direction. Mode 1 indicates that both FOWTs move in phase in the specific DOF, and Mode 2 indicates that

Table 3.1: Modal participation factors for configuration I.

Direction	Surge		Sway		Heave		Roll		Pitch		Yaw	
Mode	Mode 1	Mode 2	Mode 1	Mode 2	Mode 1	Mode 2	Mode 1	Mode 2	Mode 1	Mode 2	Mode 1	Mode 2
1	0.47	0.52	0.00	0.00	0.00	0.00	0.00	0.00	-0.01	0.00	0.00	0.00
2	0.00	0.00	-0.50	0.50	0.00	0.00	0.00	0.00	0.00	0.00	0.00	0.00
3	0.00	0.00	0.00	-0.01	0.50	0.49	0.00	0.00	0.00	0.00	0.00	0.00
4	0.00	0.00	0.00	0.00	0.00	0.00	-0.57	0.24	-0.19	-0.01	0.00	0.00
5	0.00	-0.01	0.00	0.00	0.00	0.00	0.15	-0.04	-0.73	-0.06	0.00	0.00
6	0.00	0.00	0.00	0.00	0.00	0.00	0.00	0.00	0.00	0.00	0.58	0.42
7	0.52	-0.47	0.00	0.00	0.00	0.00	0.00	0.00	0.00	0.01	0.00	0.00
8	0.00	0.00	-0.50	-0.50	0.00	0.00	0.00	0.00	0.00	0.00	0.00	0.00
9	0.00	0.00	0.00	-0.01	0.49	-0.50	0.00	0.00	0.00	0.00	0.00	0.00
10	0.00	0.00	0.00	0.00	0.00	0.00	-0.21	-0.59	-0.02	0.18	0.00	0.00
11	-0.01	0.00	0.00	0.00	0.00	0.00	0.07	0.13	-0.05	0.75	0.00	0.00
12	0.00	0.00	0.00	0.00	0.00	0.00	0.00	0.00	0.00	0.00	0.42	-0.58

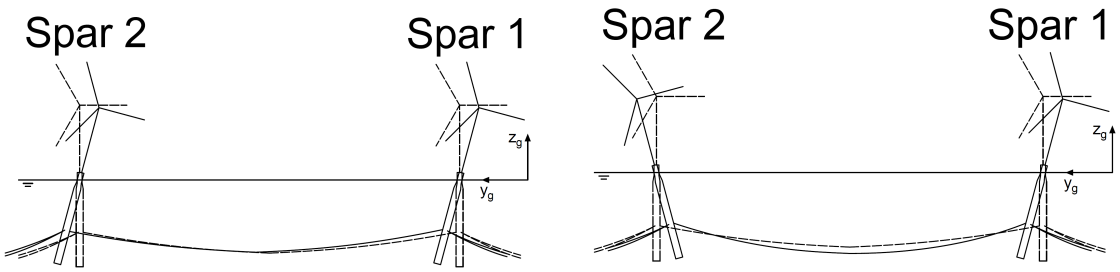

(a) Roll, mode 1

(b) Roll, mode 2

Figure 3.7: Illustration of eigenmodes in the roll direction (dashed line: initial position; solid line: mode shape).

the two FOWTs move 180 degrees out of phase in the specific DOF, as illustrated in Fig. 3.7 for eigenmodes in the roll direction. Based on the obtained eigenmodes, numerical decay tests are performed accordingly to excite the corresponding eigenmodes, from which the natural periods are estimated. A good match of natural periods obtained from the eigenvalue analysis and the numerical decay test is found;

Table 3.2: Natural periods of configuration I.

Eigenmode	Eigenvalue analysis [s]	Numerical decay test in SIMA [s]	Relative difference [%]
Surge 1	76.35	78.37	-2.57
Surge 2	75.62	77.51	-2.45
Sway 1	134.44	138.22	-2.73
Sway 2	47.01	49.88	-5.74
Heave 1	30.74	31.10	-1.17
Heave 2	30.77	31.05	-0.89
Roll 1	29.32	29.66	-1.14
Roll 2	29.33	29.69	-1.22
Pitch 1	29.31	29.59	-0.94
Pitch 2	29.31	29.59	-0.93
Yaw 1	8.27	8.46	-2.29
Yaw 2	8.27	8.46	-2.19

Table 3.3: Natural periods of a single spar FOWT.

Eigenmode	Surge	Sway	Heave	Roll	Pitch	Yaw
Eigenvalue analysis [s]	77.63	77.66	30.32	29.09	29.10	8.29
Numerical decay test in SIMA [s]	81.08	81.03	30.76	29.39	29.36	8.70
Relative difference [%]	-4.25	-4.16	-1.45	-1.00	-0.88	-4.69

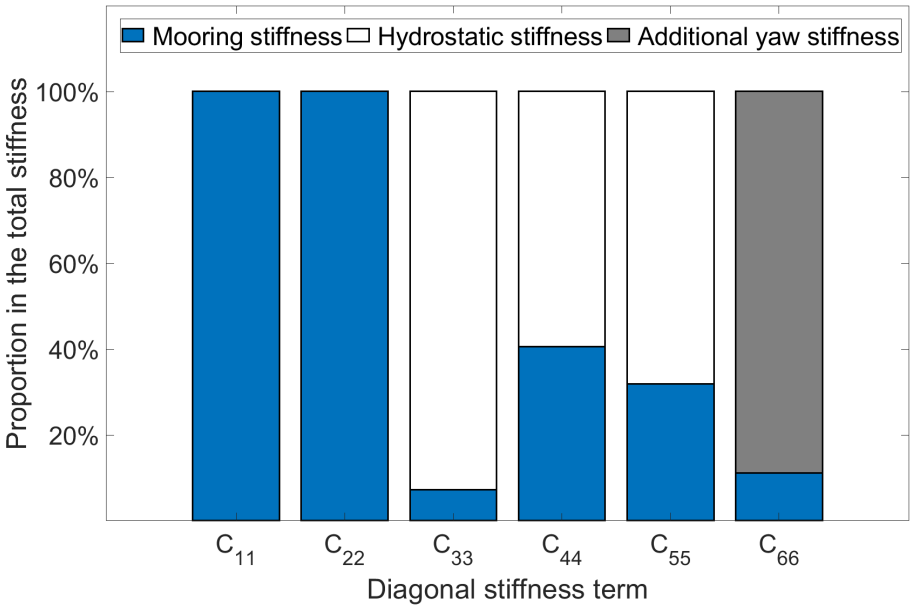

Figure 3.8: Proportions of diagonal stiffness terms of configuration I.

see Table 3.2. The difference in the natural periods can be attributed to differences in the modeling approaches (Irvine's method versus FE modeling), neglect of non-linear effects in the stiffness linearization, and uncertainties in the data extraction from the numerical decay test.

A similar comparison is done to a single spar FOWT that has three single lines with mooring properties the same as those of the single lines in configuration I. The results are presented in Table 3.3. Comparing the natural periods of configuration I and the single spar FOWT, it is found that the natural periods of the floating system in the surge and sway DOFs are largely affected by the shared mooring system. Particularly in the sway DOFs, which are aligned with the shared line, a low natural period of less than 50 s appears. As the influence of the shared line is mainly reflected in the mooring stiffness matrix, $\mathbf{C_M}$, in Eq. (3.9), the proportions of diagonal stiffness terms in the stiffness matrix are plotted in Fig. 3.8. For the diagonal stiffness terms related to the surge and sway DOFs, i.e., C_{11} and C_{22}, mooring stiffness is the only contributor, while the diagonal stiffness terms related to the other DOFs are either dominated by hydrostatic stiffness or the additional yaw stiffness from the delta-line design [61], which diminishes the influence of the mooring stiffness.

In the following sensitivity study, the influence of the mooring properties of the shared line and single lines is investigated. Readers are referred to [64] for details of the results and discussions of the sensitivity study. First, the diameter of the shared line in configuration I is increased from 90 to 130 mm with an interval of 5 mm. Eigenvalue analyses are performed for each shared line diameter, and the obtained natural periods are analyzed. Then, the mooring properties (length and diameter) of the wire segment and the chain segment of the single lines are varied respectively, and the natural periods of each variation are obtained from the eigenvalue analysis and analyzed. It is found that the natural periods of configuration I in the surge and sway DOFs are sensitive to the mooring properties of both single lines and the shared line, and a dependence of the surge and sway natural periods on the relevant mooring stiffness is observed.

3.3 Dynamic analysis of shared mooring systems

3.3.1 Numerical modeling of floating offshore wind farms

To perform fully coupled time-domain simulations, dual-spar FOWFs with different shared mooring systems are modeled in SIMA [58,59], in which the two OC3 Hywind spar FOWTs are modeled in accordance with the definition reports [60, 61]. The excitation and diffraction loads in irregular waves, aerodynamic loads in turbulent wind, and dynamic response of the coupled structural systems are computed in the time domain. The equation of motion for the dual-spar FOWF with a shared mooring system can be written in the time domain as follows:

$$(\mathbf{M}+\mathbf{A}_\infty)\ddot{\mathbf{x}}+\mathbf{B}_1\dot{\mathbf{x}}+\mathbf{B}_2\dot{\mathbf{x}}|\dot{\mathbf{x}}|+\mathbf{C}\mathbf{x}+\int_0^t \mathbf{h}(t-\tau)\dot{\mathbf{x}}(\tau)d\tau=\mathbf{f}(t,\mathbf{x},\dot{\mathbf{x}}) \tag{3.11}$$

where $\mathbf{M}$ is the structural mass matrix; $\mathbf{A}_\infty$ is the added mass matrix at infinite frequency; $\mathbf{B_1}$ is the matrix of linear damping coefficients; $\mathbf{B_2}$ is the matrix of quadratic damping coefficients; $\mathbf{C}$ is the matrix of restoring coefficients; $\mathbf{h}(\tau)$ is the retardation function; $\mathbf{x}$, $\dot{\mathbf{x}}$, and $\ddot{\mathbf{x}}$ are the vectors of the displacement, velocity, and acceleration in the time domain, respectively; $\mathbf{f}$ is the external force vector.

The spar floater, nacelle, and hub of each FOWT are modeled as rigid bodies in the SIMO module of SIMA. A panel model of the dual-spar FOWF is created and imported in WADAM [76], a potential flow program, in which the panel models of the two spar floaters are placed according to the corresponding turbine spacing. Then, a hydrodynamic analysis is performed for the panel model to obtain the hydrodynamic properties of the FOWF, such as the frequency-dependent hydrodynamic added mass and radiation damping coefficients, the first-order wave load transfer function, and the second-order mean wave drift loads, which are imported into SIMA. In *JP5*, the effect of hydrodynamic interaction between the spar floaters is imported as well, although the effect is limited because the turbine spacing is much larger than the characteristic dimensions of the floaters. Wave forces are integrated to the mean water level. Morison elements with only drag loads are added to the underwater part of the spar floaters to consider drag forces acting on the submerged floaters, which are integrated up to the instantaneous undisturbed free surface.

The tower, blades, and shaft of each FOWT are modeled as beam elements in the RIFLEX module of SIMA, which consist of segments that contains FEs with the same cross-sectional properties. As found in [77], the extreme response of a dual-spar FOWF with a shared line is not entirely wave-dominant, and aerodynamic loads acting on the rotors and towers do play a role there. Therefore, if the rotor is operating, the modified BEM theory is applied in SIMA to compute the aerodynamic loads; if the rotor is parked and the blades are feathered, the aerodynamic loads are calculated based on the steady-state airfoil coefficients [60]. Drag forces acting on the towers are considered and modeled by specifying a drag coefficient. According to the design standard [78], the drag coefficient is set to 0.65 for the tower based on an estimation of relevant Reynolds numbers. The effect of aerodynamic interaction

Table 3.4: Hydrodynamic coefficients used in the modeling of mooring lines.

Hydrodynamic coefficient [1]	Studless chain		Spiral sheating wire	
	Axial	Radial	Axial	Radial
C_a	1.0	1.0	1.0	1.0
C_d	0.2	2.4	0	1.2

[1] C_a is the added mass coefficient, and C_d is the drag coefficient.

between the FOWTs is ignored.

Fairleads and anchor points are modeled as supernodes to define both ends of a mooring line, and mooring lines are modeled as slender structures with bar elements. The properties of mooring lines presented in Sec. 2.4 are implemented in the cross-sectional properties of different segments accordingly. Hydrodynamic coefficients are specified to calculate the added mass and drag forces acting on the mooring lines, the values of which are determined with references from the design standard [78] and commercial data. In practice, drag coefficients are affected by factors such as the Reynolds number, surface roughness, and Keulegan-Carpenter number [79]. The hydrodynamic coefficients used in the modeling of mooring lines are summarized in Table 3.4.

The tethered buoys in configuration IV and configuration V are modeled as rigid SIMO bodies. The properties presented in Table 2.7 are implemented. The net

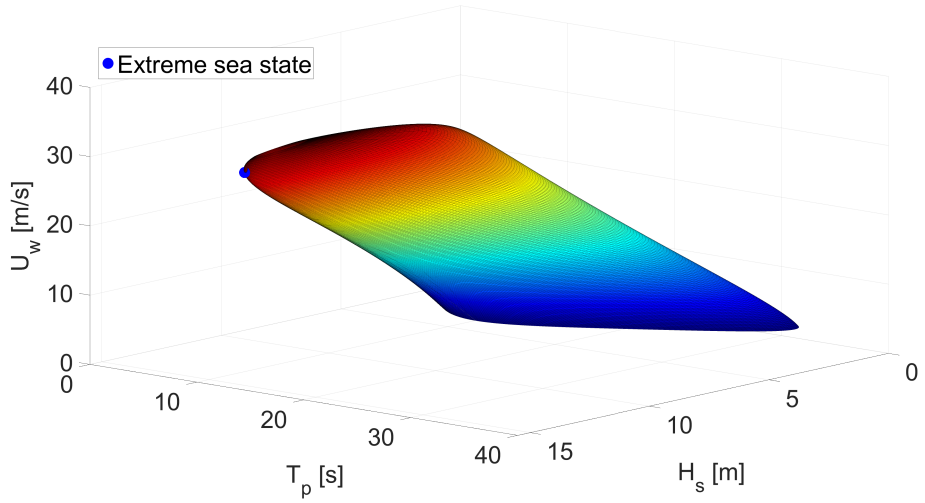

(a) Three-dimensional environmental contour surface

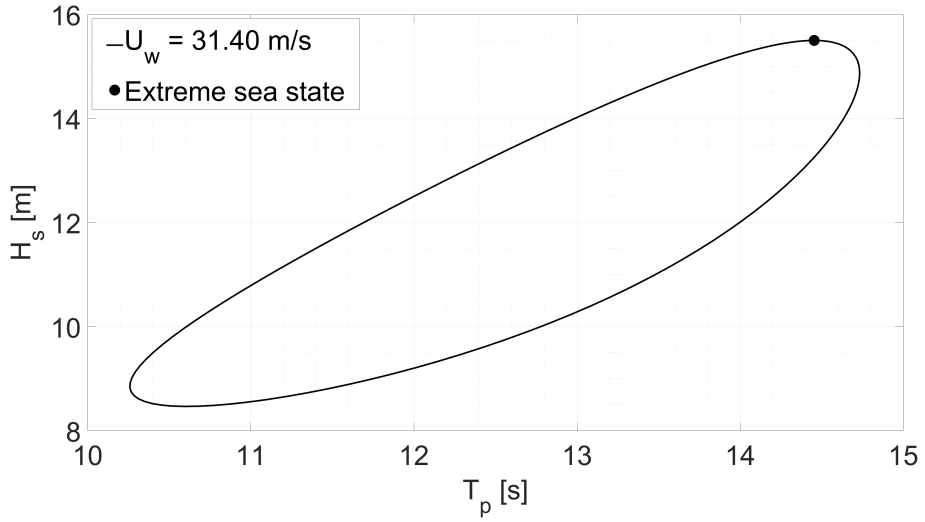

(b) Two-dimensional environmental contour line

Figure 3.9: The extreme sea state marked on the 50-year environmental contour surface/line (U_w: mean wind speed at 10-m height).

Table 3.5: Environmental parameters of the two ECs.

Parameter	EC1: operational	EC2: extreme
U_w (at hub-height) $[m/s]$	11.40	42.71
I (Turbulence intensity) $[-]$	0.17	0.11
H_s $[m]$	2.57	15.50
T_p $[s]$	11.12	14.45

buoyancy of a buoy is simplified as a constant force that always points upward. This simplification is valid as long as the buoy is fully submerged and completely sealed. Added mass and drag force acting on the buoy are modeled by specifying coefficients according to the design standard [78] and [80]. The added mass coefficient is set to 0.5, and the drag coefficient is set to 0.2.

3.3.2 Metocean conditions

The European deep-water offshore site "Norway 5" in the North Sea with a water depth of 202 m is chosen, and its ECs are considered for the dynamic analysis of shared mooring systems. The joint distribution of U_w at 10-m height, H_s and T_p, of "Norway 5" is modeled by fitting probability distributions to 10 years of simultaneous hourly mean wind and wave hindcast data [67]. One operational sea state and one extreme sea state are selected for numerical simulations. For the operational sea state, the U_w at hub height is set to 11.40 m/s, the rated wind speed of the FOWTs [60]. The H_s and T_p are set as the mean values of the conditional distributions. For the extreme sea state, a return period of 50 years is recommended by the design standard [13]. The extreme sea state is selected as the sea state with the highest H_s on the 50-year environmental contour surface, which is generated based on the joint distribution of U_w, H_s, and T_p; see Fig. 3.9. The environmental parameters of the two ECs are presented in Table 3.5.

Turbulent wind and irregular waves are considered in the dynamic analyses. To assess the performance of different shared mooring systems properly, the wind and waves are assumed to be aligned. As the two FOWTs are placed along the global surge direction, i.e., the x_g axis, the loading direction is 0 degrees if the wind and waves come along the x_g axis. As the site is located in the North Sea, the JONSWAP wave spectrum [78] is selected, and irregular waves are simulated with random wave seeds. Turbulent wind fields are generated by TurbSim [81]. The spectral model "IEC Kaimal" [82], the wind turbine Class I-B, and the IEC Normal Turbulence Model [83] are specified in the input files of TurbSim. Turbulent wind is simulated with random seeds. The size of the turbulence box is determined so that the rotors of the FOWTs in motion are always within the boundaries. The generated files of turbulent wind fields are then imported as inputs to simulations in SIMA.

Table 3.6: Summary of LCs for dynamic analyses of the shared mooring configurations.

LC	Configuration	Water depth $[m]$	Load scenario	Environmental condition [1]	Loading direction $[deg]$	Turbine state [2]		Simulation setup
						Spar 1	Spar 2	
1	I	320	Free decay	No wind, no waves	-	Parked	Parked	1 simulation for each DOF and each mode
2	I	320	Extreme	EC2	0,90	Parked	Parked	20 one-hour realizations
3	I	320	Extreme	EC2	0	Parked	Parked	20 one-hour realizations
4					30			
5					60			
6					90			
7	I	320	Extreme	EC2	0, 90	Parked	Parked	20 one-hour realizations
8	I, D_{share} [3] $= 100mm$							
9	I, $D_{share} = 110mm$							
10	I, $D_{share} = 120mm$							
11	I, $D_{share} = 130mm$							
12	II	235	Free decay	No wind, no waves	-	Parked	Parked	1 simulation for each DOF and each mode
13	IV							
14	V, F_{NB} [4] $= 5.19E + 05N$							
15	V							
16	V, $F_{NB} = 15.57E + 05N$							
17	V, $F_{NB} = 20.77E + 05N$							
18	V, $F_{NB} = 5.19E + 05N$	235	Extreme	EC2	0	Parked	Parked	15 one-hour realizations
19	V							
20	V, $F_{NB} = 15.57E + 05N$							
21	V, $F_{NB} = 20.77E + 05N$							
22	II	235	Accidental	EC1	0	Parked	Operating	15 one-hour realizations
23	IV							
24	V							
25	II	235	Extreme	EC2	0	Parked	Parked	15 one-hour realizations
26	IV							
27	V							

[1] EC1 and EC2 refer to the environmental conditions in Table 3.5.

[2] Spar 1 and Spar 2 refer to Fig. 2.1, Fig. 2.3, and Fig. 2.4.

[3] D_{share} is the diameter of the shared line in configuration I. The original diameter is 90 mm.

[4] F_{NB} is the net buoyancy of all buoys in configuration V. The original net buoyancy is 10.38E + 05 N.

3.3.3 Load cases

As described in Sec. 1.5, dynamic analyses are performed for configurations I, II, IV, and V. Convergence studies are performed prior to dynamic analyses to determine the number of realizations required for each LC, in which the ensemble averages of statistics of platform motion and mooring response are investigated. The determined number of realizations is deemed sufficient for the statistics of dynamic response to reach convergence. For each configuration and LC, one-hour simulations are performed with different random wind and wave seeds. Both the wind and wave time series realizations are one hour long. To perform numerical decay tests for a dual-spar FOWF with a shared mooring system, both FOWTs are first displaced or rotated by applying forces or moments in the respective DOFs. Then, the FOWTs are released, and the whole floating system freely oscillates in still water until the motion dies out. For each dual-spar FOWF, 12 free decay tests are performed in SIMA, which correspond to the 12 natural modes related to the rigid-body motions of the two FOWTs, as discussed in Sec. 3.2.3. The free decay tests performed in this thesis focus on the natural modes of rigid-body motions of FOWTs. For configurations IV and V, there are more than 12 natural modes if the rigid-body motions of the buoys are considered. Also, there are many natural modes in the dual-spar FOWFs, e.g., natural modes associated with the eigenmodes of mooring lines.

The LCs of the dynamic analyses are summarized in Table 3.6. Numerical decay

Table 3.7: Mooring properties of the selected shared line diameters in the sensitivity study for configuration I (LCs 7-11 in Table 3.6).

Diameter $[mm]$	90	100	110	120	130
Mass density $[kg/m]$	42.77	52.24	62.65	73.98	86.25
Weight in water per unit length $[N/m]$	324.00	398.75	481.09	571.00	668.44
Axial stiffness $[N]$	7.64E+08	9.35E+08	1.12E+09	1.32E+09	1.54E+09
Minimum breaking strength $[N]$	8.38E+06	1.04E+07	1.25E+07	1.49E+07	1.76E+07

Table 3.8: Properties of the selected net buoyancy in the sensitivity study for configuration V (LCs 18-21 in Table 3.6).

Net buoyancy $[N]$	Diameter [1] $[m]$	Mass $[kg]$
5.19E+05	5.22	2.26E+04
10.38E+05	6.58	4.53E+04
15.57E+05	7.53	6.79E+04
20.77E+05	8.29	9.05E+04

[1] Approximate diameter of the spherical buoys.

tests are performed for configuration I (LC 1), and the results are compared with those for a single spar FOWT. Then, configuration I is compared with a single spar FOWT under an extreme scenario in which both FOWTs are parked with blades feathered (LC 2), followed by a sensitivity study on loading directions (LCs 3-6) and shared line mooring properties (LCs 7-11). The mooring properties of the selected shared line diameters in the sensitivity study are presented in Table 3.7. For configurations II, IV, and V, numerical decay tests are performed first (LCs 12-17). Then, a sensitivity study is conducted for configuration V on the net buoyancy of the buoys (LCs 18-21). The properties of the selected net buoyancy in the sensitivity study are presented in Table 3.8. Finally, configuration V is compared with configurations II and IV considering an extreme scenario (LCs 25-27) and an accidental scenario (LCs 22-24), in which FOWT Spar 1 is parked at standstill with blades feathered due to assumed faults or failures and FOWT Spar 2 is in normal operation.

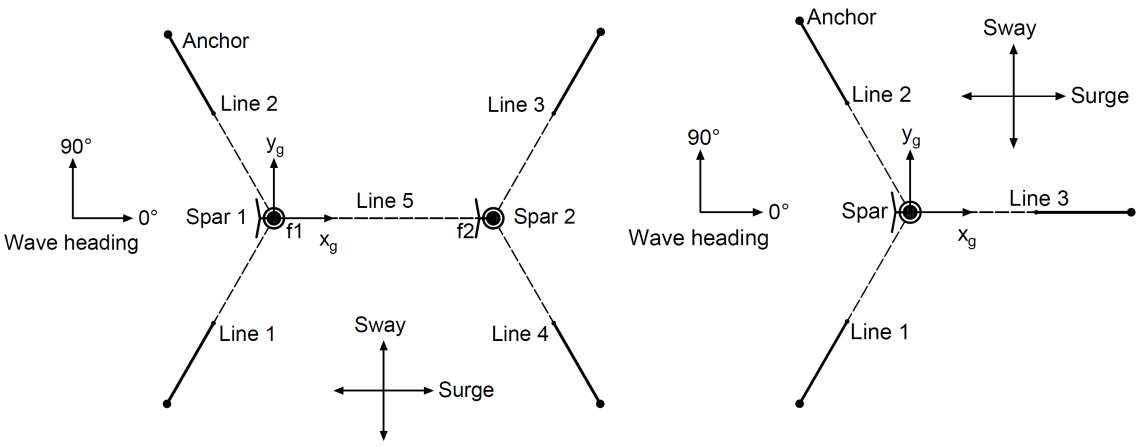

(a) Configuration I (b) Single FOWT

Figure 3.10: Top view of configuration I and the single FOWT (dashed line: wire; solid line: chain).

Table 3.9: Natural periods of configuration I and the single FOWT [s].

DOF		Surge	Sway	Heave	Roll	Pitch	Yaw
Configuration I	Mode 1 [1]	135.51	76.25	31.13	29.48	29.47	8.36
	Mode 2	63.52	75.64	31.03	29.48	29.46	8.34
Single FOWT		79.65	79.64	30.75	29.31	29.31	8.69

[1] For configuration I, Mode 1 indicates that both FOWTs move in phase in the specific DOF and Mode 2 indicates that the two FOWTs move 180 degrees out of phase in the specific DOF.

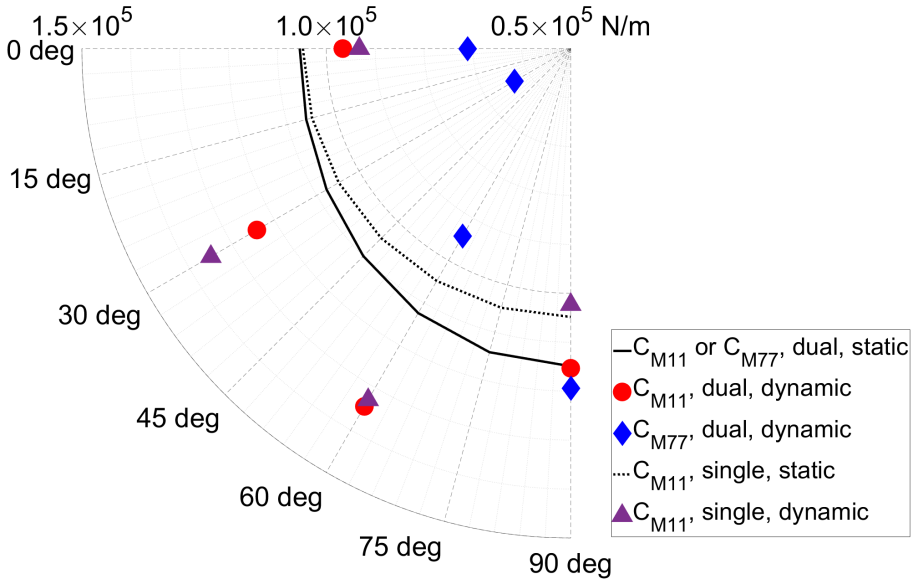

Figure 3.11: Linearized mooring stiffness terms with respect to the loading direction (dual: configuration I; single: single FOWT, static: linearized about the static equilibrium position; dynamic: linearized about the mean dynamic position).

3.3.4 Dynamic analysis of configuration I

Comparison between configuration I and a single FOWT

As described in Sec. 3.3.3, configuration I is compared with a single FOWT, which has the same mooring line orientations as Spar 1 of configuration I; see Fig. 3.10. The mooring lines of the single FOWT have the same mooring properties as the single lines of configuration I.

For configuration I and the single FOWT, Table 3.9 summarizes the natural periods estimated from the numerical decay tests described in Sec. 3.3.3. Similar to the results found in Sec. 3.2.3, the natural periods of the translational DOFs in the horizontal plane, namely in the surge and sway DOFs, are predominantly influenced by the shared line since the diagonal terms in the mooring stiffness in these DOFs only have contributions from the mooring stiffness; see Fig. 3.8.

The linearization method presented in Sec. 3.2.2 is first applied to compare the linearized mooring stiffness. The mooring stiffness is linearized about the static equilibrium positions and the mean dynamic positions of the floating system and in the coordinate system where the x-axis is aligned with the loading direction. The diagonal stiffness terms related to the motions of FOWTs in the loading direction are plotted in Fig. 3.11. For configuration I, the stiffness terms "C_{M11}, dual, static" and "C_{M77}, dual, static" are sensitive to loading directions due to the asymmetry of the mooring layout. The stiffness term "C_{M11}, single, static" is insensitive to loading directions, as the single FOWT has a symmetric mooring layout. For both configurations, the stiffness terms linearized about the mean dynamic position are sensitive to loading directions and differ from those linearized about the static equilibrium position.

The motions of an FOWT in the horizontal plane must be restricted by the

Table 3.10: Statistics of the horizontal platform motions of FOWTs in the loading direction.

Parameter	Configuration I		Single FOWT
	Spar 1	Spar 2	
Loading direction = 0 deg			
Platform, static equilibrium position [m]	(2.56, 0)	(997.70, 0)	(0,0)
Platform, mean dynamic position [m]	(13.59, 0.35)	(1006.25, 3.71)	(5.28, 0.37)
Platform, motion range [1] [m]	[-12.40, 12.90]	[-12.76, 12.95]	[-11.98, 11.94]
Platform, motion SD [2] [m]	3.64	3.83	3.43
Loading direction = 90 deg			
Platform, static equilibrium position [m]	(2.38, 0.07)	(997.50, 0.07))	(-0.08, 0.08)
Platform, mean dynamic position [m]	(1.95, 11.36)	(996.79, 11.09)	(-1.33, 12.06)
Platform, motion range [m]	[-12.72, 13.61]	[-12.94, 13.16]	[-12.98, 13.72]
Platform, motion SD [m]	3.88	3.82	3.91

[1] "Platform, motion range" refers to the range of the planar platform motions in the loading direction, and is calculated with regard to "Platform, mean dynamic position".

[2] "Platform, motion SD" refers to the standard deviation (SD) of the planar platform motions projected in the loading direction.

mooring system to maintain its operation and the structural integrity of the power cable. Although the design standards do not provide specific recommendations, e.g., [13], an excursion limit can be assumed as a function of the water depth [84]. In addition, due to the wake effects, the distance between wind turbines affects the power production of a wind farm [62]. Investigating the impact of an added shared line on the horizontal platform motions of FOWTs is therefore worth exploring. Table 3.10 presents the statistics of horizontal platform motions for configuration I and the single FOWT, which are calculated as the ensemble average of 20 realizations. Due to the self weight of the shared line, two FOWTs approach each other by around 2.5 m along the x_g-axis in the static equilibrium position. Due to the mean aerodynamic load and the mean wave drift force, FOWTs experience a large offset in the loading direction. In comparison to the single FOWT, both FOWTs of configuration I exhibit relatively larger motion ranges and dynamic motions with a 0-degree loading direction but have similar motion ranges and dynamic motions with a 90-degree loading direction. For the 0-degree loading direction, the discrepancy in the restoring force provided by Line 5 of configuration I and Line 3 of the single FOWT has a significant effect on the motions of the FOWTs. However, the difference in the restoring force has a minor influence on the motions of the FOWTs in the 90-degree loading direction, as the mooring line is nearly perpendicular to the loading direction.

Structural responses are affected by the dynamics of FOWTs, among which the mooring response and TBBM are selected for investigation. The mooring angle is

Table 3.11: Statistics of mooring tension and mooring angle at the fairleads.

Parameter	Configuration I			Single FOWT		
	Line 1	Line 2	Line 5 f1	Line 1	Line 2	Line 3
Loading direction = 0 deg						
Pretension [N]	9.50E+05	9.50E+05	8.39E+05	8.50E+05	8.50E+05	8.44E+05
Mooring tension, max [N]	2.34E+06	2.17E+06	5.35E+06	2.04E+06	1.77E+06	1.51E+05
Mooring tension, mean [N]	1.39E+06	1.36E+06	9.61E+05	1.03E+06	9.93E+05	6.86E+05
Mooring tension, SD [N]	1.80E+05	1.76E+05	6.63E+05	1.57E+05	1.43E+05	1.38E+05
Mooring angle, max [deg]	67.43	67.01	90.00	65.94	65.18	64.94
Mooring angle, mean [deg]	63.39	63.19	80.34	61.05	60.77	57.55
Mooring angle, SD [deg]	0.95	0.98	4.70	1.16	1.19	1.87
Loading direction = 90 deg						
Pretension [N]	9.47E+05	9.40E+05	8.39E+05	8.52E+05	8.45E+05	8.48E+05
Mooring tension, max [N]	2.45E+06	1.36E+06	4.29E+06	2.27E+06	1.20E+06	1.86E+06
Mooring tension, mean [N]	1.45E+06	6.24E+05	9.59E+05	1.33E+06	5.19E+05	9.59E+05
Mooring tension, SD [N]	2.16E+05	1.45E+05	5.29E+05	2.02E+05	1.16E+05	1.44E+05
Mooring angle, max [deg]	68.28	63.97	89.99	67.57	62.71	64.97
Mooring angle, mean [deg]	63.61	56.57	80.42	63.03	54.62	60.53
Mooring angle, SD [deg]	1.22	2.21	3.03	1.25	2.20	1.14

defined as the angle formed between the mooring line and the vertical direction at the fairlead, i.e., angle ϕ in Figs. 3.1 and 3.5. As illustrated in Fig. 3.10, the mooring lines connected to Spar 1 of configuration I and the mooring lines connected to the single FOWT have the same orientations. For these mooring lines, the statistics of the mooring tension and mooring angle at the fairleads are averaged over 20 realizations and presented in Table 3.11. For the 0-degree loading direction, higher fairlead tension is observed for the single lines of configuration I compared to those of the single FOWT, as Spar 1 experiences larger mean dynamic offset than the single FOWT; see Table 3.10. For the 90-degree loading direction, the mooring responses of Line 1 and Line 2 are similar between Spar 1 and the single FOWT, consistent with the mean dynamic positions of the FOWTs shown in Table 3.10. The maximum mooring angles at the fairlead Line 5 f1 are close to 90 degrees for both loading directions, which indicates the occurrence of full stretch of the shared line (Line 5). Moreover, it is noticed that the dynamic mooring tension and the standard deviations (SDs) of the mooring angle at the fairlead are considerably higher in the shared line than in the single lines for both loading directions. This is the trade-off of reducing the number of single mooring lines and anchors. Therefore, the design of the shared line is crucial to prevent premature or cascade mooring failures of FOWFs in extreme ocean environments.

Snap events can lead to premature failure of a mooring line or a considerably reduced fatigue life [85]. A snap event of a mooring line is characterized as a sharp tension spike whose magnitude surpasses typical values of local tension maxima, following a transient slackness in the mooring line [85]:

$$T_{start} \leq 0.1 \cdot T_{static} \tag{3.12}$$

$$T_{end} \geq 1.9 \cdot T_{static} \tag{3.13}$$

where T_{start} is the local tension minima at the beginning of the snap event; T_{end} corresponds to the local tension maxima at the end of the snap event; and T_{static} is the pretension along with the tension contribution caused by the mean environmental load, i.e., the mean dynamic mooring tension. Snap load events are examined for all mooring lines of configuration I. For the investigated loading directions, snap load events are only observed in the shared line. Due to the larger relative surge motions between FOWTs, the shared line experiences more snap load events in the 0-degree loading direction than in the 90-degree loading direction. The number of snap events averaged over 20 one-hour simulations is 209 at the fairlead Spar 1, Line 5 f1, for the 0-degree loading direction and 86 for the 90-degree loading direction.

The statistics of the TBBM are investigated as well, and for both loading directions, the FOWTs of configuration 1 have a TBBM comparable to that of the single FOWT. Therefore, no additional consideration is required for the structural design of the towers of configuration I.

Sensitivity study for configuration I

As mentioned in Sec. 3.3.3, a sensitivity study is conducted for configuration I to assess the influence of loading directions and shared line mooring properties. Readers are directed to [74] for detailed results and discussions of the sensitivity study. The main findings are summarized as follows:

Sensitivity study on loading directions

- As shown in Fig. 3.11, significant variations depending on the loading direction are observed for the diagonal mooring stiffness terms related to the motions of the FOWTs in the loading direction, which are attributed to the different mean dynamic positions of the FOWTs caused by the mean environmental loads under ECs with different loading directions. The diagonal stiffness term of Spar 1 differs from that of Spar 2 for each investigated loading direction, which implies that in the dynamic analyses, the two FOWTs are expected to show different motion characteristics.

- The mean dynamic positions of the FOWTs are affected by both the mean aerodynamic load and the mean wave drift force, with the former showing differences for different loading directions while the magnitude of the latter is relatively consistent across loading directions. A correlation is observed between the statistics of aerodynamic force acting on the FOWTs and the mean dynamic positions of the FOWTs. The motion ranges of the FOWTs exhibit variability depending on the loading direction as a result of the varying mooring stiffness and environmental loads in different loading directions.

- The windward single lines are expected to be more loaded than the leeward single lines. Due to the relative motions of the two FOWTs, the shared line

experiences repetitive cycles of tightness and looseness. Even though the mean tension in the shared line is not necessarily higher than that in the single lines, the shared line has a large mean mooring angle and the most significant variation in mooring tension, which leads to the maximum tension being close to the MBS in some loading directions, indicating the need for a redesign of

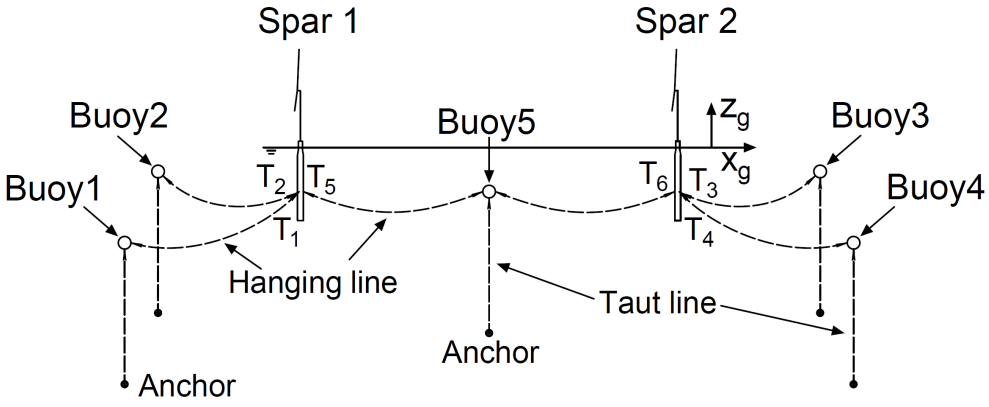

(a) Configuration V

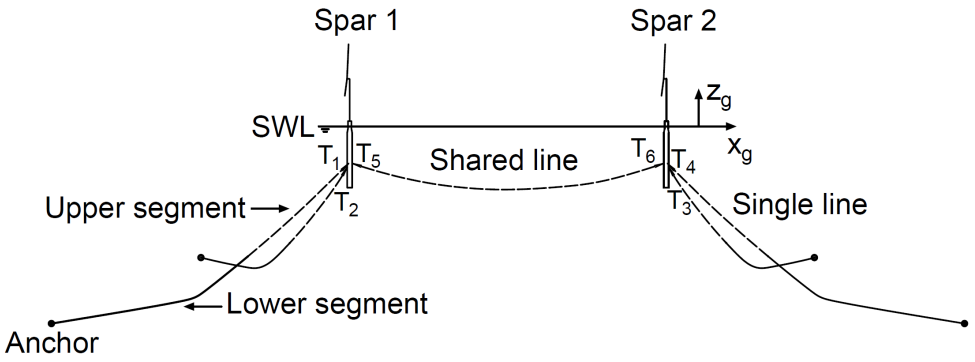

(b) Configuration II

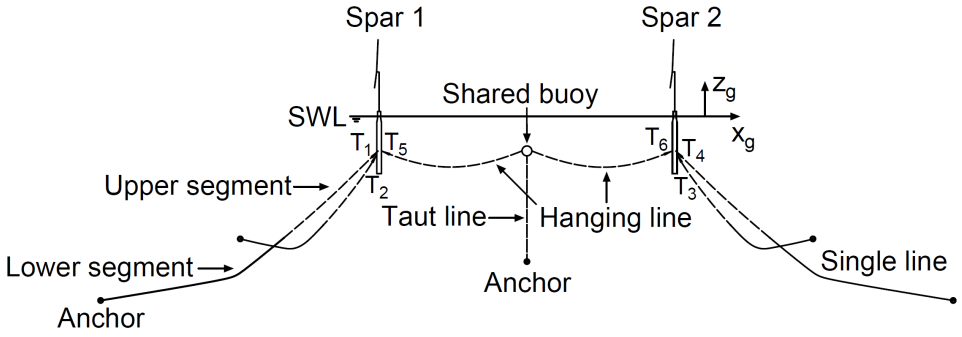

(c) Configuration IV

Figure 3.12: Illustrations of configurations V, II, and IV with fairlead tension marked as T_1, T_2, ..., T_6.

the shared line.

Sensitivity study on shared line diameters

- The variations of the shared line diameter mainly affect the mean dynamic positions of the FOWTs, which are also affected by the mean aerodynamic load. For configuration I, the impact of the shared line diameter is more noticeable in the 0-degree loading direction, which aligns with the orientation of the shared line.

- Aligned with the observations for the linearized mooring stiffness, the influence on the horizontal platform motion range is relatively small for the investigated shared line diameters.

- An increase in the shared line diameter leads to an increase in both the pre-tension and mean mooring tension across all mooring lines. However, the maximum tension in the shared line and the averaged number of snap events observed at the fairleads of the shared line decrease with the increased shared line diameter. The TBBM is less important in the design of the shared line, as it is not sensitive to changes in the shared line diameter.

3.3.5 Dynamic analysis of configurations II, IV, and V

As described in Sec. 3.3.3, configuration V is compared with configurations II and IV in terms of natural periods, platform motions, and fairlead tension in two load scenarios, one accidental scenario and one extreme scenario. In this section, the relative surge motion is calculated with regard to the initial turbine spacing. The fairlead tension is marked in Fig. 3.12 for the three configurations.

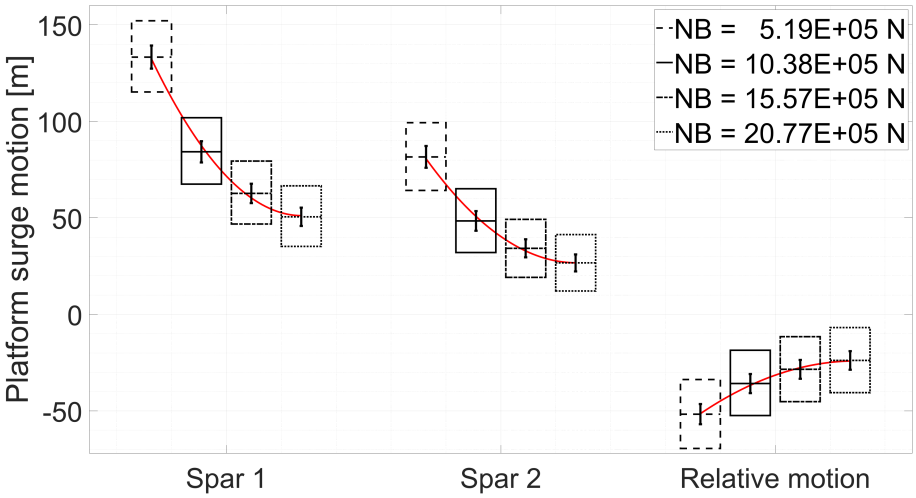

Figure 3.13: Expected values of the statistics of platform surge motion due to variation of the net buoyancy of the buoys in configuration V (NB: net buoyancy; middle line: mean; box: motion range (maximum and minimum); error bar: SD; red curve: quadratic fit of the mean values).

Sensitivity study on the net buoyancy for configuration V

As mentioned in Section 3.3.3, a sensitivity analysis is performed on the net buoyancy of all buoys for configuration V before it is compared with configurations II and IV. For more detailed results and discussions, readers are referred to [86]. The main observations from the sensitivity study are summarized below:

- The analysis of natural periods is limited to the rigid-body motions of the FOWTs. Natural periods in the surge and sway DOFs are much more sensitive to the net buoyancy of the buoys than those in the other DOFs. Increasing the net buoyancy results in a stiffer mooring system and, therefore, reduces the surge and sway natural periods. Therefore, adjusting the net buoyancy of the buoys can be an effective approach to alter the natural periods.

- It can be observed from Fig. 3.13 that an increase in the net buoyancy of the buoys leads to a decrease in the mean surge offset of the FOWTs, while the mean surge distance between the FOWTs tends to approach the initial spacing. Considering a simple tether-buoy-horizontal line system, an approximately quadratic relationship can be derived between the geometrical mooring stiffness and the net buoyancy of a submerged tethered buoy. Because the mooring stiffness of the floating system is primarily influenced by the tethered buoys, this quadratic relationship is reflected in the mean surge offset resulting from the mean environmental loads. As shown in Fig. 3.13, quadratic curves fitted to the mean surge offsets as a function of net buoyancy match well with the data points. Similar relations are also found in the sway motions of the FOWTs. For both FOWTs, an increase in net buoyancy leads to a decrease in the motion range and dynamic motions in the surge DOF. Due to the approximately quadratic relation, the influence of increasing net buoyancy

Table 3.12: Natural periods identified from decay tests for configurations V, II, and IV [s].

Mode [1]	Configuration	Surge	Sway	Heave	Roll	Pitch	Yaw
Mode 1	V	440.90	407.59	32.16	30.31	30.32	8.74
	II	153.12	87.31	30.85	29.55	29.58	8.40
	IV	151.55	89.56	30.70	29.66	29.68	8.43
Mode 2	V	305.05	405.04	32.14	30.30	30.31	8.72
	II	67.49	86.40	30.81	29.55	29.57	8.39
	IV	43.27	89.17	30.83	29.65	29.74	8.43

[1] As described in Sec. 3.2.3, Mode 1 indicates that both FOWTs move in phase in the specific DOF and Mode 2 indicates that the two FOWTs move 180 degrees out of phase in the specific DOF.

on constraining the planar motions of the FOWTs is more pronounced when the net buoyancy goes from low to medium levels than from medium to high levels.

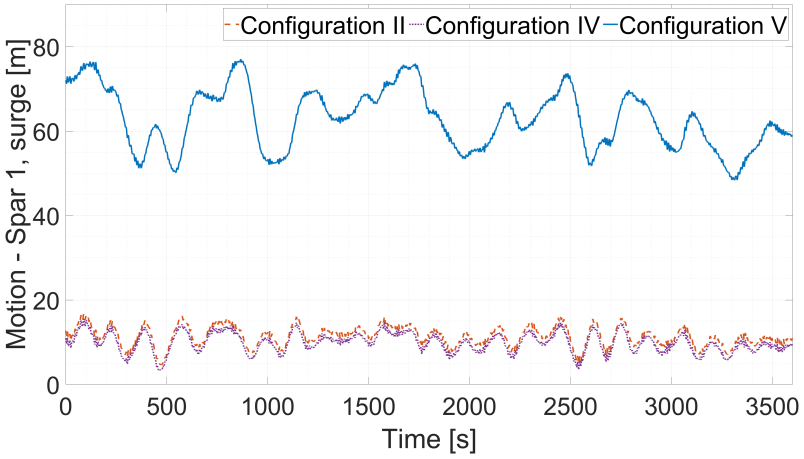

(a) Spar 1, surge motion

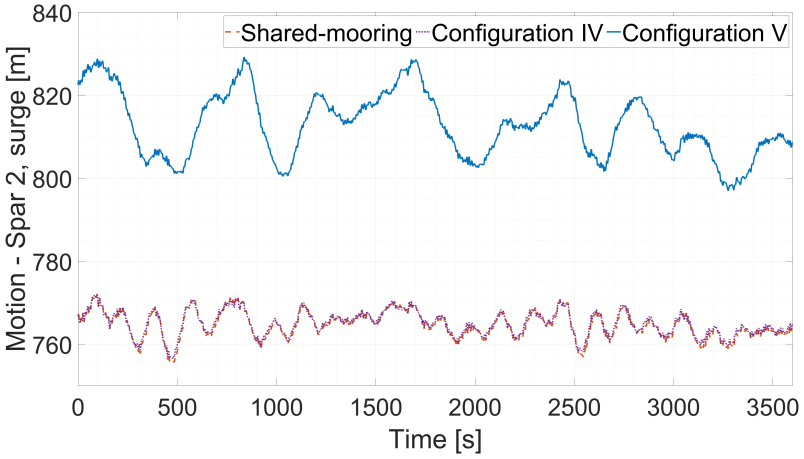

(b) Spar 2, surge motion

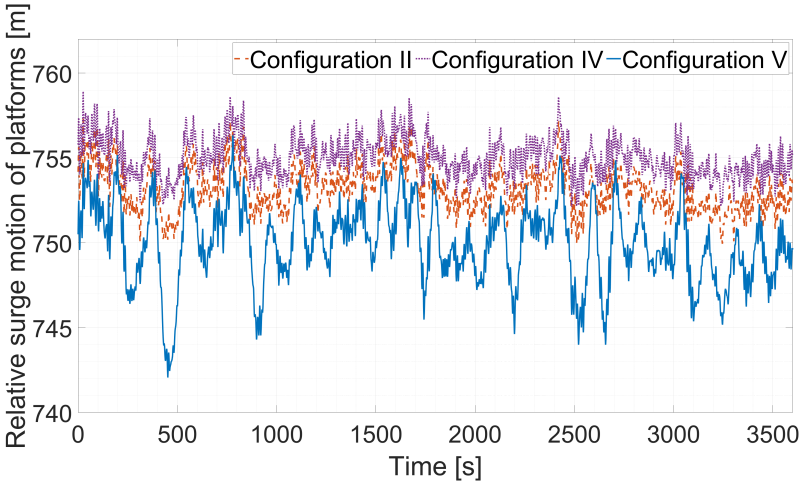

(c) Relative surge motion between Spar 1 and Spar 2

Figure 3.14: Time series of platform surge motion in the accidental scenario (random wave seed = 3).

- An increase in the net buoyancy of the buoys results in a stiffer system, leading to an increase in both the mean values and the variations of all fairlead tensions and a reduction of the magnitudes of the dynamic motions (and SDs) of the buoys. The mean tension in taut lines is close to the net buoyancy of the buoys, and the dynamic tension is minimal in comparison.

Comparison among configurations II, IV, and V

Natural periods identified from decay tests

Table 3.12 presents the natural periods identified from the decay tests for the three investigated configurations, which solely correspond to the eigenmodes related to the rigid-body motions of the FOWTs. It is revealed that significant differences are present only in the natural periods of surge and sway DOFs, while the differences in the natural periods of other DOFs are insignificant. This is attributed to the fact that the influence of the mooring systems is mainly reflected in the surge and sway DOFs, as discussed in Sec. 3.2.3. The natural periods of surge, Mode 1, and both modes of the sway DOF are similar for configurations II and IV, as the outer, conventional single lines govern the mooring stiffness. For configuration V, connections to the submerged tethered buoys through hanging lines replace all single lines, leading to a considerably softer mooring system. As a result, the natural periods in the surge and sway DOFs of configuration V are significantly larger than those in the surge and sway DOFs of the other two configurations.

Accidental load scenario

As described in Sec. 3.3.3, in the accidental load scenario, FOWT Spar 1 is parked at standstill with blades feathered due to assumed faults or failures, and FOWT Spar 2 is in normal operation.

Fig. 3.14 shows the time series of platform surge motion for the realization where the mean values and standard deviations of the FOWTs in configuration V are closest to the ensemble averages across all realizations. As the original outer single lines have been replaced with connections to the submerged tethered buoys through

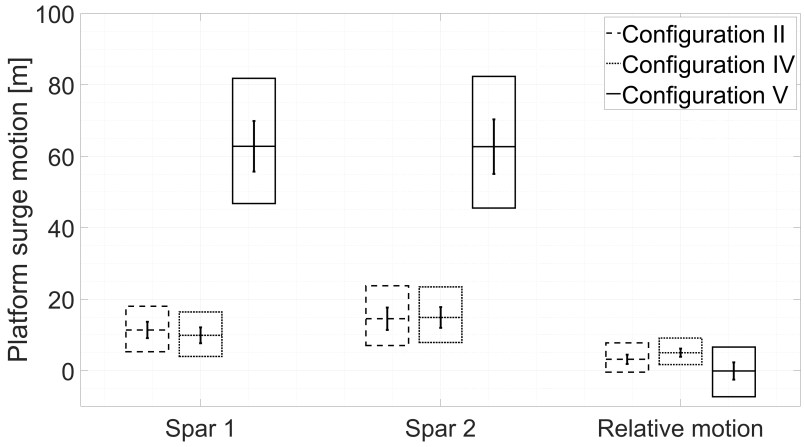

Figure 3.15: Expected values of the statistics of platform surge motion in the accidental scenario (middle line: mean; box: motion range (maximum and minimum); error bar: SD).

hanging lines, the tethered-buoy system has considerably lower mooring stiffness than the other configurations. Therefore, the FOWTs in configuration V experience much larger mean surge offsets from the initial positions and larger dynamic motions. The dynamic motions of the FOWTs are dominated by slowly-varying motions. The oscillation period of dynamic motions of configuration V is significantly longer compared to that of the other two configurations due to the longer natural periods in the surge direction shown in Table 3.12. The motion patterns of the FOWTs are very similar for configurations II and IV, as the single mooring lines play a dominant role in the mooring stiffness of these two configurations in the surge direction. Configuration V exhibits a smaller mean distance but larger dynamic oscillations between the two FOWTs when compared to the other two configurations. The latter is attributed to the reduced system stiffness in configuration V.

Fig. 3.15 presents the expected values of platform surge motion statistics, with the initial positions of the two FOWTs taken as a reference. Configurations II and

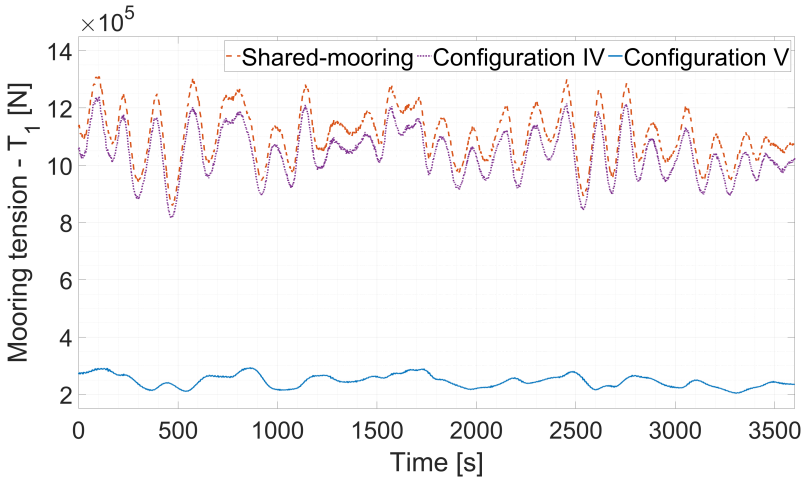

(a) T_1

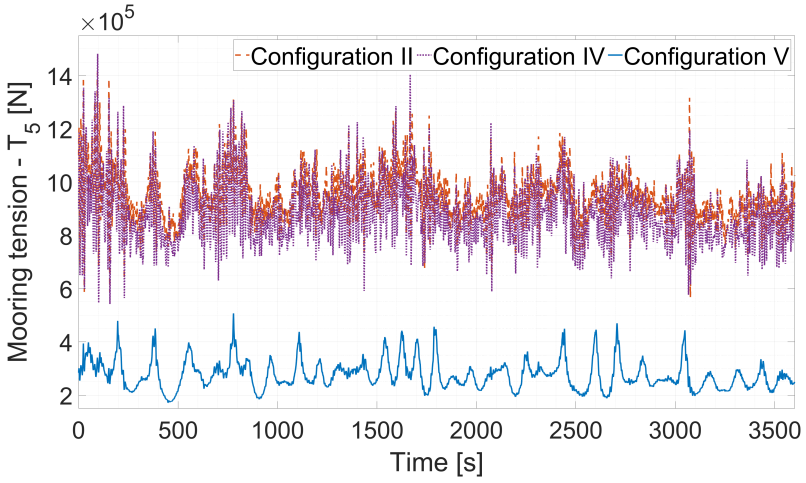

(b) T_5

Figure 3.16: Time series of fairlead tension in the accidental scenario (random wave seed = 3).

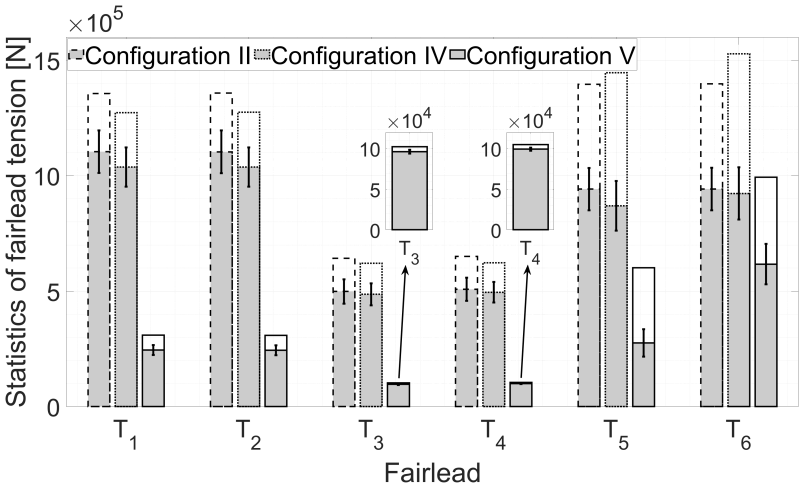

Figure 3.17: Expected values of the statistics of fairlead tension in the accidental scenario (gray bar: mean; white bar: maximum; error bar: SD).

IV show comparable mean offsets of the FOWTs from the initial positions, while configuration V exhibits considerably larger mean offsets. Additionally, configuration V shows significantly larger dynamic motions of individual FOWTs compared to the other two configurations, while the increase in dynamic relative motions between the FOWTs is moderate. The differences in the mean value of the relative surge motion are not significant between configuration V and configurations II and IV.

The time series of the fairlead tension, T_1 and T_5, are presented in Fig. 3.16 for the same realizations as shown in Fig. 3.14. Configuration V shows significantly lower mean and dynamic tension levels compared to the other two configurations at both fairleads. The variation patterns of fairlead tension are different as well. For T_1, the tension of configuration V shows slowly-varying trends with a longer period, while for T_5, the dynamic tension variations in configuration V are dominated by low-frequency oscillations, and the dynamic tension variations in the other two configurations are dominated by wave-frequency oscillations.

Fairlead tension statistics are calculated from the time series in each realization, the expected values of which are shown in Fig. 3.17. For all three investigated configurations, the windward lines, Line 1 and Line 2, experience more loads than the leeward lines, Line 3 and Line 4, as wind and waves propagate in the surge direction. Comparing configurations V and II, it is observed that the replacement of single lines with hanging lines connected to single buoys leads to a substantial reduction in both the mean and dynamic fairlead tension. Comparing the statistics of the fairlead tension in the shared line, T_5 and T_6, it is found that sharing a moored buoy between two FOWTs leads to a minor reduction in the mean tension of the lines in between; however, it results in an increase in the maximum tension and dynamic tension due to the reduced flexibility of the floating system after an anchor is added in between the two FOWTs. The replacement with hanging lines connected to single buoys also reduces the tension level in the lines between the two FOWTs and results in significant decreases in both the mean and dynamic tension, to which the reduced

mean relative surge distance shown in Fig. 3.15 contributes. For configurations IV and V, the shared buoy decouples the motions of the two FOWTs to some degree. As Spar 2 is subjected to a large aerodynamic thrust in operation, T_6 of these two

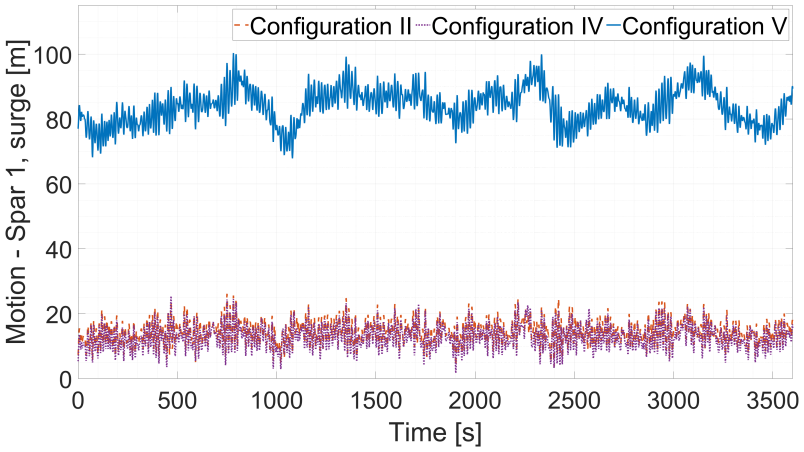

(a) Spar 1, surge motion

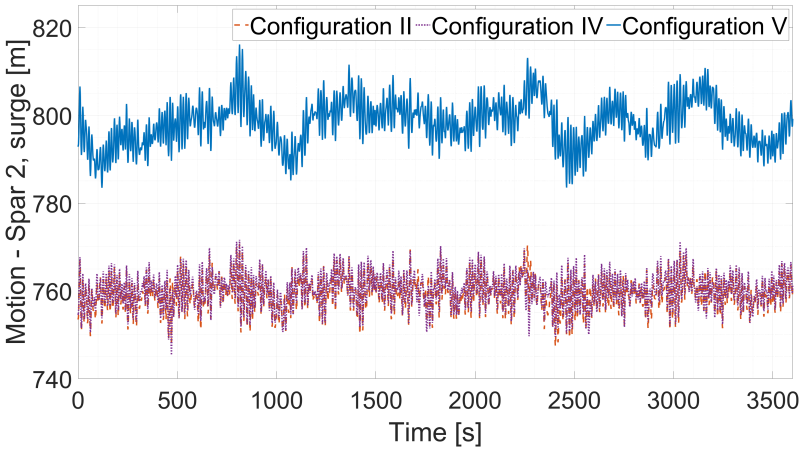

(b) Spar 2, surge motion

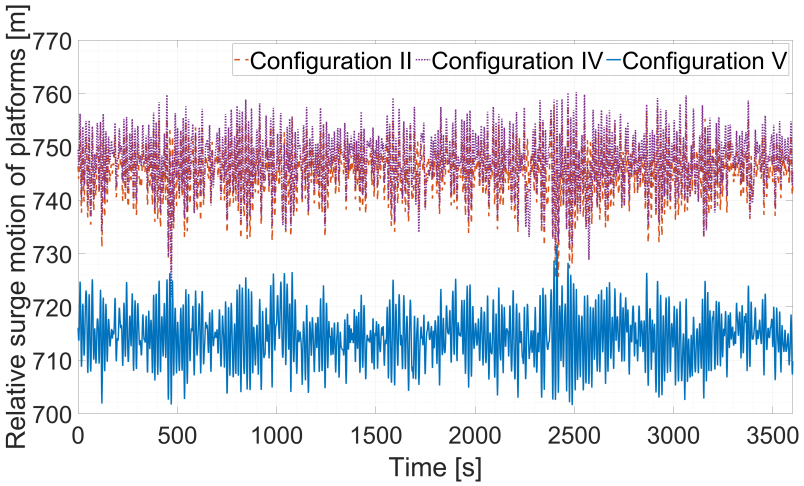

(c) Relative surge motion between Spar 1 and Spar 2

Figure 3.18: Time series of platform surge motion in the extreme scenario (random wave seed = 3).

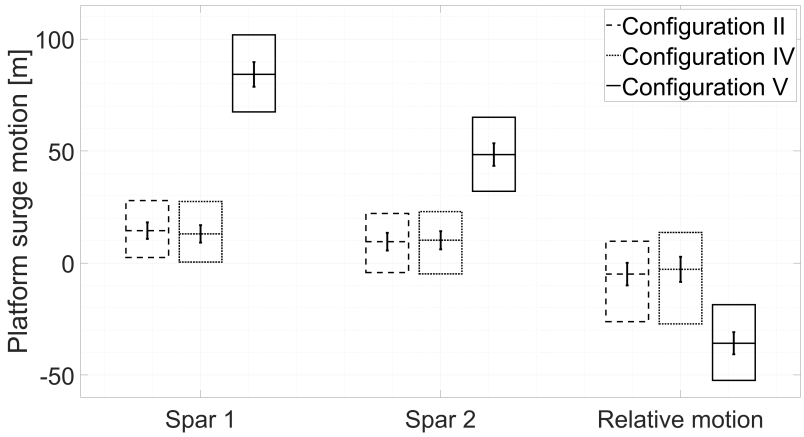

Figure 3.19: Expected values of the statistics of platform surge motion in the extreme scenario (middle line: mean; box: motion range (maximum and minimum); error bar: SD).

configurations experiences higher mean tension and dynamic tension than T_5.

Overall, although configuration V results in larger surge motions compared to the other two configurations, its lower stiffness leads to a considerable reduction in mooring line tension.

Extreme load scenario

As described in Sec. 3.3.3, in the extreme load scenario, both FOWTs are parked with blades feathered.

The surge motions of the FOWTs in the extreme scenario are plotted in Fig. 3.18 for the three configurations. The time series of the selected realization have the mean values and SDs closest to the ensemble averages over all realizations for configuration V. Similar to the accidental scenario, the FOWTs in configuration V experience larger mean surge offsets and more pronounced slow-varying motions in the surge direction than those in the other two configurations, likely due to the much larger natural surge periods of configuration V combined with the low-frequency wave and wind excitation. The surge motions of the FOWTs in the other two configurations are similar and dominated by wave-frequency contributions. The dynamic responses of the relative surge motions between the two FOWTs are comparable in all three configurations. However, configurations II and IV exhibit mean relative motions closer to the initial separation of 750 m than configuration V due to the large mooring stiffness provided by the four outer single lines.

The platform surge motion statistics are computed for each realization, and the corresponding expected values are presented in Fig. 3.19 with respect to the initial positions of the FOWTs. As the four outer single lines are replaced by hanging lines moored to submerged tethered buoys, which reduces the stiffness of the floating system, the mean offsets of both FOWTs in configuration V are considerably larger than those of the FOWTs in the other two configurations. The difference in magnitude of the dynamic surge motion between the configurations is not as significant as the difference in the mean surge offset. As shown in the sensitivity study discussed above, increasing the net buoyancy of the buoys can reduce the surge offset of the FOWTs

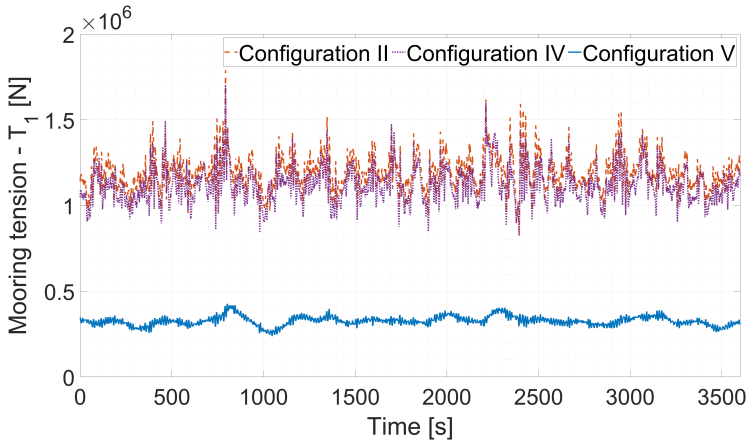

(a) T_1

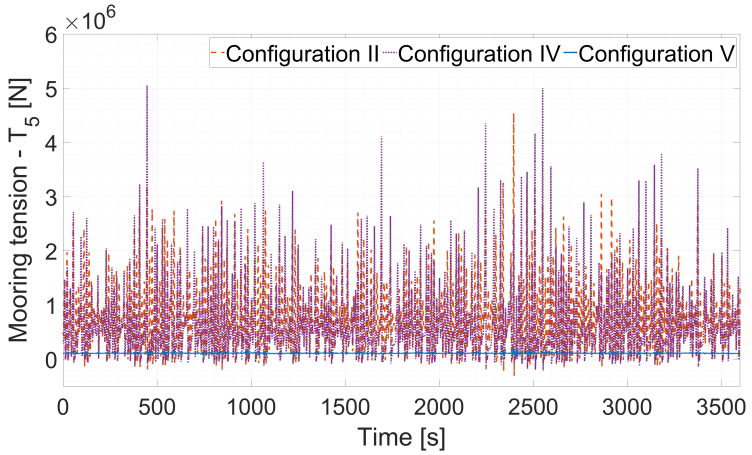

(b) T_5

Figure 3.20: Time series of fairlead tension in the extreme scenario (random wave seed = 3).

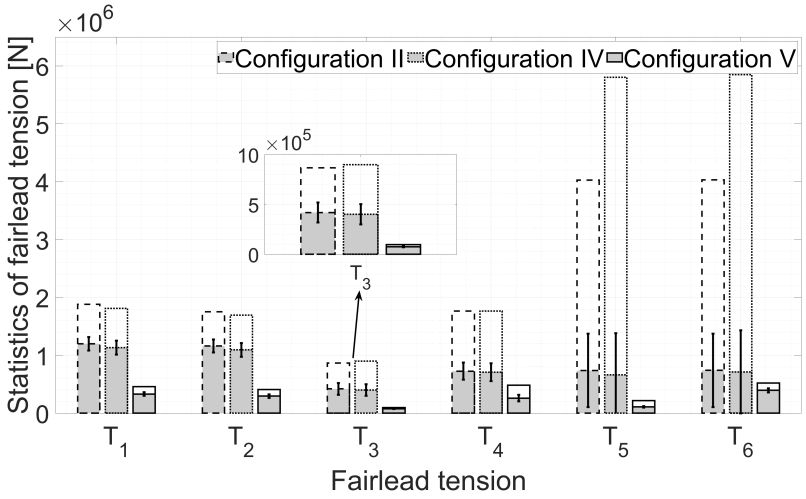

Figure 3.21: Expected values of the statistics of fairlead tension in the extreme scenario (gray bar: mean; white bar: maximum; error bar: SD).

in configuration V. As stated in Sec. 3.3.4, the horizontal excursion of FOWTs is an important design criterion to ensure the integrity of power cables, which makes the discussion of surge motion relevant. However, if dynamic power cables [87] that are suspended directly between FOWTs are utilized, then the design criterion shifts to the relative excursion between the FOWTs. In this case, it is beneficial to have reduced mooring tension in the tethered-buoy mooring system given that the SDs of the relative surge motions are on a similar level among the three configurations.

The time series of T_1 and T_5 are presented in Fig. 3.20, corresponding to the same realizations shown in Fig. 3.18. For T_1, configuration V exhibits considerably lower mean and dynamic tension than the other two configurations. The behaviors of T_5 in configurations II and IV are similar, while T_5 in configuration V has significantly smaller mean values with insignificant dynamic contributions.

Fig. 3.21 presents the expected values of the fairlead tension statistics calculated from each realization. Compared with the other two configurations, configuration V shows considerably lower tension levels in both the mean and dynamic values across all fairleads. In particular, significant reductions in tension levels are shown in T_5 and T_6, which can be attributed to the reduced mean surge distance between the FOWTs shown in Fig. 3.19. The tension levels in all fairleads appear to be more evenly distributed in configuration V compared to in the other two configurations.

A snap event analysis, as described in Sec. 3.3.4, is performed for the fairlead tension of all three configurations under the extreme scenario, in which the total number of snap events observed at each fairlead is averaged over realizations. Snap events are observed for the fairlead tension T_5 and T_6 in configurations II and IV. From configuration II to configuration IV, the average number of snap events per hour for T_5 reduces from 102 to 47, and for T_6, it reduces from 101 to 33, which is likely due to the decoupling of motions between the FOWTs, as the shared line is replaced by hanging lines connected to the submerged tethered buoy. Benefiting from the significant reduction in the tension levels, as shown in Fig. 3.21, no snap events are observed in the time series of any fairlead tension for configuration V. Thus, configuration V appears to mitigate the threat of snap loads in the mooring lines between the FOWTs.

For the three configurations, spectral analysis is applied to analyze the platform motions, and the average conditional exceedance rate method is applied to analyze the fairlead tension in both load scenarios. Readers are referred to [86] for detailed results and discussions.

3.4 Summary of the numerical analysis

This chapter presented a comprehensive analysis of the static and dynamic characteristics of dual-spar FOWFs with various shared mooring systems using both quasi-static and dynamic modeling approaches. First, the dual-spar FOWF with a shared line, i.e., configuration I, was compared to a single FOWT and studied in detail in a sensitivity study. The primary findings are summarized as follows:

- **Natural period**: The impact of the shared line on the natural periods is primarily observed in the surge and sway DOFs, wherein the mooring stiffness dominates the relevant stiffness terms. In the DOF aligned with the shared line, a higher natural period and a lower natural period in comparison to that of the single FOWT are observed.

- **Platform motion**: In the case where the loading direction is parallel to the shared line, large motion ranges and more significant dynamic motions are observed for Spar 1 in the FOWF due to the decrease in mooring stiffness. If the loading direction is perpendicular to the shared line, the platform motions of the FOWTs in the FOWF are comparable to those of the single FOWT, as the shared line is less active in providing restoring force.

- **Mooring tension**: In accordance with the observations on platform motion, when the loading direction is parallel to the shared line, Spar 1 in configuration I experiences higher tension levels in its single lines compared to the single FOWT due to the larger mean surge offset. When the loading direction is perpendicular to the shared line, tension levels in the single lines are comparable between the two configurations given that the platform motions exhibit similar magnitudes. Furthermore, in comparison to the single lines, the shared line experiences significantly higher dynamic tension and snap load events.

Then, a comparative study was carried out among FOWFs with different shared mooring systems, i.e., configurations II, IV, and V. Natural periods and motion response and structural response in different load scenarios were investigated in detail. Based on the observations, the advantages and disadvantages of configurations IV and V compared to configuration II were presented in Table 3.13 in terms of the natural period, platform motion, and mooring response.

Table 3.13: Summary of the comparison of configurations IV and V relative to configuration II. [1]

	Configuration IV	Configuration V
Natural period [2]	Natural period of Surge, Mode 2 decreases by 36%. Differences in the natural periods of the other modes are insignificant.	Natural periods in the surge and sway DOFs increase as much as 3.69 times. Differences in the natural periods of the other DOFs are insignificant.
Platform surge motion	Insignificant differences in mean offsets and dynamic motion.	Significant increase in the mean offset up to 30% of the water depth. Increased dynamic motion.
Fairlead tension in the accidental scenario	The mean tension in all fairleads is slightly reduced, but the fairleads between FOWTs experience an increase in dynamic tension of up to 23%.	The tension levels in all fairleads experience a considerable reduction. For the fairleads of single lines, both the mean and dynamic tension decrease by up to 81% and 96%, respectively. For the fairleads between FOWTs, the mean and dynamic tension decrease by up to 71% and 36%, respectively.
Fairlead tension in the extreme scenario	A slight reduction in the mean tension in all fairleads. Fairleads of single lines experience comparable maximum tension and dynamic tension. For the fairleads between FOWTs, the maximum and dynamic tension can increase by up to 45% and 13%, respectively.	The tension levels in all fairleads experience a significant reduction. The maximum and dynamic tension in the fairleads of single lines decrease by up to 89% and 96%, respectively. For fairleads between FOWTs, the maximum and dynamic tension decrease by as much as 95% and 98%, respectively.
Snap event	The average number of snap events per hour for T_5 decreases by 54%, and for T_6, it decreases by 67%.	No snap event observed.

[1] The performance of configuration II is taken as the reference for the comparison.

[2] Natural periods discussed here only relate to the rigid-body motions of FOWTs.

Chapter 4

Hydrodynamic model tests of floating offshore wind farms with shared mooring systems

4.1 General

Model tests of FOWTs can be conducted to assess a wide range of issues [19], including the following:

- hydrodynamic load characteristics
- global system concept and design verification
- individual structure component testing
- marine operations, demonstration of functionality
- validation of numerical models
- estimation of extreme loads and response
- understanding of loading mechanisms and relative importance of, and coupling between different environmental loads

As described in Sec. 1.3.2, small-scale modes tests with a scaling ratio of 1:30 to 1:100 are commonly carried out to investigate the global behaviors of FOWTs, e.g., [39,88–92]. To the best of the author's knowledge, there have been no descriptions of tests published in the public domain for FOWFs to date. To pave the way for model testing of FOWFs and investigate the dynamics of shared mooring systems from an experimental perspective, a model test campaign was carried out for dual-spar FOWFs with two different shared mooring configurations.

The model test campaign was conducted at the ocean basin in the *Canal de Ensayos Hidrodinámicos de el Pardo* (CEHIPAR), which is 150 m in length and 30 m in width; the water depth of the basin was maintained at 5 m during the tests. The

Table 4.1: Froude scaling of variables in the model tests.

Variable	Scaling factor	Value
Linear dimension	λ	1:47
Fluid or structure velocity	$\lambda^{1/2}$	1:6.86
Fluid or structure acceleration	1	1:1
Structure mass	λ^3	1:1.04E+05
Structure displacement	λ^3	1:1.04E+05
Time or period	$\lambda^{1/2}$	1:6.86
Force	λ^3	1:1.04E+05
Moment	λ^4	1:4.88E+06

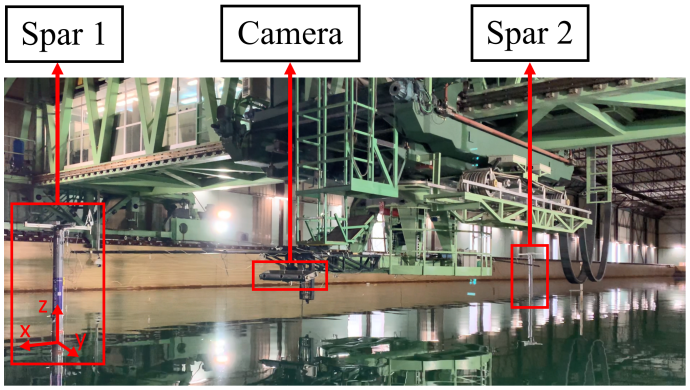

(a) CPMC and models of two FOWTs

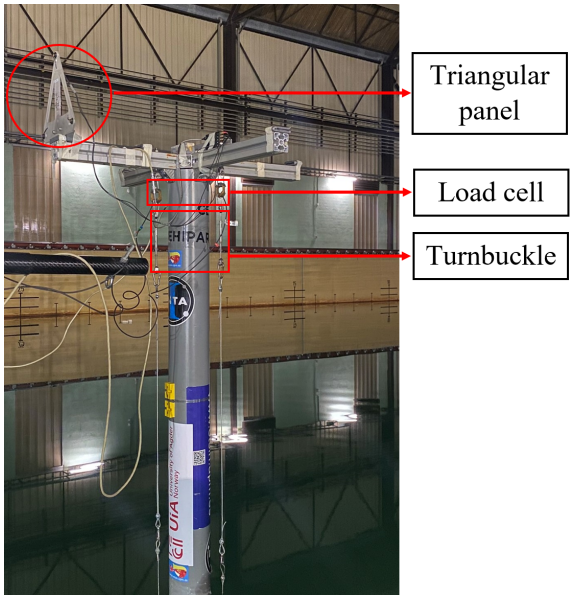

(b) Spar 1 with instrumentation

Figure 4.1: Illustration of instrument and FOWT models.

shared mooring configurations II and III were tested; see Table 2.9. Since the full-scale water depth is 235 m, the scaling ratio λ is 47, and Froude scaling [93] is applied, as gravity and inertia forces are predominant when testing floating structures in waves [94]. The scaling factors for different variables are presented in Table 4.1. As illustrated in Fig. 4.1(a), the experimental setup utilized a Computerized Planar Motion Carriage (CPMC) as the central unit for test control and data measurement, which remained stationary in the middle of the two FOWT models during the tests. Waves were generated by 60 flaps of a wavemaker, which was powered by hydraulic pumps and located at one of the 30-m sides of the basin.

The model test campaign involved decay tests and regular and irregular wave tests for two shared mooring configurations, namely configuration II and configuration III. In Sec. 4.2, the physical modeling of the FOWTs and the mooring system is introduced, followed by a description of the instrumentation in Sec. 4.3. The test program is summarized in Sec. 4.4. Sec. 4.5 compares the results of configuration II to those of a single spar FOWT, presenting the main results from *JP4*. The single spar FOWT was experimentally investigated in a previous work outside of this PhD work. A comparative study of configurations II and III is carried out, and the main results from *JP3* are presented in Sec. 4.6. Finally, a summary of findings from the experimental analysis is given in Sec. 4.7.

4.2 Physical modeling

4.2.1 Modeling of the floating offshore wind turbines

To make the models of the two FOWTs, the mass properties of the OC3 Hywind spar FOWT [61] were downscaled with the scaling ratio λ and used as references. The manufacture of the two FOWT models followed the same process. The main bodies of the FOWT models were constructed using polyvinyl chloride, while solid lead was inserted inside the spar floaters for the ballast. Various seals were applied to the FOWT models during the manufacturing process to ensure that no leakage

Table 4.2: Target and measured mass properties at model scale.

Mass property	Target value	Measured value		Relative difference [%]	
		Spar 1 [1]	Spar 2	Spar 1	Spar 2
Mass M $[kg]$	77.403	77.721	77.213	0.41	-0.25
Height of COG $[mm]$ [2]	893.62	890.76	898.19	-0.32	0.51
Moment of inertia x-axis i_{xx} $[mm]$ [3]	1029.5	1044.3	1044.3	1.44	1.44
Moment of inertia y-axis i_{yy} $[mm]$	1029.5	1044.6	1044.6	1.47	1.47
Moment of inertia z-axis i_{zz} $[mm]$	102.6	94.8	94.8	-7.60	-7.60

[1] Spar 1 and Spar 2 refer to the Figs. 2.1 and 2.2.

[2] The height of the COG is measured with regard to the keel.

[3] The moment of inertia is calculated with regard to the COG.

occurred during the experiments. The leakproofness of the two FOWT models was tested before they were towed to the test positions, and throughout the tests, the models were closely monitored for water intake to avoid changes in displacement and trim angle. As the test campaign focused on the hydrodynamic performances, the rotors and nacelles of the FOWTs were not modeled, and auxiliary aluminum frames were placed on top of the towers to accommodate the testing instruments, as shown in Fig. 4.1(b). To adjust the inertia of the upper structure, distributed weights were placed on top of the aluminum frames. A detailed description of the

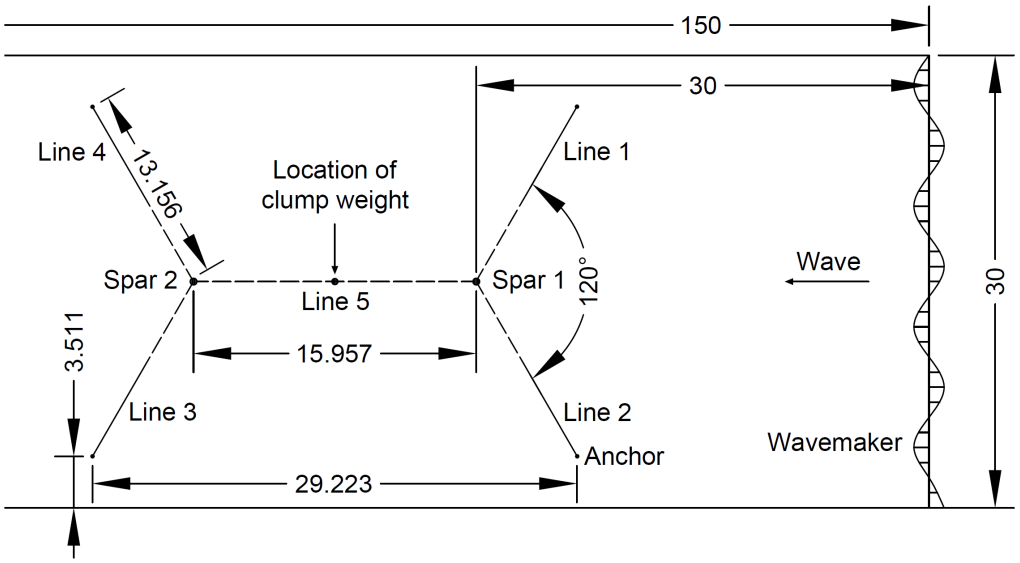

(a) Dual-spar FOWF with shared mooring configurations (configurations II and III)

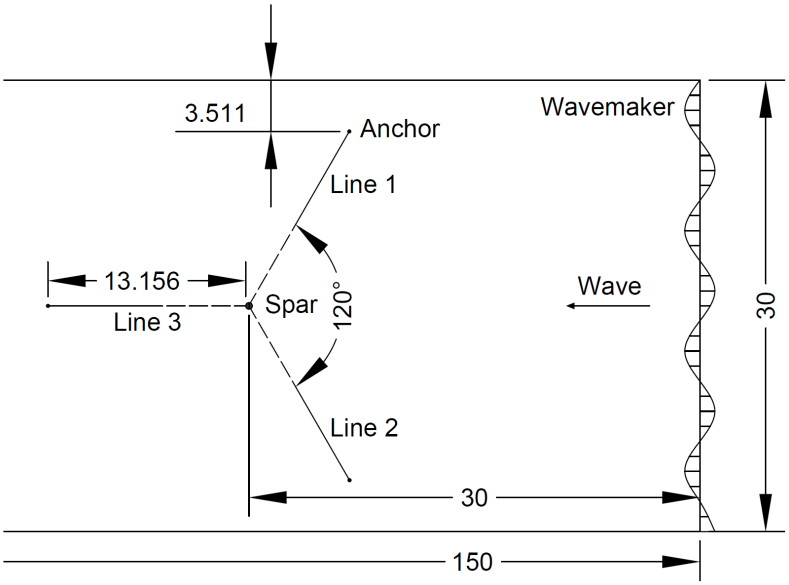

(b) Single spar FOWT (not part of this PhD work)

Figure 4.2: Experimental layouts of the model tests at model scale (dimensions in $[m]$).

physical modeling of the FOWT models can be found in Appendix A of [66].

The manufacture of the FOWT models underwent strict quality control. The mass properties of the models, both the target and measured values, are presented in Table 4.2. Overall, a good agreement was achieved between the target and the measured mass properties.

4.2.2 Modeling of two shared mooring configurations

The mooring properties of configurations II and III at full scale are described in Sec. 2.4.1 and Sec. 2.4.2, respectively. The mooring lines of the previously tested single spar FOWT had the same mooring properties as the single lines of configuration II.

Fig. 4.2(a) illustrates the experimental layout of configurations II and III. To ensure high-quality wave measurements during the tests, the first FOWT model, Spar 1, was placed 30 m away from the wavemaker. For configuration III, a flat-cylinder clump weight was attached to the midpoint of the shared line by a diver. The submerged weight of the clump weight was 144.5 g, which corresponded to 15 tonnes at full scale. The position of the clump weight on the shared line was measured to be 2.6 cm (1.22 m at full scale) from the midpoint toward Spar 2. The experimental layout of the single FOWT is illustrated in Fig. 4.2(b). Similar to Spar 1 in the shared mooring configurations, the single FOWT was placed 30 m away from the wavemaker.

The mooring properties of configuration II presented in Table 2.5 were taken as references and scaled down according to the following:

$$K = \frac{EA}{L} \tag{4.1}$$

where EA is the axial stiffness of the line and L is the unstretched length of the mooring line at model scale. The selection of the mooring line materials and the connection parts was aimed at achieving an equivalent mass density close to the reference value. Improper scaling of mooring stiffness may lead to an overprediction of the number of snap events observed [95]. Therefore, to maintain consistency in

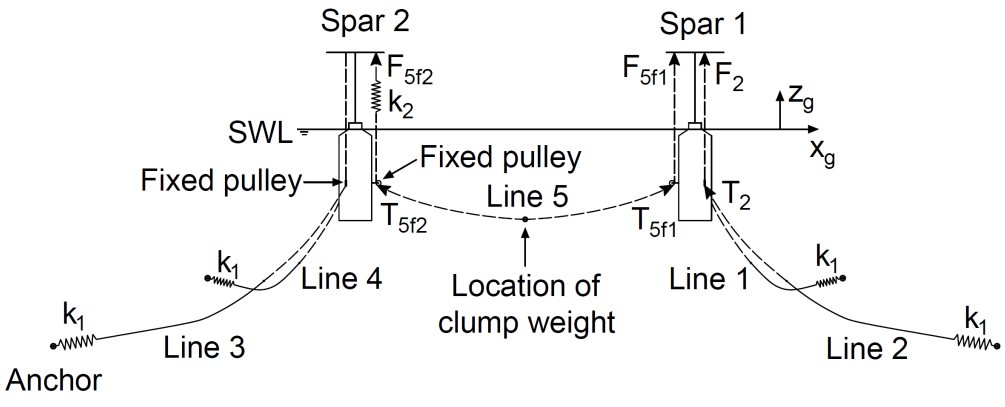

Figure 4.3: Illustration of the mooring system setup for configurations II and III.

Table 4.3: Mooring properties of configurations II and III at model scale.

Mooring properties	Single line		Shared line
	Wire segment	Chain segment	
Length $[m]$	5.32	8.83	15.74
Mass density $[kg/m]$	0.02	0.16	0.02
Equivalent spring stiffness $[N/m]$ [1]	$k_1 = 800$		$k_2 = 520$

[1] Refer to Fig. 4.3 for the spring positions.

Table 4.4: Target and measured pretension for configurations II and III at model scale.

Variable	Target value		Measured value		Relative difference [%]	
	II	III	II	III	II	III
Pretension T_1 $[N]$	7.62	8.73	7.97	9.01	4.59	3.21
Pretension T_2 $[N]$	7.62	8.73	8.04	9.07	5.51	3.89
Pretension T_{5f1} $[N]$	6.34	7.56	6.78	7.90	6.94	4.50
Pretension T_{5f2} $[N]$	6.34	7.56	6.67	7.50	5.21	0.79

the material stiffness of the mooring lines, a set of springs (k_1) was used to connect the single lines and the anchors, and a spring (k_2) was added at the connection between the shared line and Spar 2; see Fig. 4.3. The mooring properties at model scale are summarized in Table 4.3.

If load cells used to measure mooring tension had been installed at the fairleads, they would have affected the mooring angles at the fairleads due to the relatively low weight of the mooring lines. Therefore, fixed pulleys were installed at the fairlead positions to transfer the mooring lines above the water surface, where they were connected to load cells installed on the aluminum frames; see Fig. 4.1(b) and Fig. 4.3. Due to this alteration, the tuning of the mass properties of the FOWT models considered the total mooring tension instead of the vertical mooring tension component.

The two FOWT models were towed to the test positions and equipped with instruments. Anchors were placed on the bottom of the ocean basin and at the exact positions shown in Fig. 4.2. The mooring lines were set up with the assistance of the diver, who also checked and adjusted the mooring system after the setup, to prevent the mooring lines from coiling. The measured and target pretension is presented in Table 4.4, including T_1 and T_2 as the fairlead tension of Line 1 and Line 2 and T_{5f1} and T_{5f2} as the fairlead tension of Line 5; see Fig. 4.3. Overall, a good agreement was achieved between the measured and target pretension values. For configuration

III, the attached clump weight increased the pretension and changed the line shape of the shared line, driving the two FOWTs closer to each other and leading to an increase in the pretension of the single lines. Due to the limited time available in the ocean basin, the mooring stiffness in different DOFs was not estimated by additional static tests.

4.3 Instrumentation

Prior to the model tests, all installed measuring instruments were calibrated to ensure the quality and reliability of the data acquisition. The measurements were recorded at a sampling frequency of 100 Hz during the tests, which was deemed adequate given the typical frequency range of the phenomena under consideration.

The six-DOF motions of FOWT Spar 1 were measured by an optical tracking system (KRYPTON), a camera-based dynamic position measurement system [96]. Three infrared light-emitting diodes were mounted on a triangular panel and attached to the top of the aluminum frame of Spar 1; see Fig. 4.1(b). The motions of the triangular panel were tracked by the camera shown in Fig. 4.1(a) and further processed to obtain the motions of Spar 1. Due to a lack of equipment, the motions of FOWT Spar 2 were not measured during the test. For the single FOWT configuration shown in Fig. 4.2(b), the motions of the single FOWT were measured similarly to Spar 1 in the shared mooring configurations.

For the shared mooring configurations, all of the fairlead tension of the single lines of Spar 1 (T_1 and T_2) and all of the fairlead tension of Line 5 (T_{5f1} and T_{5f2}) were measured by four one-component HBM load cells with a strain gauge full bridge; see Fig. 4.3. Each upper end of the mooring lines was initially guided through the fixed pulley positioned at the fairlead and then fixed by a turnbuckle for pretension adjustment. The turnbuckle was linked to the load cells for tension measurement, which were connected to the aluminum frame, as shown in Fig. 4.1(b). The pretension of each mooring line under static equilibrium and the mooring tension due to wave loads were measured during the tests. For the previously tested single FOWT, the fairlead tension in all three mooring lines was measured in a similar way.

During the tests, the absolute wave height was measured at two measurement

Table 4.5: Environmental parameters of the two selected wave conditions in regular wave tests.

Parameter	Full-scale		Model-scale	
	Operational	Extreme	Operational	Extreme
H $[m]$	2.25	10.0	0.053	0.213
T $[s]$	9.60	16.0	1.40	2.33

points. The first measurement point was located below the CPMC, sufficiently far from both FOWT models, and an ultrasonic wave sensor was used. The second measurement was located close to FOWT Spar 2, and a capacitance wave probe was used. On average, the precision of the wave measurement was ±2.027 mm.

4.4 Test program

4.4.1 Decay tests

Decay tests were carried out to obtain the natural periods and damping ratios of the floating system for both shared mooring configurations. As discussed in Sec. 3.2.3, considering the six-DOF rigid-body motions of both FOWTs, the dual-spar FOWF had 12 natural periods and corresponding eigenmodes, in which the two FOWTs moved either in phase (Mode 1) or 180 degrees out of phase (Mode 2) in the specific

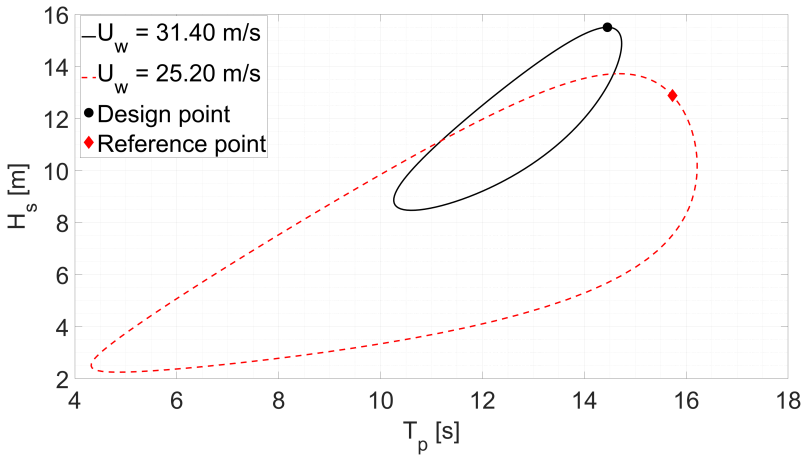

(a) Two-dimensional 50-year environmental contour lines (U_w: mean wind speed at 10-m height)

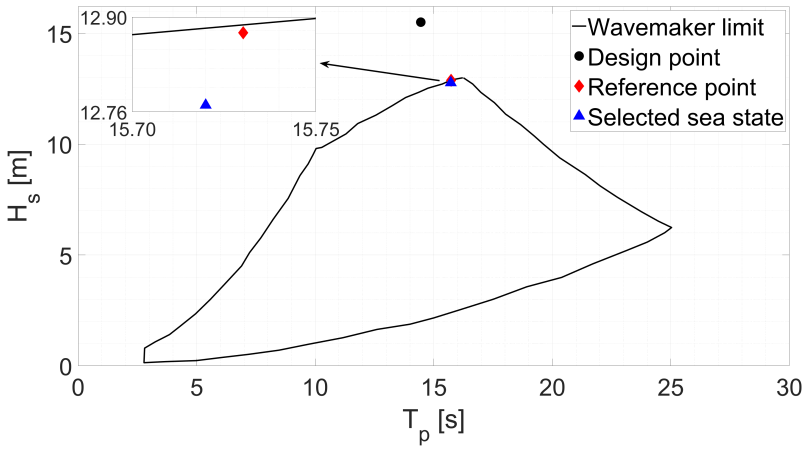

(b) Working capacity limit of the wavemaker for irregular waves

Figure 4.4: Extreme sea states marked on the 50-year environmental contour lines and the wavemaker working limit.

DOF. As described in Sec. 3.3.3, initial displacements or rotations needed to be applied to both FOWTs to excite these eigenmodes, which was difficult to implement in the model tests due to practical limitations. Therefore, only FOWT Spar 1 was manually displaced for the free decay in translational DOFs and rotated for the free decay in rotational DOFs. Consequently, only six eigenmodes were excited during the decay tests, from which the natural periods and corresponding damping ratios were estimated. Then, FOWT Spar 1 was released with an initial displacement or rotation, and its motions were recorded until the oscillation died out. For each DOF of Spar 1, the procedures were repeated three times, and the initial displacements or rotations had minor differences.

4.4.2 Wave tests

Regular wave test

For both shared mooring configurations, regular wave tests were conducted with two wave conditions. One wave condition represented a mild sea state for operation, and one wave condition represented an extreme sea state for survival. The two wave conditions are presented in Table 4.5.

Wave calibrations were carried out for the two wave conditions without the presence of the FOWT models. The error for the wave height and period was less than 5%.

Irregular wave test

To investigate the dynamic behaviors of the FOWFs with different shared mooring systems, irregular wave tests were carried out under operational and extreme ECs. The selection of the ECs is described in Sec. 3.3.2. However, as shown in Fig. 4.4(b), the "design point", the original extreme EC presented in Table 3.5, exceeded the operational capacity of the wavemaker in the ocean basin. Therefore, an extreme sea state that was within the working capacity range of the wavemaker and had the highest H_s on the 50-year environmental contour surface shown in Fig. 3.9(a) was taken as a "reference point", marked in Figs 4.4(a) and 4.4(b), and a sea state close to the "reference point" but away from the working capacity boundary of the wavemaker was selected for the model tests to ensure good wave quality; see Fig. 4.4(b). The environmental parameters of the two ECs selected for the irregular wave tests are presented in Table 4.6. Wind loads were not considered in the model tests;

Table 4.6: Environmental parameters of the two selected ECs in the irregular wave tests.

Parameter	Full scale		Model scale	
	Operational	Extreme	Operational	Extreme
H_s $[m]$	2.57	12.77	0.05	0.27
T_p $[s]$	11.12	15.72	1.62	2.29

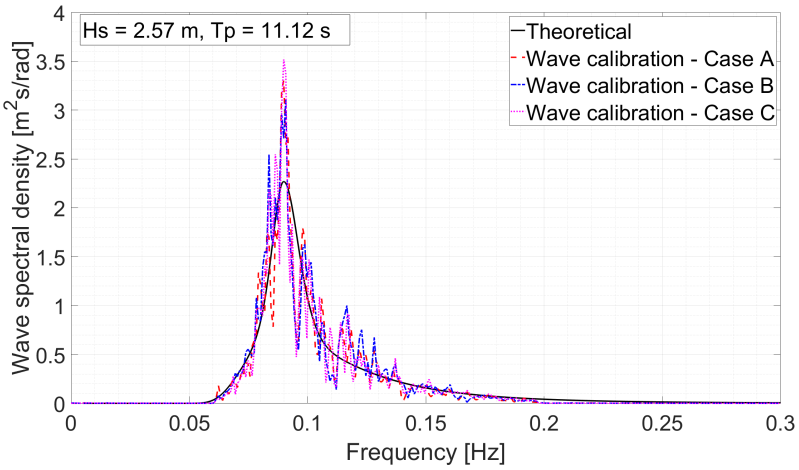

(a) The operational EC

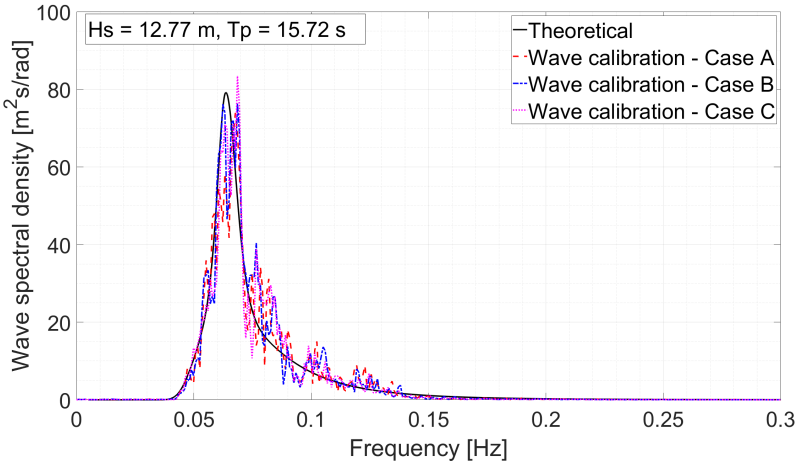

(b) The extreme EC

Figure 4.5: Wave spectra of the wave calibrations for the irregular wave tests.

hence, the scaled mean wind speeds were not included.

The waves generated by the wavemaker propagated in the global surge direction, as illustrated in Fig. 4.2. To reduce the uncertainties, irregular wave tests were carried out three times with different random wave seeds, i.e., Case A, Case B, and

Table 4.7: Comparison of the estimated natural periods and damping ratios for configuration II and the single FOWT.

Result	Configuration	Surge	Sway	Heave	Roll	Pitch	Yaw
Natural period [s]	II	142.88	83.89	30.50	31.56	31.62	23.93
	Single FOWT	93.03	87.92	29.80	31.69	31.71	24.55
Damping ratio [%]	II	3.56	3.02	1.86	1.08	1.32	1.83
	Single FOWT	3.87	2.91	1.77	1.07	1.27	1.62

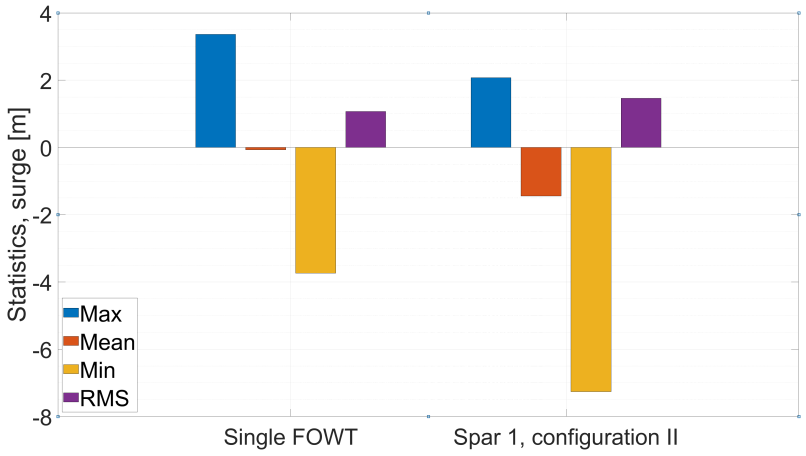

(a) Surge

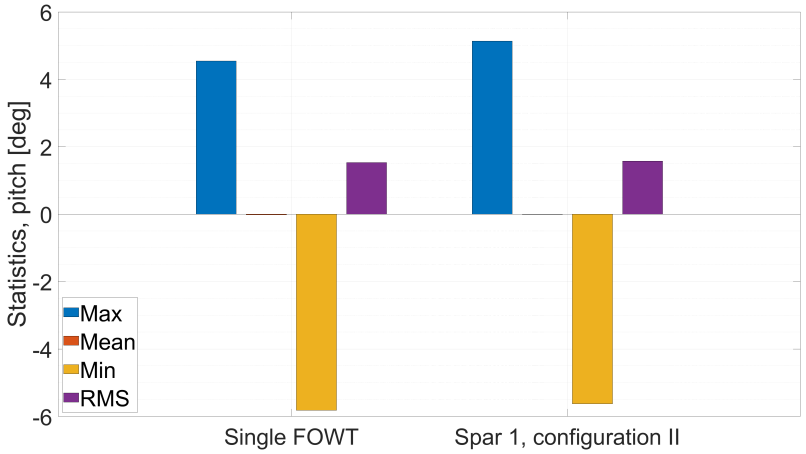

(b) Pitch

Figure 4.6: Statistics of the platform motion in the extreme EC (full scale, H_s = 12.77 m, T_p = 15.72 s, RMS: root mean square).

Case C. Each irregular wave test had a one-hour duration at full scale.

Wave calibrations without the presence of the FOWT models were executed before the test campaign for the two ECs selected for the irregular wave tests in compliance with the recommendations of the International Towing Tank Conference (ITTC) [97, 98]. The wave elevation at the location of Spar 1, which was 30 m away from the wavemaker (see Fig. 4.2(a)), was measured. The spectra of the calibrated waves in the three cases are plotted against the theoretical wave spectrum in Fig. 4.5. For both sea states, the difference in H_s and T_p between the theoretical values and the calibration results was below 5%, in compliance with the ITTC guidelines [99].

4.5 Comparative study of configuration II and the single floating offshore wind turbine

As described in Sec. 4.1, the model test results of configuration II were compared with those of a single FOWT that had the same mooring line orientations and

the same single line properties as Spar 1 of configuration II. In this section, the comparison is presented with a focus on the extreme EC in the irregular wave tests, which is the most representative scenario for parked FOWTs. Readers are referred to [66] for detailed results and discussions of the comparison in the regular wave tests and the operational EC in the irregular wave tests.

4.5.1 Natural period and damping ratio

The natural periods and damping ratios were estimated from the motions of Spar 1 in configuration II and the single FOWT in the decay tests. The corresponding results are presented in Table 4.7. It should be noted that not all of the natural periods and damping ratios of the FOWF were measured, as not all of the eigenmodes were excited in the decay tests, as previously discussed in Sec. 4.4.1. Consistent with the findings from the eigenvalue analysis in Sec. 3.2.3 and the dynamic analysis in Sec. 3.3.4, the differences in the natural periods between configuration II and the single FOWT primarily manifested in the surge and sway DOFs, where the

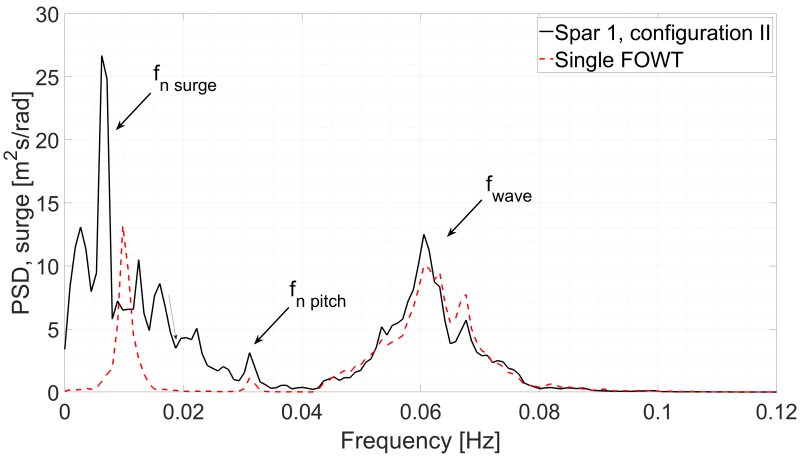

(a) Surge

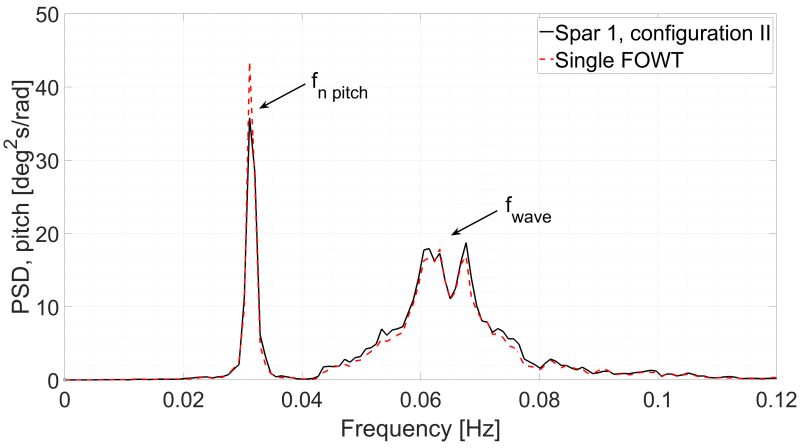

(b) Pitch

Figure 4.7: Platform motion spectrum in the extreme EC (full scale, $H_s = 12.77$ m, $T_p = 15.72$ s).

mooring stiffness dominated the relevant stiffness terms. For the other DOFs, the differences in the natural periods were minimal, as the influence of the shared line on the mooring stiffness was outweighed by other dominant stiffness contributions. No significant differences were observed in the estimated damping ratios between the two configurations.

4.5.2 Analysis of platform motion response

The statistics of the platform motions of Spar 1 in configuration II and the single FOWT were calculated and averaged over three cases. The averaged statics of the platform surge motion and pitch motion are presented in Fig. 4.6. The mean offset, motion range, and root mean square (RMS) of the surge motion experienced by Spar 1 in configuration II were larger than those of the single FOWT, consistent with the findings discussed in Sec. 3.3.4. According to the discussion in Sec. 3.3.4, the maximum surge offset of Spar 1 in configuration II was still below the rule-of-thumb excursion limit, 10% of the water depth. The statistics of the platform pitch motions for Spar 1 in configuration II and the single FOWT were comparable, as the effect of the shared line on the relevant stiffness terms associated with pitch motion was insignificant. For nonoperational LCs, the maximum allowable pitch angle was within the range of 10-15 degrees, which was satisfied by both Spar 1 in configuration II and the single FOWT in the extreme EC.

The platform motion spectra were generated from the time series of platform motion and averaged over three cases. Welch's overlapped segment averaging spectral estimation was applied in MATLAB to estimate the power spectral density (PSD), and the window parameter was set to 6 [100]. The averaged platform motion spectra are presented in Fig. 4.7 for the surge and pitch DOFs. The response of Spar 1 and the single FOWT in the wave-frequency range was similar for the platform surge motion. The surge-pitch coupling was identified as the peak frequency at approximately 30 s, as shown in Fig. 4.7(a), corresponding to the natural period of the pitch DOF presented in Table 4.7. In the low-frequency range, the spectrum of Spar 1 contained significantly higher spectral energy than that of the single FOWT, which could be attributed to certain nonlinear phenomena of the shared mooring system. No significant difference was observed between the platform pitch motion spectra of Spar 1 and the single FOWT due to the limited influence of the shared line on platform pitch motions.

Table 4.8: Measured pretension for configuration II and the single FOWT at model scale.

Variable	Configuration II	Single FOWT
Pretension T_1 $[N]$	7.97	6.24
Pretension T_2 $[N]$	8.04	6.39

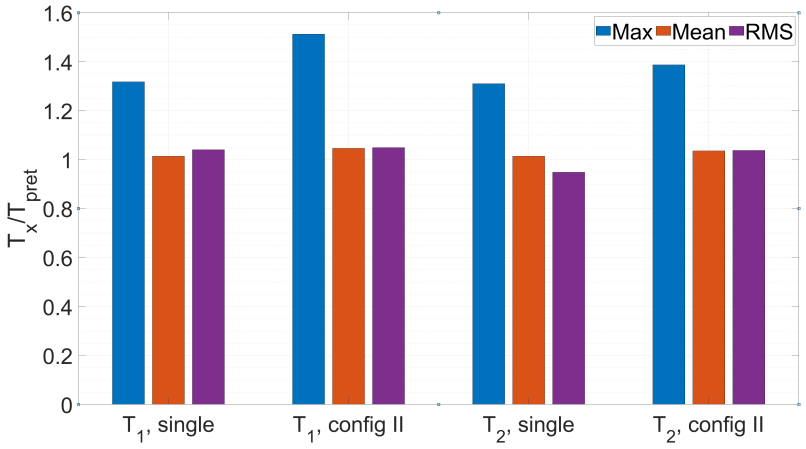

Figure 4.8: Statistics of normalized mooring tension of single lines in the extreme EC (full scale, $H_s = 12.77$ m, $T_p = 15.72$ s).

4.5.3 Analysis of mooring tension response of the single lines

The pretension values of Line 1 and Line 2, as illustrated in Figure 4.2, are presented in Table 4.8 for configuration II and the single FOWT. Due to the self weight of the shared line, Spar 1 exhibited a mean offset toward Spar 2 in static equilibrium, resulting in a greater distance from the anchor in comparison to the single FOWT. Therefore, the pretension levels in Line 1 and Line 2 were higher in configuration II than in the single FOWT. The mooring tension statistics of the single lines, represented by T_1 in Line 1 and T_2 in Line 2, were normalized by the pretension presented in Table 4.8 and averaged over three cases. The results are presented in Fig. 4.8. It was observed that the maximum normalized tension in the single lines of Spar 1 in configuration II was larger than that in the single lines of the single FOWT, which could be attributed to the larger maximum surge offset shown in Fig. 4.6(a). Despite Spar 1 in configuration II experiencing a larger mean surge offset than the single FOWT, the mean values and RMS of the normalized tension in the single lines for both configurations remained close to one. This could be attributed

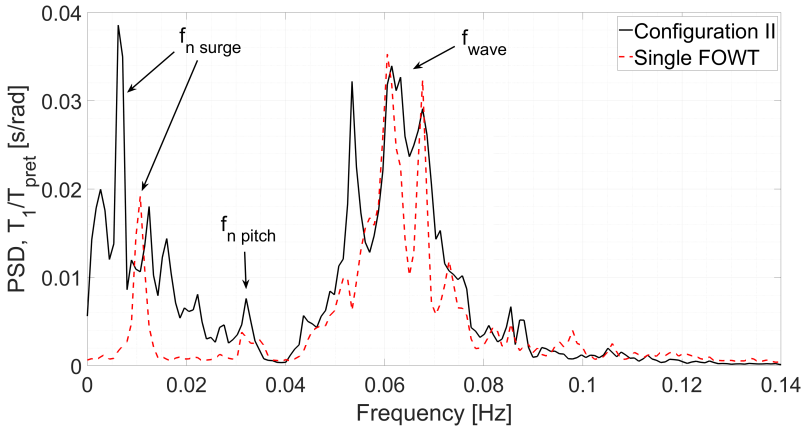

Figure 4.9: Spectrum of normalized mooring tension T_1 in the extreme EC (full scale, $H_s = 12.77$ m, $T_p = 15.72$ s).

to the reduced mooring stiffness in the surge direction resulting from the presence of the shared line.

The spectra of normalized mooring tension in Line 1, T_1/T_{pret}, were computed and averaged over three cases for both Spar 1 in configuration II and the single FOWT. Welch's PSD estimation was applied, and the window parameter was set to 6 [100]. The results are presented in Fig. 4.9. Comparing Fig. 4.7(a) and Fig. 4.9, the correlation between the platform surge motion and the dynamic tension in Line 1 could be easily observed. In both configurations, the response in the wave-frequency range exhibited similar characteristics, while in the low-frequency range, the spectrum of Spar 1 contained significantly more spectral energy than that of the single FOWT. This difference could be attributed to the difference in the platform surge motion spectra between the two configurations shown in Fig. 4.7(a).

4.6 Comparative study of configurations II and III

During the model test campaign, the shared mooring configurations II and III were tested as described in Sec. 4.1. A comprehensive comparative analysis was carried out using the experimental results. In this section, the results of the comparative study are presented with a focus on irregular wave tests. For results and discussions of the regular wave tests, readers are directed to [101].

4.6.1 Natural period and damping ratio

The mooring stiffness linearization approach discussed in Sec. 3.2.2 was applied to linearize the mooring stiffness of the two configurations about the static equilibrium position. The resulting diagonal and coupled stiffness terms of the two configurations

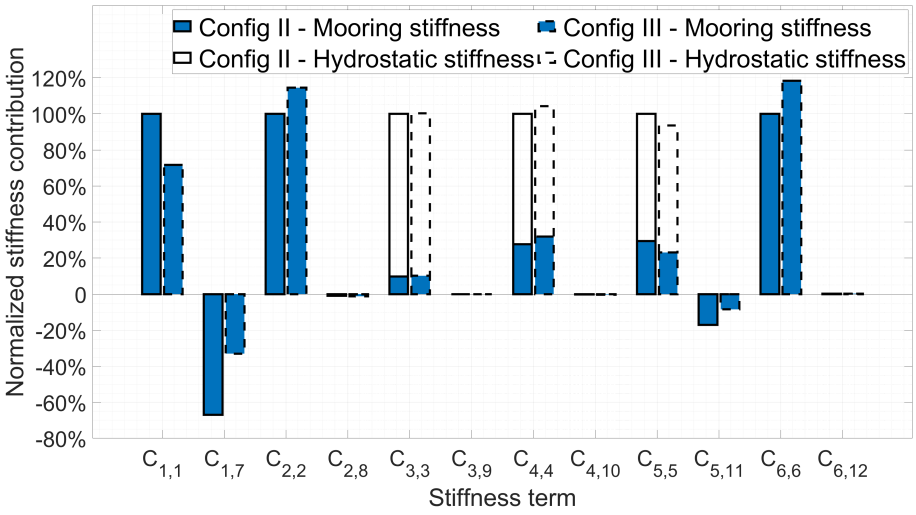

Figure 4.10: Diagonal and coupled stiffness terms of configurations II and III (the stiffness term $C_{i,j}$ indicates the restoring force in the i-th DOF induced by a unit displacement in the j-th DOF. For each DOF, the value is normalized with regard to the corresponding total diagonal stiffness, $C_{i,i}$, of configuration II).

Table 4.9: Comparison of the estimated natural periods and damping ratios for configurations II and III.

Result	Configuration	Surge [1]	Sway	Heave	Roll	Pitch	Yaw
Natural period [s]	II	142.88	83.89	30.50	31.56	31.62	23.93
	III	134.15	79.96	30.55	31.40	31.45	22.38
Damping ratio [%]	II	3.56	3.02	1.86	1.08	1.32	1.83
	III	3.82	3.30	2.02	1.22	1.17	2.04

[1] As indicated in the discussions presented in Sec. 3.2.3 and Sec. 3.3.4, the large natural period in the surge DOF estimated from the experimental decay test refers to Mode 1. For the remaining DOFs, it was difficult to determine whether Mode 1 or Mode 2 was specifically excited due to the close natural periods of these two modes and the lack of platform motion information on Spar 2.

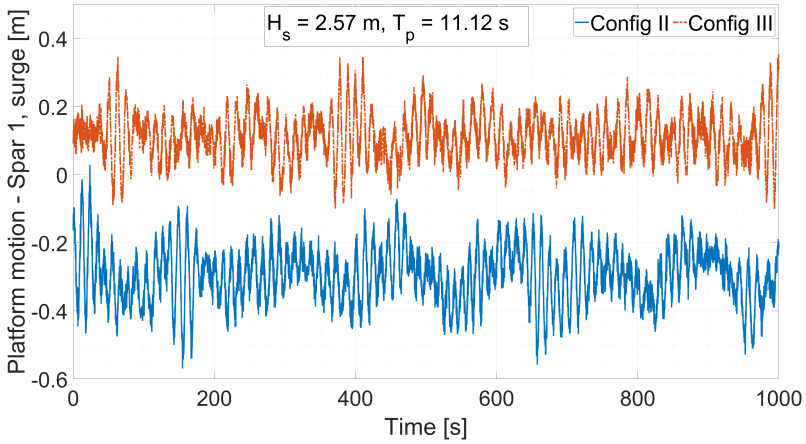

(a) Operational EC

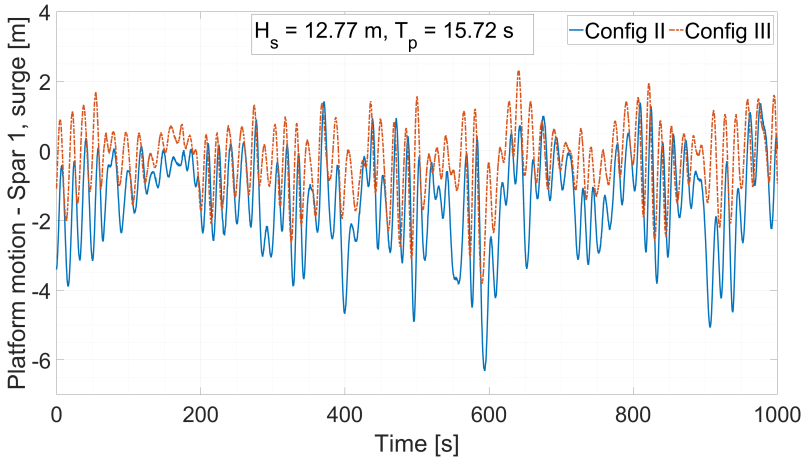

(b) Extreme EC

Figure 4.11: Time series of platform surge motion - Spar 1, Case C.

are illustrated in Fig. 4.10. The delta-line connection of the original Hywind model [68] provided yaw stiffness to the system; this was not considered in the physical modeling of the FOWTs. Therefore, the system stiffness in the yaw DOF did not have the additional yaw stiffness introduced by delta connections (see Fig. 3.8). The coupled stiffness between the two FOWTs arose due to the shared line. For configurations II and III, platform motions in the surge and pitch DOFs brought significant changes to the tension in the shared line; therefore, the mooring stiffness made noticeable contributions to the corresponding coupled stiffness. For other DOFs, the coupled stiffness was minor. The inclusion of the clump weight impacted both the mooring tension in the shared line and the static configuration of the FOWF, leading to significant differences in the stiffness terms of the surge, sway, and yaw DOFs between the two mooring configurations.

From the motion of Spar 1 in the decay tests, the natural periods and damping ratios were estimated for configurations II and III. As described in Sec. 4.4.1, decay tests were carried out three times with different excitation displacements or rotations. The averaged results are presented in Table 4.9. In comparison to configuration II, configuration III showed a decrease in natural periods of surge, sway, and yaw DOFs of 6.1%, 4.7%, and 6.5%, respectively, which could be attributed to the change in mooring stiffness caused by the added clump weight; see Fig. 4.10. The difference in the natural periods of other DOFs was relatively insignificant between the two configurations, as the hydrostatic stiffness predominated the total system stiffness in these DOFs, as shown in Fig. 4.10. Moreover, the added clump weight yielded minor changes in the damping ratios across all of the investigated DOFs.

4.6.2 Analysis of platform motion response

Fig. 4.11 presents the time series of the platform surge motions of Spar 1 in both configurations. Under the operational EC, an offset in the mean platform surge motion was observed between the two configurations, which was attributed to the difference induced by the added clump weight in the static configuration. Comparable oscillations around the mean positions were experienced for both configurations. In addition, low-frequency motions induced by wave drift forces were observed, as was expected for floating offshore structures with large volumes, limited waterplane areas, and spread mooring systems [28]. Spectral analysis revealed that the period of this low-frequency motion corresponded to the surge eigenmode with a longer natural period where both FOWTs moved in phase. Under the extreme EC, configuration III exhibited reduced motion range and less significant oscillation compared to configuration II due to the increased mooring stiffness resulting from the added clump weight. An offset in the mean platform surge motion remained between the two configurations.

The platform motion statistics of Spar 1 were averaged over three cases, and the results are presented in Table 4.10. As waves propagate in the surge direction, the influence of the clump weight on the platform motions was predominantly observed in the surge DOF. For the remaining DOFs, the platform motion statistics showed

Table 4.10: Statistics of platform motion for Spar 1 in irregular wave tests (full scale, averaged over three cases).

Value	Config	Surge [m]	Sway [m]	Heave [m]	Roll [deg]	Pitch [deg]	Yaw [deg]
Operational EC							
Range [1]	II	[-0.32, 0.33]	[-0.09, 0.09]	[-0.29, 0.31]	[-0.22, 0.22]	[-0.63, 0.65]	[-0.58, 0.54]
	III	[-0.28, 0.29]	[-0.09, 0.09]	[-0.30, 0.32]	[-0.23, 0.22]	[-0.75, 0.69]	[-0.63, 0.63]
SD	II	0.09	0.03	0.09	0.07	0.19	0.17
	III	0.08	0.02	0.08	0.06	0.20	0.18
Extreme EC							
Range [1]	II	[-5.83, 3.51]	[-0.71, 0.86]	[-2.56, 2.38]	[-1.31, 1.21]	[-5.62, 5.14]	[-13.34, 16.12]
	III	[-4.33, 2.81]	[-0.78, 0.82]	[-2.31, 2.45]	[-1.61, 1.29]	[-6.15, 4.84]	[-15.27, 17.05]
SD	II	1.46	0.22	0.72	0.35	1.57	4.06
	III	1.07	0.23	0.72	0.37	1.60	4.81

[1] Motion range with regard to the mean dynamic position.

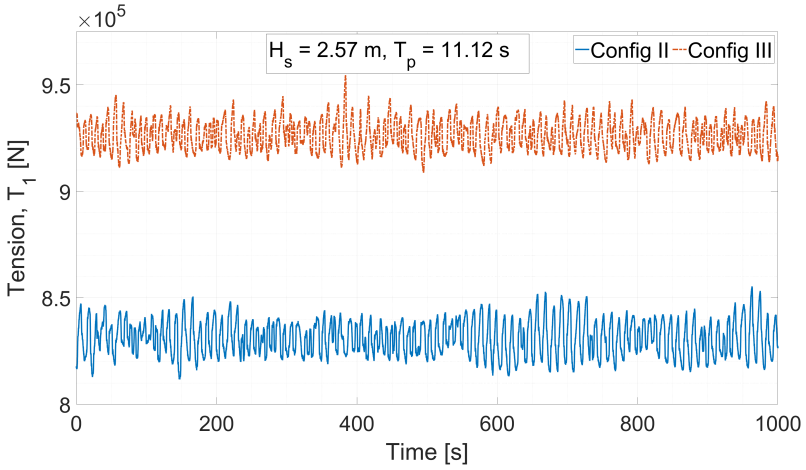

(a) Operational EC

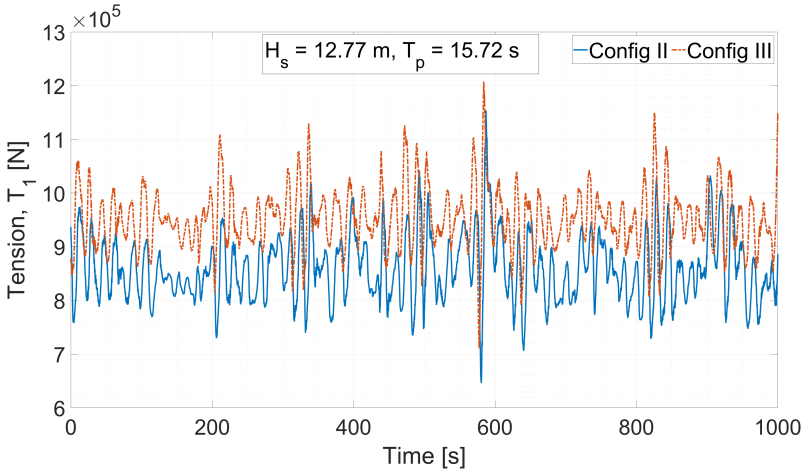

(b) Extreme EC

Figure 4.12: Time series of mooring tension T_1, Case C.

similarities between the two configurations. Under the operational EC, the influence of the clump weight on the platform surge motions of Spar 1 was limited. Configuration III exhibited slightly reduced motion range and SD in the surge direction compared to configuration II. Under the extreme EC, after adding the clump weight, the motion range of Spar 1 experienced a notable decrease of 23.6%, together with a 26.7% reduction in the SD of surge motion, indicating an improved station-keeping performance. For both configurations, the extreme motion ranges in the surge direction were less than 4.0% of the water depth, which was acceptable considering the design requirements of dynamic cables and farm layout [84].

4.6.3 Analysis of mooring tension response

Mooring tension response of the single lines

The time series of the mooring tension in Line 1 is presented in Fig. 4.12. After the clump weight was added, an increase of 12.4% in the mean mooring tension of Line 1 was observed under the operational EC. Similarly, under the extreme EC, a

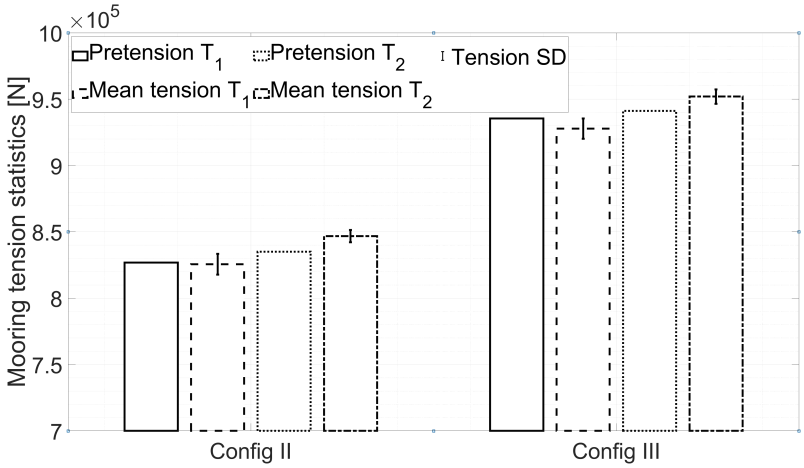

(a) Operational EC

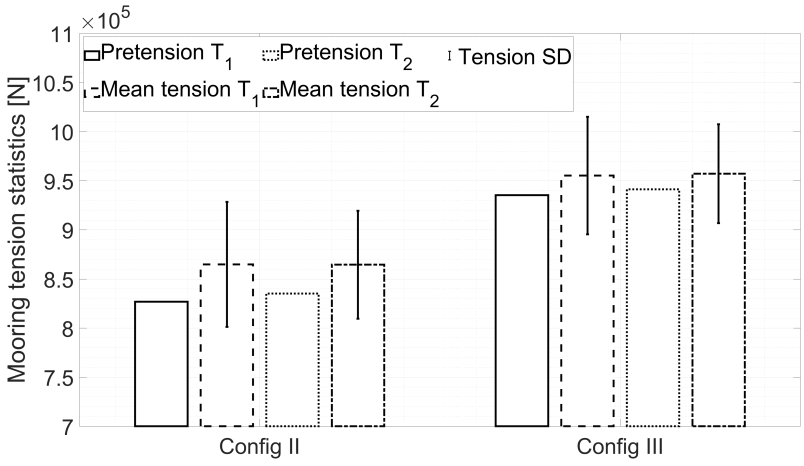

(b) Extreme EC

Figure 4.13: Statistics of the mooring tension of single lines.

mean mooring tension increase of 10.5% was recorded for Line 1. The increases in the mean mooring tension of the single lines were primarily due to the variations in pretension caused by the added clump weight; see Table 4.4.

Mooring tension statistics were computed from the time series and averaged over the three cases. The obtained mooring tension statistics for the single lines are presented in Fig. 4.13. Due to the symmetric mooring layout and the 0-degree wave heading, Line 1 and Line 2 showed comparable mooring tension statistics under both ECs. Compared to configuration II, larger pretension was observed in the single lines of configuration III. The added clump weight resulted in a reduced spacing between the two FOWTs in static equilibrium, which meant the fairleads of the single lines were further away from the anchors. As a result, the pretension in the single lines was higher for configuration III.

Under the operational EC, the difference between the pretension and the mean tension was relatively small. This was due to the fact that the mean mooring tension in the single lines was related to the mean fairlead position, which was governed by

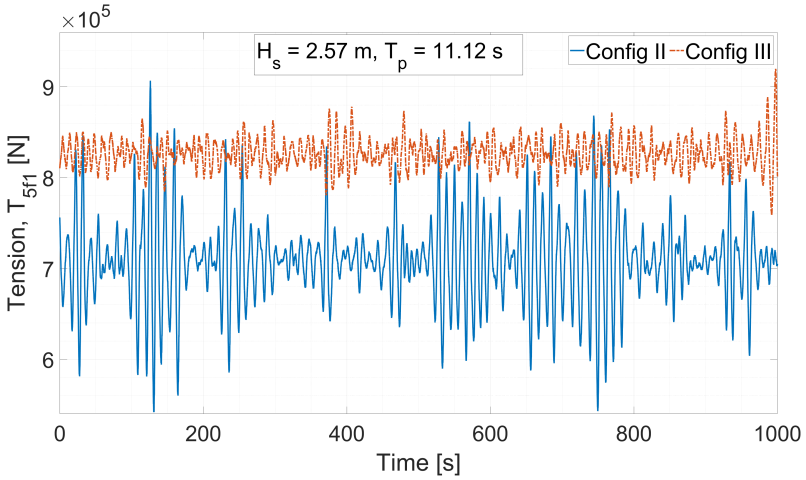

(a) Operational EC

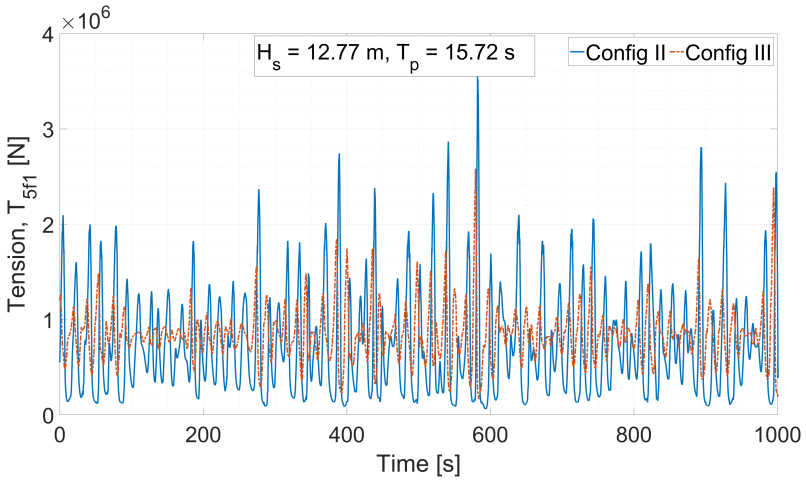

(b) Extreme EC

Figure 4.14: Time series of mooring tension T_{5f1}, Case C.

the mean platform position assuming the spar floaters as rigid bodies. For both configurations, the mean offsets of FOWTs in the surge direction induced by the mean wave drift force were minimal. Thus, the difference between the pretension and the mean mooring tension remained insignificant. For both configurations, the SDs of the mooring tension in the single lines were not substantial due to the limited SD of platform motion in the surge direction; see Table 4.10.

Under the extreme EC, the mooring tension induced by environmental loads in the single lines was higher for configuration II compared to configuration III. For instance, in Line 1, the mooring tension induced by environmental loads took 4.6% of the mean mooring tension in configuration II and 2.1% of it in configuration III. Apart from the greater pretension in configuration III, the enhanced mooring stiffness also contributed to the reduced mooring tension induced by environmental loads. Although configuration III exhibited higher pretension and mean mooring tension in the single lines, the SD of the mooring tension was 6.1% lower in Line 1 and 8.6% lower in Line 2 compared to that in configuration II, which aligned with

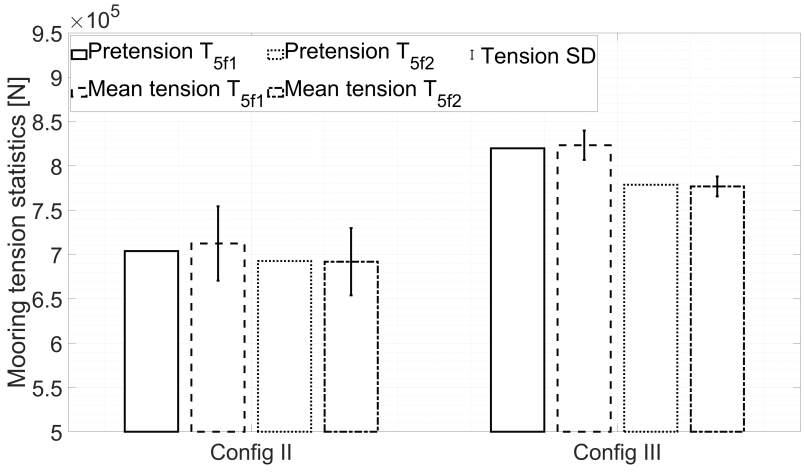

(a) Operational EC

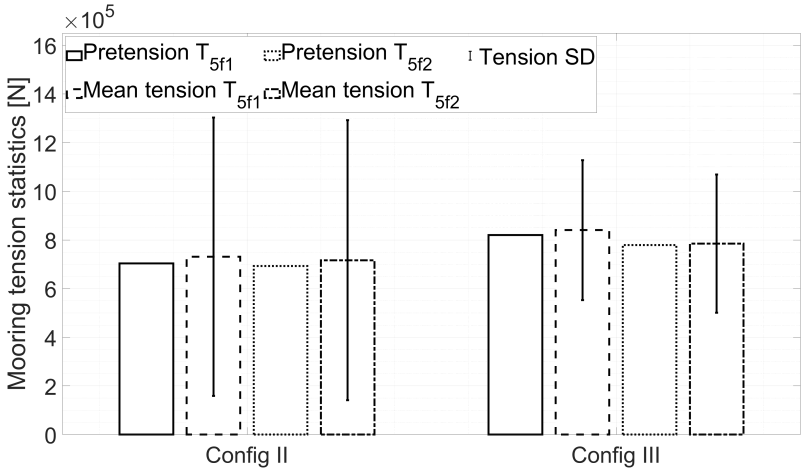

(b) Extreme EC

Figure 4.15: Statistics of the mooring tension of the shared line.

the SD of the platform surge motion presented in Table 4.10.

Mooring tension response of the shared line

Response statistics

The time series of the mooring tension in the shared line, at the fairlead of Spar 1, is presented in Fig. 4.14. Under the operational EC, configuration III experienced a higher mean mooring tension in comparison to configuration II due to the attached clump weight. However, it was evident that the mooring tension exhibited a more significant variation for configuration II. A similar trend was observed under the extreme EC. As shown in Fig. 4.14(b), the oscillation of mooring tension was more significant for configuration II compared to configuration III. The variation of mooring tension in the shared line was influenced by the relative motions between the two fairleads of the shared line. The motion ranges provided in Table 4.10 indicate that, under both ECs, the relative motions between the two FOWTs were moderately reduced for configuration III.

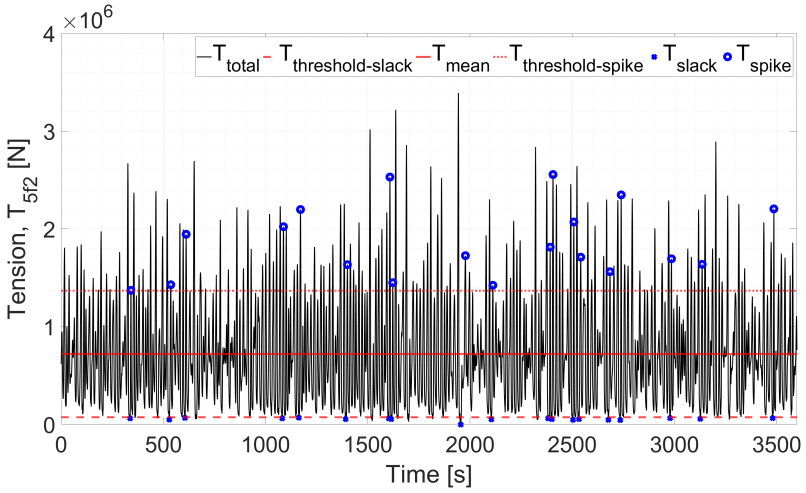

(a) Configuration II

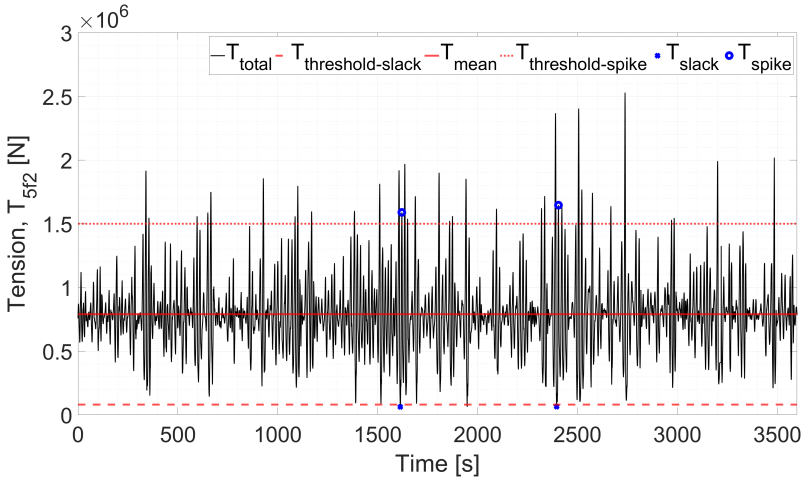

(b) Configuration III

Figure 4.16: Time series of mooring tension T_{5f2} under the extreme EC with identified snap load events marked, Case A.

The statistics of the mooring tension in the shared line were averaged over three cases, and the results are presented in Fig. 4.15. Due to the attached clump weight, configuration III experienced higher pretension in the shared line compared to configuration II.

Under the operational EC, the difference between the pretension and the mean tension of the shared line was minimal due to the moderate mean platform offset in the surge direction. This observation was similar to that for the single lines. However, the SD of the shared mooring tension was greater for configuration II than for configuration III, as shown in Fig. 4.14(a). This could have been due to the different mooring line dynamics resulting from the different shared line configurations and mean turbine spacing, even though the SD of platform motion in the surge direction was comparable for the two configurations; see Table 4.10.

Under the extreme EC, the mooring tension induced by mean wave loads was insignificant compared to the pretension. Nevertheless, the SD of mooring tension in the shared line was significant compared to the mean mooring tension. The relative motions between the two FOWTs repeatedly tightened and loosened the shared line, leading to significant oscillations in the shared line tension. The added clump weight reduced the SD of the mooring tension. For the shared mooring tension T_{5f1}, the ratio between the SD of the mooring tension and the mean mooring tension was 78.2% for configuration II and 34.2% for configuration III. The decrease in the SD of the platform surge motions shown in Table 4.10 after adding the clump weight contributed to the difference in the SD of the mooring tension.

Analysis of snap events

A snap event analysis as described in Sec. 3.3.4 was performed for all time series of the measured mooring tension under both ECs in the irregular wave tests. Snap events were only observed in the tension of the shared line (T_{5f1} and T_{5f2}) under the extreme EC. The identified snap events are marked in Fig. 4.16 for T_{5f2} in Case A. The number of snap events in the shared line significantly decreased after the clump weight was added. For instance, the average number of snap events observed in T_{5f2} was 18 for configuration II and 1 for configuration III. This reduction could be attributed to the smaller SD of the mooring tension in configuration III, as illustrated in Fig. 4.15(b). Consequently, it could be concluded that adding a clump weight to the shared line could mitigate the impact of snap loads, thereby reducing the safety margin preserved for the snap loads and facilitating a more cost-effective design of shared lines.

Analysis of extreme mooring tension

The extreme mooring tension is an important metric for mooring design based on ULS assessment of FOWT structures, as outlined in existing design guidelines [15, 19,22]. An analysis of extreme mooring tension was conducted based on the mooring tension measured under the extreme EC. First, local tension maxima were identified from the time series of mooring tension in accordance with the definition in the design standard [15]. Then, a three-parameter Weibull distribution was used to fit the identified local tension maxima [15]:

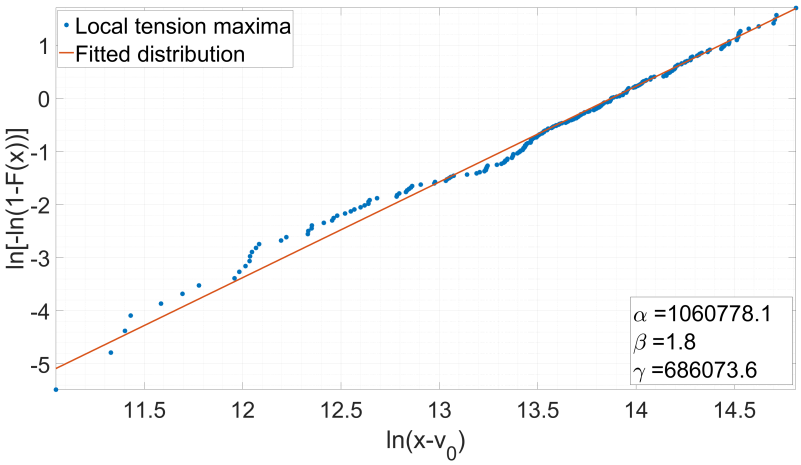

(a) Configuration II

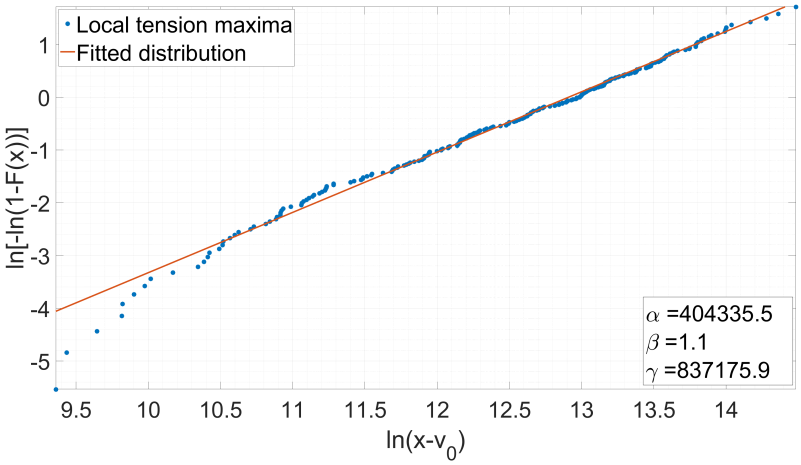

(b) Configuration III

Figure 4.17: Weibull probability papers for the fitted distribution of mooring tension T_{5f1} under the extreme EC, Case A.

$$F(T_{max}) = 1 - \mathrm{e}^{-\left(\frac{T_{max}-\gamma}{\alpha}\right)^{\beta}} \tag{4.2}$$

where α, β, and γ represent the scale, shape, and position parameters, respectively. Probability papers were generated for the fitted distributions. Examples are shown in Fig. 4.17 for the identified local tension maxima of mooring tension T_{5f1} in Case A

Table 4.11: The T_{MPME} value for configurations II and III [N] (averaged over three cases).

Configuration	T_1	T_2	T_{5f1}	T_{5f2}
II	1.18E+06	1.13E+06	3.71E+06	3.66E+06
III	1.25E+06	1.18E+06	2.65E+06	2.55E+06

under the extreme EC. The most probable maximum extreme (MPME) of mooring tension was computed based on the fitted distribution [15, 102], as follows:

$$T_{MPME} = \gamma + \alpha \left[-\ln \left(\frac{1}{N} \right) \right]^{\frac{1}{\beta}} \tag{4.3}$$

where N refers to the number of local tension maxima. For each case under the extreme EC, T_{MPME} was calculated for the mooring tension measured during the tests. The results were averaged across three cases and are presented in Table 4.11. When the clump weight was added, the extreme mooring tension in the single lines increased by 5.9% and 4.4%, while the extreme mooring tension in the shared line decreased by 28.6% and 30.3%. As the mooring properties of the shared line were the same for both configurations, adding a clump weight could have reduced the extreme mooring tension in the shared line, which resulted in a lower utilization factor. Consequently, this opens up the possibility of cost reduction through a redesign of the shared line.

4.7 Summary of the experimental study

This chapter presented an experimental investigation of dual-spar FOWFs with different shared mooring systems. Firstly, a comparison was made between a dual-spar FOWF with a shared line, i.e., configuration II, and a single FOWT. The primary findings are listed as follows:

- **Natural period**: In line with the observations in Sec. 3.2.3 and Sec. 3.3.4, the influence of the shared line was mainly reflected in the natural periods of surge and sway DOFs.
- **Platform surge motion**: In the surge DOF, Spar 1 of configuration II exhibited larger mean offset and dynamic motion compared to the single FOWT. The platform surge motion spectrum of Spar 1 demonstrated higher spectral energy in the low-frequency range in contrast to the single FOWT. The motion response in the pitch DOF was comparable between the two configurations.
- **Mooring tension of the single lines**: The single lines of Spar 1 in configuration II experienced higher maximum tension, and higher spectral energy was observed in the low-frequency range, in line with the observations regarding platform surge motion.

Then, a comparative study was carried out between configurations II and III in terms of natural periods, motion response, and structural response in different ECs. Based on the observations, the advantages and disadvantages of configuration III in comparison to configuration II can be summarized as follows:

- **Natural period**: Natural periods in the surge, sway, and yaw DOFs decreased by 6.1%, 4.7%, and 6.5%, respectively. Differences in the natural periods of other DOFs were insignificant.

- **Platform surge motion**: Due to the 0-degree wave heading, the differences in platform motions were primarily observed in the surge DOF under the extreme EC, where the motion range of Spar 1 decreased by 23.6% and the SD of surge motion decreased by 26.7%, indicating an improved station-keeping performance.
- **Mooring tension of the single lines**: The added clump weight led to higher pretension and mean tension in single lines under both ECs. Under the extreme EC, after adding the clump weight, an average decrease of 7.4% was observed in the SDs of mooring tension in the single lines of Spar 1, and the extreme mooring tension in the single lines of Spar 1 increased by approximately 5.2%.
- **Mooring tension of the shared line**: The added clump weight resulted in higher pretension and mean tension in the shared line under both ECs. However, the SD of mooring tension in the shared line decreased, especially under the extreme EC, with the ratio between the SD and mean tension decreasing from 78.2% to 34.2% for T_{5f1}. The extreme mooring tension in the shared line decreased by 29.5% on average.

Chapter 5

Conclusions and recommendations for future work

This thesis assessed the static and dynamic characteristics of dual-spar FOWFs with various shared mooring systems. First, different shared mooring configurations were introduced. Then, static analysis methods were developed, and dynamic modeling methods were applied, based on which the dynamic behaviours of different configurations were investigated in numerical analyses. Hydrodynamic model tests were conducted for selected configurations. The investigation on the experimental results verified the findings from the numerical studies and also provided an assessment of a new configuration, configuration III. The main conclusions, original contributions, and recommendations for future work are presented in this final chapter.

5.1 Conclusions

The main conclusions of the thesis are summarized as follows:

- An approach was developed and validated for the eigenvalue analysis of FOWFs with shared mooring systems, including modeling of the shared mooring system based on Irvine's elastic catenary theory for hanging cables and mooring stiffness linearization. The proposed method was applied to the eigenvalue analysis of a dual-spar FOWF with a shared line. The natural periods in the surge and sway DOFs were primarily influenced by the shared line, as the surge and sway stiffness terms were dominated by the mooring stiffness. It was also observed that the natural periods in the surge and sway DOFs were sensitive to the mooring properties of both the single lines and the shared line.

- The impact of the shared line on the dynamic characteristics of the FOWTs was investigated through numerical and experimental comparisons between a dual-spar FOWF with a shared line and a single spar FOWT. The shared line primarily affected the system stiffness in the horizontal DOFs. Due to the reduced mooring stiffness, larger motion ranges and more significant dynamic motions were observed in the FOWTs under extreme ECs with a 0-degree

loading direction. Consequently, higher tension levels were experienced in the single lines. The relative motions between the two FOWTs repeatedly tightened and loosened the shared line, resulting in dynamic mooring tension that was considerably higher than that in the single lines. Snap load events were also observed in the shared line. The loading direction significantly influenced the platform motions of the dual-spar FOWF with a shared line, and an increase in the shared line diameter led to a reduction in the number of observed snap events.

- An experimental investigation was conducted to understand the fundamental behaviors of two shared mooring systems. As the mooring stiffness dominated the system stiffness in the surge, sway, and yaw DOFs, the introduction of a clump weight decreased the natural periods in these DOFs due to the increased system stiffness. In addition, reduced dynamic motions of FOWTs around their mean positions were observed. The static positions of the FOWTs were affected by the added clump weight, resulting in increased pretension in both the single lines and the shared line. However, the dynamic tension in all mooring lines decreased, which also led to a reduction in the occurrence of snap load events in the shared line.

- A tethered-buoy shared mooring system was investigated for the dual-spar FOWF. The natural periods in the surge and sway DOFs of this configuration were considerably larger than those of the dual-spar FOWF with a shared line, as the floating system became less stiff, and the natural periods of the tethered-buoy mooring system could be adjusted by altering the net buoyancy of the buoys. Moreover, larger mean offset and dynamic motions were observed in the loading direction for the FOWTs with the tethered-buoy mooring system. Nevertheless, the replacement of single lines with hanging lines connected to tethered buoys significantly reduced the tension levels in all mooring lines, and no snap load events were observed. These features will make the tethered-buoy mooring system preferable when the FOWT excursion limits become a less important design consideration for dynamic inter-array cables in the future.

5.2 Original contributions

The main contributions of the thesis can be summarized as follows:

- *Development of a quasi-static modeling method for shared mooring systems and its application in mooring stiffness linearization*
  This modeling method applies Irvine's elastic catenary theory to model various types of shared lines and single lines, based on which mooring stiffness linearization and eigenvalue analysis of FOWFs with shared mooring systems can be performed. The present method is verified by FE modeling and experimental results. It can be used to quickly estimate natural periods of FOWFs

with different FOWT types, mooring system layouts, and farm sizes and predict dynamic behaviors of the FOWFs based on the system stiffness in the preliminary design stage.

- *Understanding of the motion and structural dynamics of a dual-spar FOWF with a shared mooring system by coupled numerical simulation*
  The influence of a shared line on the dynamic characteristics of a dual-spar FOWF was investigated through a detailed comparison to a single spar FOWT. The FOWF with a shared mooring system was modeled in a numerical simulation tool. Fully coupled time-domain simulations were performed considering various ECs with irregular waves and turbulent wind. The influence of loading directions and shared line mooring properties on the dynamics of the floating system was systematically examined through sensitivity studies.

- *Designing the hydrodynamic model tests for prototype FOWFs with shared mooring systems*
  A hydrodynamic model test campaign for a dual-spar FOWF with two different shared mooring systems was conducted for the first time in the field. Physical modeling of the FOWTs and the shared mooring systems was documented. Different types of wave tests were carried out with various ECs. A comparative study was performed with a previously tested single FOWT, validating the findings obtained from the numerical simulations. Furthermore, the influence of adding a clump weight to the shared line on the dynamic behaviors of the FOWF was shown.

- *Proposal of novel shared mooring systems and evaluation of performance of different shared mooring configurations for a dual-spar FOWF*
  The potential of different shared mooring systems was explored for a dual-spar FOWF. A tethered-buoy shared mooring system with the potential to dramatically lower line loads and mooring costs was proposed. Various types of shared mooring systems were modeled in the numerical simulation tool. Fully coupled time-domain simulations were conducted under various load scenarios. The dynamic behaviors of FOWFs with different shared mooring systems were statistically quantified, allowing for a discussion and comparison of the station-keeping performance among these configurations.

5.3 Limitations and recommendations for future work

- *Further study on the dynamic characteristics of FOWFs with shared mooring systems*
  In this study, a dual-spar prototype FOWF was selected as the initial basis for understanding the influence of shared mooring systems. It is recommended that future investigations expand the current analyses to FOWFs with different floater types, various water depths, large farm sizes, and novel mooring materials among other variables. The dynamic analyses conducted in this

study focused on the ULS of FOWFs. It is advised that future work explores operational load scenarios for FLS assessment of FOWFs. Properly tuned controllers and a consideration of the aerodynamic interactions between FOWTs are crucial for assessing these scenarios.

- *Calibration and verification of numerical models*
  The experimental results obtained from the hydrodynamic model test campaign could be utilized to calibrate and validate numerical models used in aero-hydro-servo-elastic codes and high-fidelity numerical modes used in CFD modeling, e.g., to calibrate the drag coefficients of the spar floaters and mooring lines under varying Reynolds and Keulegan-Carpenter numbers during irregular waves.

- *Further investigation on model tests of FOWFs with shared mooring systems*
  This study acknowledges there were certain limitations in the experimental investigation. Specifically, it did not account for environmental effects such as wind and currents. It is recommended that future research investigates the dynamic behaviors of FOWFs with shared mooring systems under combined environmental loading conditions and with control actions, e.g., hybrid model testing [41]. To acquire more comprehensive information and gain a better understanding of the floating system, it is suggested to measure additional responses during the model tests, which may include platform motions and accelerations of all FOWTs, mooring angles, and motions of mooring components, such as clump weights and buoys. Additionally, verification of the natural periods and eigenmodes of the coupled floating system could be achieved by accurately exciting the eigenmodes obtained from the eigenvalue analysis.

- *Design and optimization of shared mooring systems for FOWFs*
  In this study, eigenvalue analyses and dynamic analyses were performed to comprehensively assess the system properties and dynamic characteristics of FOWFs with various shared mooring systems. It is recommended that these analysis methods be applied in the design and optimization of shared mooring systems for specific FOWFs and ECs. Both the individual components and shared components of the mooring system, different shared mooring configurations, and various LCs should be considered. Efficient frequency-domain methods can be developed to facilitate the screening of feasible designs in the preliminary stage.

- *Life cycle cost evaluation of FOWFs with shared mooring systems*
  It is recommended to explore the cost-saving potential of shared mooring systems for FOWFs. Evaluating the performance of different shared mooring systems for a given FOWF in terms of station-keeping, the influence on power production, and life cycle economic analyses is of significant interest. Furthermore, it is recommended to investigate how the performance of shared mooring systems varies with different design variables, such as farm size and water depth.

References

[1] T. J. Price. James Blyth—Britain's first modern wind power pioneer. *Wind Engineering*, 29(3):191–200, 2005.

[2] WindEurope. Wind energy in Europe, 2022 Statistics and the outlook for 2023-2027. Technical report, WindEurope, 2023.

[3] GWEC. Global wind report 2023. Technical report, Global wind energy council, 2023.

[4] W. Musial, P. Spitsen, P. Duffy, P. Beiter, M. Marquis, R. Hammond, and M. Shields. Offshore Wind Market Report: 2022 Edition. Technical report, National Renewable Energy Lab.(NREL), Golden, CO (United States), 2022.

[5] Equinor ASA. Hywind Scotland, the world's first floating wind farm, 2022. https://www.equinor.com/energy/hywind-scotland. Accessed April 10, 2023.

[6] Equinor ASA. Hywind Tampen: the world's first renewable power for offshore oil and gas, 2022. https://www.equinor.com/energy/hywind-tampen. Accessed April 10, 2023.

[7] T. Stehly and P. Duffy. 2020 Cost of Wind Energy Review. Technical report, National Renewable Energy Lab.(NREL), Golden, CO (United States), 2021.

[8] DNV. Energy transition outlook 2022: a global and regional forecast to 2050. Technical report, 2022.

[9] R. James and M. C. Ros. Floating offshore wind: market and technology review. *The Carbon Trust*, 439, 2015.

[10] Vryhof Anchors B.V. VRYHOF MANUAL: The Guide to Anchoring, 2018.

[11] P. Connolly and C. Crawford. Analytical modelling of power production from un-moored floating offshore wind turbines. *Ocean Engineering*, 259:111794, 2022.

[12] Equinor ASA. Hywind Scotland, the world's first commercial floating wind farm. https://www.equinor.com/content/dam/statoil/documents/newsroom-additional-documents/news-attachments/brochure-hywind-a4.pdf. Accessed April 10, 2023.

[13] DNV. Standard DNV-ST-0119, Floating wind turbine structures. Høvik, Norway, 2021.

[14] M. Leimeister, A. Kolios, and M. Collu. Critical review of floating support structures for offshore wind farm deployment. In *Journal of Physics: Conference Series*, volume 1104, page 012007. IOP Publishing, 2018.

[15] DNV GL. Offshore standard DNVGL-OS-E301, Position mooring. Høvik, Norway, 2018.

[16] DNV GL. Offshore standard DNVGL-OS-E302, Offshore mooring chain. Høvik, Norway, 2015.

[17] K. T. Ronson. Ropes for deep water mooring. In *Offshore Technology Conference*. OnePetro, 1980.

[18] DNV GL. Offshore standard DNVGL-OS-E304, Offshore mooring steel wire ropes. Høvik, Norway, 2015.

[19] DNV. Recommended Practice DNV-RP-0286, Coupled Analysis of Floating Wind Turbines. Høvik, Norway, 2019.

[20] DNV GL. Offshore standard DNVGL-OS-E303, Offshore Fibre Ropes. Høvik, Norway, 2015.

[21] ABS. Guide for building and classing floating offshore wind turbine installations. *The American Bureau of Shipping, Houston (TX), USA*, 2013.

[22] ABS. Guidance notes on global performance analysis for floating offshore wind turbines. *The American Bureau of Shipping, Houston (TX), USA*, 2020.

[23] IEC. IEC TS 61400-3-2, Wind energy generation systems-Part 3-2: Design requirements for floating offshore wind turbines. Geneva, Switzerland, 2019.

[24] S. Weller, L. Johanning, P. Davies, and S. Banfield. Synthetic mooring ropes for marine renewable energy applications. *Renewable Energy*, 83:1268–1278, 2015.

[25] S. H. Sørum, N. Fonseca, M. Kent, and R. P. Faria. Assessment of nylon versus polyester ropes for mooring of floating wind turbines. *Ocean Engineering*, 278:114339, 2023.

[26] F. Khalid, P. R. Thies, P. Halswell, D. Newsam, and L. Johanning. Double braid mooring damper for floating offshore wind application. In *International Conference on Offshore Mechanics and Arctic Engineering*, volume 85932, page V008T09A046. American Society of Mechanical Engineers, 2022.

[27] A. L. Hopstad and F. Pollicino. Overview of offshore wind standards and certification requirements in selected countries. Technical report, DNV GL, 2020.

[28] O. Faltinsen. *Sea loads on ships and offshore structures*, volume 1. Cambridge university press, 1993.

[29] M. Masciola, J. Jonkman, and A. Robertson. Implementation of a multisegmented, quasi-static cable model. In *The Twenty-third International Offshore and Polar Engineering Conference*. OnePetro, 2013.

[30] DNV GL. MIMOSA-User's Doumentation Programme Version 5.7. Høvik, Norway, 2003.

[31] K. Larsen and P. C. Sandvik. Efficient methods for the calculation of dynamic mooring line tension. In *The First ISOPE European Offshore Mechanics Symposium*. OnePetro, 1990.

[32] M. Hall, B. Buckham, and C. Crawford. Evaluating the importance of mooring line model fidelity in floating offshore wind turbine simulations. *Wind Energy*, 17(12):1835–1853, 2014.

[33] M. O. Hansen. *Aerodynamics of wind turbines*. Routledge, 2015.

[34] M. Jeon, S. Lee, and S. Lee. Unsteady aerodynamics of offshore floating wind turbines in platform pitching motion using vortex lattice method. *Renewable Energy*, 65:207–212, 2014.

[35] Y. Liu, Q. Xiao, A. Incecik, C. Peyrard, and D. Wan. Establishing a fully coupled CFD analysis tool for floating offshore wind turbines. *Renewable Energy*, 112:280–301, 2017.

[36] M. Hall. Moordyn user's guide. *Department of Mechanical Engineering, University of Maine: Orono, ME, USA*, 15, 2015.

[37] B. W. Kim, H. G. Sung, J. H. Kim, and S. Y. Hong. Comparison of linear spring and nonlinear FEM methods in dynamic coupled analysis of floating structure and mooring system. *Journal of Fluids and Structures*, 42:205–227, 2013.

[38] T. Moan, Z. Gao, E. E. Bachynski, and A. R. Nejad. Recent advances in integrated response analysis of floating wind turbines in a reliability perspective. *Journal of Offshore Mechanics and Arctic Engineering*, 142(5), 2020.

[39] D. Roddier, C. Cermelli, A. Aubault, and A. Weinstein. WindFloat: A floating foundation for offshore wind turbines. *Journal of Renewable and Sustainable Energy*, 2(3):033104, 2010.

[40] C. L. Bottasso, F. Campagnolo, and V. Petrović. Wind tunnel testing of scaled wind turbine models: Beyond aerodynamics. *Journal of Wind Engineering and Industrial Aerodynamics*, 127:11–28, 2014.

[41] T. Sauder, V. Chabaud, M. Thys, E. E. Bachynski, and L. O. Sæther. Real-time hybrid model testing of a braceless semi-submersible wind turbine: Part I—The hybrid approach. In *International Conference on Offshore Mechanics and Arctic Engineering*, volume 49972, page V006T09A039. American Society of Mechanical Engineers, 2016.

[42] Y. Su, J. Yang, L. Xiao, and G. Chen. Experimental and numerical study on large truncation of deepwater mooring line. In *International Conference on Offshore Mechanics and Arctic Engineering*, volume 43413, pages 201–212, 2009.

[43] G. R. Tomasicchio, F. D'Alessandro, A. M. Avossa, L. Riefolo, E. Musci, F. Ricciardelli, and D. Vicinanza. Experimental modelling of the dynamic behaviour of a spar buoy wind turbine. *Renewable Energy*, 127:412–432, 2018.

[44] S. Yamamoto and W. E. Colburn Jr. Power generation assemblies, 2005. International Patent, Publication Number W0 2005/040604 A2.

[45] C. M. Fontana, S. R. Arwade, D. J. DeGroot, A. T. Myers, M. Landon, and C. Aubeny. Efficient multiline anchor systems for floating offshore wind turbines. volume 49972 of *International Conference on Offshore Mechanics and Arctic Engineering*, page V006T09A042. American Society of Mechanical Engineers, 2016.

[46] M. Goldschmidt and M. Muskulus. Coupled mooring systems for floating wind farms. *Energy Procedia*, 80:255–262, 2015.

[47] M. Hall and P. Connolly. Coupled dynamics modelling of a floating wind farm with shared mooring lines. ASME 2018 37th International Conference on Ocean, Offshore and Arctic Engineering, Madrid, Spain. American Society of Mechanical Engineers Digital Collection, 2018.

[48] J. M. Jonkman and M. L. Buhl. *FAST user's guide*, volume 365. National Renewable Energy Laboratory Golden, CO, USA, 2005.

[49] P. Connolly and M. Hall. Comparison of pilot-scale floating offshore wind farms with shared moorings. *Ocean Engineering*, 171:172–180, 2019.

[50] H. Munir, C. F. Lee, and M. C. Ong. Global analysis of floating offshore wind turbines with shared mooring system. In *IOP Conference Series: Materials Science and Engineering*, volume 1201, page 012024. IOP Publishing, 2021.

[51] Y. Zhang and H. Liu. Coupled dynamic analysis on floating wind farms with shared mooring under complex conditions. *Ocean Engineering*, 267:113323, 2023.

[52] ANSYS Inc. AQWA Theory Manual. *AQWA: Canonsburg, PA, USA*, 2016.

[53] S. Wilson, M. Hall, S. Housner, and S. Sirnivas. Linearized modeling and optimization of shared mooring systems. *Ocean Engineering*, 241:110009, 2021.

[54] M. Hall, E. Lozon, S. Housner, and S. Sirnivas. Design and analysis of a ten-turbine floating wind farm with shared mooring lines. In *Journal of Physics: Conference Series*, volume 2362, page 012016. IOP Publishing, 2022.

[55] J. M. Jonkman and K. Shaler. *FAST.Farm user's guide and theory manual*. National Renewable Energy Laboratory Golden, CO, USA, 2021.

[56] E. Lozon and M. Hall. Coupled loads analysis of a novel shared-mooring floating wind farm. *Applied Energy*, 332:120513, 2023.

[57] M. Irvine. *Cable Structures*. Dover Publications, 1992.

[58] SINTEF Ocean. SIMO 4.16.0 User Guide. Trondheim, Norway, 2019.

[59] SINTEF Ocean. RIFLEX 4.16.0 User Guide. Trondheim, Norway, 2019.

[60] J. Jonkman, S. Butterfield, W. Musial, and G. Scott. Definition of a 5-MW reference wind turbine for offshore system development. Technical Report NREL/TP-500-38060, National Renewable Energy Lab (NREL), Golden, CO (United States), 2009.

[61] J. Jonkman. Definition of the floating system for Phase IV of OC3. Technical Report NREL/TP-500-47535, National Renewable Energy Lab (NREL), Golden, CO (United States), 2010.

[62] R. J. Stevens, D. F. Gayme, and C. Meneveau. Effects of turbine spacing on the power output of extended wind-farms. *Wind Energy*, 19(2):359–370, 2016.

[63] Danish Wind Industry Association. Park effect, 2023. http://ele.aut.ac.ir/ wind/en/tour/wres/park.htm. Accessed April 10, 2023.

[64] G. Liang, Z. Jiang, and K. O. Merz. Mooring analysis of a dual-spar floating wind farm with a shared line. *Journal of Offshore Mechanics and Arctic Engineering*, 143(6), 2021.

[65] G. Liang, T. Lopez-Olocco, A. Medina-Manuel, L. S. Ynocente, A. Souto-Iglesias, and Z. Jiang. Experimental investigation of two shared mooring configurations for a dual-spar floating offshore wind farm in irregular waves. Submitted for publication, 2022.

[66] T. Lopez-Olocco, G. Liang, A. Medina-Manuel, L. S. Ynocente, Z. Jiang, and A. Souto-Iglesias. Experimental comparison of a dual-spar floating wind farm with shared mooring against a single floating wind turbine under wave conditions. *Engineering Structures*, 292:116475, 2023.

[67] L. Li, Z. Gao, and T. Moan. Joint distribution of environmental condition at five European offshore sites for design of combined wind and wave energy devices. *Journal of Offshore Mechanics and Arctic Engineering*, 137(3), 2015.

[68] B. Skaare, F. G. Nielsen, T. D. Hanson, R. Yttervik, O. Havmøller, and A. Rekdal. Analysis of measurements and simulations from the hywind demo floating wind turbine. *Wind Energy*, 18(6):1105–1122, 2015.

[69] Y. Liu and L. Bergdahl. Extreme mooring cable tensions due to wave-frequency excitations. *Applied Ocean Research*, 20(4):237–249, 1998.

[70] SEMAR AS. Honeymooring: dynamic mooring solution for floating wind farms, 2023. https://semar.no/honeymooring/. Accessed April 10, 2023.

[71] G. Liang, K. O. Merz, and Z. Jiang. Modeling of a shared mooring system for a dual-spar configuration. In *International Conference on Offshore Mechanics and Arctic Engineering*, volume 9: Ocean Renewable Energy. American Society of Mechanical Engineers, 2020.

[72] J. S. Arora. *Introduction to optimum design*. Elsevier, 2004.

[73] T. M. Inc. MATLAB version: 9.11.0 (R2021b), 2021.

[74] G. Liang, Z. Jiang, and K. O. Merz. Dynamic analysis of a dual-spar floating offshore wind farm with shared moorings in extreme environmental conditions. *Marine Structures*, 90:103441, 2023.

[75] K. O. Merz. Development of an LQR framework for rapid prototyping of offshore wind turbine controllers, with application to active load control. Technical Report 2020:00257, SINTEF Energy Research, 2020.

[76] DNV. SESAM user manual, WADAM, Wave analysis by diffraction and morison theory. Høvik, Norway, 2019.

[77] G. Liang, Z. Jiang, and K. O. Merz. Influence of aerodynamic loads on a dual-spar floating offshore wind farm with a shared line in parked conditions. In *International Conference on Offshore Mechanics and Arctic Engineering*, volume 85932, page V008T09A023. American Society of Mechanical Engineers, 2022.

[78] DNV. Recommended practice DNV-RP-C205, Environmental conditions and environmental loads. Høvik, Norway, 2010.

[79] B. Molin. *Offshore Structure Hydrodynamics*. Cambridge University Press, 2022.

[80] J. Almedeij. Drag coefficient of flow around a sphere: Matching asymptotically the wide trend. *Powder Technology*, 186(3):218–223, 2008.

[81] B. J. Jonkman. TurbSim User's Guide v2.00.00. Technical report, National Renewable Energy Lab (NREL), Golden, CO (United States), 2016.

[82] IEC. International standard IEC 61400-1, Wind turbines—Part 1: Design requirements. Geneva, Switzerland, 2005.

[83] IEC. International standard IEC 61400-3, Wind turbines—Part 3: Design requirements for offshore wind turbines. Geneva, Switzerland, 2009.

[84] M. Ikhennicheu, M. Lynch, S. Doole, F. Borisade, et al. Review of the state of the art of mooring and anchoring designs, technical challenges and identification of relevant DLCs, 2021.

[85] W.-t. Hsu, K. P. Thiagarajan, and L. Manuel. Extreme mooring tensions due to snap loads on a floating offshore wind turbine system. *Marine Structures*, 55:182–199, 2017.

[86] G. Liang, F. C. W. Hanssen, K. O. Merz, and Z. Jiang. Numerical analysis of a tethered-buoy mooring system for a prototype floating wind farm. Submitted for publication, 2023.

[87] M. U. Rentschler, F. Adam, and P. Chainho. Design optimization of dynamic inter-array cable systems for floating offshore wind turbines. *Renewable and Sustainable Energy Reviews*, 111:622–635, 2019.

[88] F. G. Nielsen, T. D. Hanson, and B. Skaare. Integrated dynamic analysis of floating offshore wind turbines. In *International conference on offshore mechanics and arctic engineering*, volume 47462, pages 671–679, 2006.

[89] F. Duan, Z. Hu, and J. M. Niedzwecki. Model test investigation of a spar floating wind turbine. *Marine Structures*, 49:76–96, 2016.

[90] K. Jessen, K. Laugesen, S. M. Mortensen, J. K. Jensen, and M. N. Soltani. Experimental validation of aero-hydro-servo-elastic models of a scaled floating offshore wind turbine. *Applied Sciences*, 9(6):1244, 2019.

[91] X. Xu and S. Day. Experimental investigation on dynamic responses of a spar-type offshore floating wind turbine and its mooring system behaviour. *Ocean Engineering*, 236:109488, 2021.

[92] T. Lopez-Olocco, L. M. González-Gutiérrez, J. Calderon-Sanchez, A. Marón Loureiro, L. Saavedra Ynocente, A. Bezunartea Barrio, and N. Vivar Valdés. Experimental and numerical study of the influence of clumped weights on a scaled mooring line. *Journal of Marine Science and Engineering*, 10(5):676, 2022.

[93] J. M. Journée and W. W. Massie. *Offshore hydromechanics*, volume 1. Delft University of Technology, 2001.

[94] S. K. Chakrabarti. *Offshore structure modeling*, volume 9. World Scientific, 1994.

[95] C. Barrera, R. Guanche, and I. J. Losada. Experimental modelling of mooring systems for floating marine energy concepts. *Marine Structures*, 63:153–180, 2019.

[96] Northern Digital Inc. Optotrak Certus., 2022. Accessed April 10, 2023.

[97] ITTC. Recommended procedures and guidelines: Model tests for offshore wind turbines, 2017.

[98] ITTC. Recommended procedures and guidelines: Floating offshore platform experiments, 2017.

[99] ITTC. Recommended procedures and guidelines: Testing and extrapolation methods loads and responses, stability model tests on intact stability, 2008.

[100] P. Stoica and R. L. Moses. *Spectral analysis of signals*, volume 452. Pearson Prentice Hall Upper Saddle River, NJ, 2005.

[101] Z. Jiang, G. Liang, T. Lopez-Olocco, A. Medina-Manuel, L. S. Ynocente, and A. Souto-Iglesias. Model test of a dual-spar floating wind farm in regular waves. In *Advances in the Analysis and Design of Marine Structures*, pages 171–177. CRC Press, 2023.

[102] Y. J. Lu, Y.-N. Chen, P.-L. Tan, and Y. Bai. Prediction of most probable extreme values for jackup dynamic analysis. *Marine Structures*, 15(1):15–34, 2002.

A.4 Paper 4

Paper 4:

Dynamic Analysis of a Dual-Spar Floating Offshore Wind Farm with Shared Moorings in Extreme Environmental Conditions

Authors: Guodong Liang, Zhiyu Jiang, Karl Otto Merz

Published in *Marine Structures, 90, 103441, 2023.*

Marine Structures 90 (2023) 103441

Contents lists available at ScienceDirect

Marine Structures

journal homepage: www.elsevier.com/locate/marstruc

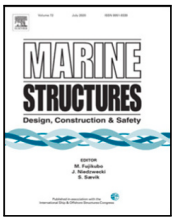

Dynamic analysis of a dual-spar floating offshore wind farm with shared moorings in extreme environmental conditions

Guodong Liang [a,*], Zhiyu Jiang [a], Karl Merz [b]

[a] Department of Engineering Sciences, University of Agder, N-4898 Grimstad, Norway
[b] SINTEF Energy Research, N-7034 Trondheim, Norway

ARTICLE INFO

Keywords:
Floating offshore wind farm
Shared mooring system
Dynamic response
Time-domain simulation
Extreme response
Wind and waves

ABSTRACT

The concept of a shared mooring system was proposed to reduce mooring and anchoring costs. Shared moorings also add complexity to the floating offshore wind farm system and pose design challenges. To understand the system dynamics, this paper presents a dynamic analysis for a dual-spar floating offshore wind farm with a shared mooring system in extreme environmental conditions. First, a numerical model of the floating offshore wind farm was established in a commercial simulation tool. Then, time-domain simulations were performed for the parked wind farm under extreme wind and wave conditions. A sensitivity study was carried out to investigate the influence of loading directions and shared line mooring properties. To highlight the influence of the shared line, the results were compared to those of a single spar floating wind turbine, and larger platform motions and higher tension loads in single lines are observed for the wind farm with shared moorings. The loading direction affects the platform motions and mooring response of the floating offshore wind farm. Comparing the investigated loading directions to the 0-deg loading direction, the variation of mean mooring tension at the fairlead is up to 84% for single lines and 16% for the shared line. The influence of the shared line properties in the platform motions and the structural responses is limited. These findings improve understanding of the dynamic characteristics of floating offshore wind farms with a shared mooring system.

1. Introduction

A floating offshore wind farm (FOWF) is a promising solution to the growing demand for clean and de-carbonized energy. The design concept of a shared mooring system has been proposed to reduce the cost of FOWFs [1]. A shared mooring system can consist of single lines and shared lines without additional mooring elements. In such a case, each single line connects a floating offshore wind turbine (FOWT) to the anchor, and a shared line connects two adjacent FOWTs directly and is completely hanging in the water. Top views of shared mooring systems for pilot-scale FOWFs are presented in Fig. 1, in which each FOWT is connected to three mooring lines. Fewer mooring lines and anchors are required for an FOWF with a shared mooring system, which indicates potential for cost-saving. However, unlike conventional FOWFs, e.g., Hywind Scotland [2], where each FOWT is separate, the novel FOWFs with shared moorings are expected to exhibit different dynamic response behavior under environmental loading. The technical feasibility of such a concept needs to be studied through detailed investigations of the system's dynamic characteristics.

Goldschmidt and Muskulus [3] studied the dynamic properties of FOWFs with shared mooring systems using simplified models for several configurations. The cost-saving potential of the shared mooring system was revealed but increasing requirements for

* Corresponding author.
E-mail addresses: guodong.liang@uia.no (G. Liang), zhiyu.jiang@uia.no (Z. Jiang), inducedvelocity@gmail.com (K. Merz).

https://doi.org/10.1016/j.marstruc.2023.103441
Received 11 May 2022; Received in revised form 23 January 2023; Accepted 27 February 2023
Available online 2 May 2023

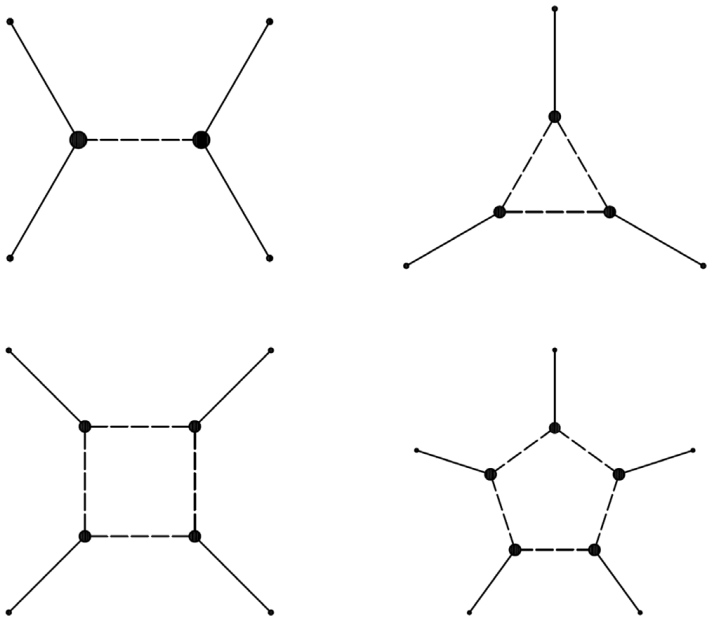

Fig. 1. Shared mooring systems for pilot-scale FOWFs (large solid circle: FOWT, small solid point: anchor, solid line: single line, dashed line: shared line).

the mooring system were reported with larger farm size. Hall and Connolly [4] investigated the dynamics of a four-turbine square-shaped FOWF with semi-submersible FOWTs and a shared mooring system. Complex restoring properties and a greater tendency for resonance were found for the mooring systems with shared lines. In a follow-up study by Connolly and Hall [5], a simplified design algorithm was proposed for the preliminary sizing of shared mooring systems for pilot-scale FOWFs. Several layouts of shared mooring systems were designed and analyzed for a four-turbine FOWF in different water depths. In [6], Hall modeled and studied the mooring failure scenario of a dual-semi-submersible FOWF in time-domain simulations. Wilson et al. [7] proposed a design optimization approach based on a linearized method to model the force-horizontal displacement relationship of FOWTs with a shared mooring system. The design approach was based on quasi-static mooring analysis and applied to different layouts of FOWFs. Munir et al. [8] studied the dynamic behavior of a dual-semi-submersible FOWF with a shared mooring system and considered two different turbine spacings. The study only examined the platform motions. Liang et al. [9] applied the theory of elastic catenary of hanging cable structures to model the shared line. In a follow-up study, Liang et al. [10] studied the influence of the shared mooring system on the natural periods and natural modes of a dual-spar FOWF.

The dynamic response of an FOWF in extreme environmental conditions is important to the survivability and structural integrity of the system. To the authors' knowledge, there is a lack of literature addressing this aspect for FOWFs with shared moorings. To explore the extreme responses of FOWFs with shared moorings, we study the dynamic behaviors of a baseline FOWF with two FOWTs, one shared line, and four single lines for a deep-water site. The influence of the shared line is investigated by comparing the structural and motion response statistics of the FOWF with those of a single FOWT under extreme wind and wave conditions. To elucidate the dynamic characteristics of the FOWF, we further consider different loading directions and shared line properties in a sensitivity study. In the following, the baseline FOWF is introduced in Section 2. The procedures of numerical modeling are described in Section 3. Section 4 presents the details of the case study. The results are analyzed and discussed in Section 5. Finally, conclusions are summarized in Section 6.

2. Concept description of the baseline FOWF

The dual-spar baseline FOWF is illustrated in Fig. 2. As shown, two OC3 Hywind spar FOWTs [11,12], Spar 1 and Spar 2, are deployed in the global surge direction, i.e., along the x_g-axis. Table 1 presents some of the main design parameters of the OC3 Hywind spar FOWT. The turbine spacing is 1000 m in the initial configuration, which is approximately eight times the rotor diameter.

The FOWTs are connected by a shared line, Line 5, in the x_g direction. Due to its self weight, the shared line is pre-tensioned and has a catenary line shape; see Fig. 3. As a result, two FOWTs move towards each other along the x_g-axis by a short distance under static equilibrium. Each FOWT has two single lines which are attached to the seabed through anchors. The projected angle between any two adjacent mooring lines is 120 deg.

The draft of fairleads and the radius from the fairleads to the corresponding floater centerlines are kept the same as in [12]. All fairleads of single lines and the shared line are located 70 m below the still water level (SWL) and 5.2 m away from the corresponding floater centerlines. The water depth is 320 m below the SWL. The radius from floater centerlines to corresponding anchors is increased to 953.87 m. A mooring design is made for a single OC3 Hywind spar FOWT in [10]. A two-segment design with chain and wire is used as it is more representative of actual mooring lines than that of the one-segment design. Detailed design

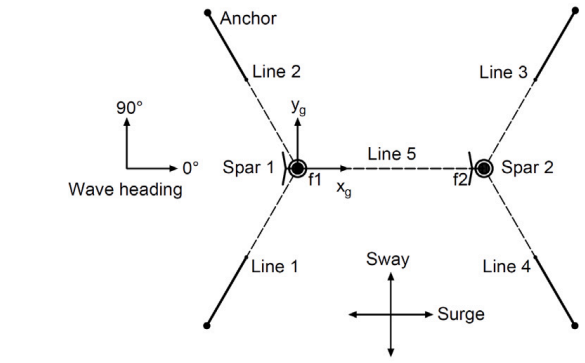

(a) Top view

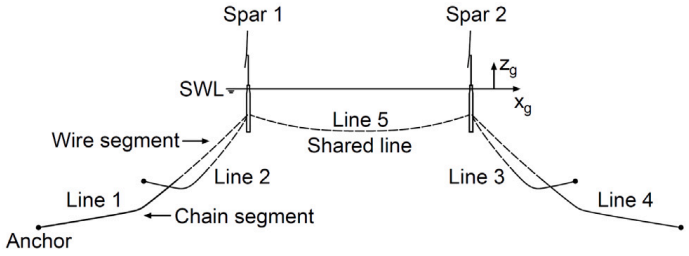

(b) Side view

Fig. 2. Illustration of the dual-spar baseline FOWF (SWL: still water level, dashed line: wire, solid line: chain).

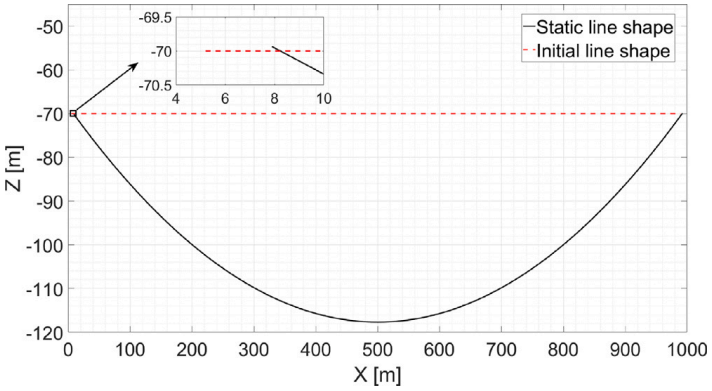

Fig. 3. Static line shape of the shared line of the dual-spar baseline FOWF (loading direction: 0 deg).

Table 1
Main design parameters of the OC3 Hywind Spar FOWT [11,12].

Design parameter	Value
Rated power capacity [MW]	5
Turbine type [–]	Upwind, 3 blades
Cut-in, rated, cut-out wind speed [m/s]	3, 11.4, 25
Rotor diameter [m]	126
Hub height [m]	90
Total draft [m]	120
Number of mooring lines [–]	3
Radius to fairleads from floater centerline [m]	5.2
Depth to fairleads below SWL [m]	70
Angle between adjacent lines [deg]	120
Water depth [m]	320

Table 2
Mooring properties of the baseline FOWF.

Mooring properties	Single line		Shared line
	Chain segment	Wire segment	
Material	R3 studless chain	Steel wire rope	Steel wire rope
Water depth [m]	320	320	320
Unstretched length [m]	550	452.2	989.6
Diameter [mm]	115	90	90
Sheath thickness [mm]	–	10	10
Mass density [kg/m]	264.50	42.77	42.77
Weight in water [N/m]	2385.86	324.00	324.00
Extensional stiffness [N]	1.06E+09	7.64E+08	7.64E+08
Minimum breaking strength [N]	1.03E+07	8.38E+06	8.38E+06

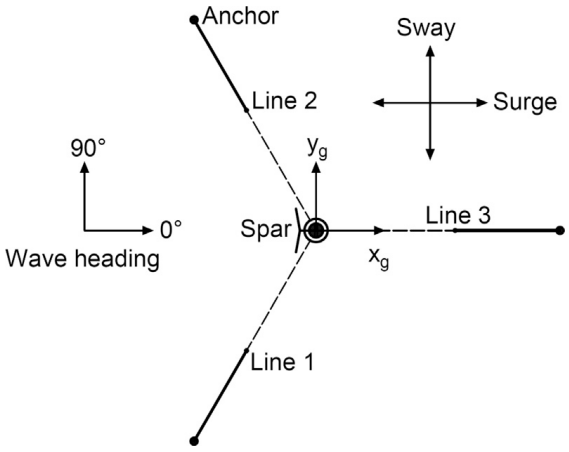

Fig. 4. Top view of the single FOWT (dashed line: wire, solid line: chain).

procedures can be found in [10]. The mooring design is applied to the single lines of the baseline FOWF. As shown in Fig. 2(b), the upper segment is made of wire and the lower segment is made of mooring chain. The shared line is supposed to be suspended and submerged in the water all the time without touching the sea bed or interfering with ship traffic. Wire is lighter than chain and is therefore used for the shared line. Because there is no design recommendation for the shared line, wire properties of the single lines are used for the shared line for simplicity. Mooring properties of the baseline FOWF are summarized in Table 2.

To investigate the influence of the shared line, a single spar FOWT is modeled as well. As illustrated in Fig. 4, the three single lines of the FOWT have the same orientations as Spar 1 in the baseline FOWF. The partial safety factors for an FOWF are not calibrated in the mooring design standards [13], so the configurations of the single lines are kept the same for the baseline FOWF and the single FOWT for comparison.

3. Numerical modeling of the dual-spar FOWF

To perform dynamic analyses, the baseline FOWF and the single FOWT described in Section 2 are modeled in SIMA [14,15] in which the OC3 Hywind spar FOWTs are modeled according to [11,12].

A hydrodynamic analysis is performed for the panel model of the single spar in the frequency domain using the potential-flow program WADAM [16] to obtain hydrodynamic properties, like the frequency-dependent hydrodynamic added mass and radiation damping coefficients, the first-order wave force transfer functions, the second-order mean wave drift forces.

The spar floaters are modeled as rigid bodies in the SIMO module of SIMA. Six degrees of freedom (DOFs) of the rigid-body motions are considered for each FOWT, namely, surge, sway, heave, roll, pitch and yaw. Mooring lines of the baseline FOWF are modeled as slender structures in the RIFLEX module of SIMA. Fifty bar elements with the same cross-section properties are used to model the chain segment and the wire segment of the single lines, respectively. One hundred bar elements are used to model the shared line. Detailed failure modes of mooring materials, e.g., wear of chain or birdcaging of wire, are not considered in the numerical modeling of the mooring system. The same modeling method is applied to model the single FOWT in SIMA.

The equation of motion for the floating system can be written in the time domain as:

$$(\mathbf{M}+\mathbf{A}_\infty)\ddot{\mathbf{x}}+\mathbf{B}_1\dot{\mathbf{x}}+\mathbf{B}_2\dot{\mathbf{x}}|\dot{\mathbf{x}}|+\mathbf{C}\mathbf{x}+\int_0^t \mathbf{h}(t-\tau)\dot{\mathbf{x}}(\tau)d\tau=\mathbf{f}(t,\mathbf{x},\dot{\mathbf{x}}) \tag{1}$$

in which $\mathbf{M}$ is the structural mass matrix; $\mathbf{A}_\infty$ is the added mass matrix at infinite frequency; $\mathbf{B_1}$ is the matrix of linear damping coefficients; $\mathbf{B_2}$ is the matrix of quadratic damping coefficients; $\mathbf{C}$ is the matrix of restoring coefficients; $\mathbf{h}(\tau)$ is the retardation

Table 3
Natural periods of the baseline FOWF and the single FOWT [s].

DOF		Surge	Sway	Heave	Roll	Pitch	Yaw
Baseline FOWF	Mode 1	135.51	76.25	31.13	29.48	29.47	8.36
	Mode 2	63.52	75.64	31.03	29.48	29.46	8.34
Single FOWT		79.65	79.64	30.75	29.31	29.31	8.69

Table 4
Environmental parameters for the extreme environmental conditions.

Parameter	Value
U_w (at hub-height) [m/s]	42.71
I [–] (Turbulence intensity)	0.12
H_s [m]	15.50
T_p [s]	14.45

function; $\mathbf{x}$, $\dot{\mathbf{x}}$, and $\ddot{\mathbf{x}}$ are the vectors of the displacement, velocity and acceleration in the time domain; $\mathbf{f}$ is the external force vector. Hydrodynamic properties obtained from WADAM are implemented in the SIMA model of the baseline FOWF to calculate wave loads. Wave forces are integrated to the mean water level. Morison elements are added to the underwater part of the spar floaters to calculate the drag forces. The hydrodynamic coupling between two FOWTs is ignored because of the large turbine spacing. In extreme environmental conditions, the FOWTs are parked (standing still) and the blades are feathered. As found in [17], the extreme response of the baseline FOWF is not entirely wave-dominant and aerodynamic loads do play a role in extreme conditions. Therefore, aerodynamic loads acting on the FOWTs are considered in extreme environmental conditions. The airfoil coefficients of the FOWT blades specified in [11] are used, based on which the aerodynamic loads are calculated. Drag coefficients are specified to consider the drag force acting on the tower. According to the offshore standard [18], the drag coefficients are set to 0.65 based on the Reynolds number calculation. Since two FOWTs are in a parked condition with rotors at standstill, the aerodynamic interaction effect between the FOWTs is ignored.

Twelve free decay tests are performed for the baseline FOWF and six free decay tests are performed for the single FOWT in SIMA. For the FOWF, forces or moments are applied to the FOWTs to obtain initial displacements or rotations in the corresponding DOFs. Then the FOWTs are released and oscillate in the still water. As studied in [10], the baseline FOWF has twelve natural modes and natural periods. The estimated natural periods of the baseline FOWF and the single FOWT are summarized in Table 3. For the FOWF, two natural modes, Mode 1 and Mode 2, are identified for all six DOFs. Mode 1 indicates that the two FOWTs move in the same direction and Mode 2 indicates that they move in opposite directions. From Table 3, it is seen that the natural periods of translational DOFs in the horizontal plane are mostly influenced by the presence of the shared line, i.e., in the surge and sway directions, because the diagonal terms of stiffness matrix in these two directions only have contributions from mooring stiffness [10].

4. Case study

A case study is conducted to investigate the dynamic characteristics of the baseline FOWF in extreme environmental conditions. First, the influence of the shared mooring on the FOWTs is demonstrated by comparing the dynamic responses to those of the single FOWT. Then, the influence of loading directions and shared line diameters are further explored for the baseline FOWF.

4.1. Metocean condition

In accordance with the offshore standard [19], the extreme environmental conditions are determined with a return period of 50 years. The metocean condition of a European offshore site, "Norway 5" [20], is used. The 50-year environmental contour surface is calculated based on the joint distribution of the mean wind speed (U_w), the significant wave height (H_s) and the spectral peak period (T_p). The sea state on the contour surface with the highest H_s is selected. Other environmental loads like current are not considered in this study. The wind turbine Class I-B and the IEC Normal Turbulence Model are chosen [21,22]. The environmental parameters are listed in Table 4.

Turbulent wind and irregular waves are considered in simulations. The wind and waves are assumed to come in the same direction and are specified by a parameter, the loading direction. In SIMA, irregular waves are generated with random wave seeds. Turbulent wind fields are simulated in Turbsim [23] and used in SIMA. The size of the turbulent wind fields is determined to ensure that the FOWTs stay inside during motions.

4.2. Dynamic analysis of the baseline FOWF

To study how the dynamic characteristics of the FOWTs are influenced by the shared line, dynamic analyses are performed for the baseline FOWF and the single FOWT under the extreme environmental conditions described in Section 4.1. Two loading directions, 0 deg and 90 deg, are considered; see Figs. 2(a) and 4.

Table 5
Mooring properties for different shared line diameters in the sensitivity study.

Diameter [mm]	90	100	110	120	130
Mass density [kg/m]	42.77	52.24	62.65	73.98	86.25
Weight in water [N/m]	324.00	398.75	481.09	571.00	668.44
Cross-sectional area [m^2]	0.0095	0.0113	0.0133	0.0154	0.0177
Extensional stiffness [N]	7.64E+08	9.35E+08	1.12E+09	1.32E+09	1.54E+09
Minimum breaking strength [N]	8.38E+06	1.04E+07	1.25E+07	1.49E+07	1.76E+07

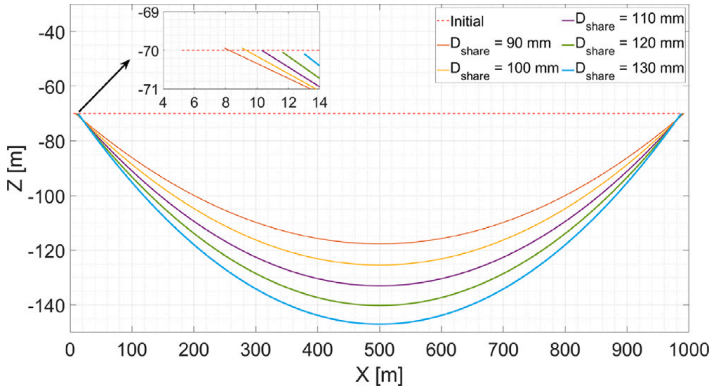

Fig. 5. Static line shape of the shared line in the sensitivity study of the shared line diameter (loading direction: 0 deg).

To determine the number of realizations for the dynamic analyses, a convergence study was conducted with the 0-deg loading direction. Platform motions and structural responses of the baseline FOWF are considered. The results show that twenty one-hour realizations are sufficient for the extreme response statistics to reach convergence. Therefore, for each considered environmental condition, twenty one-hour time-domain simulations were performed for the baseline FOWF and the single FOWT.

4.3. Sensitivity study

4.3.1. Sensitivity study on the loading direction

A sensitivity study is conducted for the loading direction to investigate how it will influence the dynamic behavior of the baseline FOWF. Because of the symmetry of the dual-spar configuration, we select four loading directions, 0 deg, 30 deg, 60 deg and 90 deg. For each loading direction, 20 one-hour time-domain simulations are performed. The results of platform motions and structural responses are analyzed and compared.

4.3.2. Sensitivity study on the shared line diameter

To investigate the influence of the shared line on the system's dynamic characteristics, various shared line mooring properties are investigated as well. Based on the catalogue data of wires, four shared line diameters are selected besides the original shared line diameter for the baseline FOWF. The mooring properties of different shared line diameters are listed in Table 5. The length of the shared line is kept unchanged. The static line shapes of the shared line are plotted in Fig. 5 for different shared line diameters. With an increasing shared line diameter, the shared line is heavier and therefore, the horizontal displacements of FOWTs from their initial positions are larger and so does the sagging depth of the shared line in static equilibrium. Two loading directions, 0 deg and 90 deg, are considered in this sensitivity study. For each loading direction, twenty one-hour time-domain simulations are performed for every configuration with a different shared line diameter and the simulation results are post-processed.

5. Results and discussion

Simulation results obtained from the case study in Section 4 are analyzed and discussed in this section. In Section 5.1, dynamic behaviors of the baseline FOWF are first analyzed and presented through a comparison to the single FOWT in terms of the linearized mooring stiffness, the horizontal platform motions and selected structural responses. Then, results of the sensitivity study are presented in Section 5.2 in which the linearized mooring stiffness, the horizontal platform motions of FOWTs and the selected structural responses are compared step by step. In the following sections, "Spar 1" and "Spar 2" refer to the FOWTs in the dual-spar configuration; see Fig. 2. "Spar" refers to the single FOWT; see Fig. 4.

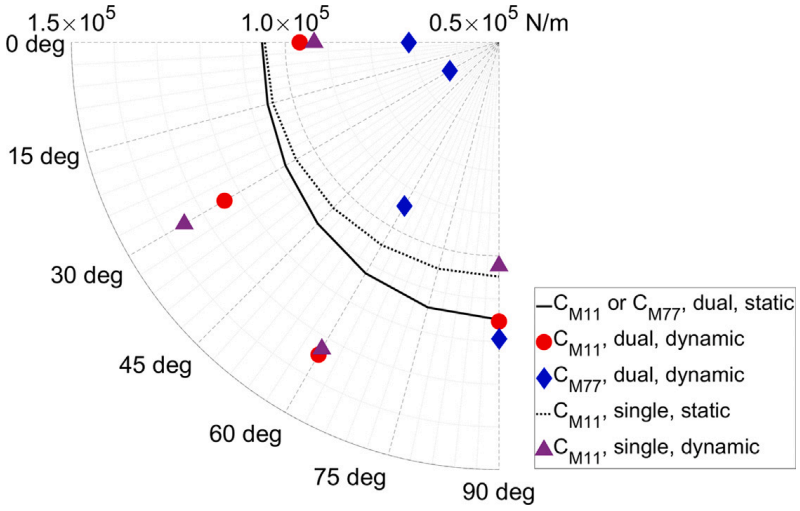

Fig. 6. Linearized mooring stiffness with respect to different loading directions (dual: baseline FOWF, single: single FOWT, static: linearized around the static equilibrium position, dynamic: linearized around the mean dynamic position).

Table 6
Results of horizontal platform motions of FOWTs in the dynamic analysis.

Parameter	Baseline FOWF		Single FOWT
	Spar 1	Spar 2	Spar
Loading direction = 0 deg			
Platform, static equilibrium position [m]	(2.56, 0)	(997.70, 0)	(0,0)
Platform, mean dynamic position [m]	(13.59, 0.35)	(1006.25, 3.71)	(5.28, 0.37)
Platform, motion range[a] [m]	[−12.40, 12.90]	[−12.76, 12.95]	[−11.98, 11.94]
Platform, motion SD[b] [m]	3.64	3.83	3.43
Loading direction = 90 deg			
Platform, static equilibrium position [m]	(2.38, 0.07)	(997.50, 0.07))	(−0.08, 0.08)
Platform, mean dynamic position [m]	(1.95, 11.36)	(996.79, 11.09)	(−1.33, 12.06)
Platform, motion range [m]	[−12.72, 13.61]	[−12.94, 13.16]	[−12.98, 13.72]
Platform, motion SD [m]	3.88	3.82	3.91

[a]"Platform, motion range" refers to the planar platform motions projected in the $x_g - y_g$ plane and along the loading direction. It is calculated with regard to the "Platform, mean dynamic position".
[b]"Platform, motion SD" stands for the standard deviation of the planar platform motions projected in the loading direction.

5.1. Comparison between the baseline FOWF and the single FOWT

5.1.1. Comparison of linearized mooring stiffness

The method presented in [10] is applied to calculate the linearized mooring stiffness of the baseline FOWF and the single FOWT. Both the static equilibrium positions and the mean dynamic positions of the system are taken as the reference position for linearization. The mooring stiffness is linearized in the coordinate system where the x-axis is along the loading direction. The results are plotted in Fig. 6. For the baseline FOWF, the stiffness terms C_{M11} and C_{M77} are the diagonal terms in the linearized mooring stiffness matrix and relate to the motions of Spar 1 and Spar 2 in the loading direction. For the single FOWT, the stiffness terms C_{M11} relate to the motion of Spar in the loading direction.

As shown in Fig. 6, for the baseline FOWF, the stiffness terms "C_{M11}, dual, static" and "C_{M77}, dual, static" experience large changes when the loading direction varies from 0 deg to 90 deg, which is caused by the asymmetry of the shared mooring layout. The stiffness term "C_{M11}, single, static" is insensitive to loading directions due to the symmetry of the mooring layout. For both configurations, the mooring stiffness terms linearized around the mean dynamic position differ from those linearized around the static equilibrium position.

5.1.2. Comparison of platform motion in the horizontal plane

To maintain the structural integrity of power cables and the operation of FOWTs, the motion of FOWTs in the horizontal plane must be limited by the mooring system. Though there is no specific recommendation in the design standards, e.g., [19], an excursion limit as a function of the water depth can be assumed [24]. On the other hand, to utilize the space efficiently, the turbine spacing of an FOWF is not very large in practice. Due to the wake effects, the turbine spacing will influence the power output of wind turbines in a wind farm [25]. Therefore, it is of interest to check the horizontal platform motions of FOWTs.

Platform motions are presented in the global coordinate system. The statistics of horizontal platform motions are shown in Table 6 for the baseline FOWF and the single FOWT, where the ensemble average of the 20 realizations is presented. From Table 6,

Table 7
Results of mooring response in the dynamic analysis.

Parameter	Baseline FOWF			Single FOWT		
	Line 1	Line 2	Line 5 f1	Line 1	Line 2	Line 3
Loading direction = 0 deg						
Pretension [N]	9.50E+05	9.50E+05	8.39E+05	8.50E+05	8.50E+05	8.44E+05
Mooring tension, max [N]	2.34E+06	2.17E+06	5.35E+06	2.04E+06	1.77E+06	1.51E+05
Mooring tension, mean [N]	1.39E+06	1.36E+06	9.61E+05	1.03E+06	9.93E+05	6.86E+05
Mooring tension, SD [N]	1.80E+05	1.76E+05	6.63E+05	1.57E+05	1.43E+05	1.38E+05
Mooring angle, max [deg]	67.43	67.01	90.00	65.94	65.18	64.94
Mooring angle, mean [deg]	63.39	63.19	80.34	61.05	60.77	57.55
Mooring angle, SD [deg]	0.95	0.98	4.70	1.16	1.19	1.87
Loading direction = 90 deg						
Pretension [N]	9.47E+05	9.40E+05	8.39E+05	8.52E+05	8.45E+05	8.48E+05
Mooring tension, max [N]	2.45E+06	1.36E+06	4.29E+06	2.27E+06	1.20E+06	1.86E+06
Mooring tension, mean [N]	1.45E+06	6.24E+05	9.59E+05	1.33E+06	5.19E+05	9.59E+05
Mooring tension, SD [N]	2.16E+05	1.45E+05	5.29E+05	2.02E+05	1.16E+05	1.44E+05
Mooring angle, max [deg]	68.28	63.97	89.99	67.57	62.71	64.97
Mooring angle, mean [deg]	63.61	56.57	80.42	63.03	54.62	60.53
Mooring angle, SD [deg]	1.22	2.21	3.03	1.25	2.20	1.14

after reaching a static equilibrium, the two FOWTs of the baseline FOWF approach each other by approximately 2.5 m along the x_g-axis compared to their initial positions. This is caused by the self weight of the shared line, as explained in Section 2. For the mean dynamic positions, a large offset is observed in the loading direction, which is caused by the mean aerodynamic load and the mean wave drift force. Compared with the single FOWT, Spar 1 and Spar 2 have relatively larger motion ranges and standard deviations (SDs) with 0-deg loading direction and similar motion ranges and SDs with 90-deg loading direction. This observation is due to the shared line configuration (one shared line in the x_g-direction) of the baseline FOWF and is expected to change for other shared line configurations. The difference of the restoring force provided by Line 5 of the baseline FOWF and Line 3 of the single FOWT is important for the motions of FOWTs in the 0-deg loading direction, but the influence of the difference in the restoring force is not significant for the motions of FOWTs in the 90-deg loading direction because the line is nearly perpendicular to the loading direction.

5.1.3. Comparison of structural response

Among the structural response variables, the mooring tension and tower-base bending moment (TBBM) are selected as key indicators affected by the dynamics of the FOWTs. For each mooring line, the mooring tension and angle at the fairlead are of interest. The mooring angle is defined as the angle between the mooring line and the vertical direction at the fairlead. The sagging depth, $Z_{sagging}$, is investigated to study the line shape of the shared line under dynamic responses. $Z_{sagging}$ is defined as the vertical distance from the lowest point on the shared line to the SWL. $Z_{sagging}$ must be sufficiently large, e.g., > 20 m, if vessels are to pass between FOWTs.

The statistics of mooring tension and mooring angles at the fairleads are summarized in Table 7 for mooring lines connected to Spar 1 and Spar. The maximum value, mean value and SD presented in the table are averaged over 20 realizations. For the 0-deg loading direction, higher tension at the fairlead is observed for single lines of the baseline FOWF than for those of the single FOWT. This is because Spar 1 has a larger mean dynamic offset than Spar, as shown in Table 6. For the 90-deg loading direction, the mooring responses of Line 1 and Line 2 are comparable between Spar 1 and Spar. This is in agreement with the mean dynamic positions of FOWTs shown in Table 6. The maximum mooring angles at the fairlead Line 5 f1 are close to 90 deg for both loading directions, indicating a tightened shared line. It is observed that for both loading directions, the SDs of mooring tension and mooring angle at the fairlead are much higher in the shared line than in the single lines. This is the trade-off of the reduced number of single mooring lines and anchors. Therefore, the design of the shared line is of importance to avoid premature or cascade mooring failures of FOWFs in extreme ocean environments.

A snap event of a mooring line is characterized as a sharp tension spike whose magnitude exceeds typical values of local tension maxima, after a temporary slackness in the mooring line [26]:

$$T_{start} \leq 0.1 \cdot T_{static} \tag{2}$$

$$T_{end} \geq 1.9 \cdot T_{static} \tag{3}$$

where T_{start} is the local tension minima when the snap event starts; T_{end} is the local tension maxima when the snap event ends; T_{static} is the pretension plus the contribution caused by the mean environmental load, i.e., the mean dynamic mooring tension. Snap load events are checked for all mooring lines of the baseline FOWF. For the investigated loading directions, snap load events are only observed in the shared line. The shared line experiences more snap load events in the 0-deg loading direction than in the 90-deg loading direction due to larger relative surge motions between FOWTs. For twenty one-hour time-domain simulations, the averaged number of snap events observed at the fairlead Spar 1, Line 5 f1 is 209.35 for the 0-deg loading direction and 86.05 for the 90-deg

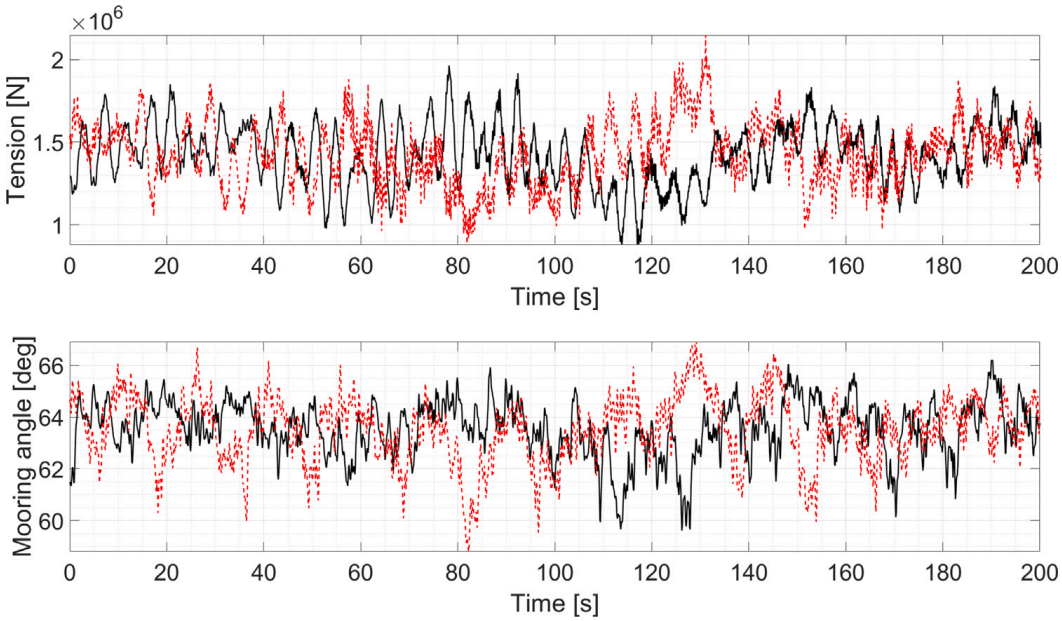

Fig. 7. Mooring response time series of Line 1 (solid line: 0 deg, dashed line: 90 deg).

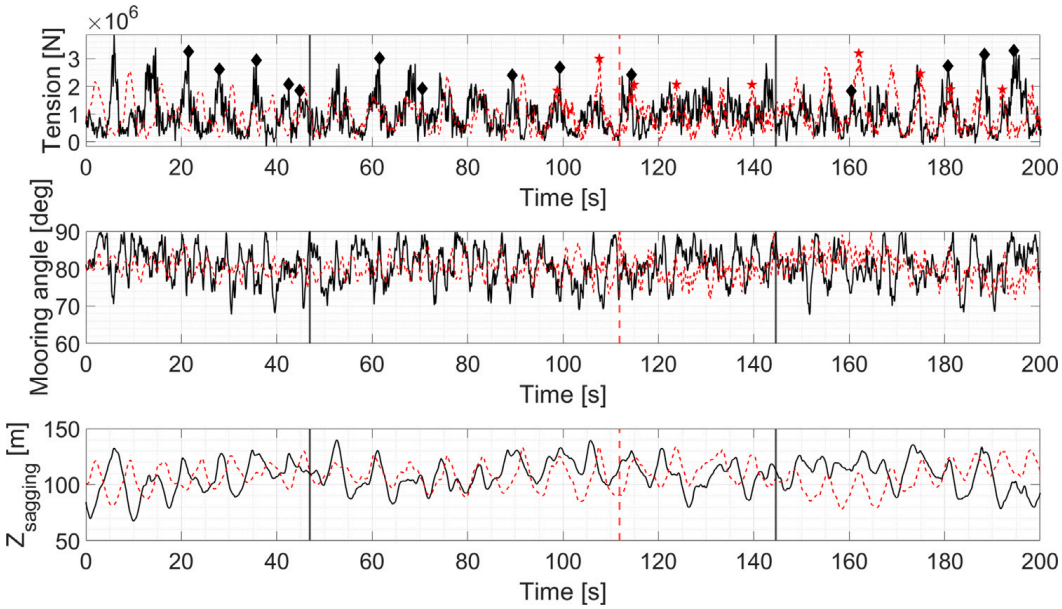

Fig. 8. Mooring response time series of Line 5 f1 (solid line: 0 deg, dashed line: 90 deg).

loading direction. For the realization with the closest platform motion SD to the mean SD over twenty realizations, the time series of mooring responses of Spar 1, Line 1 are plotted in Fig. 7; the time series of mooring responses of Spar 1, Line 5 f1 are plotted in Fig. 8 with T_{end} of snap load events marked in the time series of mooring tension. Smaller mooring tension with larger variation is found for Line 5 f1 compared with that for Line 1. Time instants where the mooring angle is close to 90 deg are marked with solid lines in Fig. 8. It is observed that the peaks of mooring tension and the mooring angle do not occur simultaneously.

TBBM is presented in the local coordinate system of the tower. In the initial condition, a positive fore-aft TBBM is about the negative y_g-axis and a positive side-side TBBM is about the positive x_g-axis (refer to Fig. 2(a)). The statistics of TBBM are summarized in Table 8 for the baseline FOWF and the single FOWT, in which the mean value and SD are averaged over twenty realizations. It is observed that in the loading direction, both Spar 1 and Spar 2 of the baseline FOWF have comparable TBBM statistics as the single FOWT does. This indicates that for the baseline FOWF with the shared mooring system, the structural design of the towers does not involve additional considerations.

Table 8
Statistics of TBBMs in the dynamic analyses.

Parameter	Baseline FOWF				Single FOWT	
	Spar 1 fore-aft	Spar 1 side-side	Spar 2 fore-aft	Spar 2 side-side	Spar fore-aft	Spar side-side
Loading direction = 0 deg						
TBBM, mean [Nm]	−2.43E+07	−2.95E+06	−2.18E+07	−8.88E+06	−2.48E+07	−2.86E+06
TBBM, SD [Nm]	5.59E+07	6.50E+06	5.57E+07	8.98E+06	5.58E+07	6.54E+06
Loading direction = 90 deg						
TBBM, mean [Nm]	4.09E+06	−7.47E+07	2.98E+06	−7.43E+07	3.56E+06	−7.44E+07
TBBM, SD [Nm]	4.06E+06	5.77E+07	3.95E+06	5.77E+07	2.44E+06	5.78E+07

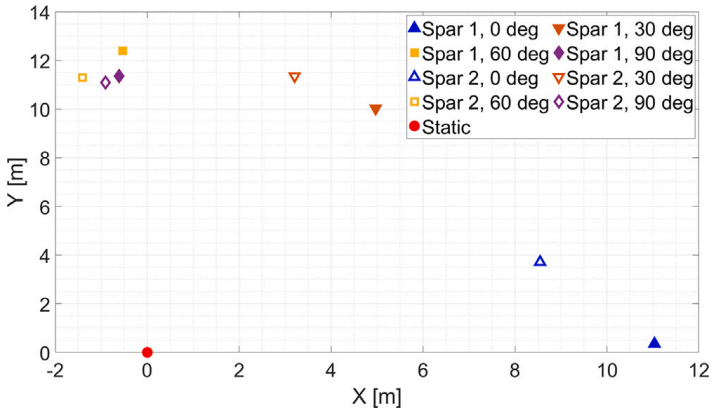

Fig. 9. Mean position of body origins of FOWTs in the horizontal plane due to variation of the loading direction.

5.2. Sensitivity study

In the following sections, results of the sensitivity study on the loading direction are presented in Section 5.2.1 and results of the sensitivity study on the shared line diameter are discussed in Section 5.2.2. In sensitivity studies, simulations and analyses are carried out for the dual-spar FOWF only.

5.2.1. Sensitivity study on the loading direction

As discussed in Section 4.3.1, dynamic analyses have been performed for the baseline FOWF in four loading directions, i.e., 0 deg, 30 deg, 60 deg and 90 deg. The linearized mooring stiffness, horizontal platform motions and structural response are investigated and discussed below.

Influence on linearized mooring stiffness

As mentioned in Section 5.1.1, for the investigated loading directions, the mooring stiffness is linearized around the mean dynamic position in the coordinate system where the x-axis is along the loading direction. The results are presented in Fig. 6 with markers. For the baseline FOWF, large variations with respect to the loading direction are observed in both the stiffness terms "C_{M11}, dual, dynamic" and "C_{M77}, dual, dynamic". This is caused by different mean dynamic positions of FOWTs due to mean environmental loads under environmental conditions with different loading directions. For each investigated loading direction, the stiffness term "C_{M11}, dual, dynamic" of Spar 1 is different from the stiffness term "C_{M77}, dual, dynamic" of Spar 2, which indicates that unlike the static condition, Spar 1 and Spar 2 are expected to show different motion characteristics in the dynamic analyses. The linearized mooring stiffness is plotted for the single FOWT for comparison. The stiffness term "C_{M11}, dual, dynamic" of Spar 1 and the stiffness term "C_{M11}, single, dynamic" of Spar show similar variations with respect to the loading directions, resulting from similar mooring layouts as shown in Figs. 2(a) and 4.

Influence on platform motion in the horizontal plane

The mean dynamic positions of FOWTs averaged over 20 realizations are plotted in Fig. 9, in which the static equilibrium positions of FOWTs are taken as the reference and put at the original point. Therefore, Fig. 9 presents how far the mean dynamic positions of Spar 1 and Spar 2 move from the static condition in different loading directions. The mean dynamic positions have contributions from both the mean aerodynamic load and the mean wave drift force. The magnitude of the mean wave drift force is on the same level with respect to loading directions, while the mean aerodynamic load differs. The statistics of aerodynamic force acting on the FOWTs are plotted in Fig. 10 with respect to the variation of the loading direction. In Fig. 10, the aerodynamic force is presented in the main shaft coordinate system. The x-shaft-axis is along the shaft line and the y-shaft-axis is perpendicular to the shaft line and in the same direction as the y_g-axis in the initial condition. As described in Section 4.1, the blades of the FOWTs are feathered. Therefore, the mean angles of attack of the blades increase with the increasing loading direction. When the loading direction is 0 deg, the blades are parallel to the main wind direction, and the drag forces acting on the blades are small which leads

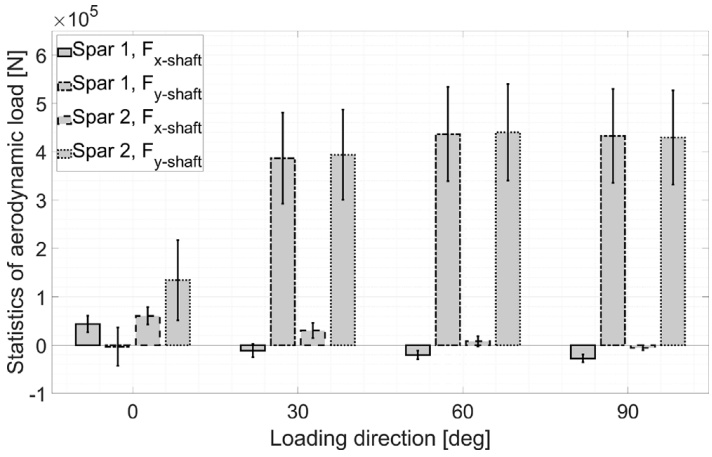

Fig. 10. Statistics of aerodynamic force acting on the FOWTs due to variation of the loading direction (bar: mean value averaged over realizations, error bar: SD averaged over realizations).

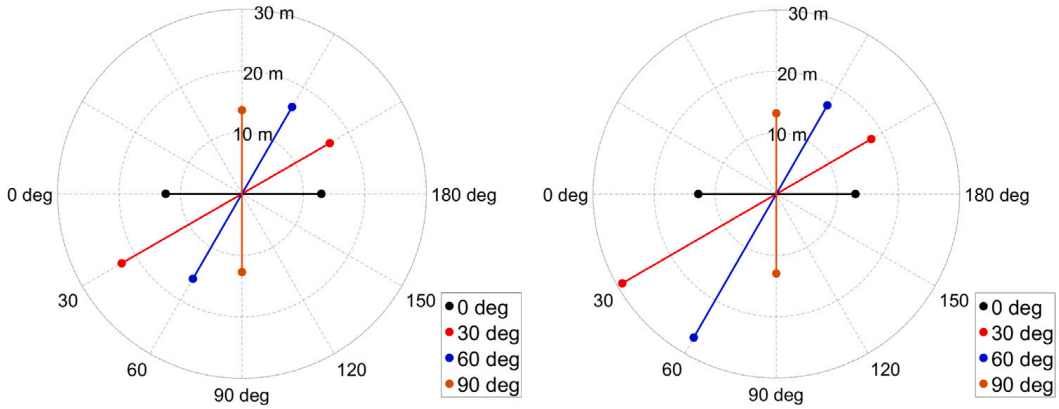

(a) Spar 1 (b) Spar 2

Fig. 11. Platform motion range of FOWTs in the loading direction due to variation of the loading direction.

to small aerodynamic forces in the x-shaft direction. When the loading direction is 90 deg, the drag forces acting on the blades are large which results in large aerodynamic forces in the y-shaft direction. In Fig. 9, it is observed that with the 0-deg loading direction, Spar 2 has a mean offset perpendicular to the loading direction. This is explained by the aerodynamic force acting on Spar 2 in the y-shaft direction, as shown in Fig. 10. From Figs. 9 and 10, it is seen that the component of aerodynamic force acting in the y-shaft direction is positively correlated to the mean offset of FOWTs in the y_g direction.

The platform motion ranges in the loading direction are averaged over the realizations and plotted in Fig. 11 with respect to different loading directions. It is observed that Spar 2 has larger motion ranges than Spar 1 in the 30-deg and 60-deg loading directions. This interesting observation is explained by the mooring stiffness linearized about the mean dynamic positions, shown in Fig. 6. In the 30-deg and 60-deg loading directions, the stiffness terms "C_{M77}, dual, dynamic" are much smaller than "C_{M11}, dual, dynamic".

Influence on structural response

Statistics of mooring responses are plotted in Fig. 12 with respect to the variation of the loading direction.

In Fig. 12(a), it is observed that Line 1 and Line 4 are more loaded than the rest single lines in loading directions except for the 0-deg loading direction. This can be explained by the mean dynamic positions of FOWTs shown in Fig. 9. The windward single lines are expected to be more loaded than the leeward single lines. When the loading direction is 0 deg, Spar 1 and Spar 2 are driven to move along the x_g axis. Therefore, the windward single lines, Line 1 and Line 2, are the most loaded. For Line 4, the averaged maximum mooring tension is over the minimum breaking strength (MBS) for the 30-deg loading direction and close to the MBS for the 60-deg loading direction, resulting from the large platform motion ranges in these two loading directions shown in Fig. 11(b). It is noticed that although the mean tension in the shared line is not necessarily higher than those in the single lines, the variation of the mooring tension is the most significant. This is caused by the relative motions between Spar 1 and Spar 2. The shared line is tightened and loosened back-and-forth because of the dynamic motions of the two FOWTs. Due to the large motion ranges of both FOWTs shown in Fig. 11, the maximum mooring tension experienced by the shared line is close to the MBS in the 30-deg and 60-deg loading directions, indicating the necessity of a redesign for the shared line.

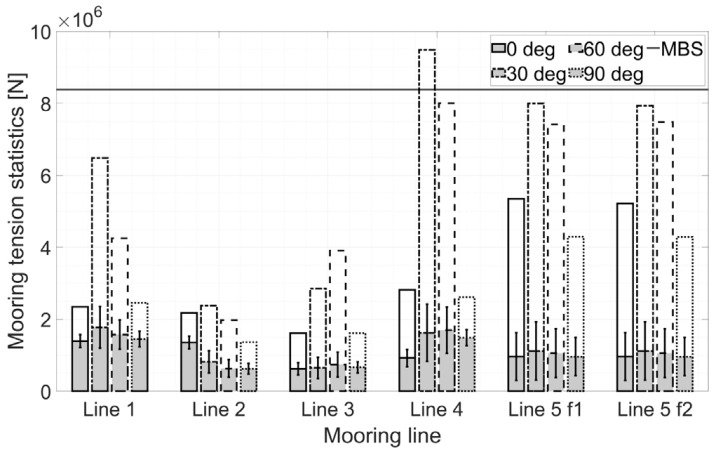

(a) Mooring tension at the fairlead

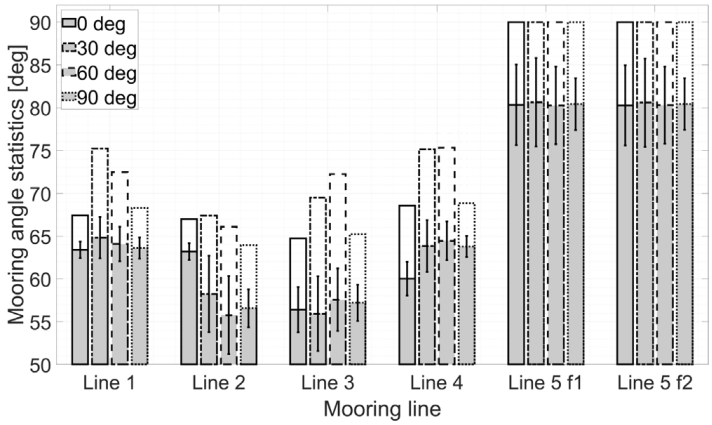

(b) Mooring angle at the fairlead

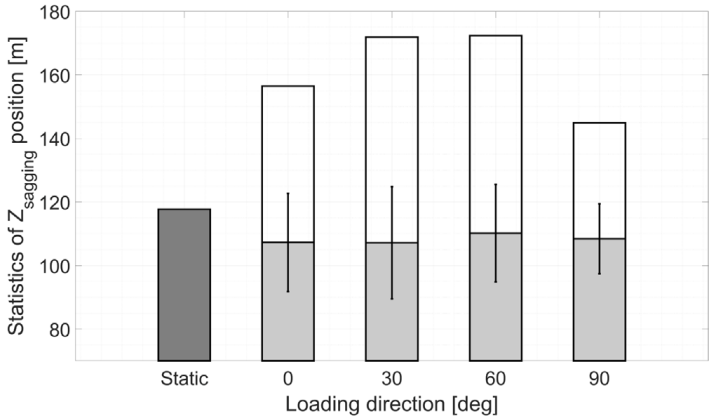

(c) The sagging depth $Z_{Sagging}$

Fig. 12. Statistics of mooring responses due to variation of the loading direction (gray bar: mean value averaged over realizations, white bar: maximum value averaged over realizations, error bar: SD averaged over realizations).

In Fig. 12(b), it is found that Line 1 and Line 4 have larger mean and maximum mooring angles while Line 2 and Line 3 have larger SDs of the mooring angle. This is due to the mean dynamic positions and the motion ranges of FOWTs, as shown in Figs. 9 and 11. The more loaded windward single lines have larger mean and maximum mooring angles and the less loaded leeward single lines have larger variations of mooring angles. The shared line has a large mean mooring angle as expected. For all investigated loading directions, the shared line is tightened when the mooring angle reaches 90 deg. Therefore, additional attention should be paid to the design of the shared line. Clump weights or alternative material compositions may be considered in the design of the shared line to alter the line shape and to reduce the tension variations.

From Fig. 12(c), it is seen that the sagging depth has the largest mean value in the static equilibrium, while in dynamic analyses, the mean sagging depth is smaller due to the relative motion of FOWTs. For different loading directions, the difference in the mean sagging depth is not significant. A positive correlation is found between the platform motion ranges of FOWTs shown in Fig. 11(b) and the maximum and the SD of the sagging depth of the shared line shown in Fig. 12(c) as the maximum and the SD of the sagging

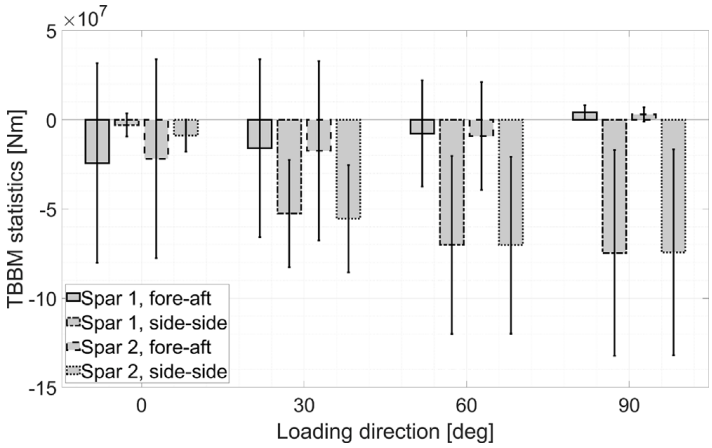

Fig. 13. Statistics of TBBM due to the variation of the loading direction (bar: mean value averaged over realizations, error bar: SD averaged over realizations).

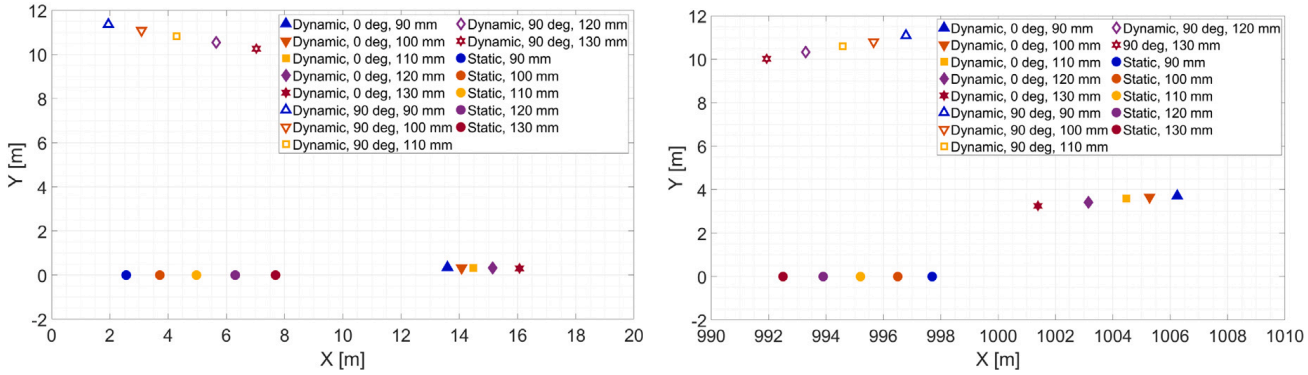

(a) Spar 1 (b) Spar 2

Fig. 14. Mean positions of body origins of FOWTs in the horizontal plane due to variation of the shared line diameter.

depth depends on the level of relative motions between FOWTs. This sagging depth can potentially affect the vessels passing between the FOWTs.

Statistics of TBBM are plotted in Fig. 13 with respect to the loading directions. It is observed that with an increasing loading direction, the fore-aft TBBMs of both FOWTs decrease and the side-side TBBMs increase. This is in agreement with the variation of aerodynamic forces acting on the FOWTs, as shown in Fig. 10.

5.2.2. Sensitivity study on the shared line diameter

As mentioned in Section 4.3.2, to investigate the influence of the shared line, dynamic analyses have been performed for the dual-spar configuration with different shared line diameters presented in Table 5. Two loading directions, 0 deg and 90 deg are considered. The results are discussed in the following sections.

Influence on linearized mooring stiffness

The mean dynamic positions of FOWTs are averaged over all realizations and plotted in Fig. 14 with respect to dual-spar configurations with different shared line diameters. The static equilibrium positions of body origins of FOWTs are marked in the plot as well. Because the total length of the shared line remains fixed, the self weight of the shared line is proportional to the diameter. The shared line is heavier with a larger diameter, and the two FOWTs are drawn closer to each other under the static equilibrium. As shown in Fig. 14, the variation trend of the mean position of the two FOWTs with regard to the shared line diameter remains the same in both dynamic and static conditions.

The mooring stiffness is linearized for the dual-spar configurations with different shared line diameters. The linearization procedures described in Section 5.1.1 have been applied. The linearized mooring stiffness terms in the loading direction, C_{M11} and C_{M77}, are plotted in Fig. 15 with respect to different shared line diameters.

For the 0-deg loading direction, the shared line is heavier with a larger diameter and two FOWTs are closer to each other in the x_g direction under the static equilibrium, shown in Fig. 14. The mooring tension at the fairleads is affected in both single lines and the shared line. As a result, the increase of the shared line diameter leads to a decrease in the mooring stiffness linearized about the static positions. The variation of the linearized mooring stiffness, "$C_{M11/77}$, 0 deg, static", is around 28%. Due to the mean aerodynamic load acting on FOWTs in the dynamic condition, both Spar 1 and Spar 2 are driven along the x_g direction as

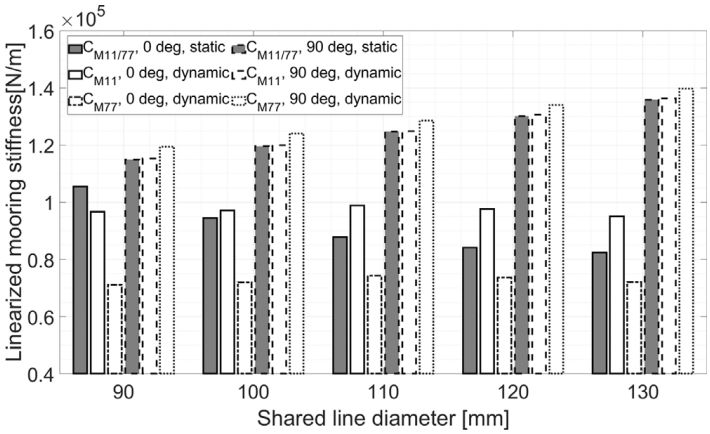

Fig. 15. Linearized mooring stiffness for dual-spar FOWFs with different shared line diameters.

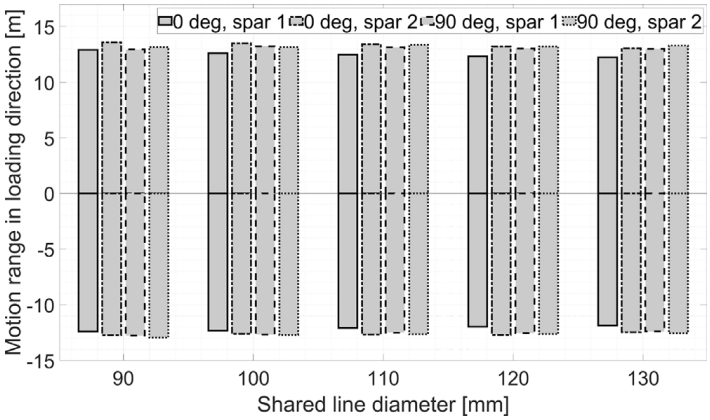

Fig. 16. Mean platform motion range of FOWTs in the loading direction due to variation of the shared line diameter.

shown in Fig. 14. Two single lines connected to Spar 1 are stretched more and two single lines connected to Spar 2 are stretched less. Therefore, the linearized mooring stiffness of Spar 1 is larger than that of Spar 2 in the dynamic condition. For the 0-deg loading direction, the influence of the shared line diameter is less significant on the linearized mooring stiffness in the dynamic case compared to that in the static case. The variation of the linearized mooring stiffness, "C_{M11}, 0 deg, dynamic" and "C_{M77}, 0 deg, dynamic" due to the variation of the shared line diameter is less than 5%.

For the 90-deg loading direction, the mooring tension in the shared line is nearly perpendicular to the loading direction in both static and dynamic cases. The major influence on the variation of the linearized mooring stiffness is dominated by the single lines connected to the FOWTs. As shown in Fig. 14, a shared line with a larger diameter drives two FOWTs closer towards each other and tightens the single lines more. Therefore, the linearized mooring stiffness rises with increasing shared line diameter for both FOWTs. From Fig. 15, the variation of the linearized mooring stiffness in the 90-deg loading direction is around 18%.

Influence on platform motion in the horizontal plane

The horizontal platform motion range in the loading direction is averaged over realizations and plotted in Fig. 16 with respect to the shared line diameter. The largest variation of the horizontal platform motion range is 5.5% in Fig. 16, which is relatively small considering the variation of the shared line diameter. The finding is in agreement with the observations for the linearized mooring stiffness presented in Fig. 15.

Influence on structural response

Statistics of mooring tension are plotted in Fig. 17 for the dual-spar configurations with different shared line diameters. From Figs. 17(a) and 17(b), it is observed that the influence of the shared line diameter on the pretension of the mooring lines is significant. The variation of pretension is approximately 23% for the single lines and 30% for the shared line. For the shared line, the pretension increases along with the shared line diameter due to the self weight of the shared line. For the single lines, the variation of the pretension is caused by the static equilibrium positions of FOWTs. The single lines are stretched more when two FOWTs are closer to each other with a heavier shared line, as shown in Fig. 14. For different loading directions, the windward single lines are more loaded than the leeward single lines, as shown in Figs. 17(c) and 17(d). Due to the relative motions of the FOWTs, significant variations of mooring tension are found in the shared line, which should be considered in the design of the shared line. For both loading directions, the mean mooring tension is higher in all mooring lines with a larger shared line diameter. This is expected because a

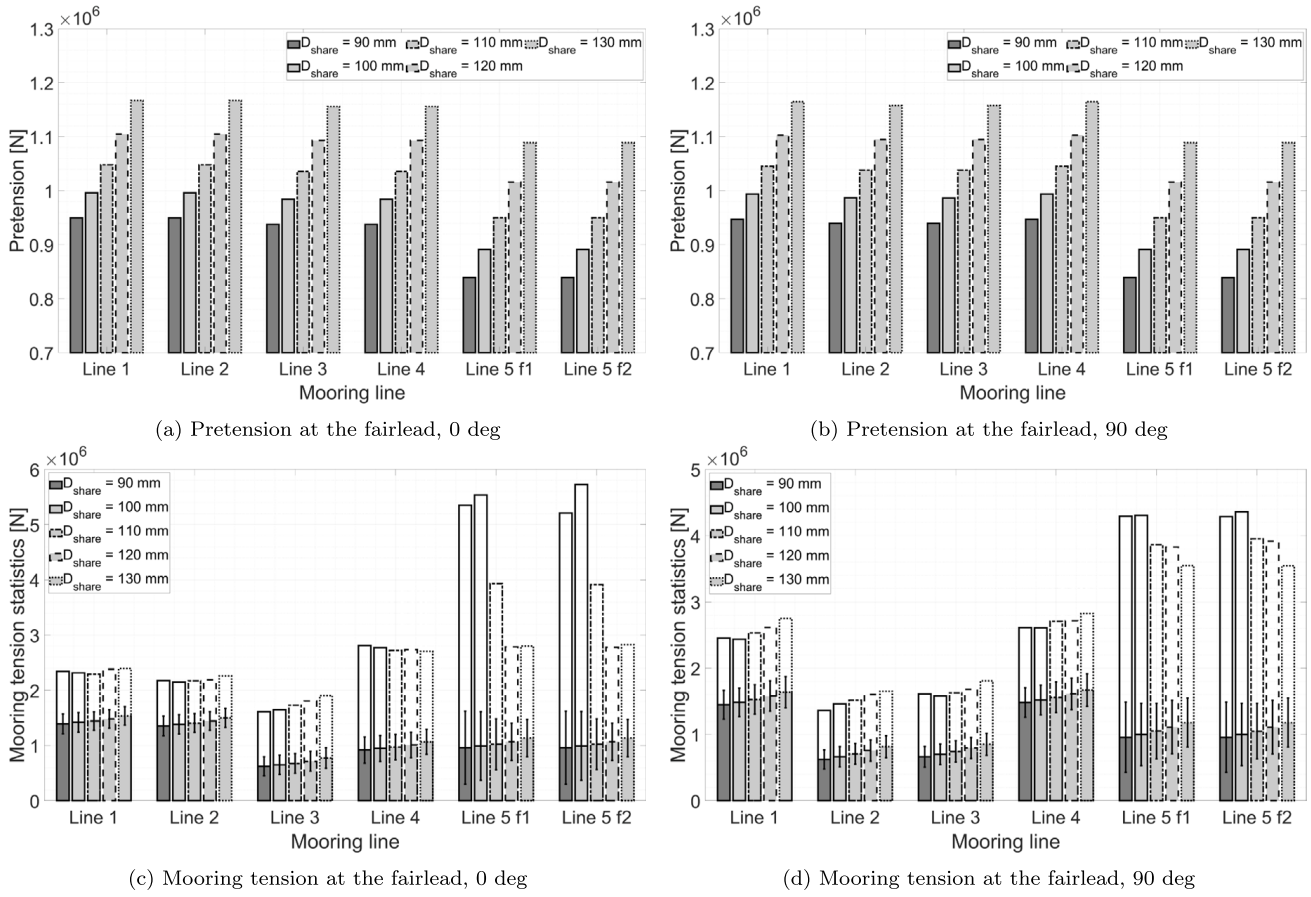

(a) Pretension at the fairlead, 0 deg

(b) Pretension at the fairlead, 90 deg

(c) Mooring tension at the fairlead, 0 deg

(d) Mooring tension at the fairlead, 90 deg

Fig. 17. Statistics of mooring tension due to variation of the shared line diameter (gray bar: mean value averaged over realizations, white bar: maximum value averaged over realizations, error bar: SD averaged over realizations).

heavier shared line results in higher mean tension in the shared line, and the fairleads of single lines are farther from the anchors, which increases the mean tension in the single lines as well. For the two loading directions, though the pretension in the shared line increases with the increasing shared line diameter, the maximum mooring tension in the shared line decreases. All the maximum tension in Figs. 17(c) and 17(d) is below the MBS presented in Table 5. The analysis of snap load events described in Section 5.1.3 has been performed in this sensitivity study as well. With the increasing shared line diameter, the averaged number of snap events observed at the fairlead Spar 1, Line 5 f1 decreases from 209.35 to 3.20 for the 0-deg loading direction and decreases from 86.05 to 5.50 for the 90-deg loading direction, which shows a similar variation trend as the maximum mooring tension presented in Figs. 17(c) and 17(d).

Statistics of the mooring angles and sagging depth are plotted in Fig. 18 for the dual-spar FOWF with different shared line diameters. From Figs. 18(a) and 18(b), it is observed that the mean mooring angles of all single lines increase along with the shared line diameters. The mooring properties of single lines are not changed in the sensitivity study. With an increasing shared line diameter, the FOWTs move towards each other and the fairleads move away from the anchors. Therefore, the mean mooring angles increase accordingly. The line shape of a shared line in the static condition has been studied in [9] for different materials and diameters. It is found that the mooring angle of the shared line decreases with increasing diameter. This is observed in the dynamic condition as well, shown in Figs. 18(a) and 18(b) for the mean and the maximum mooring angles. From Fig. 18(c), in the static condition, the sagging depth of the shared line increases with the increasing shared line diameter, as discussed in [9]. In the dynamic condition, the maximum sagging depth and the mean sagging depth increase with the increasing shared line diameter while the SD of the sagging depth decreases. Therefore, if the sagging depth of the shared line may potentially affect the vessels passing through the FOWF, heavier shared lines with larger diameters should be considered.

Statistics of the TBBM due to the variation of the shared line diameter are investigated as well. It is found that the TBBMs of FOWTs are not sensitive to the shared line diameter, which makes the TBBMs less important in the design of the shared line. For the shared line diameters and loading directions investigated, the variations of all TBBMs are less than 4%.

6. Conclusion

This paper presents a dynamic analysis of a dual-spar floating offshore wind farm (FOWF) with a shared mooring system in extreme environmental conditions. To investigate the influence of the shared mooring on the system behavior, a baseline FOWF is

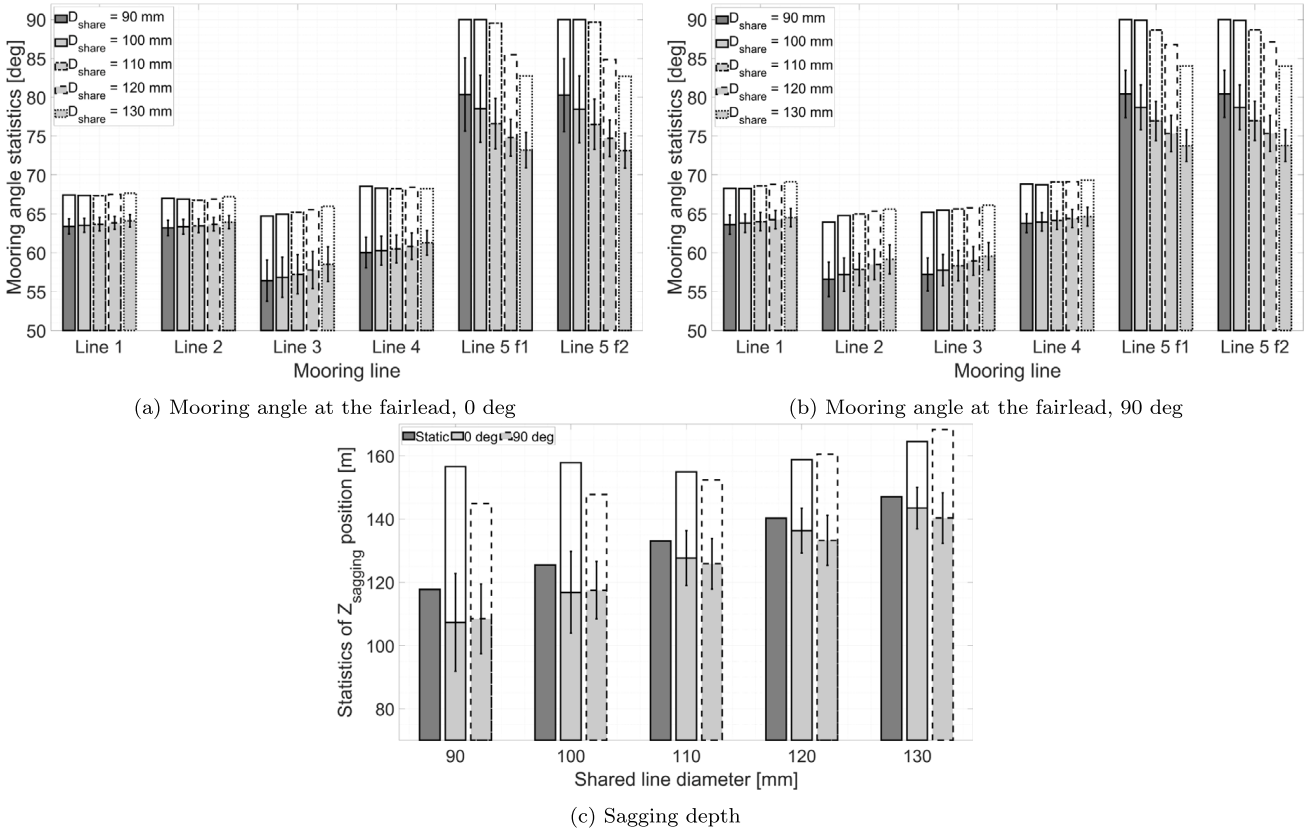

(a) Mooring angle at the fairlead, 0 deg

(b) Mooring angle at the fairlead, 90 deg

(c) Sagging depth

Fig. 18. Statistics of mooring angles and sagging depth due to variation of the shared line diameter (gray bar: mean value averaged over realizations, white bar: maximum value averaged over realizations, error bar: SD averaged over realizations).

numerically modeled followed by a detailed case study. Metocean conditions with a 50-year return period are considered and the platform motion and structural responses of the baseline FOWF are compared to those of a single floating offshore wind turbine (FOWT). Then, a sensitivity study is performed to assess the influence of different loading directions and shared line diameters. The main conclusions of this paper are as follows:

- Compared to the single FOWT, larger horizontal platform motions of FOWTs and higher mooring tension in single lines are found for the dual-spar FOWF. Although the tension level is below the minimum breaking strength in the simulations, large tension variations and snap events are experienced by the shared line. The design should address snap load events considering the consequences of snap loads including line breakage and loss of a turbine.
- It is seen that the loading direction has a significant influence on the platform motions of the FOWTs. The present mooring system layout with one shared line contributes to the variation of station-keeping performance in different directions. The directional dependence of other FOWF layouts, such as four FOWTs arranged in a square, may exhibit different trends. For different loading directions, the windward single lines are more loaded than the leeward single lines. The sagging depth of the shared line experiences large variations up to 16% of the mean sagging depth in dynamic simulations with different loading directions. For shared mooring applications with small static sagging depth, the potential effects on the passing vessels should be taken into account in the design of the shared mooring system.
- From the sensitivity study, it is found that the horizontal platform motions and the tower-base bending moments are not sensitive to the shared line diameter. The influence of the shared line diameter is observed on the mooring responses. In the sensitivity study, the variation of the pretension is approximately 23% for the single lines and 30% for the shared line. It is also demonstrated that the shared line diameter has a strong effect on the likelihood of snap loads because the number of snap events drops dramatically as the shared line diameter increases.

7. Limitations and future work

This paper is limited to a dual-spar FOWF. In future, it would be interesting to investigate the dynamics of FOWFs with additional wind turbines and alternative shared mooring system configurations. It is also of interest to study the dynamic behaviors of the baseline FOWF under operational loading conditions, and further, to explore the influence of the shared mooring configuration on the structural fatigue life. As the natural periods of the FOWF with a shared mooring system are quite different from those of the original OC3 Hywind spar FOWT [27], the controllers used in operational conditions need to be tuned properly so that

the control algorithm can provide enhanced damping control at multiple resonant frequencies experienced by the FOWF with the shared mooring [28–31]. In addition, if the FOWTs are too close to each other during operation, the aerodynamic interactions must be addressed in numerical simulations. For the design check of the fatigue limit state, different load cases need to be considered together with their probabilities of occurrence [32,33].

As shared lines connect adjacent FOWTs and integrate the FOWF as one floating system, it is of interest to study the failure of the shared mooring system. Risk assessments and consequence analysis of different mooring failure scenarios, especially in the case of a cascade failure, should be addressed in future work.

Declaration of competing interest

The authors declare that they have no known competing financial interests or personal relationships that could have appeared to influence the work reported in this paper.

Data availability

Data will be made available on request.

Acknowledgments

The authors acknowledge the financial support from the Norwegian Ministry of Education and Research granted through the Department of Engineering Sciences, University of Agder.

References

[1] Yamamoto S, Colburn Jr WE. Power generation assemblies. 2005, International Patent, Publication Number W0 2005/040604 A2.
[2] Hill JS. Hywind Scotland, world's first floating wind farm, performing better than expected, Vol. 16. Sustainable Enterprises Media, Inc; 2018.
[3] Goldschmidt M, Muskulus M. Coupled mooring systems for floating wind farms. Energy Procedia 2015;80:255–62.
[4] Hall M, Connolly P. Coupled dynamics modelling of a floating wind farm with shared mooring lines. In: ASME 2018 37th international conference on ocean, offshore and arctic engineering, Madrid, Spain. American Society of Mechanical Engineers Digital Collection; 2018.
[5] Connolly P, Hall M. Comparison of pilot-scale floating offshore wind farms with shared moorings. Ocean Eng 2019;171:172–80.
[6] Hall M. MoorDyn V2: New capabilities in mooring system components and load cases. Technical report, Golden, CO (United States): National Renewable Energy Lab. (NREL); 2020.
[7] Wilson S, Hall M, Housner S, Sirnivas S. Linearized modeling and optimization of shared mooring systems. Ocean Eng 2021;241:110009.
[8] Munir H, Lee CF, Ong MC. Global analysis of floating offshore wind turbines with shared mooring system. In: IOP conference series: materials science and engineering, Vol. 1201. IOP Publishing; 2021, 012024.
[9] Liang G, Merz K, Jiang Z. Modeling of a shared mooring system for a dual-spar configuration. In: International conference on offshore mechanics and arctic engineering, volume 9: Ocean renewable energy. American Society of Mechanical Engineers; 2020.
[10] Liang G, Jiang Z, Merz K. Mooring analysis of a dual-spar floating wind farm with a shared line. J Offshore Mech Arct Eng 2021;143(6):062003.
[11] Jonkman J, Butterfield S, Musial W, Scott G. Definition of a 5-MW reference wind turbine for offshore system development. Technical report NREL/TP-500-38060, Golden, CO (United States): National Renewable Energy Lab. (NREL); 2009.
[12] Jonkman J. Definition of the floating system for phase IV of OC3. Technical report NREL/TP-500-47535, Golden, CO (United States): National Renewable Energy Lab. (NREL); 2010.
[13] DNV GL. Offshore standard DNVGL-OS-E301, position mooring. Høvik, Norway; 2015.
[14] SINTEF Ocean. SIMO 4.16.0 user guide. Trondheim, Norway; 2019.
[15] SINTEF Ocean. RIFLEX 4.16.0 user guide. Trondheim, Norway; 2019.
[16] DNV GL. SESAM user manual, wave analysis by diffraction and Morison theory. Høvik, Norway; 2019.
[17] Liang G, Jiang Z, Merz K. Influence of aerodynamic loads on a dual-spar floating offshore wind farm with a shared line in parked conditions. In: International conference on offshore mechanics and arctic engineering, Vol. 85932. American Society of Mechanical Engineers; 2022, V008T09A023.
[18] DNV. Recommended practice DNV-RP-C205, environmental conditions and environmental loads. Høvik, Norway; 2010.
[19] DNV. Standard DNV-ST-0119, floating wind turbine structures. Høvik, Norway; 2018.
[20] Li L, Gao Z, Moan T. Joint distribution of environmental condition at five European offshore sites for design of combined wind and wave energy devices. J Offshore Mech Arct Eng 2015;137(3).
[21] IEC. International standard IEC 61400-1, wind turbines—Part 1: Design requirements. Geneva, Switzerland; 2005.
[22] IEC. International standard IEC 61400-3, wind turbines—Part 3: Design requirements for offshore wind turbines. Geneva, Switzerland; 2009.
[23] Jonkman BJ, Buhl Jr ML. TurbSim user's guide. Technical report, Golden, CO (United States): National Renewable Energy Lab. (NREL); 2006.
[24] Ikhennicheu M, Lynch M, Doole S, Borisade, et al. Review of the state of the art of mooring and anchoring designs, technical challenges and identification of relevant DLCs. 2021.
[25] Stevens RJ, Gayme DF, Meneveau C. Effects of turbine spacing on the power output of extended wind-farms. Wind Energy 2016;19(2):359–70.
[26] Hsu W-t, Thiagarajan KP, Manuel L. Extreme mooring tensions due to snap loads on a floating offshore wind turbine system. Mar Struct 2017;55:182–99.
[27] Jonkman J, Larsen T, Hansen A, Nygaard T, Maus K, Karimirad M, Gao Z, Moan T, Fylling I. Offshore code comparison collaboration within IEA wind task 23: Phase IV results regarding floating wind turbine modeling. Technical report, Golden, CO (United States): National Renewable Energy Lab. (NREL); 2010.
[28] Larsen TJ, Hanson TD. A method to avoid negative damped low frequent tower vibrations for a floating, pitch controlled wind turbine. In: Journal of physics: conference series, Vol. 75. IOP Publishing; 2007, 012073.
[29] Nielsen FG, Skaare B, Tande JOG, Norheim I, Uhlen K. Method for damping tower vibrations in a wind turbine installation. 2012, US Patent 8, 186, 949.
[30] Skaare B, Nielsen FG, Hanson TD, Yttervik R, Havmøller O, Rekdal A. Analysis of measurements and simulations from the hywind demo floating wind turbine. Wind Energy 2015;18(6):1105–22.
[31] Merz K. Basic controller tuning for large offshore wind turbines. Wind Energy Sci 2016;1(2):153–75.
[32] DNV. Recommended practice DNV-RP-0286, coupled analysis of floating wind turbines. Høvik, Oslo, Norway; 2019.
[33] ABS. Guidance notes on global performance analysis for Floating Offshore wind turbines installations. Houston (TX), USA; 2020.

A.7 Paper 7

Paper 7:
Experimental Comparison of a Dual-Spar Floating Wind Farm with Shared Mooring against a Single Floating Wind Turbine under Wave Conditions
Authors: Tomas Lopez-Olocco, Guodong Liang, Antonio Medina-Manuel, Leandro Antonio Saavedra-Ynocente, Zhiyu Jiang, Antonio Souto-Iglesias
Published in *Engineering Structures, 292, 116475, 2023.*

Experimental comparison of a dual-spar floating wind farm with shared mooring against a single floating wind turbine under wave conditions

Tomas Lopez-Olocco[a,b], Guodong Liang[c], Antonio Medina-Manuel[a,b], Leandro Saavedra Ynocente[d], Zhiyu Jiang[c,*], Antonio Souto-Iglesias[a,b]

[a] *Universidad Politécnica de Madrid, Av. de la Memoria 4, Madrid, 28040, Spain*
[b] *CEHINAV, DACSON, ETSIN, Av. de la Memoria 4, Madrid, 28040, Spain*
[c] *Department of Engineering Sciences, University of Agder, N-4898 Grimstad, Norway*
[d] *Laboratorio de Dinámica del Buque, Canal de Ensayos Hidrodinámicos el Pardo (INTA-CEHIPAR), Madrid, 28040, Spain*

Abstract

Shared mooring can potentially be a cost-reduction driver for future floating wind farms. To assess the effect of shared mooring on the response dynamics of floating wind turbines (FWTs), experiments have been conducted for two spar FWTs with a shared mooring configuration and for a single spar FWT with catenary mooring, both at a scale of 1:47. Various regular and irregular wave conditions were tested and only one wave heading was considered. From the test results, the response amplitude operators and response spectra of platform motions and statistics of mooring tensions are compared for the two configurations. In the extreme wave condition, the shared mooring configuration leads to a 40% increase in the platform surge motion compared with the single spar FWT. Still, the absolute offset is within allowable limits prescribed by power cables. The fairlead tensions of the anchor lines are not significantly increased in the shared mooring configurations, but the shared line shows extreme tension peak events that are seldom present in the anchor lines. This study demonstrates the technological promises and challenges of a shared mooring system from an experimental perspective. Results and videos are made available and can be used to validate numerical models.

Keywords: Offshore wind farm, spar floating wind turbine, hydrodynamic model tests, shared mooring, measurement, dynamic response

*Corresponding author
Email address: zhiyu.jiang@uia.no (Zhiyu Jiang)

1. Introduction

With an installed capacity of 12 gigawatt (GW) in 2020 and a target of 60 GW of installed capacity by 2030, the European Union aims to position herself as a leader in clean technologies [1]. To reach this objective in the next years, using conventional bottom-fixed substructures in depths below 50 m may not be sufficient. For offshore sites with deep water and convenient wind conditions, bottom-fixed platforms are unfeasible from an economic point of view. Therefore, floating offshore wind installations have the potential to expand in the near future, making them a pillar of Europe's research and development agenda [2].

Among different floating wind turbine (FWT) concepts [3], the spar FWT is one of the most technically mature and widely studied, as shown by the Hywind Demo project [4]. A spar buoy usually has a deep draft and is ballast-stabilized. To understand physical behavior and to demonstrate technical feasibility, important experimental works of spar FWTs have been carried out in the past [5, 6, 7]. The performance of spar FWT has been compared against that of other floating concepts, e.g., semi-submersible and the tension leg platform FWTs [8, 9, 10]. Generally, in wave-only conditions, the spar FWT showed smaller surge response and larger pitch responses compared to the other FWT concepts. The past experimental research on spar FWTs is interesting, but limited to a single spar FWT with catenary mooring at a certain water depth, to the authors' knowledge. There is lack of experimental work considering deepwater sites and alternative mooring configurations, especially on a farm scale.

The demand of the evolution of floating offshore wind technology implies the development of innovative floating platform substructures with reliable and cost-efficient mooring solutions. The total cost for the substructure and foundation (including moorings), assembly and installation of a floating offshore wind project was estimated to be approximately 35% [11]. As the offshore wind industry has shown growing interest in locations like the Mediterranean sea [12] where deep-water floating solutions are preferable, efforts to reduce these costs are needed in current and future offshore projects. For the mooring and anchoring system of a floating wind farm (FWF), novel solutions like shared anchor or shared mooring configurations can be considered to achieve cost reductions in material consumption and installation. Shared anchors can reduce the mooring costs for floating wind farms by reducing the number of of anchors and hence the installation costs; see [13, 14, 15]. This solution has been adopted by the Hywind Tampen FWF [16]. Shared mooring decreases the capital expenditure by reducing the total length of the mooring lines and the number of anchors [17, 18], but the principles of shared mooring are yet to be further understood prior to any practical implementations.

Shared mooring systems for spar platforms have been studied in recent years in several numerical works. The elastic catenary theory for hanging cables was used to model the shared line of a dual-spar FWF [19]. In a subsequent study, Liang et al. [20] investigated the natural periods of a dual-spar FWF with a shared mooring system. The anchor lines were designed based on analysis of a single FWT. Different mooring properties were studied and a sensitivity study was performed to evaluate their contributions. The shared line showed a primary influence on the surge and sway natural periods. Also, based on the mooring design of a single FWT, Wang et al. [21] proposed an array of 9 wind turbines on spars buoys in a 3-by-3 square with only eight anchors and twelve shared lines. The numerical study was intended to provide a rough estimation of cost saving in terms of number of anchors and length of mooring lines. The investigation showed larger tensions in the shared FWF than in the single FWTs for all the load cases. Wilson et al. [22] studied the optimization of shared mooring systems using a linearized model for the force-displacement relationship of floating platforms. The study showed that the more complicated the shared layout

is, the greater the restoring demand for the shared lines. Similar works on FWFs can be found for floating platform concepts other than spars. For example, semi-submersibles FWF with shared mooring have been studied by Goldschmidt and Muskulus [23], Hall and Connolly [24], Connolly and Hall [25], Lozon and Hall [26]. Overall, FWFs with shared mooring can achieve great cost reduction potentials compared with FWFs that consist of single, but larger platform motions and mooring tensions can be the trade-off.

Considering the above literature review, we observe a lack of experimental literature on the hydrodynamics of FWFs with shared mooring systems, a key aspect in validation and calibration of numerical models. To partially fill in this research gap, an experimental investigation on a dual-spar FWF with a shared mooring system is presented herein. For comparison purposes, model tests have been also conducted for a single spar FWT with a catenary mooring system. Since the focus is set on the wave-induced hydrodynamics, wind loads have not been considered.

The findings of this experimental work aim to investigate and understand the complex multi-body dynamics involved in shared mooring FWFs and, hopefully, foster the development of shared-mooring concepts, with the subsequent impact on cost reduction of FWFs. To make the effort more useful to the research community, the data discussed in the paper and videos of the experiments are made available in Section 7.

This paper is organized as follows. In Section 2, the case studies, the mooring system design, and the environmental conditions are presented. In Section 3, the experimental setup is described and the test matrix proposed. In Section 4, the wave calibration method and post-processing

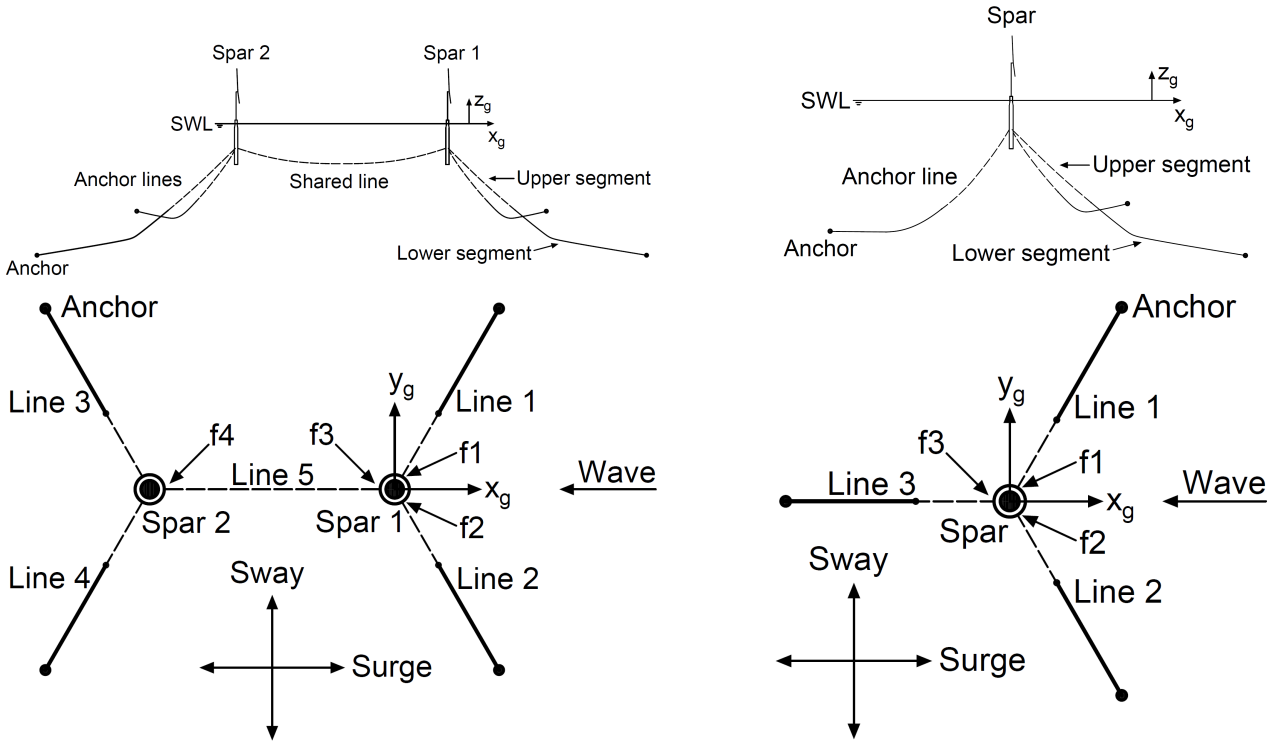

(a) Dual-spar FWF

(b) Single spar FWT

Figure 1: Top and side view of the two configurations with different mooring systems (dashed line: wire; solid line: chain). The symbols $f1$, $f2$, $f3$, $f4$ denote the fairlead connections.

Table 1: Environmental parameters for mooring system design.

Environmental variable	Operational	Extreme
U_w (hub-height) $[m/s]$	11.40	42.71
H_s $[m]$	2.57	15.50
T_p $[s]$	11.12	14.45

techniques that are conducted during the analysis are explained. In Section 5, the experimental results are presented and discussed. Finally, conclusions and future lines of work are enumerated.

2. Case studies

2.1. Description of the FWT and the FWF

The 5-megawatt spar FWT, OC3-Hywind [27, 28], is selected in the present experimental campaign. Two different mooring configurations have been tested. As illustrated in Fig. 1, a shared mooring system is applied to the dual-spar FWF and a conventional catenary mooring system is applied to the single spar FWT. For the dual-spar FWF, two FWTs are placed along the defined surge direction. The initial turbine spacing is 750 m, which is approximately six times the rotor diameter. The static drafts of all FWTs are 120 m and all the fairleads are 70 m below the still water level, the same as specified in [27]. Each FWT is moored to the seabed by two single lines through anchors (anchor lines). One shared line connects the two FWTs. The single spar FWT is connected to the seabed by three anchor lines. For both configurations, the projected angle between any neighboring mooring lines is 120 deg.

The studied water depth (235 m) of this FWT was selected considering the typical range of 200-300 m among commercial projects, e.g., Hywind Tampen [16]. Because this depth is different from the one specified in [27], a more realistic mooring design is desired. A proper redesign has been carried out with details presented in Section 2.3.

2.2. Environmental conditions

Metocean conditions of the "Norway 5" offshore site [29] are considered for the mooring design and for defining the test matrix of the experimental campaign. The joint probability distribution of the mean wind speed (U_w), the significant wave height (H_s) and the spectral peak period (T_p) is used to calculate the conditional distributions from which the mean values of H_s and T_p are taken for the operational condition. For the extreme condition, the 50-year environmental contour is generated based on the joint distribution. The sea state with the highest H_s on the contour line is selected. The environmental conditions are summarized in Table 1. The wind speed is included for the sake of completeness, but wind loads were not considered in the tests.

2.3. Mooring system design

The anchor lines of the spar FWT are redesigned for the selected water depth. We follow a design process similar to the one presented in Liang et al. [20]. A two-segment mooring design is considered for the anchor lines in which the upper segment is made of sheathed steel wire rope, and the lower segment is made of a R3 studless mooring chain. The delta connection [4] is not considered for simplicity. Four design parameters are considered, including the total mooring line length, the

Table 2: Design variables and design space of the anchor lines

Design variable	Sampling range	Sampling interval
Total mooring line length L_{line} $[m]$	[660, 680]	5
Wire segment length L_{wire} $[m]$	[250, 350]	10
Wire segment diameter D_{wire} $[mm]$	[90, 130]	5
Chain segment length D_{chain} $[mm]$	[110, 150]	5

Table 3: Properties of the mooring lines

Mooring property	Anchor line		shared line
	Lower segment	Upper segment	
Material	R3 studless chain	Sheathed steel wire rope	Sheathed steel wire rope
Length $[m]$	415	250	739.6
Diameter $[mm]$	140	95	95
Sheath thickness $[mm]$	-	10	10
Mass density $[kg/m]$	392.00	47.39	47.39
Submerged weight $[N/m]$	3535.94	360.42	360.42
Extensional stiffness $[N]$	1.53E+09	8.47E+08	8.47E+08
Minimum breaking strength $[N]$	1.43E+07	9.34E+06	9.34E+06

length of the wire segment and the diameters of the wire segment and the chain segment. The design space of variables is presented in Table 2, and the orthogonal sampling method is applied. The design objective is to minimize the material costs in production and manufacturing of mooring lines. First, static analyses are performed in MIMOSA [30], a program for moored vessel analysis. Then, dynamic analyses are performed in SIMA [31, 32], a numerical simulation tool for marine operations and floating systems. Details of the objective function, design constraints, analysis procedures and design check can be found in Liang et al. [20]. The sample from the design space which fulfils the design constraints with the lowest mooring cost is selected as the final design for the anchor lines of the spar FWT.

As shown in Fig. 1, the selected mooring properties are applied to the three mooring lines of the single spar FWT and to the four anchor lines of the dual-spar FWF. For the shared line of the dual spar FWF, steel wire rope is chosen as the material because it is lighter than chain. There is no design recommendation for the shared line design [33, 34], so the same wire properties of the anchor lines are used for the shared line. Also, the length of the shared line was determined such that the distance between the platforms is equal to the target turbine spacing of approximately six times the rotor diameter in the static condition. When the floating system reaches the static equilibrium, the two FWTs are driven towards each other for a short distance due to the self weight of the shared line, leading to differences in the static pretensions between the single-spar and dual-spar configurations. The material properties of the mooring lines are summarized in Table 3.

Table 4: Target and measured mass properties at model scale.

Mass property	Target value	Measured value	Units	Error
Mass	77.403	77.721	kg	0.41 %
Height of COG above keel	0.894	0.891	m	0.67 %
Radius of inertia about x-axis*	1.03	1.04	m	2.94 %
Radius of inertia about y-axis*	1.03	1.04	m	2.95 %
Radius of inertia about z-axis*	0.10	0.94	m	2.02 %

* Measured with reference to center of gravity (COG).

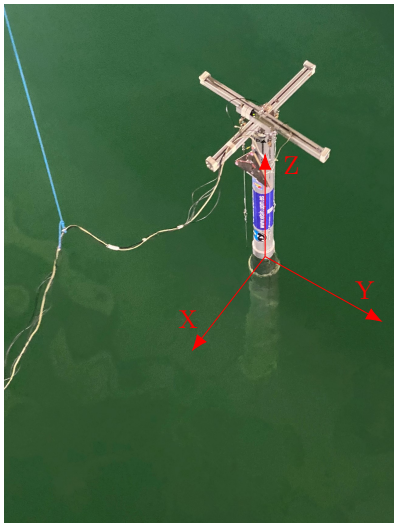

Figure 2: Top view of the model with the aluminum structure, including the instrumentation cables.

3. Experimental setup

The experimental campaign was conducted in the ocean basin at the *Canal de Ensayos Hidrodinámicos de el Pardo* (INTA-CEHIPAR). The dimensions of the tank are 150 m in length, 30 m in width and 5 m in depth. The tank is equipped with a towing carriage, in which the data acquisition systems reside.

As described in Section 2, the water depth of the site is 235 m. Therefore, considering the water depth of the tank, a scale ratio λ of 47 is selected.

3.1. Single FWT

When testing floating platforms in waves, gravity and inertia forces are predominant [35]. Therefore, the Froude scaling similarity laws were applied in these tests. The target model scale properties are listed in Table 4. The model was constructed with PVC plastic, and solid lead was used for the ballast. To avoid water leakage during the experiments, several seals were applied and checked before placing the model into the testing position. In addition, during the entire experimental campaign, the models were constantly inspected for water intake to avoid changes in displacement and trim angle. A detailed description of the model design is included in Appendix A.

The construction of the model resulted in errors below 5%. A comparison with the target values can be found in Table 4. The model mass was set to obtain the exact scaled draft. Errors in lengths are normalized with respect to $\nabla^{1/3}$, with ∇ being the target displacement volume.

Because the mooring lines were too lightweight, the submersible load cells could affect the mooring angle due to their elevated weight. Therefore, the lines are sent to the aluminium structure showed in Fig. 2 above the water surface, where they were connected to the measurement devices. Pulleys were installed at the fairlead positions for that purpose. A submerged view of the fairlead connection and the pulleys used is found in Fig. 3a. This modification forces us to consider the full pretensions instead of just the vertical component in the design process to adjust the mass properties of the model.

Special care was taken to reproduce the properties when scaling the mooring lines. The exact length was ensured and the weight per unit length of the available mooring material was chosen to be close to the ones at full scale (see Table 3). The connection parts were selected to take this into account and increase the equivalent weight per unit length when needed. The resulting model

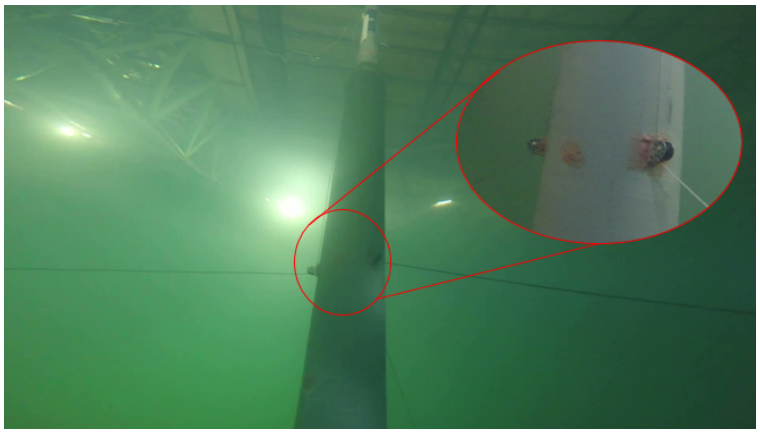

(a) Fairlead connection.

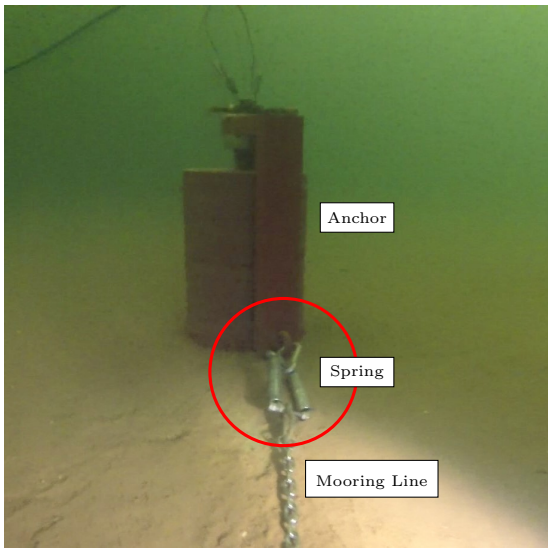

(b) Connection between the mooring line and the anchor.

Figure 3: Mooring line connections.

Table 5: Physical properties of the mooring lines

	Component	$L\ [m]$	$w\ [Kg/m]$	$K\ [N/m]$
Anchor line	Chain	8.83	0.160	800
	Steel wire	5.32	0.020	
Shared line	Steel wire	15.736	0.020	520

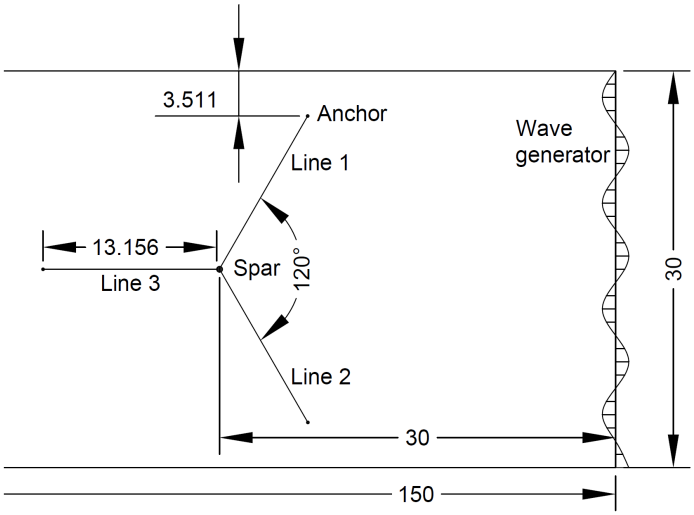

Figure 4: Experimental layout of the single spar FWT. Dimensions at model scale [m]

Table 6: Target and measured pretensions for both configurations.

	Pretension	T_{f1}	T_{f2}	T_{f3}	T_{f4}	Units
Single spar FWT	Target	6.91	6.91	6.91	(-)	N
	Measured	6.24	6.39	5.99	(-)	N
Dual-spar FWF	Target	7.62	7.62	6.34	6.34	N
	Measured	7.97	8.04	6.78	6.67	N

scale line properties are listed in Table 5.

The number of snap events may be overpredicted if the mooring stiffness is not adequately scaled [36]. In order to have line tensions which approximately scale as the other forces involved in the system, a set of springs was placed at the anchor aiming at properly modeling the line stiffness. This connection is encircled in red in Fig. 3b.

To select the spring, an equivalent linear stiffness of the full-scale mooring line is computed. Since the stiffness of the line should scale with λ^3 when the Froude scaling laws are applied, the linear spring stiffness, K, was selected according to Eq. (1)

$$K = \frac{EA}{L}, \tag{1}$$

where EA is the axial stiffness of the line and L is the unstretched length of the line at model scale. Results are shown in Table 5.

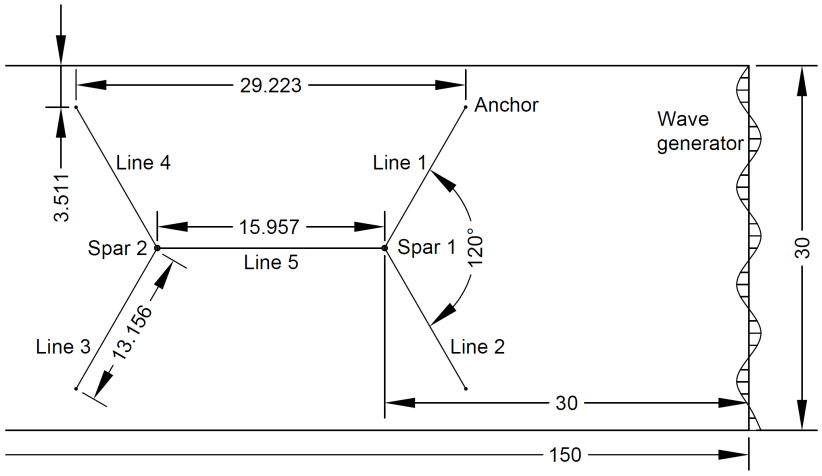

Figure 5: Experimental layout of the dual-spar FWF. Dimensions at model scale [m]

For the single spar FWT with catenary mooring, the model is placed 30 m away from the wave generator; see Fig. 4. In this test setup, the anchors were placed at the exact scaled positions. Also, a diver ensured the correct laying of the line at the bottom preventing the chain from crooking due to the manipulation of the chain during the installation, and conducted minor adjustments to set the pretensions prior to the tests. Table 6 shows a comparison between the measured and the target pretensions at the fairlead. Due to lack of available time in the tank, additional static tests to estimate the stiffness in the various degrees of freedom were not carried out. They are left for future work.

3.2. Dual-spar FWF

In the dual-spar FWF, two FWTs with the same physical properties described in Section 3.1 are used. To scale down the mooring lines and their properties for this configuration, the same procedure described in Section 3.1 is followed. The layout of the mooring system of this configuration is detailed in Fig. 5.

The downscaled mooring properties and a comparison between the target and measured pretensions are listed in Tables 5 and 6. To check the installation accuracy, the distance between models was measured several times at the position of static equilibrium with a mean value of 16.054 m.

3.3. Test matrix

In total, 28 tests were carried out in this study, consisting of six decay tests, two irregular wave cases, one white noise case, and five regular wave cases for each configuration. For the wave cases, the amplitudes and periods described in Section 2.2 were scaled down according to the Froude scaling laws.

Due to the mechanical limitations of the wave generator with the selected scale ratio, the environmental conditions for irregular wave cases described in Section 2.2 were modified and listed in Table 7a, where the white noise case is also listed. The set of regular wave cases, listed in Table 7b covers both operational and extreme conditions.

3.4. Instrumentation

All measuring instruments were calibrated prior to testing to ensure quality and reliability of the data acquisition system. Measurements were recorded with a sampling rate of 100 Hz, which

Table 7: Summary of test cases with irregular and regular waves.

(a) Irregular wave

	H_s $[m]$	T_p $[s]$
Operational (IRR01)	2.57	11.12
Extreme (IRR02)	12.70	15.45
White noise (WN)	2.00	5-20

(b) Regular wave

	H $[m]$	T $[s]$
REG01	2.5	5.48
REG02	2.5	9.60
REG03	2.5	10.97
REG04	5.0	8.0
REG05	10.0	16.0

(a) Spar 1 with all the instrumentation. (b) Spar 2 with all the instrumentation.

Figure 6: The two spar models in testing position with the instrumentation circled in red.

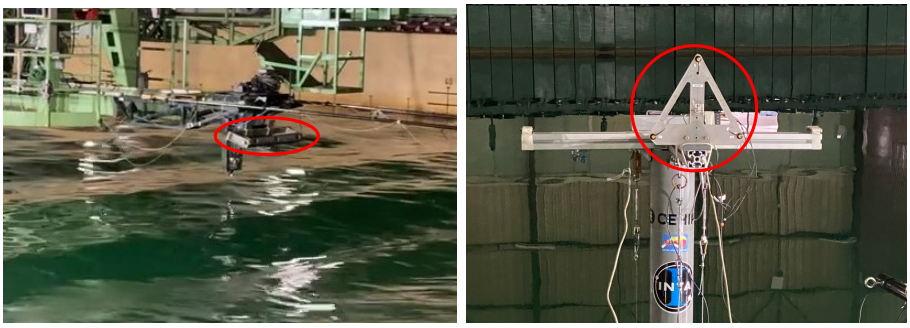

(a) Optical tracking camera. (b) Lead frame.

Figure 7: Detailed view of the instruments used for motion measurement during the tests.

was sufficient considering typical frequencies of the phenomena involved (maximum 1.2 Hz). Fig. 6 shows the sensor positions during the experiments of the dual-spar FWF. The instrumentation

setup for the single FWT is identical to Spar 1 of the FWF.

In this work, the 6 degrees of freedom (DOF) rigid body motions of the model placed 30 m from the wave generator were measured using an optical tracking system, KRYPTON. The system is a camera-based dynamic position measurement of the location of one or more infrared LEDs. The frame equipped with the LEDs was attached to the model on top of the aluminum structure. In Figs. 7a– 7b, the lead frame and the cameras that point to Spar 1 are encircled in red. The measured motions must be further post-processed to obtain the motions of the model's COG.

For the dual-spar configuration, the fairlead tensions of the two anchor lines of Spar 1 and the tensions of the shared line at both ends are measured with four load cells. For the single spar configuration, all three mooring tensions are measured. Four one-component load cells HBM with a SGfull bridge were used. The measured range of the load cell is 0 to 200 N and the precision is ± 0.081 N based on the residual values of its calibration. The load cell was covered with an insulating material to prevent drift caused by the environment during the experiments. A detailed

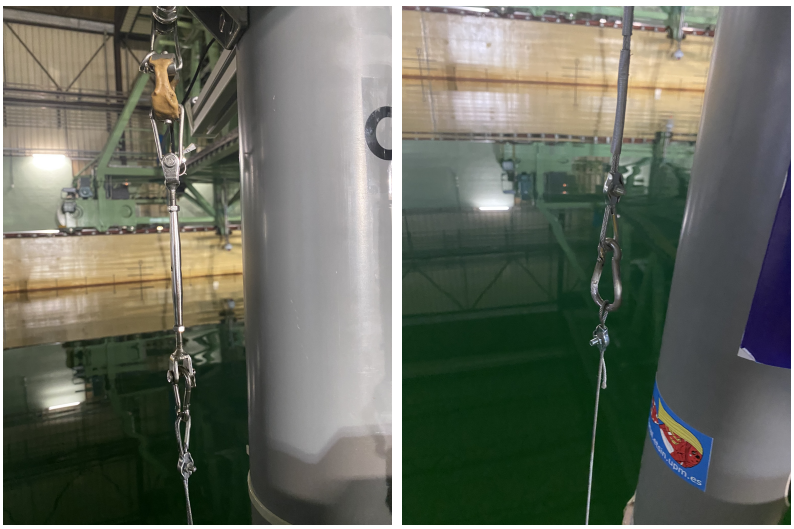

(a) Detailed view of one of the load cells with the turnbuckle.

(b) Detailed view of the line arrangement.

Figure 8: Detailed view of the load used during the tests and the line arrangement.

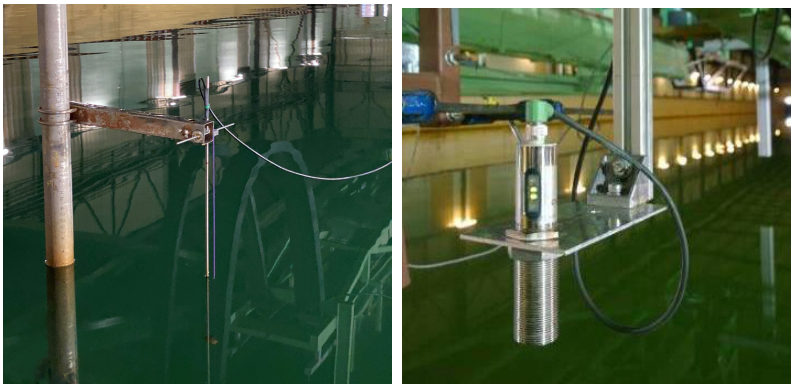

(a) Capacitance wave probe.

(b) Ultrasonic wave probe.

Figure 9: Detailed view of the instruments for measurements of water surface elevation.

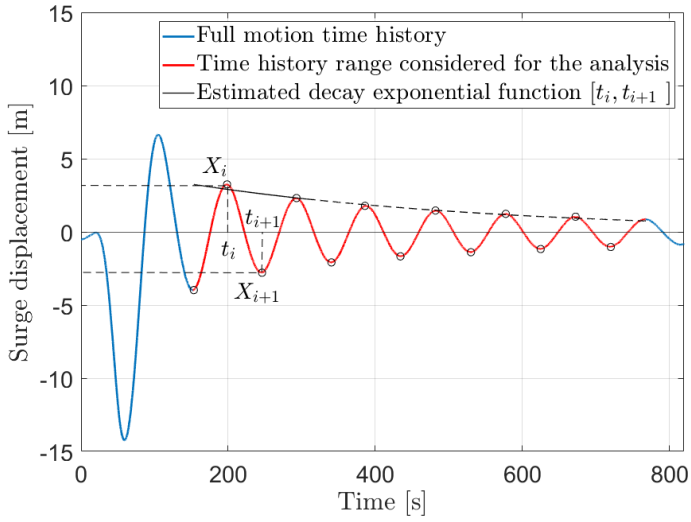

Figure 10: Exemplied analysis of a decay time series.

view of the sensor can be seen in Fig. 8a. A load cell, a turnbuckle for fine adjustment of the target pretension, and a steel wire connected to the catenary line are used. The arrangement can be seen in Fig. 8b.

The incoming waves were measured by means of an ultrasonic wave sensor located in the carriage. In addition, a capacitance wave probe is used to measure the wave elevation next to Spar 2. The precision of the measuring devices is $\pm$ 2.027 mm on average. These sensors are shown in Figs. 9a and 9b.

4. Methodology

4.1. Decay tests

To determine the natural periods of the platform with the mooring system designed, decay tests were performed in 6 DOFs of a single spar. The model was manually displaced from equilibrium and then released. The initial and last transient cycles are discarded for each test. Then, the remaining half cycles are analyzed. In the following, the subscript i refers to the ith-half cycle, starting at time t_i in a local extreme (see Fig. 10).

Decay experiments are analyzed by assuming that the measured data of each half cycle can be approximated to the theoretical solution of a damped linear single-DOF system. For example, Eq. (2) represents the motion of the uncoupled heave DOF in free vibration.

$$\ddot{z} + 2\mu_{eq,i}\dot{z} + \omega_{3,eq,i}^2 \; z = 0 \tag{2}$$

where $\mu_{eq,i}$, is the equivalent linear damping coefficient expressed as

$$\mu_{eq,i} = \frac{B_{33,i}}{2 \cdot (M + A_{33,i})} \tag{3}$$

and $\omega_{3,eq,i}$ is the equivalent undamped circular natural frequency expressed as

$$\omega_{3,eq,i} = \sqrt{\frac{C_{33}}{M + A_{33,i}}} \tag{4}$$

where M, C_{33}, B_{33}, $A_{33,i}$ are the mass, stiffness, linear damping and added mass in heave, respectively. Assuming that the system is lightly damped, the solution of the motion model of Eq. (2) can be approximated by the following analytical solution:

$$z(\tau) = e^{-\mu_{eq,i}\cdot\tau} Z_i \cos(\omega_{3,d,i} \cdot \tau), \tag{5}$$

with $\tau = t - t_i$ and $\omega_{3,d,i}$ is the damped circular natural frequency expressed as

$$\omega_{3,d,i} = \sqrt{\omega_{3,eq,i}^2 - \mu_{eq,i}^2} \tag{6}$$

Which can be determined approximately from the time between consecutive peaks:

$$\omega_{3,d,i} = \frac{\pi}{t_{i+1} - t_i} \tag{7}$$

By taking the logarithms of the Eq. (5) for two consecutive peaks in the time interval $[t_i, t_{i+1}]$, the characteristic parameter $\mu_{eq,i}$ is given by:

$$\mu_{eq,i} = \frac{1}{t_{i+1} - t_i} \log\left(\frac{|Z_i|}{|Z_{i+1}|}\right) \tag{8}$$

Both are assumed to vary slowly across the decay cycles. Therefore, the mean values of all the analyzed half cycles can be selected as representative values [37].

Finally, the nondimensional damping ratio, ξ, is defined as a fraction of the critical damping, B_{33}^{crit}, as follows

$$\xi = \frac{\mu_{eq}}{\omega_{3,eq}} = \frac{B_{eq,33}}{B_{33}^{crit}} \tag{9}$$

Three repetitions for each decay test were performed and different amplitude magnitudes and heading directions were applied to minimize the error in the measurements.

Considering the 6-DOF rigid body motions of each FWT, the dual-spar FWF has twelve natural periods and corresponding eigenmodes [20]. In these eigenmodes, two FWTs move in the same heading or the opposite directions of a DOF. However, due to the difficulty of applying initial displacements or rotations to both FWTs to excite the eigenmodes, for the dual-spar FWF in the decay tests, an initial displacement or rotation was applied to Spar 1 only. The same experimental procedures as for the Single FWT are applied to the Dual-spar FWF, and natural periods and damping ratios of the FWT were estimated. In order to calibrate the multibody numerical models, we suggest that the viscous damping forces estimated from the single spar tests can be applied to each individual FWT of the FWF as a starting point. Then, numerical decay tests can be carried out for the FWF, and the obtained damping ratio and natural periods of the coupled modes will be compared with the experimentally measured ones. An iterative procedure may be needed to adjust the damping and drag coefficients of the system components (FWTs and mooring lines) to achieve a good match.

4.2. Wave tests

4.2.1. Wave calibration

All wave cases described in Section 3.3 were tested for both configurations following recommendations by the International Towing Tank Conference (ITTC) [38, 39]. A calibration of the

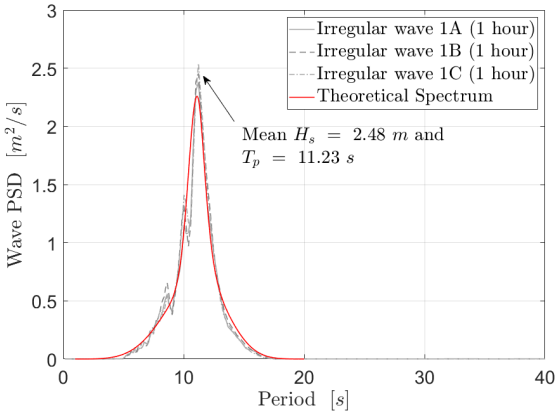

(a) Calibration of wave spectra; wave case IRR01.

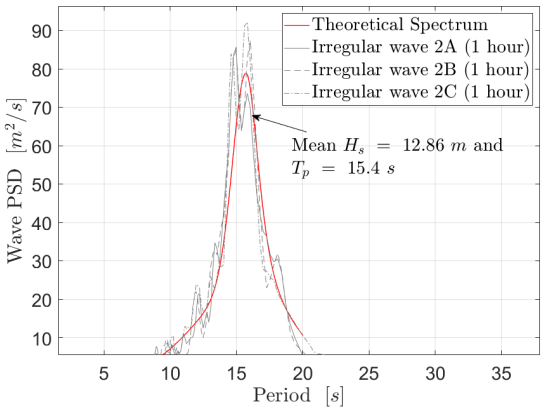

(b) Calibration of wave spectra; wave case IRR02.

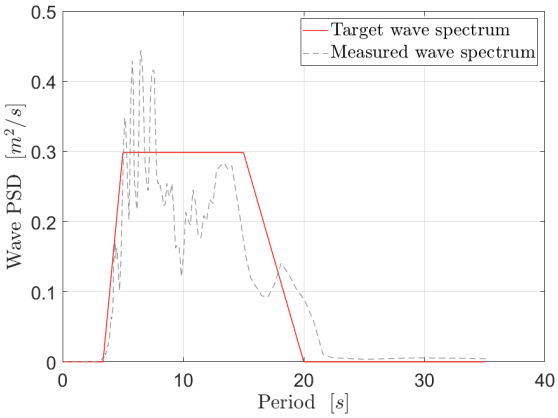

(c) Calibration of wave spectra; white noise case.

Figure 11: Calibration of the wave power spectra.

waves without the presence of the model was performed to ensure comparable wave loads between the two configurations.

According to ITTC [40], for irregular wave tests, a duration of 20-30 minutes at full scale is generally sufficient to collect statistically representative samples under wave-frequency responses. In this study, to obtain better response statistics with reduced statistical uncertainty [41], a duration of 1 hour with three realizations is considered for each irregular sea state.

A comparison of the wave power spectrum density (PSD) between the theoretical and experimental results of the two irregular cases, with 3 seeds each, is presented in Figs. 11a–11b. The calibration of the significant wave height (H_s) and the significant wave period (T_p) of the spectra are within acceptable errors (lower than 5%).

A white noise spectrum was also calibrated. This case was characterized by a target significant wave height H_s of 2 m and a frequency bandwidth between 0.05 and 0.20 Hz on full scale. Fig. 11c shows a comparison of the wave spectra between the theoretical and experimental results.

The same quality criteria was adopted for the regular wave calibration, achieving an error of less than 5% for the wave height and period.

4.2.2. Response amplitude operators (RAOs)

In a linear hydrodynamic model, the response of the model (in motions and tensions) to regular waves is expected to be periodic with the same frequency as the incident wave. The forcing input of a regular wave with amplitude η_0 is expressed as follows:

$$\eta = \eta_0 \cos(\omega t) \tag{10}$$

Then, the output of a linear system is

$$X = X_0 \cos(\omega t + \epsilon_X) \tag{11}$$

Both the amplitude of the wave and the amplitude of the response were obtained with the first Fourier harmonic of the corresponding time series. The magnitude of the first-order RAO for a given frequency is calculated according to Eq. (12).

$$RAO_X(\omega) = \left| \frac{X_0}{\eta_0} \right| \tag{12}$$

The period and height of the calibrated regular waves tested have previously been shown in Table 7b. Between 10 and 20 cycles were used to determine the transfer function, following the ITTC recommendations [42].

Alternatively, signals of the calibrated white noise case are utilized to perform a frequency domain analysis of the model responses. Then, the RAO magnitudes can be determined according to Eq. (13) [35]. Here, S_{xy} and S_{xx} are the cross- and auto-spectral energy density spectra of the wave, respectively.

$$RAO_X = \frac{S_{xy}}{S_{xx}} \tag{13}$$

Units of the RAOs are m/m for translational motions, deg/m for rotational motions, t/m for tensions and forces, and $t \cdot m/m$ for moments.

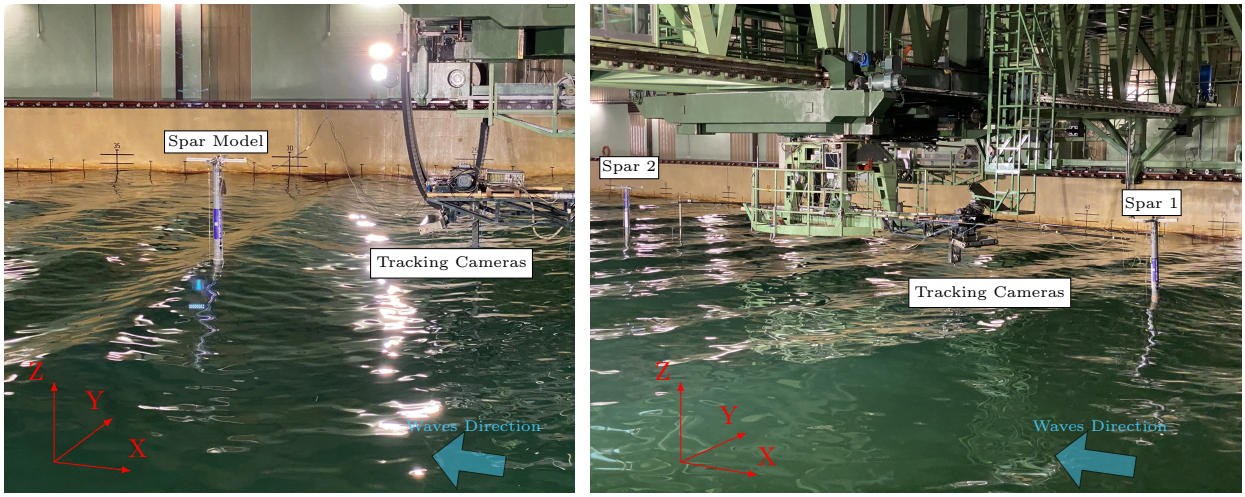

(a) Single-spar configuration.

(b) Dual-spar configuration.

Figure 12: Illustration of the wo configurations during seakeeping tests.

Table 8: Natural period estimation for the two configurations [s].

	Surge	Sway	Heave	Roll	Pitch	Yaw
Single	93.03	87.92	29.80	31.69	31.71	24.55
Dual	142.88	83.89	30.50	31.56	31.32	23.93

Table 9: Estimation of the damping ratio ξ for the two configurations [%].

	Surge	Sway	Heave	Roll	Pitch	Yaw
Single	3.87	2.91	1.77	1.07	1.27	1.62
Dual	3.56	3.02	1.86	1.08	1.32	1.83

5. Results

Results will be presented focusing on a comparison between the two configurations explained in Section 3. In the figures, the single spar FWT and the dual-spar FWF are called "Single" and "Dual", respectively. Fig. 12 shows snapshots of both configurations during the experiments; refer to Figs. 4–5 for the layout. The 0 *deg* wave heading is pointed in the figure with the light blue arrow.

The estimated natural frequencies and damping ratios of the two configurations are presented in Section 5.1. RAOs are presented in Section 5.2. Finally, motions and mooring tension analysis for the irregular waves are conducted in Section 5.3. As only one wave heading is considered, the platform motion analysis focuses on surge, heave, and pitch.

5.1. Natural frequencies and damping of the two configurations

Following the procedure detailed in Section 4, the natural periods and damping ratios are estimated for both configurations. As presented in Table 8, no significant differences between the two configurations are found for heave, roll, and pitch because these DOFs are hardly affected by the considered mooring configuration. Note that the most noticeable differences appear in the surge (51%) and sway (7%). This is due to the system reduction in stiffness by changing two anchor lines to a shared line in the dual configuration. Estimations of the average damping ratios ξ are listed in Table 9, showing no significant differences between the two configurations.

5.2. First-order RAOs from the regular wave and white noise tests

The estimated motion RAOs for both configurations are shown in Fig. 13. A comparison is presented between the white noise and the regular wave results, obtained based on methods described in Section 4.2.2. Generally, a good match between the two tests is achieved for both configurations. This is an indication of the system's linear behavior in this frequency range as energy is not transferred between different frequencies in the white noise tests.

Comparing the single- and dual-spar configurations, we observe that the differences between them are not substantial in the first-order frequency range. The reason is that the motion dynamics in this frequency range is not affected by the mooring used in this study.

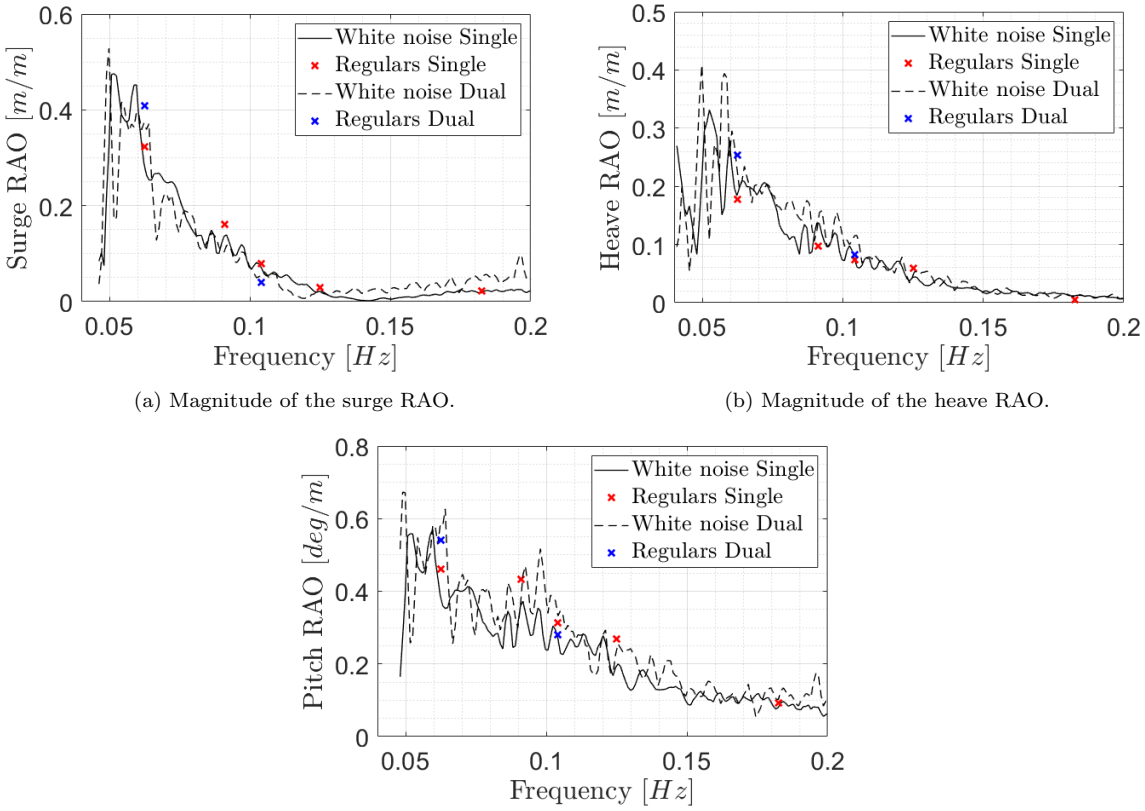

(a) Magnitude of the surge RAO.

(b) Magnitude of the heave RAO.

(c) Magnitude of the pitch RAO.

Figure 13: Comparison of response amplitude operators for surge, heave and pitch motions, single- and dual-spar configurations.

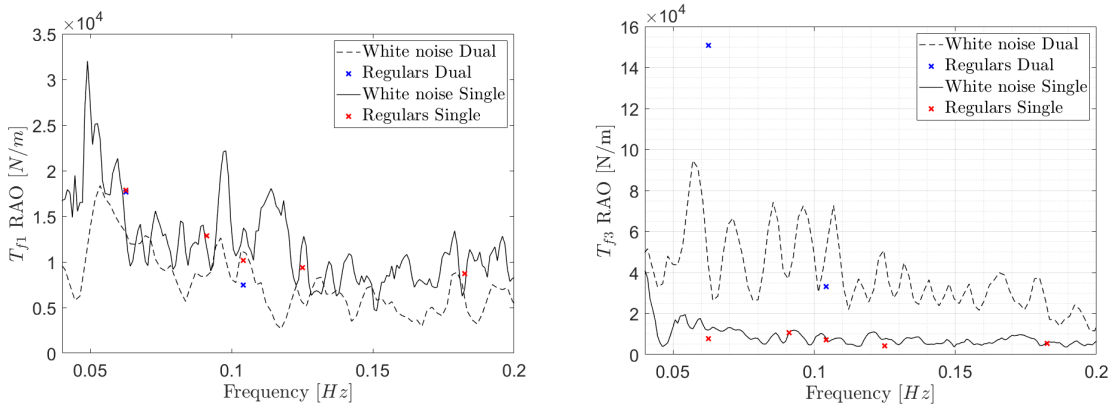

(a) T_{f1} RAO.

(b) T_{f3} RAO.

Figure 14: Comparison of response amplitude operators for anchor lines (T_{f1}) and shared line (T_{f3}); single- and dual-spar configurations.

As RAOs are just linear operators whereas the catenary mooring system has nonlinear restoring characteristics, the tension RAOs must be interpreted with caution. To evaluate the impact of the mooring system on tension responses, the tension RAOs have been estimated and are presented

in Fig. 14. The results are similar for the anchor lines but substantial differences can be found for the shared line. A possible explanation is that since additional nonlinearities are present in an FWF with shared mooring (primarily due to the shared line), one can expect differences between the transfer function obtained from the white noise tests and from the regular wave. For a deeper investigation on this matter, more repetitions of these tests, and other white noise tests with different wave amplitudes and regular waves with different amplitudes and frequencies should be carried out. This has been left for future work.

5.3. Response analysis for the irregular wave tests

As discussed in Section 3.3, an operational and an extreme sea state have been tested. For FWTs in normal operation, aerodynamic loads have a significant impact on the motion and structural responses in addition to hydrodynamic loads. As wind loads were not considered during the tests, the studied load cases are representative of scenarios where the spar FWTs are parked due to maintenance or faults [43]. Under such scenarios, FWTs are usually parked with feathered blades and wave loads are dominant. To highlight the extreme responses of the FWF and to improve the narrative of the article, results of the operational condition are moved to Appendix B and Appendix C.

In order to present the results, first, motions will be analyzed, with a focus on surge motion, the crucial one in terms of the inter-array power cable design, and the one that is most affected by the change in the mooring configuration from "Single" to "Dual". The platform-pitch motions will be also discussed as the floater's tilt angle relates to serviceability limit state and is determined by tolerance requirements by turbine manufacturers. Mooring tensions will be discussed to close this section.

5.3.1. Motion responses

5.3.1.1 Spectral analysis

The PSDs are averaged across the three realizations of the surge motion in the extreme wave condition and are shown in Fig. 15. Individual PSD plots of the three realizations of the single- and dual-spar configurations are included in Appendix B.

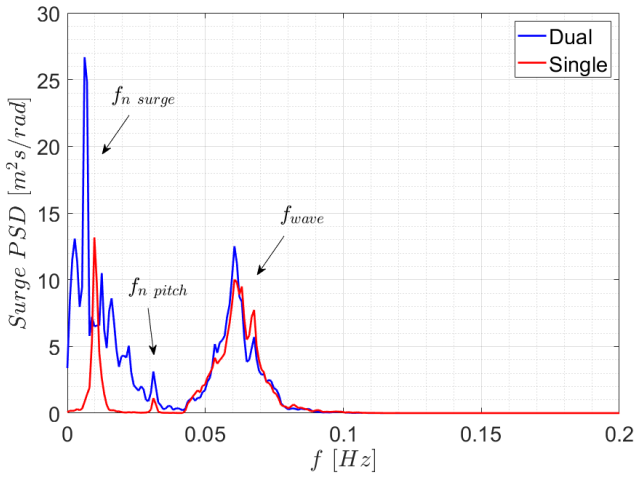

Figure 15: Averaged surge spectra for the IRR02 wave case. $H_s = 12.7\ m$ and $T_p = 15.45\ s$

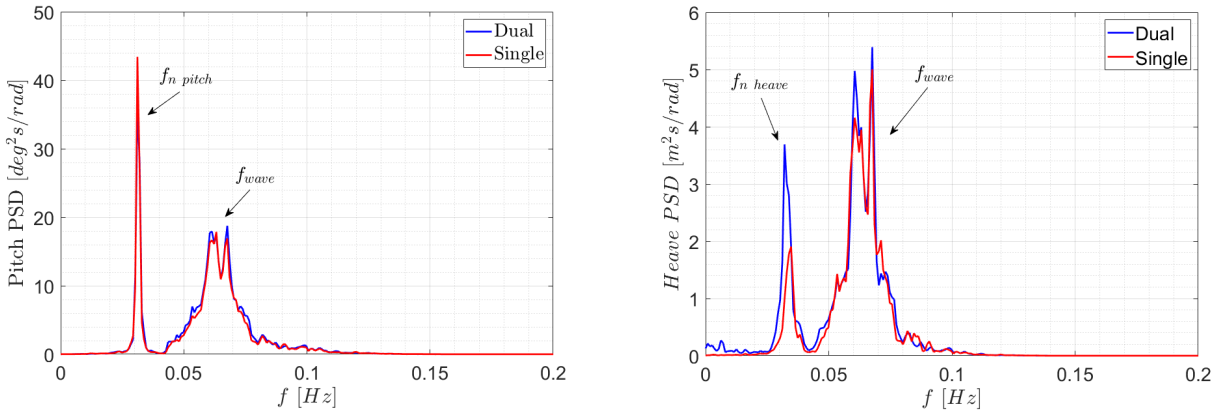

(a) Pitch (b) Heave

Figure 16: Comparison of averaged pitch and heave spectra for the IRR02 wave case. $H_s = 12.7\ m$ and $T_p = 15.45\ s$

As illustrated in Fig. 15, the surge motion PSDs have similar peaks in the first-order wave frequency range for both configurations despite clear differences in the low frequency range.

The surge-pitch coupling is evidenced by the peak around 30 s (0.033 Hz), which corresponds to the estimated natural period in pitch (see Table 8). This was also observed in Ramachandran et al. [44] and verified in other tests of spar FWTs, e.g., Meng et al. [45], Yang et al. [46].

In the low-frequency range, surge resonant motions of both configurations are excited at peaks around 0.01 Hz; see Table 8. Compared with the single-spar configuration, the dual-spar configuration displays a larger amount of energy in periods 60 to 120 s (0.02 to 0.0075 Hz). This may be correlated with additional eigenmodes of the FWF due to the complex multibody dynamics present in the configuration, as discussed in section 4.1 and in Liang et al. [20]. Future work is needed for a proper understanding of this particular energy distribution.

For the pitch DOF, the averaged PSDs are presented in Fig. 16a and are similar for both configurations. The differences in the heave motions between the two configurations are not large either (Fig. 16b). The reason for this observation is that both the heave and pitch motions are governed by the mass properties and the dominant hydrodynamic stiffness, while the mooring stiffness plays a secondary role.

Among the investigated DOFs, the surge motion is most affected by mooring configurations. Hence, one should focus on the surge offset when assessing the feasibility of the shared mooring in an FWF.

5.3.1.2 Statistics

A probability of exceedance (POE) curve measures the number of times a stochastic process exceeds some critical value per unit time. In the extreme sea state, excessive surge or pitch motions of the spar FWT may lead to damage of the inter-array power cables or drivetrain components. According to feedback from industrial partners in various initiatives, the experimentally obtained POEs can also be useful in verification of numerical models for design and certification purposes. Hence, we use POE together with conventional statistics to compare the two configurations. Fig. 17 presents the POEs obtained from time histories of the surge and pitch motions for the three realizations. First, it is observed that the shapes of the POEs are consistent across the three realizations. Second,

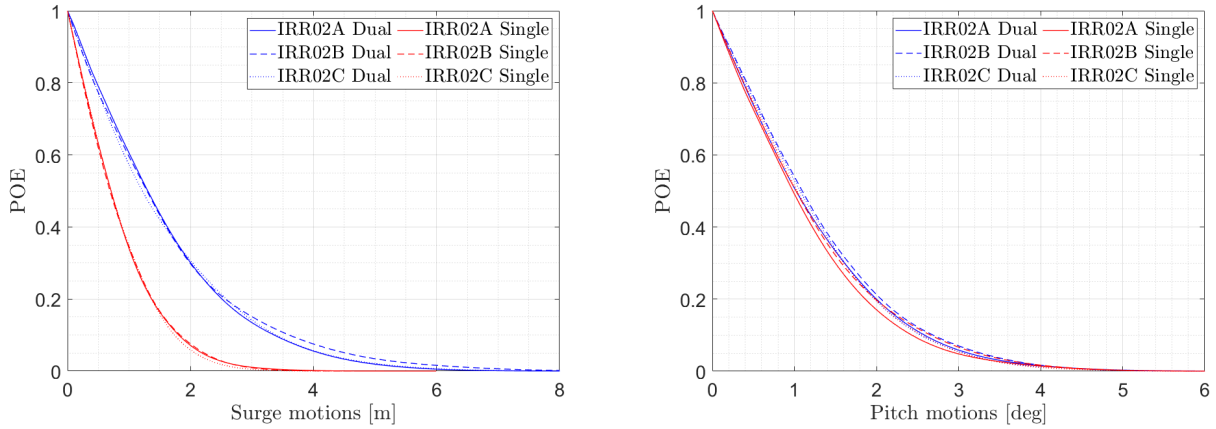

(a) Surge (b) Pitch

Figure 17: POE of surge and pitch for the IRR02 wave case. $H_s = 12.7\ m$ and $T_p = 15.45\ s$.

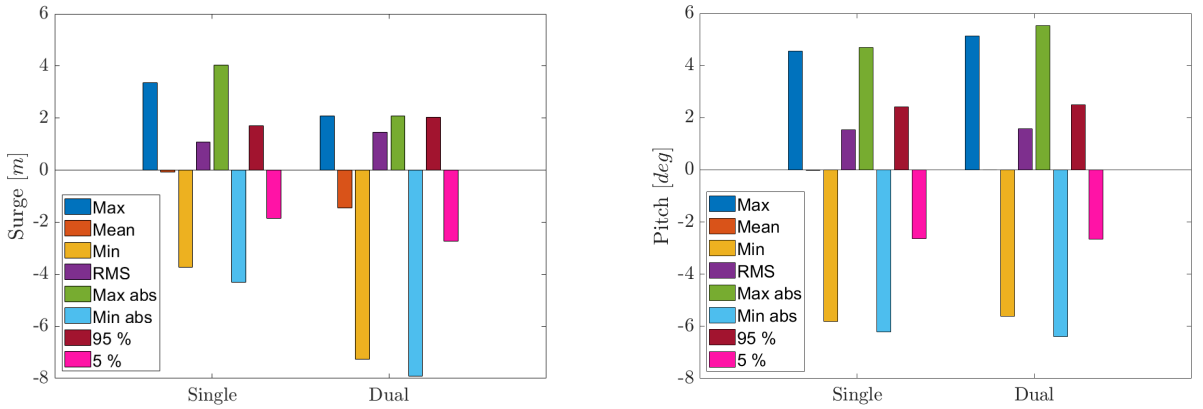

(a) Surge (b) Pitch

Figure 18: Comparison of surge and pitch motion statistics for the IRR02 wave case. $H_s = 12.7\ m$ and $T_p = 15.45\ s$. The statistical values are averaged across three realizations except "Max abs" and "Min abs". "Max abs": total maximum among three realizations; "Min abs": total minimum among three realizations; "Max": maximum; "Min": minimum; 'RMS": root mean square; "95%": 95% quantile; "5%": 5% quantile.

for a given level of POE, e.g., 0.1, the corresponding surge motion (blue curve) of the dual-spar configuration are significantly larger than that (red curve) of the single-spar configuration. This observation is consistent with previous observation for the surge PSDs. Additionally, the differences in the pitch motion POEs between the two configurations are negligible.

Eight statistical values of the surge and pitch motions are presented in Fig. 18 to facilitate a quantitative comparison of the two configurations. The design standards of FWTs, e.g., DNV-ST-0119 [34], require that the characteristic extreme responses for design are obtained by fitting probability models to the global maxima of each realization and for a sea state, many realizations should be simulated with different seeds. Due to the limited number of realizations from the experiments, we do not perform a design check but only compare the representative statistics.

As shown in Fig. 18a, the total maxima and minima are mildly above the averaged maxima

and minima for the surge motion for both configurations. This indicates a degree of stochastic uncertainty among the three realizations. Consistent with the POEs, there is larger maximum, mean, and RMS in surge for the dual-spar configuration than for the single-spar configuration. Such an observation is aligned with the case of semi-submersible FWF as well [47]. For the mooring system design of FWF, there are no strict criteria regarding the maximum offset and a rule-of-thumb threshold is 10% of the water depth because of constraints of the inter-array power cables. For the present water depth, the maximum surge offset (approximately 8 m) of the dual-spar FWF is still below the threshold of 23.5 m.

It is interesting to notice that mean surge of the single spar FWT is substantially smaller than that of Spar1 of the FWF, whereas the RMS values of the two configurations are comparable. While the mean drift of the spars in the two configurations experiences a minor difference, the larger mean surge of the dual-spar configuration is mainly due to the reduced mooring stiffness in the surge direction as the shared line's contribution to the stiffness is relatively small.

Regarding the platform pitch motion, the two configurations display quite similar statistics, as shown in Fig. 18a. The dual-spar configuration has slightly higher maximum and RMS than the single-spar configuration. This trend is consistent with the POEs presented before. Currently, the maximum allowable pitch angle in the range of 10-15 *deg* [48] is common for the nonoperational load cases, e.g., design load cases 6.1 and 6.2 in the IEC standard [49]. This design criterion is also fulfilled for both configurations in the extreme wave case.

5.3.2. Tension responses of the anchor lines

For both configurations, the fairlead tension T_{f1} (see Fig. 1) of one selected anchor line (Line 1) is focused on in the analysis. As Line 1 and Line 2 are symmetrical, the discussion for Line 2 is not included here.

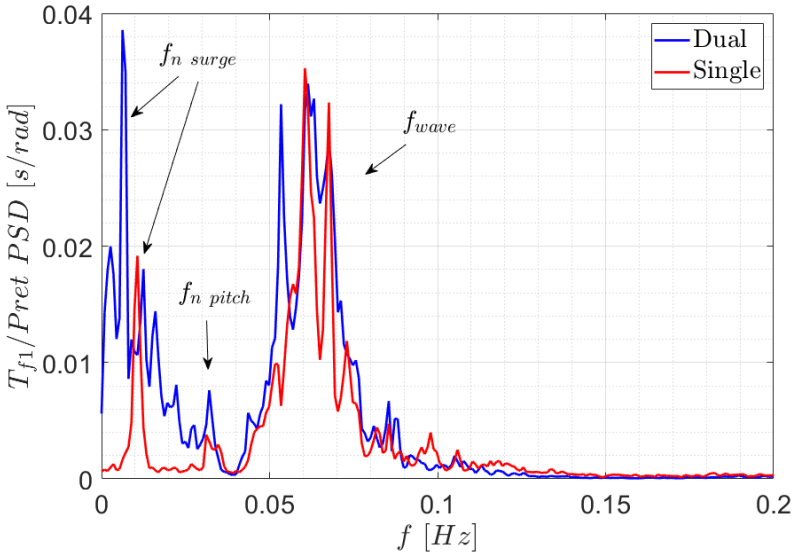

Figure 19: Comparison of the anchor line tension PSDs for the IRR02 wave case. $H_s = 12.7\ m$ and $T_p = 15.45\ s$.

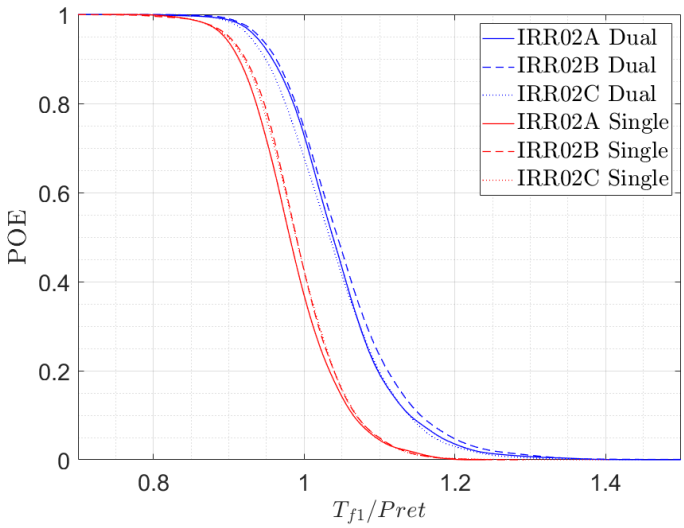

Figure 20: Comparison of the anchor line tension POEs for the IRR02 wave case. $H_s = 12.7\ m$ and $T_p = 15.45\ s$.

5.3.2.1 Spectral analysis

As PSDs of individual realizations of the two configurations are included in Appendix C, the averaged PSD across the three realizations of the anchor line tensions for the extreme wave case is shown in Fig. 19. It is observed that the response in the first-order wave frequency range is more similar for both configurations than the response in the low frequency range. This is in line with the observations in Section 5.3.1.1 regarding the surge motion PSDs. In the low frequency range, the estimated natural surge periods and the surge-pitch coupling are also observed. In addition, a considerable amount of energy between 60-120 s (0.02 to 0.0075 Hz) is also be observed in the line tensions because of the correlation between the dynamic line tension and surge motions.

5.3.2.2 Statistics

Fig. 20 shows the POE curves of the time series of the fairlead tension ,T_{f1}. In order to account for the different pretensions in the single- and dual-spar configurations, the statistics are normalized with the pretension. Similar to POEs of the motions 5.3.1.2, these POEs can also be used in verification of numerical analysis results of mooring lines. As expected, the normalized T_{f1} fairlead tension POEs show relatively small variability across the three realizations for both configurations. This observation is similar to that of the surge or pitch motion. Generally, the tension POEs have similar trends in both configurations. For a given POE level, a moderately larger tension is observed for the dual-spar configuration.

As mentioned in Section 5.3.1.2, the statistical quantities, e.g., the 5% and 95% quantiles, mean, and standard deviation, can be used to verify numerical models. Hence, these values for the fairlead tensions in the anchor lines are presented in Fig. 21. It is interesting to notice that the mean value of the fairlead tension is close to the pretension in both configurations, indicating that the mean drift in surge for the dual-spar FWF does not significantly impact the mean tension. This can be attributed to the reduced mooring stiffness in the FWF as discussed above. Among other quantities, the RMS and the 5% and 95% quantiles are slightly larger for the dual-spar configuration than for the single-spar configuration. This trend is consistent with the POEs shown

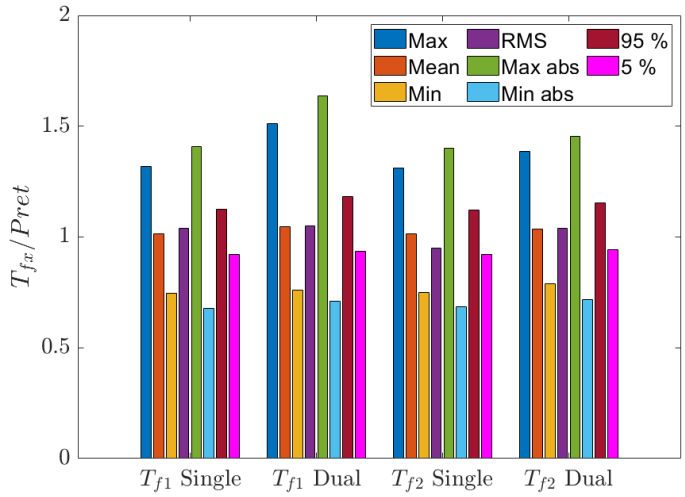

Figure 21: Anchor lines tension statistics (normalized with the pretension) for the IRR02 wave case. $H_s = 12.7\ m$ and $T_p = 15.45\ s$.

in Fig. 20. Similar to the observation for the motions, the total maxima and minima of the three realizations are of the same order of the average maxima and minima.

Here, the discussion is focused on the extreme wave case. Results on the operational case and discussions on the differences in tension responses between Line 1 and Line 2 are found in Appendix C.

5.3.3. Tension responses of the shared line

Because the dynamics of the shared line is different from that of the anchor lines, the fairlead tensions in the shared line should be analyzed separately. This difference was shown when analyzing tension RAOs in Section 5.2 and can be clearly appreciated by observing the time histories for

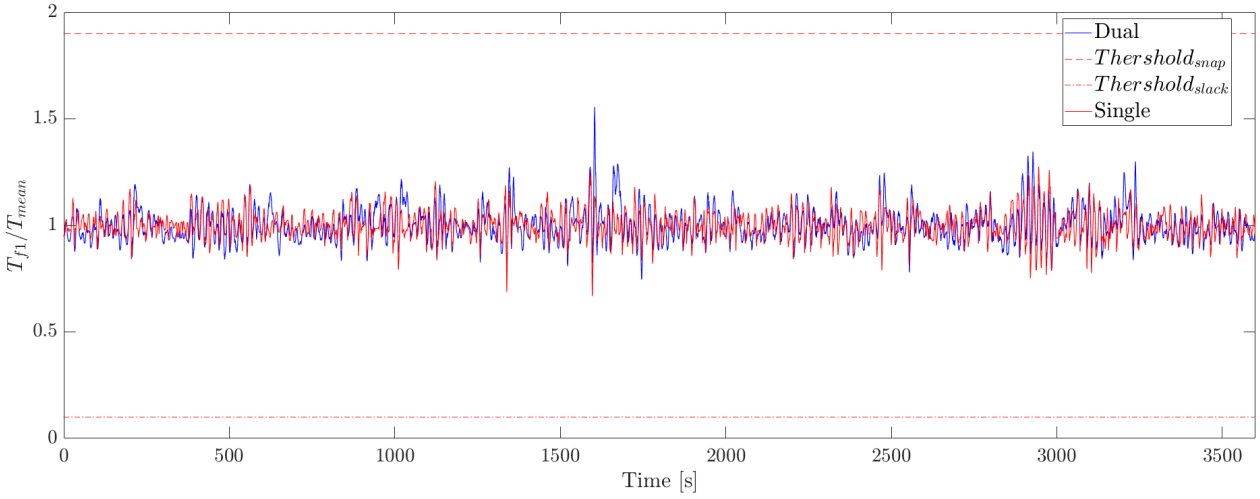

Figure 22: Comparison of the anchor line tension in both configurations for extreme case IRR02B. The snap/slack thresholds and events are marked.

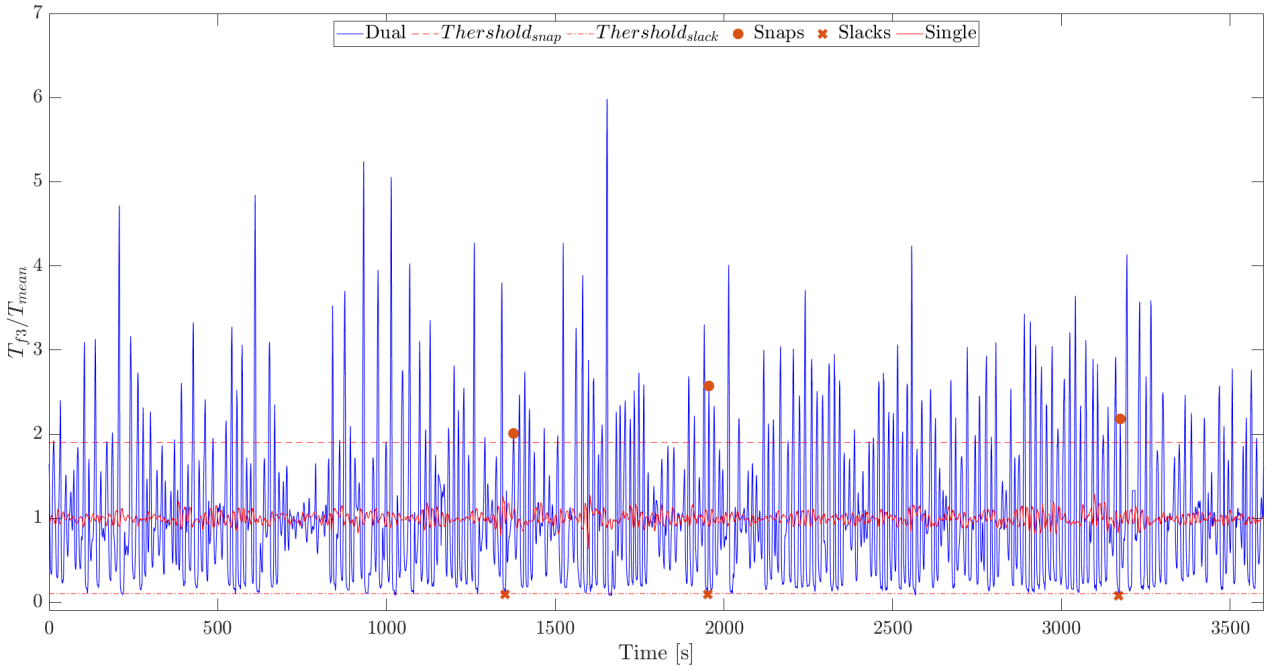

Figure 23: Comparison of the shared line tension in both configurations for extreme case IRR02B. The snap/slack thresholds and events are marked.

the extreme wave condition for the anchor lines and shared line for the single- and dual-spar configurations, as presented in Figs. 22– 23.

When analyzing the dynamic mooring tensions, an interesting factor to consider is the snap events. According to Hsu et al. [50], a snap event can be described as a sudden and violent increase in tension that appears after a slack in the line. They proposed the following snap criteria based on the DNV guideline [51]:

$$T_{slack} \leq 0.1 \cdot T_{mean} \quad ; \quad T_{snap} \geq 1.9 \cdot T_{mean} \tag{14}$$

where T_{slack} is the local tension minima, T_{snap} is the local tension maxima, and T_{mean} is the mean tension.

In Figs. 22 and 23 the snap and slack events and their thresholds are highlighted following the above criteria. As shown in Fig. 22, for the anchor lines in both configurations, the thresholds (dashed lines) are far from the maximum ranges of the tension time histories. In contrast, for the shared line, a number of snap and slack events can be identified; see Fig. 23). This extreme dynamics for shared lines in terms of snap and slack events can also be observed in the time series presented by Gomes et al.[52] who devised a shared mooring system for a set of five wave energy converters. As the present dual-spar FWF has one shared line, there is a significant reduction in the mooring stiffness in surge. In addition, the motions of Spar 1 and Spar 2 are not in phase in irregular waves and the relative distance between them vary. These factors contribute to the observed snap/slack events. Oscillations in the shared line tension due to these events are critical for the mooring design.

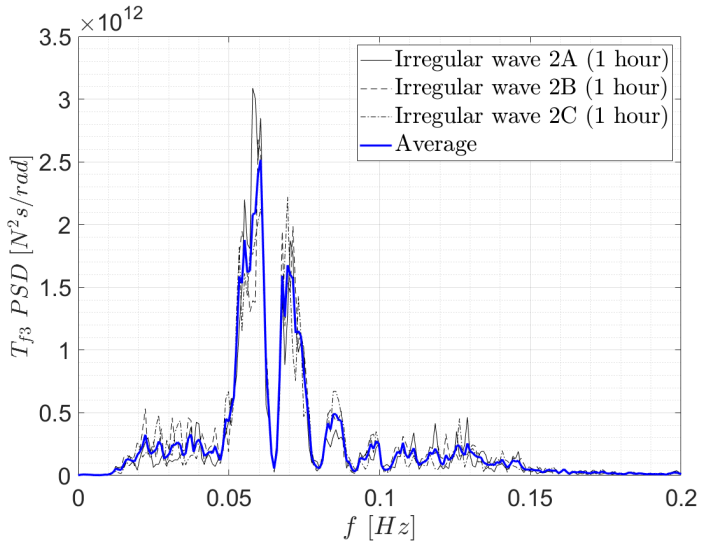

Figure 24: Shared line fairlead tension T_{f3} PSD for the extreme IRR02 wave case. $H_s = 12.7\ m$ and $T_p = 15.45\ s$.

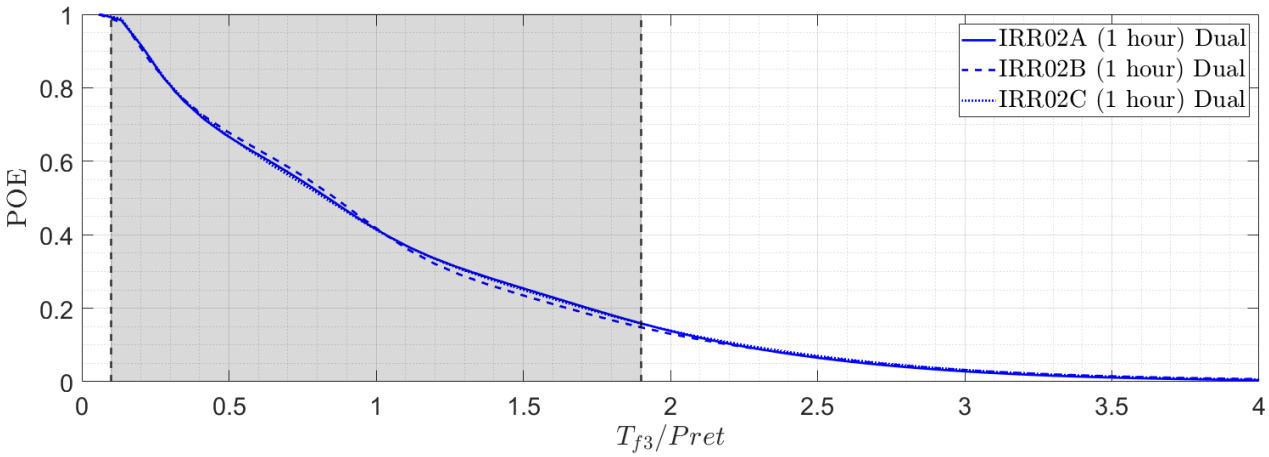

Figure 25: POE of the time history of the shared line fairlead tensions Tf_3 for the extreme IRR02 wave case. $H_s = 12.7\ m$ and $T_p = 15.45\ s$.

5.3.3.1 Spectral analysis

The average PSD and the PSDs of the three realizations for the shared line tension Tf_3 time histories are presented in Fig. 24. Consistency in the PSDs across the three realizations can be observed. Interestingly, unlike the PSDs of the anchor line tension (see Section 5.3.1.1), the PSD of the shared line tension displays peaks in the first-order wave frequency range (5–20s). This observation agrees with Fig. 13 of a numerical study for an array of semi-submersible FWTs by Wang et al. [21].

5.3.3.2 Statistics

Fig. 25 shows POEs of the times series of the shared line tension Tf_3 in the extreme irregular wave case. The grey zone refers to the region where the line tension is within the thresholds of the

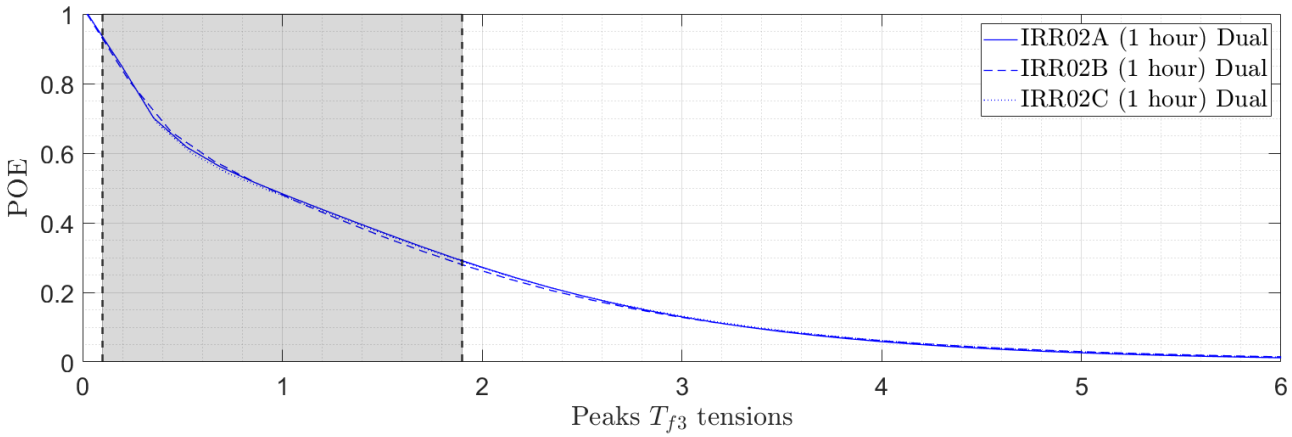

Figure 26: POE of the peaks of the time history of the shared line fairlead tensions Tf_3 for the extreme IRR02 wave case. $H_s = 12.7\ m$ and $T_p = 15.45\ s$.

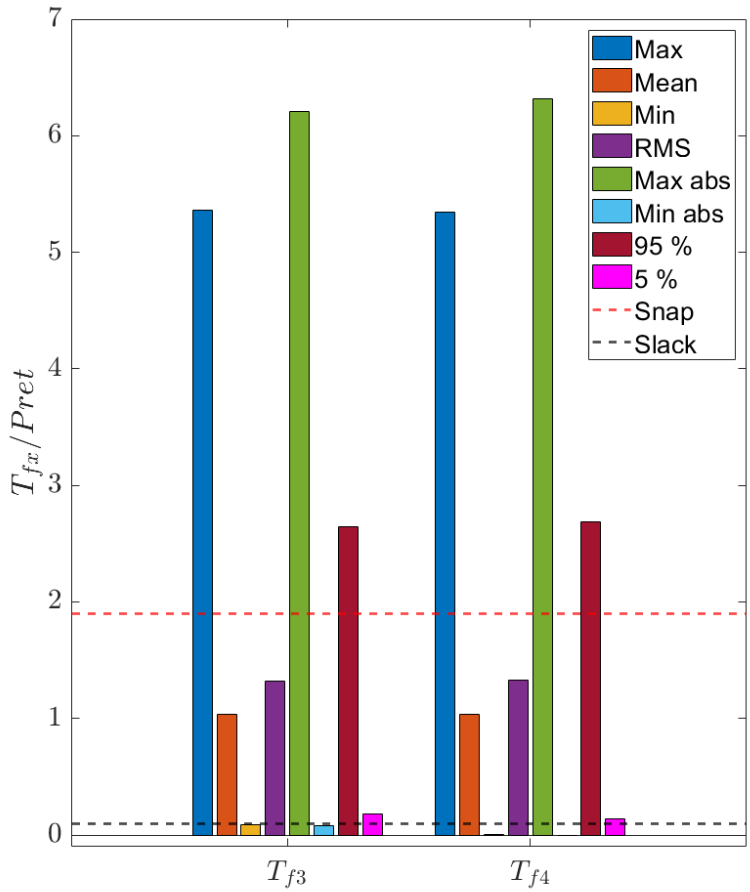

Figure 27: shared line fairlead tension statistics (normalized with the pretension) for the extreme sea state. IRR02 wave case. $H_s = 12.7\ m$ and $T_p = 15.45\ s$

slack/snap criteria; refer to Eq. (14).

Regarding the snap events, one can observe that the shared line tension Tf_3 exceeds the snap

threshold during 15% of the time. Regarding slack events, the occurrence rate is far lower.

POEs of the peak tensions (maxima and minima) are presented in Fig. 26. It is remarkable that approximately 30% of the peaks are above the snap-event threshold and 5% are below the slack-event threshold. The frequent occurrence of the snap events evidence should be addressed to avoid premature failure of the shared line due to fatigue or mooring breakage. One strategy to reduce the likelihood of these events is to include clump weights in the lines, as Cabrerizo et al. [53] studied in the context of offshore operations. A detailed analysis of this approach for a shared mooring system for FWFs can be found in Liang et al. [54].

Statistics of the shared line tension are presented in Fig. 27. As shown, the normalized value of the maximum tension exceeds five. Compared with the anchor line (see Fig. 21), the shared line displays a higher level of dynamic tension and the difference between the maximum tension and the 95% quantile grows larger. As the large peak tensions and dynamic tensions are associated with the snap events, a proper design of the shared line with higher steel grade, increased wire diameter, or with additional mooring components can be carried out in future.

6. Conclusions

In this work, the dynamic performance of a dual-spar floating wind farm (FWF) with a shared line has been compared against a single floating wind turbine (FWT) with a catenary mooring system. To this aim, model-scale experiments were carried out at the INTA-CEHIPAR ocean basin in Madrid, Spain. The floater is the OC3-Hywind spar with a scale ratio of 1:47. Following discussions with industry advisors, a different water depth location from that of the original Hywind is chosen (235 m instead of 320 m). Consequently, a different mooring system is proposed.

Natural periods and damping ratios have been estimated with decay tests. Two irregular wave conditions, a white noise, and five regular wave conditions have been tested. Only a wave heading has been tested, in which the shared line is collinear with the wave propagation direction. Response amplitude operators of motion and tension, motion and tensions spectra, and motion and tension statistics have been obtained under these conditions. To make the present effort more useful to the research community, the data discussed in the paper and videos of the experiments are made available (see Section 7). The main observations are listed as follows:

- The surge natural period for the dual-spar configuration is 51% larger than that of the single spar configuration due to the change in mooring stiffness between the two configurations. The natural periods in heave and pitch experience small changes by moving to a shared mooring configuration. This is also expected as they are hardly affected by catenary mooring.

- Larger platform surge motion is observed for the dual-spar configuration than for the single-spar configuration. This fact is attributed to the reduction in the mooring stiffness due to the shared line. The platform heave and pitch remain similar between the two configurations. The proposed design criteria for surge (allowable offset of 10% water depth) and pitch (maximum 10 deg) are fulfilled in both configurations.

- Spectral analysis of the shared line tension reveals that the tension response has dominant peaks in the first-order wave frequency range.

- The tension responses in the anchor lines are of the same order and display no slack/snap events for both configurations, whereas large tension peaks, significant dynamic tension, and a number of slack/snap events have been identified in the shared line in the FWF.

The results of this work help to better understand the complex multibody dynamics, and the performance of the highly attractive mooring solution as the shared mooring system. However, the scope of this work is limited. Future work may include testing of FWFs with additional instrumentation, conducting a number of static tests to estimate the mooring stiffness in the various degrees of freedom, generation of wind loads and combined load cases in the experiments, and improved design of the shared mooring systems.

7. Data Availability

The dataset used in the present study is made available on the server of CEHINAV Research Group (`http://canal.etsin.upm.es/papers/lopezoloccoetal_sharedmooring_2023/`).

Acknowledgements

The financial supports from UH-nett Vest (Project No. 720025) and ImpactWind South-West (Project No. 332034) are gratefully acknowledged. This research has also been partially funded by the Ministry of Science and Innovation of Spain through projects FWT-DAMP2 (References: PID2021-123437OB-C21, FWT-PLATE-MOOR and TED2021-130951B-I00). Thanks are extended to Dr. Carlos Lopez-Pavon from COREMARINE SOLUTIONS, Spain and Prof. Simos from University of Sao Paulo, for fruitful discussions leading to the definition of some parameters of the tested configurations. The authors are also grateful to Javier Medina Galera for the assistance during the experimental campaign and for providing the sketch of the model design presented in Appendix A.

References

[1] E. An, Strategy to harness the potential of offshore renewable energy for a climate neutral future, European Commission: Brussels, Belgium (2020).

[2] G. Sannino, G. Pisacane, A. Carillo, M. Struglia, Strategic research agenda towards innovation in blue energy (2019).

[3] S. Chakrabarti, Handbook of Offshore Engineering (2-volume set), Elsevier, 2005.

[4] B. Skaare, F. G. Nielsen, T. D. Hanson, R. Yttervik, O. Havmøller, A. Rekdal, Analysis of measurements and simulations from the hywind demo floating wind turbine, Wind Energy 18 (2015) 1105–1122.

[5] F. G. Nielsen, T. D. Hanson, B. Skaare, Integrated dynamic analysis of floating offshore wind turbines, in: International conference on offshore mechanics and arctic engineering, volume 47462, 2006, pp. 671–679.

[6] G. R. Tomasicchio, F. D'Alessandro, A. M. Avossa, L. Riefolo, E. Musci, F. Ricciardelli, D. Vicinanza, Experimental modelling of the dynamic behaviour of a spar buoy wind turbine, Renewable energy 127 (2018) 412–432.

[7] S. Russo, P. Contestabile, A. Bardazzi, E. Leone, G. Iglesias, G. R. Tomasicchio, D. Vicinanza, Dynamic loads and response of a spar buoy wind turbine with pitch-controlled rotating blades: An experimental study, Energies 14 (2021) 3598.

[8] A. Myhr, K. J. Maus, T. A. Nygaard, Experimental and computational comparisons of the OC3-HYWIND and Tension-Leg-Buoy (TLB) floating wind turbine conceptual designs, in: The Twenty-first International Offshore and Polar Engineering Conference, OnePetro, 2011.

[9] A. J. Goupee, B. J. Koo, R. W. Kimball, K. F. Lambrakos, H. J. Dagher, Experimental Comparison of Three Floating Wind Turbine Concepts, Journal of Offshore Mechanics and Arctic Engineering 136 (2014). 020906.

[10] B. J. Koo, A. J. Goupee, R. W. Kimball, K. F. Lambrakos, Model tests for a floating wind turbine on three different floaters, Journal of Offshore Mechanics and Arctic Engineering 136 (2014).

[11] T. Stehly, P. Beiter, P. Duffy, 2019 cost of wind energy review, Technical Report, National Renewable Energy Lab.(NREL), Golden, CO (United States), 2020.

[12] D. Pantusa, G. Tomasicchio, Large-scale offshore wind production in the mediterranean sea, Cogent Engineering 6 (2019) 1661112.

[13] M. C. Devin, B. L. DuPont, S. T. Hallowell, S. R. Arwade, Optimizing the cost and reliability of shared anchors in an array of floating offshore wind turbines, ASCE-ASME J Risk and Uncert in Engrg Sys Part B Mech Engrg 7 (2021).

[14] C. Fontana, S. Arwade, D. DeGroot, S. Hallowell, C. Aubeny, B. Diaz, M. Landon, S. Ozmutlu, A. Myers, Force dynamics and stationkeeping costs for multiline anchor systems in floating wind farms with different spatial parameters, in: International Conference on Offshore Mechanics and Arctic Engineering, volume 58899, American Society of Mechanical Engineers, 2019, p. V010T09A079.

[15] C. M. Fontana, S. R. Arwade, D. J. DeGroot, A. T. Myers, M. Landon, C. Aubeny, Efficient multiline anchor systems for floating offshore wind turbines, in: International Conference on Offshore Mechanics and Arctic Engineering, volume 49972, American Society of Mechanical Engineers, 2016, p. V006T09A042.

[16] Equinor, Hywind Tampen: The World's First Renewable Power for Offshore Oil and Gas, `https://www.equinor.com/energy/hywind-tampen`, 2019. [Online; accessed 12-October-2022].

[17] R. Chitteth Ramachandran, C. Desmond, F. Judge, J.-J. Serraris, J. Murphy, Floating wind turbines: marine operations challenges and opportunities, Wind Energy Science 7 (2022) 903–924.

[18] C. Sloan, M. Hall, S. Housner, E. Lozon, S. Sirnivas, Shared Mooring Systems for Deep-Water Floating Wind Farms, Technical Report NYSERDA Contract 142869, National Renewable Energy Lab.(NREL), Golden, CO (United States), 2022.

[19] G. Liang, K. Merz, Z. Jiang, Modeling of a shared mooring system for a dual-spar configuration, in: International Conference on Offshore Mechanics and Arctic Engineering, volume 9: Ocean Renewable Energy, American Society of Mechanical Engineers, 2020.

[20] G. Liang, Z. Jiang, K. Merz, Mooring analysis of a dual-spar floating wind farm with a shared line, Journal of Offshore Mechanics and Arctic Engineering 143 (2021) 062003.

[21] Y. Wang, H. Wolgamot, P. Watson, C. Gaudin, W. Zhao, I. Milne, Preliminary investigation of a shared mooring arrangement for a floating offshore wind turbine farm in deep water, in: International Conference on Offshore Mechanics and Arctic Engineering, volume 85932, American Society of Mechanical Engineers, 2022, p. V008T09A061.

[22] S. Wilson, M. Hall, S. Housner, S. Sirnivas, Linearized modeling and optimization of shared mooring systems, Ocean Engineering 241 (2021) 110009.

[23] M. Goldschmidt, M. Muskulus, Coupled mooring systems for floating wind farms, Energy Procedia 80 (2015) 255–262.

[24] M. Hall, P. Connolly, Coupled dynamics modelling of a floating wind farm with shared mooring lines, in: International Conference on Offshore Mechanics and Arctic Engineering, volume 51319, American Society of Mechanical Engineers, 2018, p. V010T09A087.

[25] P. Connolly, M. Hall, Comparison of pilot-scale floating offshore wind farms with shared moorings, Ocean Engineering 171 (2019) 172–180.

[26] E. Lozon, M. Hall, Coupled loads analysis of a novel shared-mooring floating wind farm, Applied Energy 332 (2023) 120513.

[27] J. Jonkman, Definition of the Floating System for Phase IV of OC3, Technical Report NREL/TP-500-47535, National Renewable Energy Lab.(NREL), Golden, CO (United States), 2010.

[28] J. Jonkman, S. Butterfield, W. Musial, G. Scott, Definition of a 5-MW reference wind turbine for offshore system development, Technical Report NREL/TP-500-38060, National Renewable Energy Lab.(NREL), Golden, CO (United States), 2009.

[29] L. Li, Z. Gao, T. Moan, Joint distribution of environmental condition at five European offshore sites for design of combined wind and wave energy devices, Journal of Offshore Mechanics and Arctic Engineering 137 (2015).

[30] DNV GL, MIMOSA-User's Doumentation Programme Version 5.7, Høvik, Norway, 2003.

[31] SINTEF Ocean, RIFLEX 4.16.0 User Guide, Trondheim, Norway, 2019.

[32] SINTEF Ocean, SIMO 4.16.0 User Guide, Trondheim, Norway, 2019.

[33] D. N. Veritas, Position mooring, offshore standard os-e301, Technical Report, DNV-OS-E301, 2008.

[34] DNV, DNV-ST-0119 Floating wind turbine structures, Oslo, Norway, 2021.

[35] S. K. Chakrabarti, Offshore structure modeling, volume 9, world scientific, 1994.

[36] C. Barrera, R. Guanche, I. J. Losada, Experimental modelling of mooring systems for floating marine energy concepts, Marine Structures 63 (2019) 153–180.

[37] A. Medina-Manuel, E. Botia-Vera, S. Saettone, J. Calderon-Sanchez, G. Bulian, A. Souto-Iglesias, Hydrodynamic coefficients from forced and decay heave motion tests of a scaled model of a column of a floating wind turbine equipped with a heave plate, Ocean Engineering 252 (2022) 110985.

[38] ITTC, Recommended procedures and guidelines: Seakeeping experiments, 2017.

[39] ITTC, Recommended procedures and guidelines: Model tests for offshore wind turbines, 2017.

[40] ITTC, Recommended procedures and guidelines: Floating offshore platform experiments, 2017.

[41] DNV GL, Dnvgl-rp-0286: Coupled analysis of floating wind turbines, Recommend Practice DNVGL-RP-0286; DNV GL: Oslo, Norway (2019).

[42] ITTC, Recommended procedures and guidelines: Analysis procedure for model tests in regular waves, 2017.

[43] Z. Jiang, M. Karimirad, T. Moan, Response analysis of parked spar-type wind turbine considering blade-pitch mechanism fault, International Journal of Offshore and Polar Engineering 23 (2013).

[44] G. Ramachandran, A. Robertson, J. Jonkman, M. D. Masciola, Investigation of response amplitude operators for floating offshore wind turbines, in: The Twenty-third International Offshore and Polar Engineering Conference, OnePetro, 2013.

[45] L. Meng, Y.-p. He, Y.-s. Zhao, J. Yang, H. Yang, Z.-l. Han, L. Yu, W.-g. Mao, W.-k. Du, Dynamic response of 6mw spar type floating offshore wind turbine by experiment and numerical analyses, China Ocean Engineering 34 (2020) 608–620.

[46] J. Yang, Y.-P. He, Y.-S. Zhao, Y.-L. Shao, Z.-L. Han, Experimental and numerical studies on the low-frequency responses of a spar-type floating offshore wind turbine, Ocean Engineering 222 (2021) 108571.

[47] H. Munir, C. F. Lee, M. C. Ong, Global analysis of floating offshore wind turbines with shared mooring system, in: IOP Conference Series: Materials Science and Engineering, volume 1201, IOP Publishing, 2021, p. 012024.

[48] B. T. Pereyra, Z. Jiang, Z. Gao, M. T. Andersen, H. Stiesdal, Parametric study of a counter weight suspension system for the tetraspar floating wind turbine, in: International Conference on Offshore Mechanics and Arctic Engineering, volume 51975, American Society of Mechanical Engineers, 2018, p. V001T01A003.

[49] IEC, 61400-3-1. wind energy generation systems part 3-1: Design requirements for fixed offshore wind turbines., IEC 61400-3-Ed. 1.0 (2019).

[50] W.-t. Hsu, K. P. Thiagarajan, L. Manuel, Extreme mooring tensions due to snap loads on a floating offshore wind turbine system, Marine Structures 55 (2017) 182–199.

[51] DNV, DNV-RP-H103: modelling and analysis of marine operations, Det Norske Veritas, Høvik, Norway (2011).

[52] R. P. Gomes, L. M. Gato, J. C. Henriques, J. C. Portillo, B. D. Howey, K. M. Collins, M. R. Hann, D. M. Greaves, Compact floating wave energy converters arrays: Mooring loads and survivability through scale physical modelling, Applied Energy 280 (2020) 115982.

[53] M. Cabrerizo-Morales, R. Molina-Sanchez, L. Pérez-Rojas, Small-scale study of mooring line tension thresholds based on impulsive load analysis during big floating structure operation and commissioning, Water 13 (2021) 1056.

[54] G. Liang, T. Lopez-Olocco, A. Medina-Manuel, L. S. Ynocente, A. Souto-Iglesias, Z. Jiang, Experimental investigation of two shared mooring configurations for a dual-spar floating offshore wind farm in irregular waves, 2022. Submitted for publication.

Appendix A. Design drawings of the tested models

Fig. A.28 shows the different labeled components used in the construction of the model. The main body is composed of two PVC tubes rigidly assembled together by means of a series of guides and PVC components. (Labels 4, 5, 6, 8 and 9). More details regarding the connections can be seen Details E and F of Fig. A.29. For the coned shaped transition part, a 3D-printed piece was used (Label 7).

Because of the low center of mass of the spar, an important amount of weight made of lead is placed at the bottom part (Label 12). This module is made of a series of lead disks, packed together with a screw. It was fixed to the bottom tube by means of 10 screws and supported by thick Necuron part (Label 2). More details of this connection can be seen in Detail D of Fig. A.29.

As mentioned in Section 3.1, the aluminum frame to reproduce the inertia properties as well to support the DAQ devices, is composed of three Bosch Rexroth extruded profiles (Label 15). The connection with the top tube can be seen in Detail K of Fig. A.29.

Also, as mentioned in Section 3.1 three pulleys were used as the fairlead connections (Label 14). Section H-H shows of Fig. A.29 the 120 *deg* arrangement. In addition, More details of this connection can be seen Detail C of Fig. A.29.

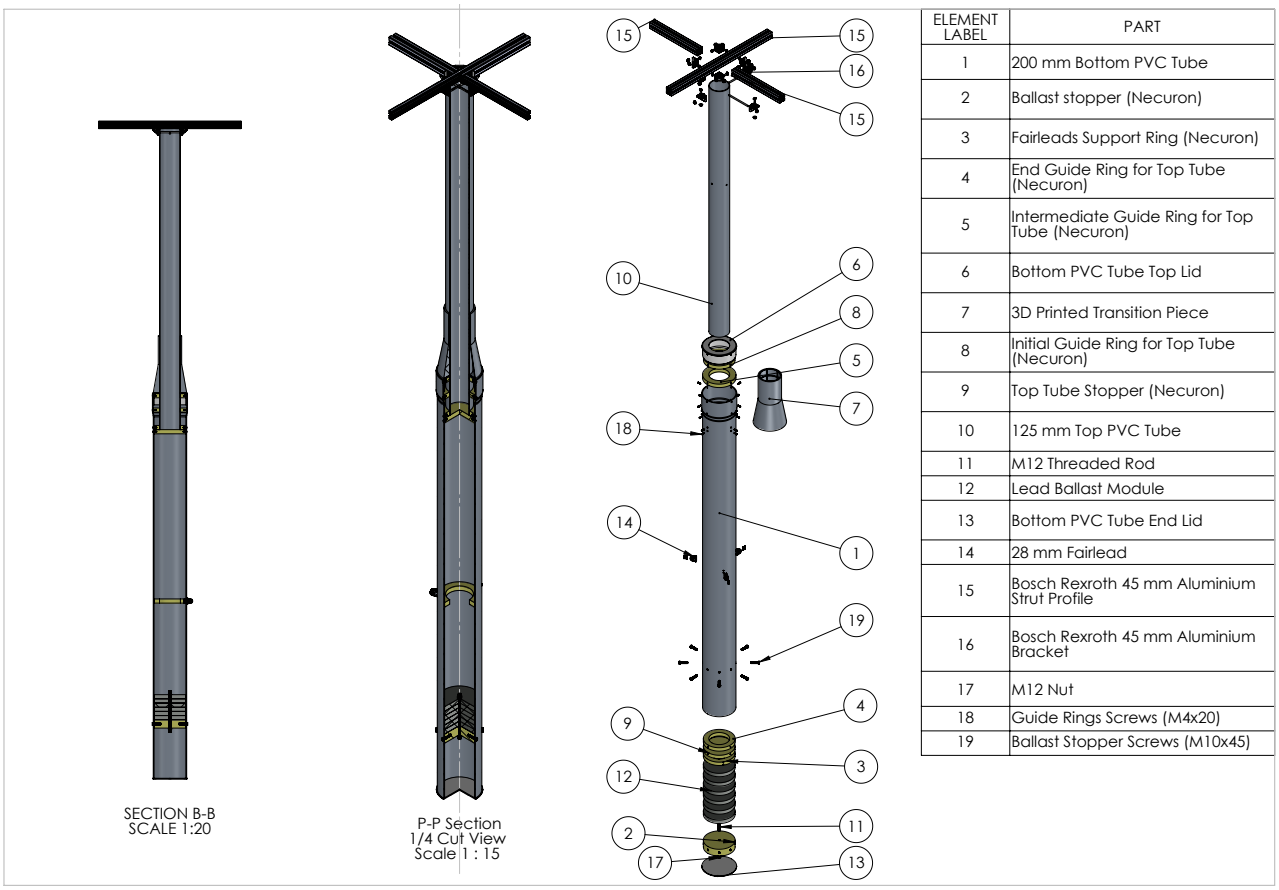

ELEMENT LABEL	PART
1	200 mm Bottom PVC Tube
2	Ballast stopper (Necuron)
3	Fairleads Support Ring (Necuron)
4	End Guide Ring for Top Tube (Necuron)
5	Intermediate Guide Ring for Top Tube (Necuron)
6	Bottom PVC Tube Top Lid
7	3D Printed Transition Piece
8	Initial Guide Ring for Top Tube (Necuron)
9	Top Tube Stopper (Necuron)
10	125 mm Top PVC Tube
11	M12 Threaded Rod
12	Lead Ballast Module
13	Bottom PVC Tube End Lid
14	28 mm Fairlead
15	Bosch Rexroth 45 mm Aluminium Strut Profile
16	Bosch Rexroth 45 mm Aluminium Bracket
17	M12 Nut
18	Guide Rings Screws (M4x20)
19	Ballast Stopper Screws (M10x45)

Figure A.28: Design drawing of the model: component's view.

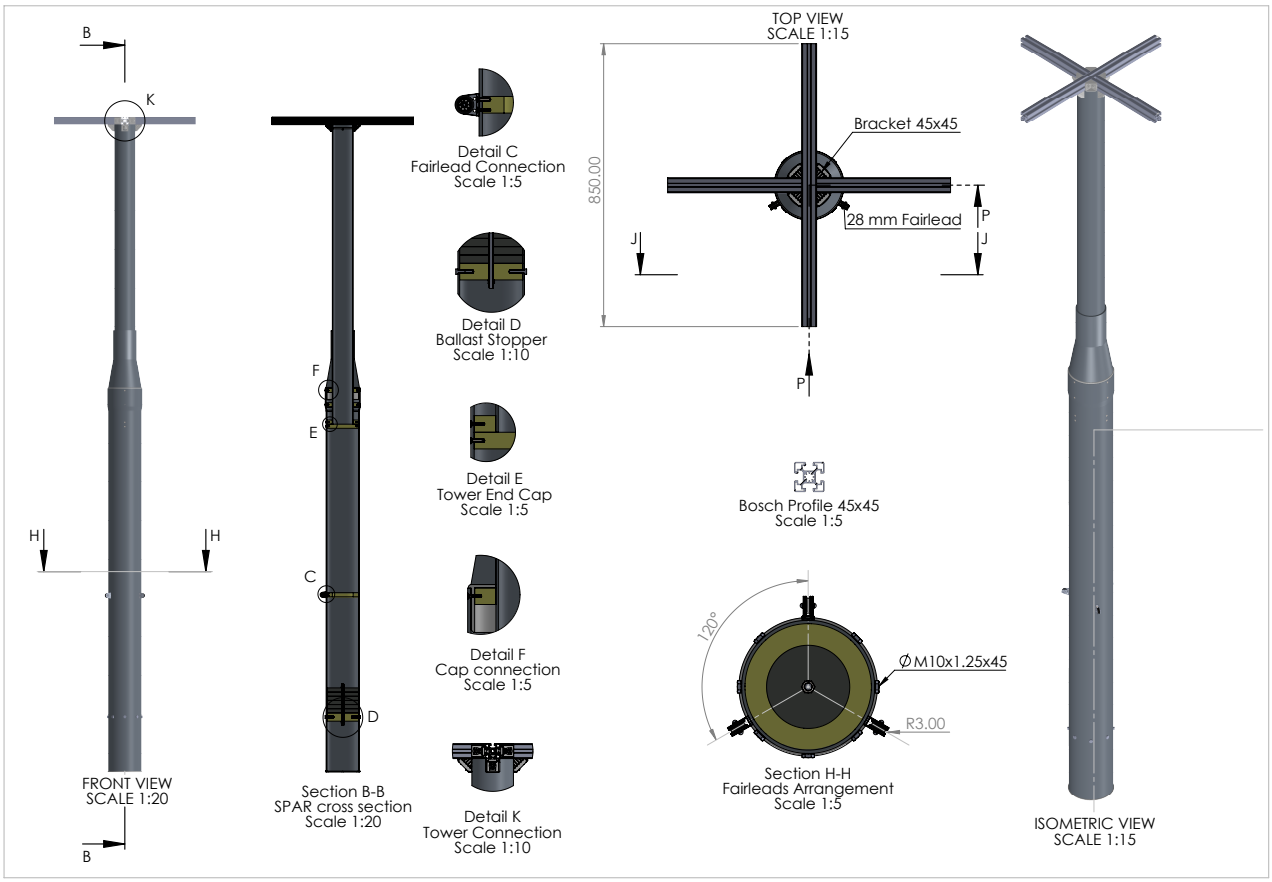

Figure A.29: Design drawing of the model: external view.

Appendix B. Motion responses: analysis through realizations

Appendix B.1. Operational sea state: IRR01 $H_s = 2.57\ m$ and $T_p = 11.12\ s$

Appendix B.1.1. PSDs

PSDs are consistent across realizations and the differences in the low frequency range are attributed to the limited number of cycles for those frequencies.

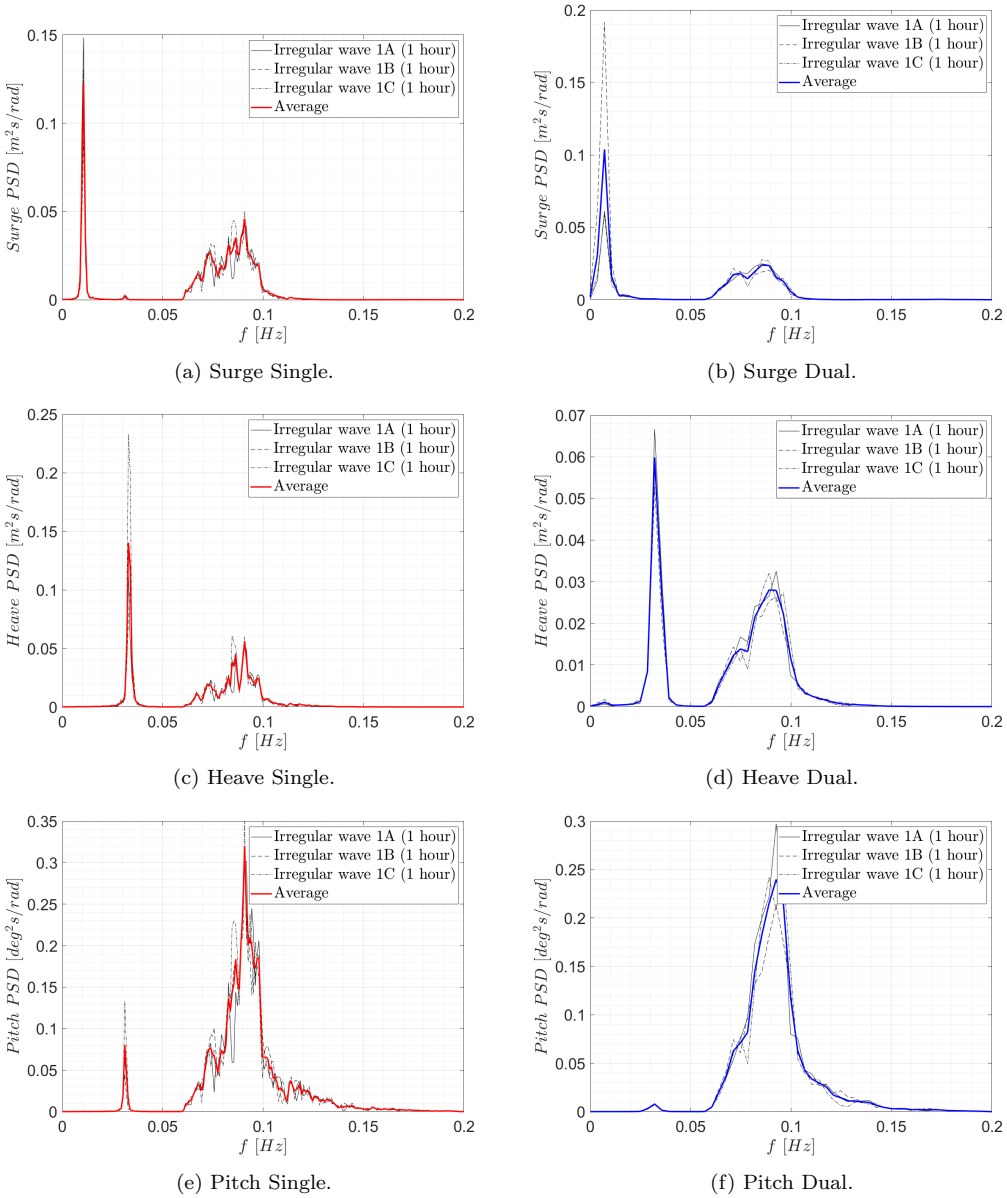

(a) Surge Single.

(b) Surge Dual.

(c) Heave Single.

(d) Heave Dual.

(e) Pitch Single.

(f) Pitch Dual.

Figure B.30: Surge, heave and pitch motion PSDs of all realizations and the average for both configurations. IRR01 ($H_s = 2.57\ m$ and $T_p = 11.12\ s$).

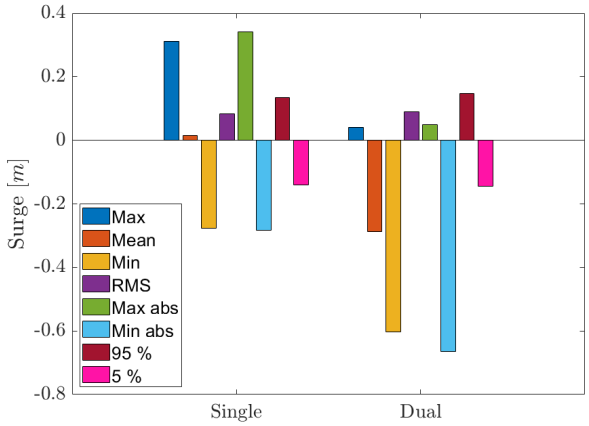

(a) Surge

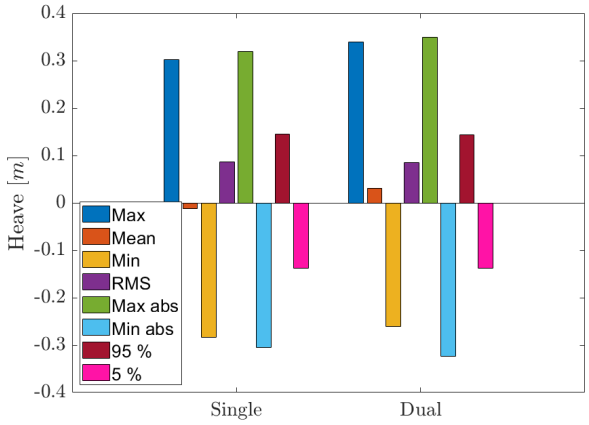

(b) Heave

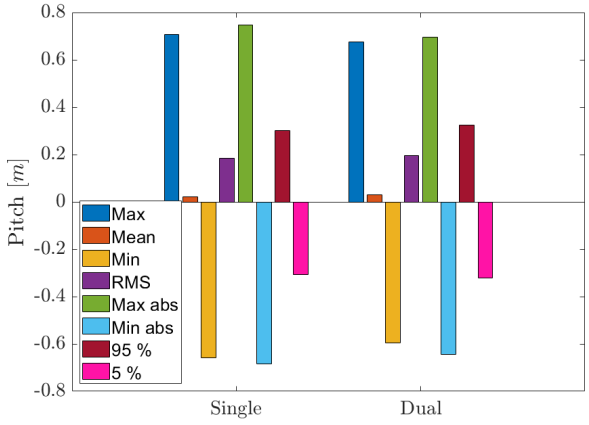

(c) Pitch

Figure B.31: Comparison of surge, heave and pitch motion statistics for the IRR01 wave case ($H_s = 2.57\ m$ and $T_p = 11.12\ s$).

Appendix B.2. Extreme sea state: IRR02 $H_s = 12.7\ m$ and $T_p = 15.45\ s$

Appendix B.2.1. PSDs

PSDs are consistent across realizations and the differences in the low frequency range are attributed to the limited number of cycles for those frequencies.

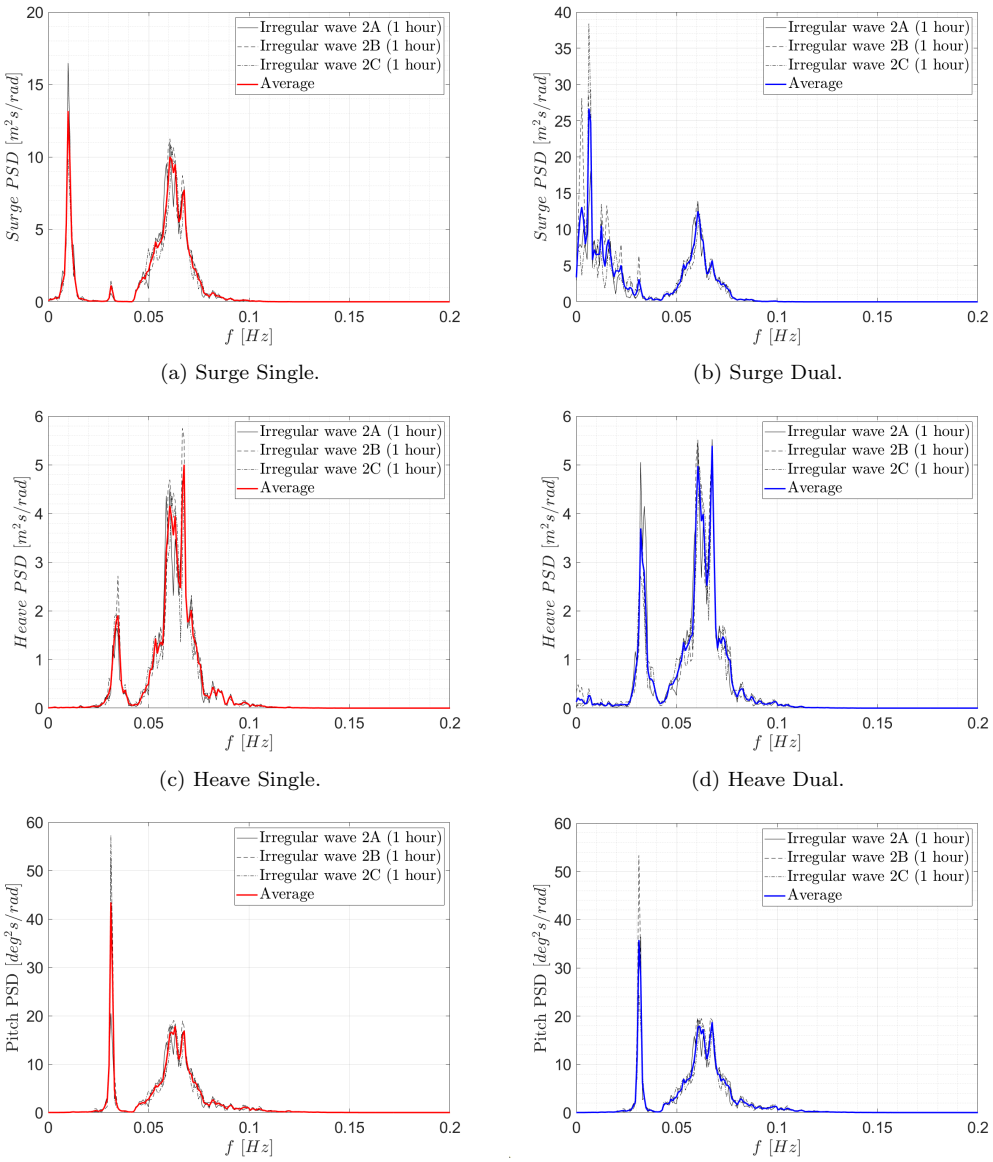

(a) Surge Single.

(b) Surge Dual.

(c) Heave Single.

(d) Heave Dual.

(e) Pitch Single.

(f) Pitch Dual.

Figure B.32: Surge, heave and pitch motion PSDs of individual realizations for the IRR02 wave case ($H_s = 12.7\ m$ and $T_p = 15.45\ s$).

Appendix B.2.2. Statistics

Consistently with the observations in 5.3.1.2, the differences in the pitch motion POEs between the two configurations are also negligible in heave. This is shown in Fig. B.33

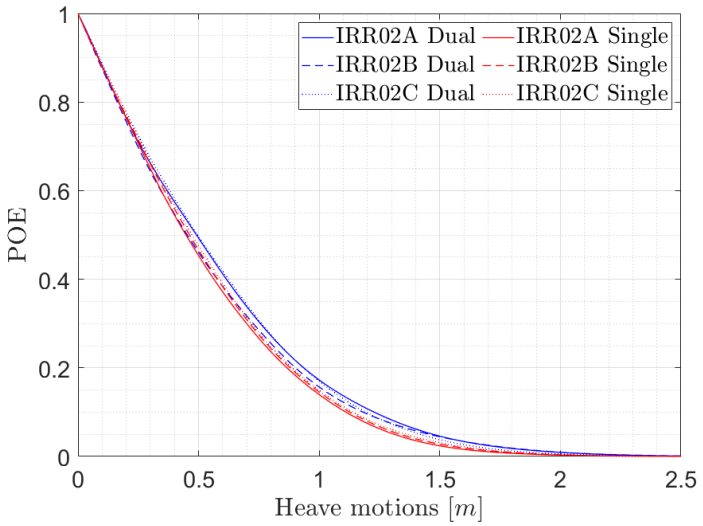

Figure B.33: POE of heave for the IRR02 wave case ($H_s = 12.7\ m$ and $T_p = 15.45\ s$).

A similar consistency is shown in the statistics for this DOF in the extreme wave condition.

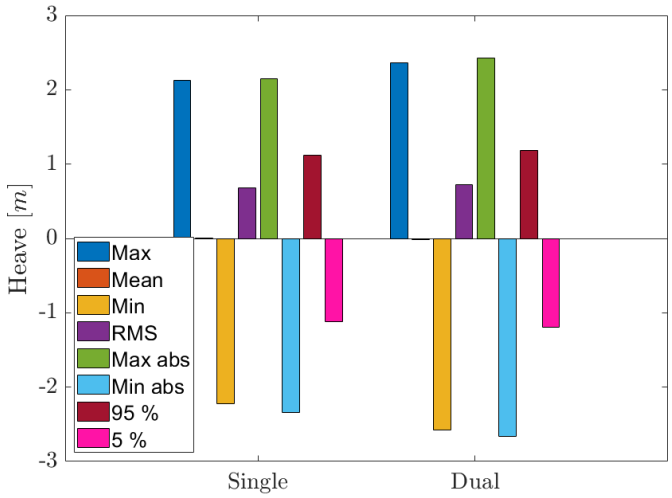

Figure B.34: Comparison of heave motion statistics for the IRR02 wave case ($H_s = 12.7\ m$ and $T_p = 15.45\ s$).

Appendix C. Tensions responses: analysis through realizations

Appendix C.1. Operational sea state: IRR01 $H_s = 2.57\ m$ and $T_p = 11.12\ s$

Appendix C.1.1. PSDs

PSDs are consistent across realizations and the differences in the low frequency range are attributed to the limited number of cycles for those frequencies.

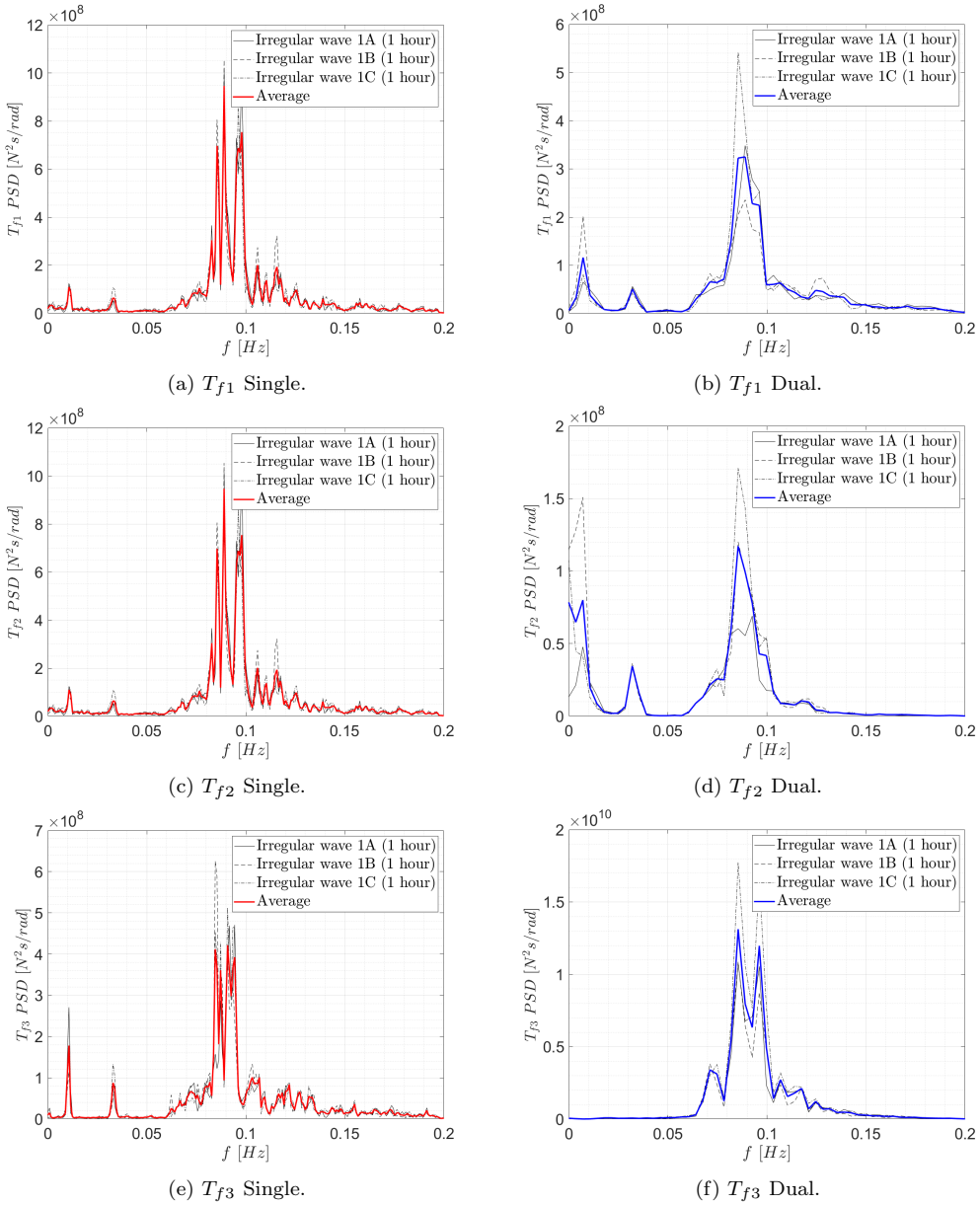

(a) T_{f1} Single. (b) T_{f1} Dual.

(c) T_{f2} Single. (d) T_{f2} Dual.

(e) T_{f3} Single. (f) T_{f3} Dual.

Figure C.35: PSDs of individual realizations of mooring tensions (T_{f1}, T_{f2} and T_{f3}) for the IRR01 wave case ($H_s = 2.57\ m$ and $T_p = 11.12\ s$).

Appendix C.1.2. Statistics

Figs. C.36 and C.37 show the tension statistics for the anchor lines and shared line in the operational sea state. The fairlead tension statistics normalized with the pretension of the anchor lines are close to each other, when comparing both configurations. In the operational sea state, the shared line does not experience snap events, as described in 5.3.3.

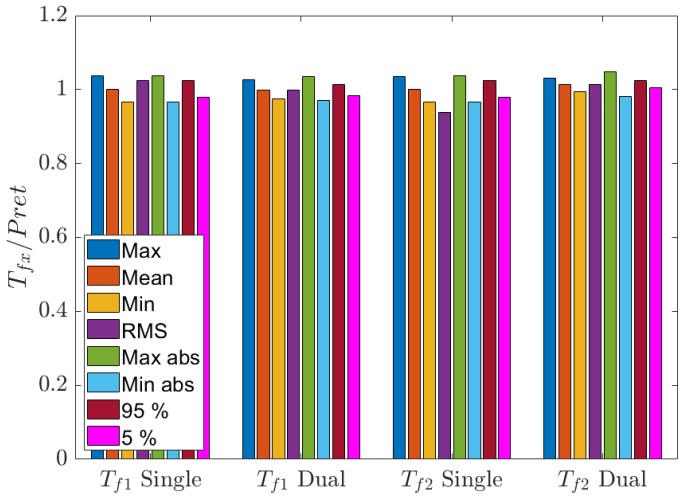

Figure C.36: Statistics of anchor line tensions normalized against pretension for the IRR01 wave case ($H_s = 2.57\ m$ and $T_p = 11.12\ s$).

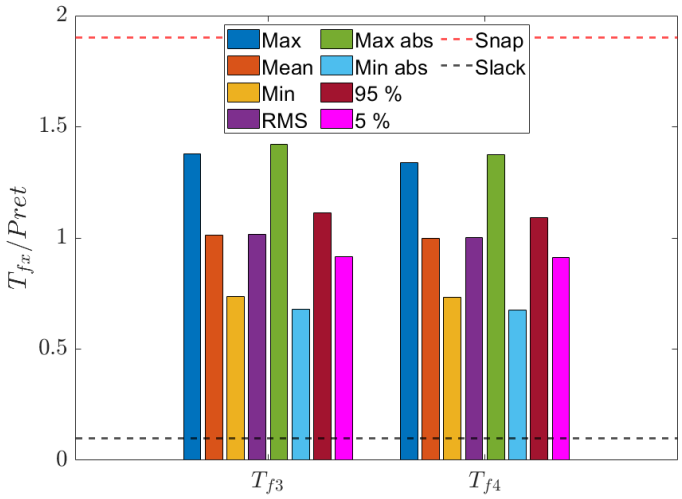

Figure C.37: Statistics of shared line tensions normalized against pretension for the IRR01 wave case ($H_s = 2.57\ m$ and $T_p = 11.12\ s$).

Appendix C.2. Extreme sea state: IRR02 $H_s = 12.7\ m$ and $T_p = 15.45\ s$

Appendix C.2.1. PSDs

PSDs are consistent across realizations and the dispersion in the low frequency range is attributed to the limited number of cycles for those frequencies.

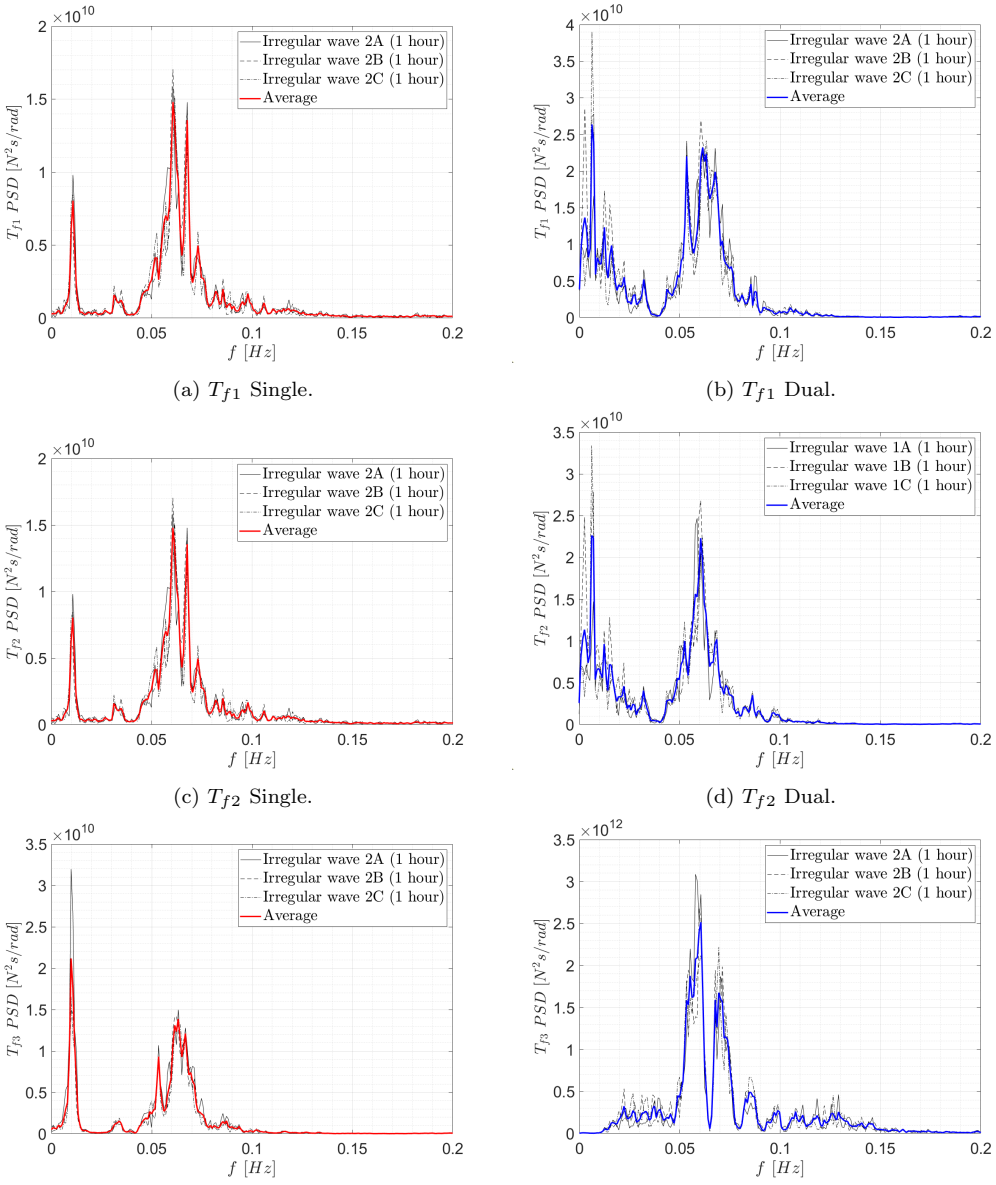

(a) T_{f1} Single.

(b) T_{f1} Dual.

(c) T_{f2} Single.

(d) T_{f2} Dual.

(e) T_{f3} Single.

(f) T_{f3} Dual.

Figure C.38: PSDs of individual realizations of mooring tensions (T_{f1}, T_{f2} and T_{f3}) for the IRR02 wave case ($H_s = 12.7\ m$ and $T_p = 15.45\ s$).

Appendix C.2.2. Statistics

Appendix C.2.2.1 Anchor lines

POEs of the fairlead tension for the other anchor line that was not presented in Section 5.3.2.2 (T_{f2}) are shown in Fig. C.39a. Consistency across realizations is also appreciated in these figures. The considerable reduction of yaw stiffness for not using the delta connection explained in [27], together with minor errors in the construction of the model, might be accountable for differences that appear between T_{f1} and T_{f2} in the dual-spar configuration. In order to check the relevance of such lack of balance, Fig. C.39b shows POEs for the averaged fairlead tension T_{f1} and T_{f2}. As shown, when averaging both tensions, a good similarity with the Single configuration is found. It could be interesting in the future campaigns to assess the influence of the implementation of the delta connection on these disparities between anchor line tensions for the dual-spar configuration.

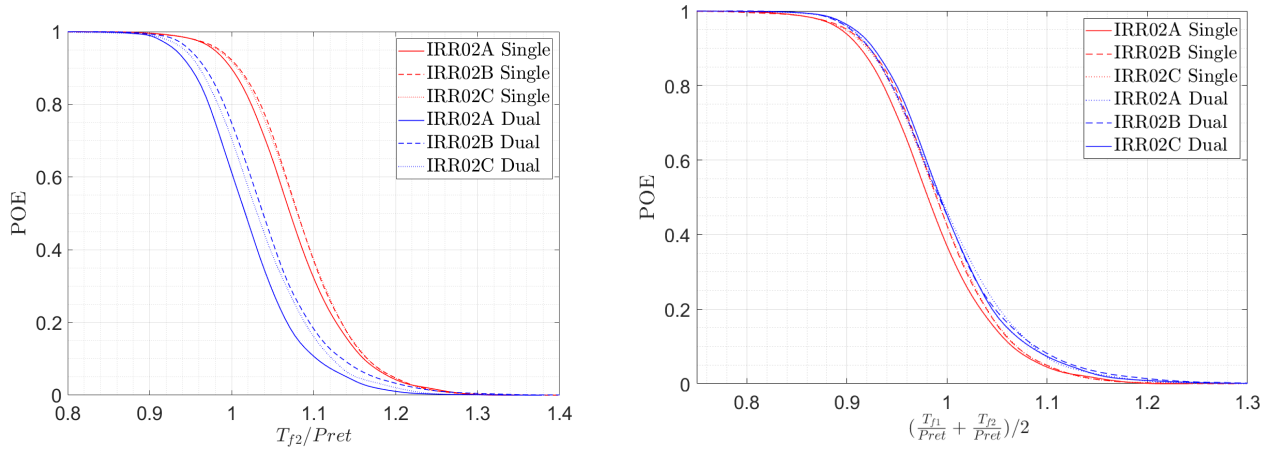

(a) T_{f2} normalized with the pretension

(b) Averaged T_{f1} and T_{f2} normalized with the pretension.

Figure C.39: Comparison of POEs of mooring tensions for the IRR02 wave case ($H_s = 12.7\ m$ and $T_p = 15.45\ s$).

Appendix C.2.2.2 Shared line

Fig. C.40 shows a comparison between the fairlead tensions of the shared line in Spar 1 (T_{f3}) and Spar 2 (T_{f4}). As can be seen, the tensions response is similar for both fairleads. The same analysis described in Section 5.3.3 for the snap/slack condition has been performed. Some small differences are encountered in the peaks, and therefore more slack/snap events happen during the time histories. These differences appear to be caused by motions of the springs used to scale the stiffness of the line (see Table 5) during the experiments.

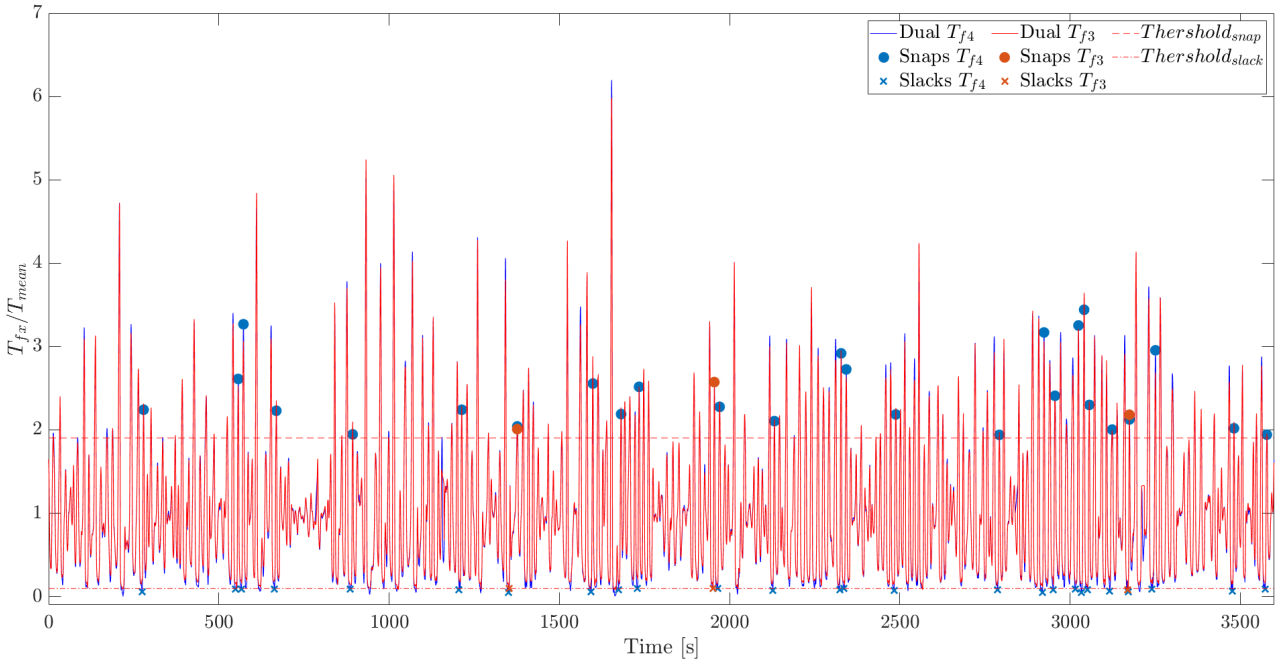

Figure C.40: Fairlead tension T_{f3} and T_{f4} of the shared line for the wave case IRR02B. The snap/slack criteria and events are also shown.